A Rational Dynamical-Systems Approach to Plankton Population Modelling

Andrew Michael Edwards

University of Leeds
Department of Applied Mathematical Studies

Submitted in accordance with the requirements for the degree of
Doctor of Philosophy

September 1997

The candidate confirms that the work submitted is his own and that appropriate credit has been given where reference has been made to the work of others.

Abstract

Understanding the dynamics of plankton populations is of major importance since plankton form the basis of marine food webs throughout the world's oceans and play a significant role in the global carbon cycle. In this thesis we examine the dynamical behaviour of plankton models, exploring sensitivities to the number of variables explicitly modelled, to the functional forms used to describe interactions, and to the parameter values chosen. The practical difficulties involved in data collection lead to uncertainties in each of these aspects of model formulation.

The first model we investigate consists of three coupled ordinary differential equations, which measure changes in the concentrations of nutrient, phytoplankton and zooplankton. Nutrient fuels the growth of the phytoplankton, which are in turn grazed by the zooplankton. The recycling of excretion adds feedback loops to the system. In contrast to a previous hypothesis, the three variables can undergo oscillations when a quadratic function for zooplankton mortality is used. The oscillations arise from Hopf bifurcations, which we track numerically as parameters are varied. The resulting bifurcation diagrams show that the oscillations persist over a wide region of parameter space, and illustrate to which parameters such behaviour is most sensitive. The oscillations have a period of about one month, in agreement with some observational data and with output of larger seven-component models. The model also exhibits fold bifurcations, three-way transcritical bifurcations and Bogdanov-Takens bifurcations, resulting in homoclinic connections and hysteresis.

Under different ecological assumptions, zooplankton mortality is expressed by a linear function, rather than the quadratic one. Using the linear function does not greatly affect the nature of the Hopf bifurcations and oscillations, although it does eliminate the homoclinicity and hysteresis. We re-examine the influential paper by Steele and Henderson (1992), in which they considered the linear and quadratic mortality functions. We correct an anomalous normalisation, and then use our bifurcation diagrams to interpret their findings.

A fourth variable, explicitly modelling detritus (non-living organic matter), is then added to our original system, giving four coupled ordinary differential equations. The dynamics of the new model are remarkably similar to those of the original model, as demonstrated by the persistence of the oscillations and the similarity of the bifurcation diagrams. A second four-component model is constructed, for which zooplankton can graze on detritus in addition to phytoplankton. The oscillatory behaviour is retained, but with a longer period. Finally, seasonal forcing is introduced to all of the models, demonstrating how our dynamical systems approach aids understanding of model behaviour and can assist with model formulation.

Acknowledgements

First and foremost I thank Professor John Brindley for his enthusiastic supervision and lively discussions throughout the course of my research, and for providing me with ample opportunity to attend various workshops and conferences. Such attendance enabled me to benefit from the advice and guidance of Dr. John Steele (Woods Hole Oceanographic Institution, USA), Dr. Trevor Platt (Bedford Institute of Oceanography, Canada), Dr. Shubha Sathyendranath (Dalhousie University, Canada) and Dr. Michael Fasham (Southampton Oceanographic Centre). Such help is greatly appreciated, particularly with regards to aspects of model formulation.

Andrew Yool (University of Warwick) has been invaluable in enthusiastically answering many of my biological questions, and in participating in many insightful discussions over recent months, most of which were actually work-related. Closer to home, Dr. Jon Pitchford, Louise Matthews and Rob Clother have helped with the understanding and clarification of various aspects of this work.

Thanks also to the other members of the Biolunch group, plus the staff and 'non-bio' postgraduate students in the School of Mathematics for contributing to an enjoyable and stimulating working environment. In particular, thanks to Dr. Tim Hainsworth for keeping the computers working and coping with our ever-increasing demands for disk space. And thanks to Will Hyslop for generous use of his PC.

To friends in Leeds and elsewhere – thanks for being supportive and taking an interest in what I've been doing (or at least pretending to!).

I thank the University of Leeds for funding this work through a William Wright Smith Scholarship.

And to Mum, Dad and Chris – thank you for your continual love and support, for which I am truly grateful.

To Kester,

forever in my thoughts.

Contents

List of Figures

List of Tables

Chapter 1

Introduction

1.1 Why model plankton populations?

The sunlit surface waters of the world's oceans are populated by tiny plankton. Plankton is a general term used to describe freely-floating and weakly-swimming marine and freshwater organisms. Plankton are broadly divided into two groups. Phytoplankton are the plants and are mostly microscopic in size and unicellular; they are consumed by zooplankton, the animals. The zooplankton in turn are eaten by larger organisms, and consequently plankton form the basis of food webs around the world, supporting a diverse range of life, from shrimps and cod to blue whales and man.

Perhaps of greater importance is phytoplankton's role in influencing the Earth's climate. Phytoplankton synthesise energy-rich organic molecules from inorganic materials via the process known as photosynthesis, which requires carbon dioxide that is dissolved in seawater. Although most of the organic matter is rapidly recycled in the surface waters, a small proportion sinks to the deep water in the form of faeces and dead plants and animals. This *biological pump* has led, for example, to carbon concentrations in the deep waters of the North Pacific exceeding those in the surface waters by 20% (Evans and Fasham, 1993). Ocean circulations eventually bring deep waters to the surface, but such processes can take hundreds of years. On a shorter time-scale, the carbon dioxide lost from the surface waters is replenished by carbon dioxide from the atmosphere. The amounts of carbon dioxide entering and leaving the oceans are usually close to global balance each year, but at present it is not known whether likely feedbacks from marine biota in response to climate-related changes will act in a positive or a negative direction (Denman *et al.*, 1996), either mitigating or enhancing the greenhouse effect.

Understanding the dynamics of plankton populations is therefore of major importance in predicting future fish harvests and in assessing the possible consequences of global warming. Direct measurement of plankton biomass is difficult and expensive. Historically, data has come from analyses of samples taken 'over the side' from ships, and is inevitably sparse and patchy. More recently it has been possible to use satellite observations, though the identification and interpretation of the part of the radiation spectrum which relates to plankton is a formidable task (Robinson, 1990).

In this situation, the modelling of plankton populations is an essential tool to improve our understanding of the physical and biological processes which affect the population dynamics. Models are thus used to not only to simulate ecosystems and predict future behaviour under possibly changing climate scenarios, but also to enhance our knowledge of oceanic processes.

The word plankton comes from a Greek word (πλανκτος) meaning wandering or drifting, and was introduced by the German scientist Victor Hensen in 1887. At around the same time, the French mathematician Henri Poincaré was laying down the foundations for a geometric approach to analysing the dynamics of nonlinear systems. In this thesis we invoke the theory of dynamical systems that has arisen from Poincaré's pioneering work to investigate the behaviour of plankton population models.

1.2 The physics of the plankton's environment

Phytoplankton require sunlight and nutrients to perform photosynthesis. The amount of sunlight that an area of ocean receives depends upon factors such as latitude, time of day, time of year and atmospheric transmittance. The tilt of the earth's axis combined with the earth's orbit around the sun provide the seasonal variation, which is most pronounced at the poles and least pronounced at the equator. Geometric calculations give the flux of radiation per unit area at the sea-surface (neglecting atmospheric effects) as a function of latitude, time of day and time of year. However, the variation in the transmission of light through the atmosphere due to absorption and scattering by clouds is much harder to model. This variable transmission can have a dramatic effect on the amount of radiation reaching the sea surface (e.g. Figure 1.2 of Sathyendranath and Platt (1990) shows a large variation in the observed surface irradiance during a seven-week cruise), and different cloud-cover algorithms give quite different results, as shown by Figure 4 of Fasham (1993).

Some of the light that does reach the ocean gets reflected from the surface, depending on the angle of incidence with which the light strikes the water. When the light then penetrates the water column, the water itself absorbs some of the light. In the clearest tropical water sufficient light for photosynthesis may reach a depth of 120 m. But elsewhere, living and non-living particles in the water absorb or reflect light, restricting photosynthesis to much shallower depths. The modelling of this attenuation of light through the water column is discussed in Chapter 2 and Appendix A.

Energy from the sun plays a second important role in defining the plankton's environment, by heating the surface waters. Warm water is less dense than, and hence floats upon, colder water. The narrow depth-range which exhibits the most rapid change in temperature is called a *thermocline*, and acts to separate the warm surface layer of water from the colder deeper layer. The surface layer is kept well-mixed by wind-induced wave action, and hence is called the *mixed layer*. In many models (e.g. Fasham *et al.*, 1990; Steele and Henderson, 1992) it is thus assumed to be a biologically homogeneous environment.

A strong thermocline is a persistent feature of tropical oceans, since the lack of seasonal variation provides warm conditions throughout the year. In polar seas a slight thermocline may appear only during the short summer period. In the intermediate temperate waters, no thermocline occurs in the winter due to the cold stormy conditions. With the onset of the warm and calm conditions of spring, a thermocline forms and persists through the summer months. In autumn the amount of solar energy decreases with the sun appearing lower in the sky and the days becoming shorter, and eventually the density of the surface waters reaches a similar value to that of the underlying waters. The two water masses then become mixed, and the thermocline disappears for the winter.

The stable mixed layer of the tropical waters, together with favourable year-long sunlight, meant that in the late nineteenth century most biologists expected to find more plankton in these waters than in the colder oceans. However, Victor Hensen's Plankton Expedition in 1889 found the reverse to be true. This was later deduced to be due to the lack of nutrients in the warmer waters - because the thermocline persists all year long, when the nutrients get used up in the mixed layer they cannot be easily replenished, since there is little mixing with the deep nutrient-rich water. Whereas during winter in the temperate regions, the thermocline breaks down and the deep nutrient-rich water becomes mixed with the depleted surface water. When the thermocline forms in spring the mixed layer contains nutrient-rich water, and together with the favourable sunlight conditions provides the perfect environment for phytoplankton to flourish - a *spring bloom* can then occur.

However, 20% of the world's open-ocean surface waters are light-rich and abundant with the major nutrients required by phytoplankton, such as nitrate and phosphate, but phytoplankton populations remain low. These so-called *high-nitrate, low-chlorophyll* (HNLC) regions are the eastern equatorial Pacific, the ice-free Southern Ocean and the open subarctic North Pacific Ocean. Recent ambitious and successful experiments in the former of these regions investigated whether extremely low concentrations of iron, an essential trace element required by phytoplankton, have the potential to prohibit phytoplankton from fully utilising the major nutrients (Martin *et al.*, 1994; Frost, 1996; Coale *et al.*, 1996). The experiments involved infusing dissolved iron into the water from a ship, staying with the iron-enriched patch of water, and monitoring the biological and biogeochemical changes in the surface waters. Results from the second experiment, IronEx II, included a 20-fold increase in phytoplankton abundance coupled with a reduction in half of nitrate concentration

(Coale *et al.*, 1996), and a three-fold increase in the concentration of dimethyl sulphide (Turner *et al.*, 1996). Dimethyl sulphide is formed from the breakdown of dimethylsulphonium propionate, a salt produced by phytoplankton, and it can react in the atmosphere to produce particles about which water vapour condenses to form clouds (see Fell and Liss, 1993). This is another example of plankton's importance, since any large-scale changes in cloud formation could have profound climatological consequences.

1.3 The biology of plankton

In addition to being partitioned into phytoplankton and zooplankton, plankton have also been classified by their size. The classes range from macroplankton, 0.2 - 2 mm in size, to the ultraplankton which are less than 5 μm (= 5 x 10^{-6} m), although these ranges are not absolute definitions, and different authors use different values (e.g. Nybakken, 1982, and Tait, 1981). The ultraplankton are too small to be captured in nets, since the required mesh-size would be so fine that when the nets were pulled behind a boat, the water would not be able to pass through the nets. Ultraplankton can be obtained by filtering water samples on fine filters or by centrifuging water samples. Exceptionally large plankton, above 2 mm in size, are called megaplankton.

Another division of plankton concerns the life history of the organisms. Holoplankton (permanent plankton) are organisms who spend their entire life span as plankton, whilst meroplankton (temporary plankton) are organisms who spend only a portion of their life span as plankton. The great majority of marine animals spend hours, and often several weeks, as developmental stages such as eggs or larvae, during which time they are considered as meroplankton. For the purpose of this thesis we only need to consider the partition of plankton into phytoplankton and zooplankton, and we now give a short summary of the nature of the constituents of these two divisions.

1.3.1 Phytoplankton

The larger phytoplankton consist predominantly of two groups, diatoms and dinoflagellates. The majority of diatoms are unicellular, with an external skeleton that consists largely of silica, giving a transparent glassy quality. The skeleton comprises two overlapping halves, called valves, which in the simplest diatoms overlap to fit together as a simple flat cylinder, much like a petri dish. Between species, the valves can vary in shape, being circular, elliptical, triangular, square or polygonal, and some have large projections such as protruding spines. Some diatoms join up to form chains by interlocking these spines, and others unite together by means of sticky secretions.

Simple asexual division of the cell is the usual method of reproduction of diatoms. Under favourable environmental conditions this may occur three or four times a day, yielding a rapid growth in numbers. The two valves gradually separate, resulting in two daughter cells which each grow a new second valve.

During unfavourable conditions for growth, some diatoms can form resistant spores which sink to the bottom, and in shallow waters may return at a later date to germinate. In polar regions, spores become trapped in sea ice during the winter months, and then germinate when the ice melts.

The dinoflagellates possess, as their name suggests, two flagella which they use to move themselves through the water, but such powers of locomotion are so weak that the organisms do not move far compared to the distances that they are transported by the water motion. Typically, one flagellum is wrapped around the cell, lying within a groove encircling the cell. The second flagellum is like a whip projecting behind the cell, and the combined effects of the movement of the flagella drive the organism forward along a spiral path. Unlike diatoms, dinoflagellates rarely form chains, but they do reproduce by asexual division.

Dinoflagellates are capable of producing toxins. When dinoflagellates are extremely abundant (hundreds of thousands of cells per millilitre of water in some cases) the cumulative effects of the toxins may affect other organisms, causing mass mortality. Such extreme concentrations, or blooms, are called *red tides* because of the discolouration of the water. *Red tides* is a general term covering more than just toxic blooms which colour the water red - the water can also turn brown or green, or not be discoloured at all. Furthermore some blooms can discolour the water but are not toxic.

Anderson (1994) gives a lucid account of some of the devastating effects that red tides can have on marine organisms and humans. In 1987, 14 humpback whales died and were washed ashore in Cape Cod Bay, on the eastern coast of the USA. Anderson and many other scientists concluded, after intense investigations, that the most likely cause of these mortalities was that toxins produced by dinoflagellates had worked their way up the food web, via zooplankton and mackerel. The whales may have been killed directly by the toxins, or may have become disorientated and unable to resurface after diving.

Humans can be directly affected by toxins when they eat shellfish, such as clams or mussels, which have consumed the phytoplankton. The toxins accumulate in the tissues of the shellfish, but only slightly harm the shellfish. Sometimes one clam can contain enough toxin to kill a human; over 300 deaths have been documented worldwide. Human illnesses from poisonings include diarrhoea, abdominal pain, dizziness and permanent loss of short-term memory.

Some dinoflagellates are highly pigmented, and in large numbers can give the water a distinctive green, red or yellow tint. Some species are even highly bioluminescent. An example is *Noctiluca* which sometimes occurs in swarms around the British Isles, and their luminescence can be visible to the naked eye when stimulated by the breaking waves on a beach or in the wake of a boat.

The remaining constituents of phytoplankton include blue-green algae, coccolithophores and silicoflagellates. Despite being classed as a blue-green alga, *Trichodesmium erythraeum* is actually red in colour, a feature which gives the Red Sea its name.

1.3.2 Zooplankton

The group of zooplankton known as copepods dominate the zooplankton throughout the world's oceans. These small crustaceans are of vital importance to oceanic ecosystems, since by grazing on the phytoplankton they provide the link between the primary producers, the phytoplankton, and all the carnivorous creatures, great and small.

Copepods are generally between one and several millimetres in length, and swim weakly with a characteristic jerky movement. They capture their food either by means of a complex filtering mechanism that sieves phytoplankton from the water, or by grasping phytoplankton with their appendages. Copepods predominantly feed on phytoplankton, although some are carnivorous and some are omnivorous. Zooplankton can also feed on detritus, which consists of dead plankton and faecal pellets, and bacteria (Fasham *et al.*, 1990). The models investigated in Chapters 3-6 consider zooplankton grazing solely on phytoplankton, whereas in Chapter 7 we investigate the effect of allowing zooplankton to additionally feed on detritus.

Copepods reproduce sexually, with the sperm transferred to the female as packaged spermatophores. The fertilised eggs hatch as *nauplius* larvae and progress through six distinct naupliar stages and then five *copepodite* (juvenile) stages before becoming sexually active adults. This cycle typically takes about two months.

Other types of zooplankton include fish larvae, arrowworms, salps and krill, the latter forming the diet of blue whales, the largest animals on Earth.

The general background information concerning oceanographic processes presented in these introductory sections has been taken from the books by Parsons and Takahashi (1973), Bougis (1976), Raymont (1980, 1983), Tait (1981), Nybakken (1982) and Thurman (1997).

1.4 Plankton population models

There have been numerous plankton models produced over the past few decades, varying in temporal, biological, chemical and physical structure, with many differences in the mathematical formulae used to model these processes. The models comprising of differential equations may be crudely divided into two classes.

The first class, containing models composed of many coupled nonlinear differential equations, is amenable only to numerical experimentation. The seven-component mixed-layer model formulated by Fasham *et al.* (1990) is an example. It consists of seven coupled ordinary differential equations to model the state variables, plus two time-dependent functions to represent the seasonal changes in mixed-layer depth and incident radiation. These two functions are used to force the system through the year. The model has a total of 30 parameters, some of which are so difficult to measure or prescribe values to that they are kept free, and their values adjusted to try and fit the model to data from Bermuda Station "S" near Bermuda, 1120 km east of South Carolina in the Atlantic Ocean. This ecosystem model has been coupled with a general circulation model of the North Atlantic (Fasham *et al.*, 1993; Sarmiento *et al.*, 1993), to more explicitly incorporate the physics of the ocean. The biological model has since been modified by Fasham (1993), and the modified model has provided the base model for investigations by Yool (1997) regarding the number of components that need to be retained in order to reproduce the results of the full system.

Whilst Fasham's models consider just two plankton compartments, one for phytoplankton and one for zooplankton, Hofmann and Ambler (1988) explicitly modelled two phytoplankton size classes, plus five stages of zooplankton. With further equations representing nitrate, ammonium and detritus, the model has a total of ten coupled ordinary differential equations. The model of Taylor *et al.* (1993) has twelve ordinary differential equations, yet the authors still refer to it as a 'a simple model' - a view taken from a biological rather than a mathematical viewpoint. The degree of mathematical complexity of such models renders them too complex to approach from a dynamical systems viewpoint, in particular using analytical (non-numerical) techniques.

The second class of models covers models consisting of only two or three ordinary differential equations, (e.g. Steele and Henderson, 1981; Evans and Parslow, 1985;

Truscott and Brindley, 1994). These recognise the uncertainties and shortcomings in observational data, and refrain from trying to fit model output to specific data, instead seeking to capture aspects of the qualitative behaviours to be expected from the models.

The models investigated in this thesis are based on the nutrient-phytoplankton-zooplankton (NPZ) model of Steele and Henderson (1981), extended in the manner of Steele and Henderson (1993). The NPZ model will be described in detail in Chapter 2, and amendments to it will be detailed in subsequent chapters. The two-component phytoplankton-zooplankton model of Steele and Henderson (1981) has since been used as a fish model (whereby the variables represent fish populations rather than plankton populations) by Collie and Spencer (1994) to model fluctuations in abundances of Pacific hake (predator) and Pacific herring (prey) off the west coast of Vancouver Island, British Columbia. Evans and Parslow (1985) showed, with an NPZ model and a PZ model, how a spring phytoplankton bloom may occur even without a rapid shallowing of the mixed layer, provided that the phytoplankton growth rate is high enough.

Steele and Henderson (1992) demonstrated that the choice of functional form and parameter values used to model zooplankton mortality can have a major influence on the dynamics of simple models. They found that, for their particular parameter values, limit cycle behaviour (unforced oscillations) which occurs for linear zooplankton mortality does not occur when quadratic zooplankton mortality is used. In contrast to this, our first NPZ model, investigated in Chapter3, has quadratic zooplankton mortality and exhibits limit cycle behaviour over broad ranges of parameters. This motivates us to re-examine our NPZ model, but with linear rather than quadratic zooplankton mortality, in Chapter 4. Our results then prompt a review of the results of Steele and Henderson (1992) in Chapter 5.

Our crude separation of models into two classes may seem to suggest that there is no interchange of ideas between 'small' and 'large' models, but this is certainly not so. Indeed, results from simple models can indicate to modellers dealing with large models which aspects of model formulation are most crucial in determining the output. In particular, the works of Evans and Parslow (1985) and Steele and Henderson (1992) are often considered when larger models are being formulated (e.g. Fasham, 1993).

In this thesis we shall not consider species diversity of plankton, or spatial patchiness of plankton populations. However, these two features of plankton populations have been the focus of recent research. Pitchford (1997) has extended the work of Truscott (1994) to explicitly model multiple species of plankton. Whilst Matthews and Brindley (1997) have added diffusion-driven instability and spatially-varying forcing to Truscott's model, concluding that the former mechanism is unlikely to be a mechanism capable of producing observable spatial patterns. One of the important features of simple models is that they are amenable to such extensions in ways that the changes in behaviour due to the modifications can be understood. This is evident in the work presented in Chapters 6 and 7, in which we add a fourth component, explicitly modelling detritus, to the original NPZ model.

Although the models in this thesis consist of deterministic differential equations, other types of equations have been used to model plankton populations. Woods and Barkmann (1994, and references therein) have developed the Lagrangian Ensemble method. 'Families' of plankton follow trajectories through the environment, which is described by chemical and physical values at points on a fixed array of spatial locations (usually one metre cubes). Each 'family' comprises an identical set of plankton organisms - to track each single organism would be too computationally expensive. Demographic analysis can be performed, since the progress of each family (involving birth, natural mortality and predation) is recorded chronologically in a 'Parish Register'. For models comprising of ordinary differential equations, such as those in this thesis, the mixed layer is assumed to be a homogeneous environment, and biological entities are expressed as volumetric concentrations, preventing the abstraction of detailed demographic information.

Further approaches that have been advocated as useful tools for biological oceanography come from the fields of network analysis, thermodynamics and statistical mechanics (Platt *et al.*, 1981; Ulanowicz and Platt, 1985). A branch of dynamical systems that we do not consider in this thesis involves coupled maps, or difference equations. A recent model proposed by Platt *et al.* (1997) consists of a pair of coupled maps, and is used to show how intermittent forcing of the mixed-layer depth may produce an HNLC situation.

Over 100 models are surveyed by Totterdell (1993), who groups them together according to features of their formulation, such as physical structure, temporal forcing and how many biological components are explicitly modelled.

Ryabchenko *et al.* (1997) have recently investigated the occurrence of short-term oscillations which can arise in both phytoplankton data (Williams, 1988) and in the output of large ecosystem models (Fasham, 1993, Fasham *et al.*, 1993). Such oscillations occur some years in the North Atlantic Ocean during the summer, and have a period of the order of one month. For the remainder of the year such short-term oscillations do not occur. This suggests that the seasonal forcing of some of the parameters may be taking the system from a region of parameter space where the unforced system would be attracted to a stable steady state, into a region during the summer months where the unforced system would exhibit stable oscillatory behaviour. In this thesis we show such regions of oscillatory behaviour for each of our models, as defined by the location of Hopf bifurcations, and incorporate seasonal forcing into all of our models in Chapter 8.

McCauley and Murdoch (1987) analysed data from over 30 studies in 12 countries which reported the seasonal dynamics of the crustacean zooplankton *Daphnia* and their phytoplankton prey across a wide variety of freshwater habitats. Excluding data from the spring rise and fall in populations, which is driven by external environmental factors, they found internally-driven cycles of the populations in 15 cases. The means of the periods of the cycles range from 25-54 days, and the cycles were claimed to be internally driven because of similarities with laboratory populations, from which external influences are excluded. We find internally-driven cycles of such periods in our models in this thesis; the models are not forced by any external factors (until Chapter 8), and so the cycles must be internally driven. Although the work of McCauley and Murdoch (1987) is concerned with freshwater rather than marine plankton, we mention it here as evidence that the cycling of populations does occur; in the ocean, the less-stable environment could act to conceal any clear signal identifying such cycles.

1.5 A dynamical systems approach

The nature of the Steele and Henderson (1981) model and the subsequent models developed from it in this thesis, consisting of relatively few coupled ordinary differential equations, makes them amenable to rational study using a dynamical systems approach. Such an approach firstly involves locating steady states of the systems and examining their stability. For each of our models we attempt to calculate the steady states analytically, without specifying numerical values for the parameters, but the nonlinearity of the equations means that not all of the steady states can be explicitly written down. For these states numerical methods are necessary. Numerical methods require specification of parameter values, and so we take the values used by Steele and Henderson (1981) as 'default' parameter values, and determine realistic ranges for each parameter from values used by previous authors across a broad spectrum of models (this is detailed in Chapter 2).

For our first NPZ model (Chapter 3), with the parameters at their default values a steady state is found by integrating the system in time from an initial condition. The rate of zooplankton mortality, d, was varied by Steele and Henderson (1981), and so we choose to increase it. We find that the steady state loses stability at a Hopf bifurcation, and then regains stability at a second Hopf bifurcation, as d is increased. By constructing two-parameter bifurcation diagrams which demonstrate how the Hopf bifurcations persist as each of the other parameters in the model is independently varied, together with d, we build up a picture of the bifurcational behaviour of the model across all parameters. By repeating this process with amended versions of the models in subsequent chapters, we can then easily compare the dynamical behaviour of the models, identifying which amendments to the models are most critical in determining the output.

As well as Hopf bifurcations, we find an array of dynamical features, including transcritical bifurcations, 'three-way' transcritical bifurcations and fold bifurcations of steady states; fold bifurcations and period-doubling bifurcations of limit cycles plus homoclinic connections arising from Bogdanov-Takens bifurcations. The definitions of these will become apparent when they are discovered during the investigations. The mathematical details regarding the theory of dynamical systems can be found in the books by Guckenheimer and Holmes (1983), Thompson and Stewart (1986), Wiggins (1988, 1990) and Kuznetsov (1995).

We emphasise here that we have not needed to 'search around' parameter space in the pursuit of Hopf bifurcations; using the original parameters of Steele and Henderson (1981), and varying d within the range that they used, we come across such bifurcations. By varying a second parameter within its realistic range we then find the further bifurcations that we have just mentioned.

Although much attention in this thesis will be given to oscillations, motivated by the work of Steele and Henderson (1992) and arising from the prevalence of Hopf bifurcations, our philosophy is that the bifurcation diagrams we compute represent qualitative features across broad regions of parameter space, and tell us more than just information regarding oscillations. If one model exhibits Hopf bifurcations but a second does not, then we would expect this to also translate into quantitative differences between computed time series of the models. This expectation is borne out by the time series we present for all of our models in Chapter 8.

The numerical investigations in this thesis have involved a combination of the numerical bifurcation packages AUTO (Doedel *et al.*, 1994) and LOCBIF (Khibnik *et al.*, 1992) to examine the bifurcations, and the dynamical systems packages TraX (Levitin and Khibnik, 1991) and Dstool (Guckenheimer *et al.*, 1991) to integrate and observe trajectories. The graphics package IDL (Interactive Data Language) was used to produce the diagrams from the output of LOCBIF, whilst the built-in graphics program PLAUT was used to produce diagrams from AUTO. The computer-algebra package Maple was used for some of the more complex analytical calculations (such as those involving tenth-order polynomials) and for calculations of some graphs (including the nullsurfaces presented in Chapter 4).

1.6 Outline of thesis

This thesis contains investigations into the dynamical behaviour of two NPZ models and two $NPZD$ models, where N, P, Z and D represent nutrient, phytoplankton, zooplankton and detritus respectively. The two NPZ models (Chapters 3 and 4) contain different zooplankton mortality functions, and our results prompt a re-examination of the results of Steele and Henderson (1992) in Chapter 5. The two $NPZD$ models (Chapters 6 and 7) assume different feeding practices of the zooplankton. All four of our models are then seasonally forced in Chapter 8, demonstrating the usefulness of our approach in explaining the dynamics of the models. We now briefly explain the contents of each chapter in turn.

In Chapter 2 we formulate the NPZ model, which is essentially that of Steele and Henderson (1981). The model consists of three coupled ordinary differential equations, and forms the basis of all the models formulated in this thesis. In Appendix A the phytoplankton growth term is explicitly formulated using the canonical form of primary production derived by Platt *et al.* (1990) and Platt and Sathyendranath (1993), correcting a slight anomaly in the original formulation of the model. For each parameter in the model, a range of numerical values is obtained from the values used by previous modellers. These ranges reflect the uncertainties involved in the estimation of parameter values, and form the basis for our numerical investigations in the subsequent chapters.

We investigate the dynamical behaviour of the NPZ model in Chapter 3. An analytical ('paper and pencil') approach is taken initially, to try and calculate steady states and their stabilities without specifying the numerical values of the parameters. The nature of the equations means that this analysis only provides limited information about the system, and so a numerical approach is required. Simulations of the system show that as time proceeds, N, P and Z may either settle down to steady-state values or undergo oscillations, depending on the value of d, the parameter representing the higher predation on the zooplankton. This suggests the presence of a Hopf bifurcation of a steady state, which is confirmed by computation of bifurcation diagrams. Further bifurcation diagrams illustrate how the region of oscillatory behaviour, as defined by the locations in parameter space of two Hopf bifurcations, persists as each of the parameters, together with d, is varied. Fold bifurcations also occur, delineating regions of multiple steady states, and the presence of homoclinic behaviour is illustrated. Further two-parameter diagrams show how the period of the oscillations vary with respect to each parameter, and finally the behaviour associated with a Bogdanov-Takens bifurcation is explicitly shown.

A quadratic function is used to model the mortality of zooplankton in Chapter 3. As discussed earlier, Steele and Henderson (1992) demonstrated that the precise function used to model zooplankton mortality can have an influential effect upon the dynamics of a system. This motivates us, in Chapter 4, to investigate the model studied in Chapter 3, but with the quadratic mortality term replaced by a linear term, representing different ecological assumptions. The analytical calculation of the steady states is more tractable than for the quadratic mortality model, and the numerical investigations again reveal Hopf bifurcations. The construction of bifurcation diagrams allows comparison with the quadratic mortality model across parameter space.

Results from Chapters 3 and 4 showing that oscillations occur whichever function is used to model zooplankton mortality, contrast with some of the results of Steele and Henderson (1992), and so we re-examine their influential paper in Chapter 5. The bifurcation diagrams of the previous chapters aid us in explaining the differences between our findings and those of Steele and Henderson.

In Chapter 6 we add a fourth component to the NPZ model of Chapter 3, to explicitly model detritus, D. The investigation into the dynamical behaviour reveals similar dynamics to that of the NPZ model. In Chapter 7 we then alter the structure of the four-component model, allowing zooplankton to graze on detritus as well as on phytoplankton. Bifurcation diagrams indicate that this structural change has more of an effect on the dynamical behaviour than that of adding the detritus compartment to the original NPZ model.

Finally, in Chapter 8 we add seasonal forcing to the NPZ and $NPZD$ models, and demonstrate how the results from our dynamical systems approach explain and predict the output of the models. We present our conclusions in Chapter 9.

Sections of Chapters 2 and 3 have already appeared in print (Edwards and Brindley, 1996).

Chapter 2

Formulation of the three-component model

2.1 Introduction

We present the three-component model which is used as the basis for the analytical and numerical investigations throughout the thesis. The model is based on that of Steele and Henderson (1981), with one modification in a similar fashion to that of Steele and Henderson (1993). We use the parameter values of Steele and Henderson (1981) as our default parameters, and obtain a range for each parameter by taking values used by previous authors across a broad class of models. The model consists of three coupled ordinary differential equations, modelling changes in concentrations of nutrient, phytoplankton and zooplankton. The equations are presented in Section 2.2; a slight anomaly in the model derivation is discussed and corrected in Appendix A. The parameter ranges are presented in Section 2.3.

2.2 The mathematical model

We follow closely the approach of Steele and Henderson (1981), hereafter referred to as SH81, using a simple three-component model explicitly representing nutrient, phytoplankton and herbivorous zooplankton, the concentrations of which are given by

N, P and Z respectively. The interactions between these components are illustrated in Figure 2.1. The arrows indicate flows of matter through the system, and the parameterisations of the rates of these flows are indicated on each arrow. The input to the system is the $k(N_0 - N)$ arrow, and arrows not ending in the N, P or Z compartments are losses from the system. The phytoplankton take up nutrient, and are then grazed upon by the zooplankton; the various recycling effects make the situation more complicated than a simple food chain. The flows and the equations are discussed in detail in Section 2.3.

We assume that the layer in which the plankton growth takes place is thoroughly mixed at all times, so that there are no spatial gradients of concentrations and the changes in N, P and Z can be represented by three coupled ordinary differential equations:

$$\begin{aligned}
\frac{dN}{dt} &= -\text{uptake} + \text{respiration} + Z \text{ excretion} + Z \text{ predation excretion} + \text{mixing}, \\
\frac{dP}{dt} &= \text{uptake} - \text{respiration} - \text{grazing by } Z - \text{sinking} - \text{mixing}, \\
\frac{dZ}{dt} &= \text{growth} - \text{higher predation}.
\end{aligned}$$

The specific functional forms used (discussed in Section 2.3) are:

$$\begin{aligned}
\frac{dN}{dt} &= -\frac{N}{e+N}\frac{a}{b+cP}P + rP + \frac{\beta\lambda P^2}{\mu^2+P^2}Z + \gamma d Z^2 + k(N_0 - N), && (2.1) \\
\frac{dP}{dt} &= \frac{N}{e+N}\frac{a}{b+cP}P - rP - \frac{\lambda P^2}{\mu^2+P^2}Z - (s+k)P, && (2.2) \\
\frac{dZ}{dt} &= \frac{\alpha\lambda P^2}{\mu^2+P^2}Z - dZ^2. && (2.3)
\end{aligned}$$

Units of N, P and Z are $g\ C\ m^{-3}$, and time units are days. The conversion equivalences, as used by SH81, are $1\ g\ C \equiv 20\ mg\ Chl \equiv 10\ m\ mol\ N$, where C is carbon, Chl is chlorophyll and N here is nitrogen. All parameters are positive, with $\alpha + \beta \leq 1$ and $\gamma \leq 1$ required from their definitions. The original SH81 model considered mesocosm experiments (mesocosms are giant plastic test-tubes, 5-10m in diameter and 15-20m deep, which are placed in the sea, enclosing a fixed volume of sea water). We have adapted it to the more usual 'open sea' case by incorporating diffusive mixing with deep water, in a similar way to Steele and Henderson (1993),

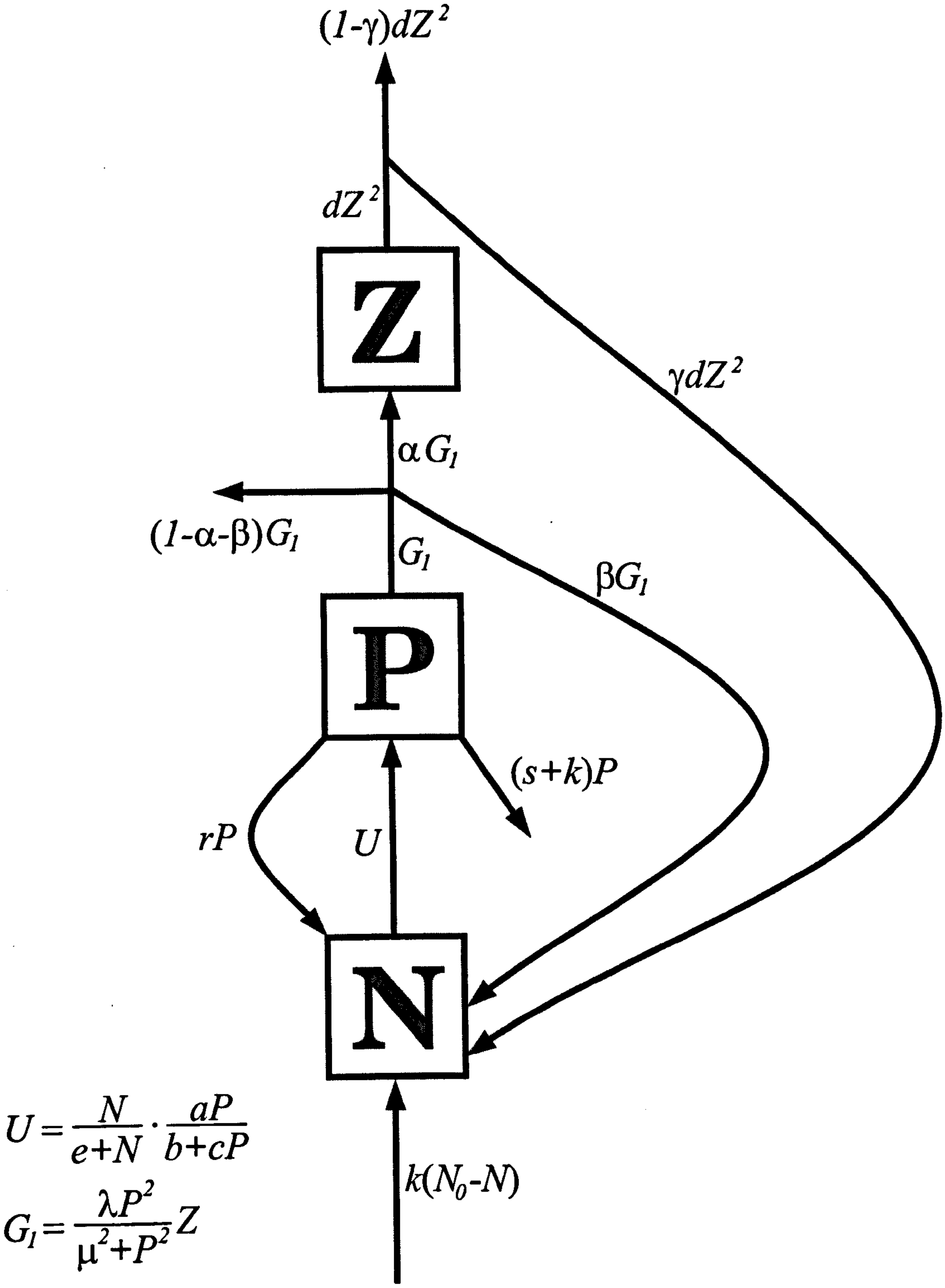

Figure 2.1: Interactions between nutrients (N), phytoplankton (P) and zooplankton (Z). Arrows indicate flows of matter through the system, and the rates of these flows are labelled. Arrows not starting or not finishing at a compartment indicate input to and losses from the system. U is the phytoplankton uptake function, and G_1 is the zooplankton grazing term.

and defer consideration of a varying mixed-layer depth until Chapter 8. The only difference between our model and that of SH81 is therefore the inclusion of the $-kN$ term in (2.1) and the $-kP$ term in (2.2). We discuss the value of k, related to the mixed-layer depth, in Section 2.3.

The equations have not been nondimensionalised. Although this is not usual mathematical practice it means that, when a parameter is varied in the model, it is clear exactly which single biological or physical effect is being considered. In fact non-dimensionalising the system only reduces the number of parameters from 14 to 9, which is not worthwhile for the analysis. Also a, b and c could be redefined as two distinct parameters, but are kept separate as b represents a physical property of the water, while c is the self-shading effect of the phytoplankton, and a/b gives the maximum phytoplankton growth rate, all of which have different values in different models.

2.3 The range of parameter values

For the numerical investigations in subsequent chapters, we require ranges of values for all of the parameters. To obtain a realistic range we abstract values from twelve other models, ranging in complexity from a simple two-component model to larger seven-component models. Table 2.1 gives our default parameter values, taken from SH81, plus the range of values used in the other models; these partly reflect different geographical or other physical influences, but are somewhat attributable to uncertainties and lack of data.

The models considered are abbreviated as follows: Steele and Frost (1977) - SF77, Evans and Parslow (1985) - EP85, Frost (1987) - Fr87, Hofmann and Ambler (1988) - HA88, Wroblewski (1989) - Wr89, Fasham *et al.* (1990) - FDM90, Taylor and Joint (1990) - TJ90, Steele and Henderson (1992) - SH92, Fasham (1993) - Fa93, Steele and Henderson (1993) - SH93, Armstrong (1994) - Ar94, and Henderson and Steele (1995) - HS95.

A description of the functional forms we use (in the order in which they appear in

Parameter	Symbol	Default value	Reported range
a/b gives maximum P growth rate	a	0.2 m^{-1} day^{-1}	0.07 - 0.28
Light attenuation by water	b	0.2 m^{-1}	0.04 - 0.2
P self-shading coefficient	c	0.4 m^2g^{-1}	0.3 - 1.2
Higher predation on Z	d	1 $m^3g^{-1}day^{-1}$	0.25 - 2.0
Half-saturation constant for N uptake	e	0.03 g m^{-3}	0.02 - 0.15
Cross-thermocline exchange rate	k	0.05 day^{-1}	0.0008 - 0.13
P respiration rate	r	0.15 day^{-1}	0.05 - 0.15
P sinking loss rate	s	0.04 day^{-1}	0.032 - 0.08
N concentration below mixed layer	N_0	0.6 g m^{-3}	0.1 - 2.0
Z growth efficiency	α	0.25	0.2 - 0.5
Z excretion fraction	β	0.33	0.33 - 0.8
Regeneration of Z predation excretion	γ	0.5	0.5 - 0.9
Maximum Z grazing rate	λ	0.6 day^{-1}	0.6 - 1.4
Z grazing half-saturation coefficient	μ	0.035 g m^{-3}	0.02 - 0.1

Table 2.1: Abbreviations, default values and ranges of the parameters. The ranges are those used by a variety of authors in different models, as discussed in the text.

the equations) and the parameter ranges used by other authors (converted into $g\ m^{-3}$ values using the aforementioned equivalences, where g represents grammes of carbon) are given below. Variation of parameter values across models is inevitable and direct comparisons are not always easy since different functional forms are sometimes used, but in many cases the parameter definitions are the same, allowing Table 2.1 to be constructed.

Following SH81 we consider a fixed mixed-layer depth of $12.5m$. This designation of a fixed depth is borne out by the data given by FDM90, Fa93 and SH93 at Bermuda Station "S" and Ocean Weather Station (OWS) "India" in the North Atlantic Ocean, which display remarkable uniformity of mixed-layer depth over the period May to October. The mixed layer deepens considerably during the winter months, and inclusion of this process explicitly into the model would require a forcing (time-dependent) function, plus incorporation of a dilution rate of the N, P and Z concentrations, as proposed by EP85. However, it is insightful to first understand the behaviour of the unforced system, with the physical conditions set to summer values. In Chapter 8 we do force the mixed-layer depth through an annual cycle, and show how the investigations into the bifurcations of the unforced models, presented in Chapters 3, 4, 6 and 7, explain the output of the forced models. The mixed-layer depth is implicitly incorporated in the values of a, k and s, as is discussed below.

A Michaelis-Menten function $N/(e+N)$ models nutrient uptake by phytoplankton; a standard choice by many authors. Values of the half-saturation constant e vary from 0.02 ($g\ m^{-3}$) by Wr89 and SH93, to 0.03 by SH81, 0.05 by EP85 and FDM90, 0.1 by Fr87 and 0.15 by HA88. Thus in Table 2.1 our default value of e is 0.03, the SH81 value, and our range is 0.02-0.15.

The term $a/(b+cP)$ represents (non-nutrient limited) phytoplankton growth with limitations due to both light attenuation by the water (b) and self-shading of the phytoplankton (c). The value of a/b gives the maximum daily growth rate averaged over the depth of the mixed layer. The term $a/(b+cP)$ was equated by SH81 to the depth-averaged daily phytoplankton growth rate $2.58V_p/(b+cP)Z_m$ derived by SF77, where V_p is the maximum phytoplankton growth rate under optimal light conditions and Z_m represents the depth of the mixed layer. However, this derivation was implicitly based on the equation for the photosynthesis-light curve given by Steele (1962) which, as Platt and Sathyendranath (1993) have indicated, should be avoided since it includes photoinhibition and has no extended range of light-saturation. Also, the equation of Steele (1962) implies that the maximum photosynthesis rate occurs at a depth which is independent of the surface irradiance, which should not be the case.

In Appendix A we show that the function $a/(b + cP)$ can, however, still be used, since it can be obtained from the canonical form for primary production derived by Platt *et al.* (1990) and Platt and Sathyendranath (1993). This provides a formulation of our parameter a in a way that will allow the value of a to be explicitly calculated for any location and for any time of the year. It is then possible to prescribe how the value of a will vary through the year, due to changes in incident radiation and daylength, such that a can be used to provide temporal forcing of the system.

Care must be taken when translating values of 'maximum P growth rate', to see whether such a value is equivalent to our a/b (and is thus, in a mixed-layer model, the non-nutrient-limited daily maximum phytoplankton growth rate averaged over the depth of the mixed layer), or whether the 'maximum P growth rate' is an equivalent V_p value which is put into some formula which then averages over the depth of the mixed layer. The first case covers the values used by SH92, Ar94 and HS95, which were, respectively, 0.35 (day^{-1}), 1.4 (and 0.7 for a micronutrient-limited case) and 0.5. Keeping b fixed, these are equivalent to values for a in the range 0.07-0.28.

Values of V_p used were 1.25 (day^{-1}) for OWS "India" and 2.9 for Bermuda Station "S" by Fa93, and 2.0 by EP85 and Wr89. In Appendix A we use these locations and values to calculate values for a, and obtain a range of summertime values for a of 0.11-0.16. This falls within the range of 0.07-0.28 just obtained, which is therefore the range that we use, with the SH81 value of $a = 0.2\ m^{-1}\ day^{-1}$ as our default value.

Light attenuation by the water is represented by b, where $b = (\ln 100)/z_e$ corresponds to the 1% light maximum at a depth of z_e metres (taken by SH81 to be $20m$, giving $b = 0.2\ m^{-1}$). SF77, EP85 and HS95 used $b = 0.1$ (m^{-1}), corresponding to $z_e = 46m$, the usual definition for the euphotic zone, while Fa93 and SH93 took $b = 0.04$, giving $z_e = 115m$. The term cP represents phytoplankton self-shading; as the phytoplankton concentration increases the average light received per organism, and therefore the average growth rate, is reduced. The coefficient c, for which SH81 used the SF77 value of 0.4 $(g\ m^{-3})^{-1}\ m^{-1}$, was taken to be 0.3 by SH93 and Fa93, 0.5 by HS95, and EP85 used 1.2 while suggesting the possible use of 0.6.

The default respiration rate of $r = 0.15$ (day^{-1}) from SH81 is the SF77 value at $10°C$ for a 10-μm diameter cell at the North Sea temperature. HS95 used 0.05 and EP85 used 0.07. FDM90 had no respiration term as such, but they did have an equivalent natural mortality rate of 0.09 day^{-1}, some of which is subsequently recycled back through the microbial loop, becoming a food source for both phytoplankton and zooplankton. FDM90 found that this linear phytoplankton loss was the most sensitive and hardest to measure parameter, and allowed it to vary freely in order to fit the data. Our respiration term is recycled immediately into nutrient (as were those of HS95 and EP85), whilst none of our linear sinking term is recycled. We consider r to represent both respiration and natural mortality, since both processes are modelled by other authors as linear losses.

A sigmoidal Holling type III zooplankton grazing term, $\lambda P^2/(\mu^2 + P^2)$, is used, with maximum zooplankton grazing rate of $\lambda = 0.6$ (day^{-1}) and half-saturation constant of $\mu = 0.035$ $(g\ m^{-3})$. The type III form is chosen by SH81 (and SH93) based on the zooplankton grazing data presented by Adams and Steele (1966) which indicates low grazing rates at low phytoplankton concentrations. EP85 used a Holling type II (or Michaelis-Menten) function with a lower grazing threshold. Such a function can be smoothly approximated by the type III function with the same values of λ and μ, and can be inferred from the data of Parsons *et al.* (1969). HS95 used a type II function, the seven-component model of FDM90 had alternative food sources (phytoplankton, bacteria and detritus) for the zooplankton, while Ar94 used a non-standard piecewise linear function (for simplification reasons), but in all cases equivalent values of λ and μ were given. The values used for λ were 1.0 by FDM90, SH93 and HS95, and 1.4 by Ar94, while μ was taken to be 0.02 by SH93, 0.025 by HS95, and 0.1 by

EP85 and Ar94.

Values used for the zooplankton growth efficiency α were 0.2 by SH93, and 0.5 by EP85 and SH92. The proportion β of zooplankton grazing represents zooplankton excretion, and is regenerated immediately into the nutrient compartment. The remaining fraction $1-\alpha-\beta$ is zooplankton faecal pellets, which are assumed to sink out of the mixed layer. Values of β used were 0.5 by SH92 and 0.8 by SH93, thus for both of these models $\alpha+\beta=1$, and so there was no loss from the system (all of the phytoplankton consumed were either converted to zooplankton growth or recycled into nutrient). However, EP85 did not have such a β term in their NPZ model, and thus 0.5 of consumed phytoplankton was lost from the system ($1-\alpha=0.5$).

Fa93 had a zooplankton *assimilation* efficiency of 0.75 multiplying the zooplankton grazing term, together with zooplankton excretion being a constant proportion of zooplankton biomass (rather than a proportion of consumption, such as our β). Thus the Fa93 value of 0.75 should not be assigned to our α. The remaining fraction 0.25 of the grazing in Fa93 represents unassimilated food, and enters a detritus compartment as faecal pellets which can then sink out of the mixed layer; this is similar to our $1-\alpha-\beta$ fraction which is lost from the system. In Chapter 6 we add an explicit detritus compartment to our NPZ model. We thus have a range for α of 0.2-0.5, and a range for β of 0.33-0.8; our default values of $\alpha=0.25$ and $\beta=0.33$ sum to 0.58, allowing both regeneration and a loss from the system.

Higher predation of the zooplankton by invertebrate carnivores, such as ctenophores, is modelled by the quadratic form $-dZ^2$, since the carnivore population is assumed to change in proportion to the zooplankton population. SH81 showed, for their mesocosm case, the initial paths of some trajectories of the system for various values of d. They noted that the system changed its behaviour significantly at a value of d around 1.0 $(g\ m^{-3})^{-1}\ day^{-1}$; their range of d considered was 0.25-1.75. Their results, together with the fact that d is a particularly difficult parameter to measure and assign a fixed value to (SH93 stated that in any model it is essentially a free choice), motivate us to use d as the primary bifurcation parameter, with a range of 0.25-2.0 and a default value of 1.0.

We have commented in Chapter 1 on the potential significance of the functional form of the zooplankton mortality closure term. SH93 used the quadratic form with a default value of $d = 1.0$ which was allowed to vary in order to fit the model to data, and TJ90 also used a quadratic closure term, defining it as zooplankton cannibalism. SH81 and SH92 discussed the use of either a linear or a quadratic function - FDM90 used the simple linear term $-qZ$. In Chapter 4 we investigate the consequences of replacing the quadratic form with the linear form. Holling-type functions, which saturate for large Z, have been used in the higher-order models of Fr87, HA88 and Fa93, but require estimation of an extra poorly known parameter (see SH92). However, in a recent paper Fasham (1995) investigated a six-component ecosystem model which explicitly modelled carnivores grazing on herbivorous zooplankton using a Holling type III function. He concluded that, if the carnivores are then not to be explicitly modelled (as in our case), then a quadratic closure term (in the herbivorous zooplankton equation) is indeed an appropriate function to use.

The parameter γ is the proportion of the zooplankton loss that is regenerated as nutrient, taken by SH81 and SH92 to be 0.5, and by SH93 to be 0.8. FDM90 considered linear zooplankton losses due to both mortality and excretion, of which 89% was retained in the system (but would undergo further losses before being utilised by phytoplankton), and 90% of the loss in Fa93 was similarly recycled. Some models (e.g. Franks *et al.*, 1986) consider a totally conservative system from which nothing is lost, thus $\gamma = 1.0$, whereas EP85 did not consider any such recycling.

The $k(N_0 - N)$ term models the exchange of nutrients with the water below the mixed layer, where the exchange rate k defines the fraction of the mixed layer which is exchanged daily with the deeper water due to diffusive processes, and N_0 is the sub-mixed-layer nutrient concentration. SH92 used $k = 0.033$ (day^{-1}) and 0.1 and found, with linear zooplankton mortality, that 0.033 gave a steady state of the system (which, when the system was forced, simply tracked the forcing), but 0.1 (or a larger N_0 value) resulted in limit cycles. FDM90 used a cross-thermocline mixing rate of 0.1 $m\ day^{-1}$ which Fa93 later decreased to 0.01 $m\ day^{-1}$ to give an improved fit to summer phytoplankton data. Dividing these rates by our mixed-layer depth (and their approximate minimum depth) of 12.5m to obtain the daily exchange rate yields the respective values of $k = 0.008$ (day^{-1}) and 0.0008. EP85 used a much higher mixing rate of 3 $m\ day^{-1}$ (which they noted was a particularly uncertain estimate), and from their graph of seasonally varying mixed-layer depth a range for k of 0.038 - 0.13 can be abstracted, the lower values representing winter levels due to a deep mixed layer (whereas the aforementioned low values of 0.008 and 0.0008 were due to low mixing rates).

FDM90 suggested the N_0 range of $0.1-0.2$ ($g\ m^{-3}$) and used N_0 as a free parameter tuned so that the output best fitted the data, because of the difficulty in assigning a constant value to it. HS95 used $N_0 = 0.3$, TJ90 used 0.6, and EP85 used 1.0, whilst Fr87 took a range of 0.7 - 2.0.

The final parameter to be discussed is the sinking rate, s, of phytoplankton out of the mixed layer. SH81 took $s = 0.04$ (day^{-1}) to correspond to a sinking velocity of 0.5 $m\ day^{-1}$, the same velocity used by SH93. FDM90 did not have a sinking term, but did have a linear phytoplankton mortality rate, as discussed earlier with respect to the respiration term. HS95 assumed a range of $0.4 - 1.0\ m\ day^{-1}$, with a varying mixed-layer depth used to determine the loss rate, which would equal 0.032-0.08 using our fixed mixed-layer depth.

In Edwards and Brindley (1996), where the bulk of this chapter has already been published, we inadvertently equated the aforementioned Fa93, EP85 and Wr89 values of V_p to our a/b, and also included the Fa93 assimilation efficiency of 0.75 when constructing the range for α. This simply resulted in the corresponding two-parameter bifurcation diagrams of Figures 4(a) and 4(h) in Edwards and Brindley (1996) showing too large a range of values for a/b and α, but does not affect the results (the corrected diagrams are Figures 3.4(a) and 3.4(h) in Chapter 3). We thank Trevor Platt and Shubha Sathyendranath for highlighting these minor anomalies.

Chapter 3

Dynamical behaviour of the three-component model

3.1 Introduction

We now investigate the dynamical behaviour of the NPZ model formulated in Chapter 2. We firstly proceed analytically, without substituting actual parameter values into the equations. The steady states of the system are calculated in Section 3.2, but only those where zooplankton are absent can be expressed explicitly, and so numerical methods need to be invoked.

In Section 3.3 we present the trajectories of N, P and Z when all of the parameters are set to their default values, and show that this picture changes qualitatively when the higher predation on zooplankton, d, is set at a higher value. Section 3.4 demonstrates precisely how this change occurs by constructing one-parameter bifurcation diagrams for which d is continuously increased. Section 3.5 then indicates how these one-parameter diagrams change as each of the other parameters in the model is varied, in turn, across the default ranges of values given in Table 2.1. This is done by tracking the location of Hopf bifurcations. In Section 3.6 we show explicitly how the one-parameter diagram for N changes as the sub-mixed-layer nutrient concentration, N_0, is increased, revealing an interesting array of dynamical behaviour. 'Period-contour diagrams' are constructed in Section 3.7, showing how the periods of the oscillations change as each parameter is varied. Finally, in Section 3.8 we construct the complete bifurcation diagram for N_0 against d, illustrating local and global bifurcations of limit cycles, as well as the local bifurcations of steady states.

The equations for the model, as formulated in Chapter 2, are

$$\begin{aligned}
\frac{dN}{dt} &= -\frac{N}{e+N}\frac{a}{b+cP}P + rP + \frac{\beta\lambda P^2}{\mu^2+P^2}Z + \gamma dZ^2 + k(N_0 - N), && (3.1)\\
\frac{dP}{dt} &= \frac{N}{e+N}\frac{a}{b+cP}P - rP - \frac{\lambda P^2}{\mu^2+P^2}Z - (s+k)P, && (3.2)\\
\frac{dZ}{dt} &= \frac{\alpha\lambda P^2}{\mu^2+P^2}Z - dZ^2. && (3.3)
\end{aligned}$$

3.2 Analysis

The analysis of this section provides the groundwork for the numerical investigation presented in Sections 3.3-3.8. The powerful reduced nullsurface technique used by McCann and Yodzis (1995), in their analysis of the three-species food chain proposed by Hastings and Powell (1991), cannot be used here. This is due to the more complicated formulation of our equations, which is in part due to the recycling effects which are present in the system. The nullsurfaces, the equivalents to the nullclines of a two-component system, are the surfaces in $N-P-Z$ space defined by each of $dN/dt = 0, dP/dt = 0$ and $dZ/dt = 0$. Points at which all three surfaces intersect define the steady states of the system, but plotting them for this system does not help greatly, due to the difficulties in displaying three intersecting surfaces on one figure. However, the nullsurfaces do help when comparing the current model to the model with linear zooplankton mortality investigated in Chapter 4, and we thus defer nullsurface discussion to Chapter 4.

The steady states of the system and their stability are now calculated. The analysis of a general NPZ system by Truscott and Brindley (1994) and Truscott (1994) can be partly followed and is extended for our model. We firstly perform the analysis, and then numerically compute the bifurcational behaviour to graphically illustrate the analytical results.

A steady state, or equilibrium, is a solution (N, P, Z) to $dN/dt = dP/dt =$

$dZ/dt = 0$. The stability of a steady state is determined by the eigenvalues of the Jacobian matrix, which is given by

$$\mathbf{A} = \begin{bmatrix} -\frac{aeP}{(e+N)^2(b+cP)} - k & -\frac{abN}{(e+N)(b+cP)^2} + r + \frac{2\beta\lambda\mu^2 PZ}{(\mu^2+P^2)^2} & \frac{\beta\lambda P^2}{\mu^2+P^2} + 2\gamma dZ \\ \frac{aeP}{(e+N)^2(b+cP)} & \frac{abN}{(e+N)(b+cP)^2} - r - s - k - \frac{2\lambda\mu^2 PZ}{(\mu^2+P^2)^2} & -\frac{\lambda P^2}{\mu^2+P^2} \\ 0 & \frac{2\alpha\lambda\mu^2 PZ}{(\mu^2+P^2)^2} & \frac{\alpha\lambda P^2}{\mu^2+P^2} - 2dZ \end{bmatrix}$$

evaluated at the steady-state values of N, P and Z.

There is a steady-state solution of the form $(N, P, Z) = (N_0, 0, 0)$, which exists for all parameter values. The Jacobian at $(N_0, 0, 0)$ is

$$\mathbf{A} = \begin{bmatrix} -k & -\frac{aN_0}{b(e+N_0)} + r & 0 \\ 0 & \frac{aN_0}{b(e+N_0)} - r - s - k & 0 \\ 0 & 0 & 0 \end{bmatrix}.$$

It can be seen that there is always one zero eigenvalue for $(N_0, 0, 0)$, and the other two eigenvalues are $-k$ and Φ, where

$$\Phi = \frac{aN_0}{b(e+N_0)} - r - s - k.$$

Truscott calculated the centre manifold for such a steady state, and concluded that for $\Phi < 0$ $(N_0, 0, 0)$ is stable, and for $\Phi > 0$ it is unstable. At $\Phi = 0$, $(N_0, 0, 0)$ has two zero eigenvalues and undergoes a 'three-way transcritical bifurcation' of codimension two, which is discussed below. For the default parameter values $\Phi = 0.71$, and Φ remains positive as any one parameter varies over its reported range. Φ can become negative if more than one parameter is allowed to vary (but this only occurs for certain extreme values within the ranges), or if the mixed-layer depth, which appears implicitly in three of the parameter definitions, is increased (recall that the ranges in Table 2.1 assume a constant mixed-layer depth). But Φ remains positive throughout our numerical investigations of Sections 3.4-3.8, since we only vary one of these parameters at a time.

Two steady states of the form $(N_1{}^*, P_1{}^*, 0)$ and $(N_2{}^*, P_2{}^*, 0)$ also exist, where $N_1{}^*, N_2{}^*$ are solutions to the following quadratic equation, which is obtained by solving the simultaneous equations $dN/dt = 0$ and $dP/dt = 0$ (with $Z = 0$):

$$ckN^2 + \left[\frac{a(s+k)}{r+s+k} - b(s+k) + ck(e - N_0)\right] N - \left[b(s+k) + ckN_0\right] e = 0, \tag{3.4}$$

and ${P_1}^*, {P_2}^*$ are given by

$$P_i^* = \frac{k(N_0 - N_i^*)}{s+k} \tag{3.5}$$

for $i = 1, 2$.

The constant term of the quadratic is negative, so the discriminant is strictly positive and the solutions for ${N_1}^*, {N_2}^*$ are real, and one is positive (call this ${N_1}^*$) while the other is always negative (${N_2}^*$). $({N_2}^*, {P_2}^*, 0)$ is therefore ecologically unrealistic and can never enter the positive octant of phase space, given by $\{N, P, Z \geq 0\}$. From (3.5) it is clear that ${P_1}^* > 0$ for ${N_1}^* < N_0$, and ${P_1}^* < 0$ for ${N_1}^* > N_0$. By considering the quadratic for P obtained by substituting (3.5) into (3.4) it can be shown that ${P_1}^* > 0$ for $\Phi > 0$ and ${P_1}^* < 0$ for $\Phi < 0$. When $\Phi = 0$, $({N_1}^*, {P_1}^*, 0) = (N_0, 0, 0)$, which is the previously calculated steady state at the codimension two bifurcation.

The third row of the Jacobian of $({N_1}^*, {P_1}^*, 0)$ is

$$\begin{pmatrix} 0 & 0 & \dfrac{\alpha\lambda {P_1}^{*2}}{\mu^2 + {P_1}^{*2}} \end{pmatrix}.$$

The third term is therefore an eigenvalue, and since it is always positive (for ${P_1}^* \neq 0$), the steady state $({N_1}^*, {P_1}^*, 0)$ can never be stable.

From (3.3) it is clear that steady-state solutions (N^*, P^*, Z^*) with $Z \neq 0$ must satisfy

$$Z = \frac{\alpha\lambda P^2}{d(\mu^2 + P^2)}. \tag{3.6}$$

Substituting this into (3.1) and (3.2), equating these equations to zero, and eliminating N from them, results in a tenth-order polynomial in P, the solution of which gives the non-zero steady-state value of P^*. Such a polynomial precludes the possibility of writing down an analytical form for (N^*, P^*, Z^*). When the polynomial is written such that the coefficient of P^{10} is one, the constant term of the polynomial is Ψ, where

$$\Psi = \frac{bk\mu^8(e+N_0)\Phi}{c(s+k)(r+s+k)}.$$

Therefore $\Psi \longrightarrow 0$ as $\Phi \longrightarrow 0$, and at $\Phi = 0$, $P = 0$ becomes a solution of the tenth order polynomial. The (N^*, P^*, Z^*) solution thus degenerates to $(N_0, 0, 0)$, at the three-way transcritical bifurcation point $\Phi = 0$.

Equation (3.6) can be used to simplify the Jacobian at (N^*, P^*, Z^*), which becomes

$$\mathbf{A} = \begin{bmatrix} -\frac{aeP}{(e+N)^2(b+cP)} - k & -\frac{abN}{(e+N)(b+cP)^2} + r + \frac{2d^2\beta\mu^2 Z^3}{\alpha^2\lambda P^3} & \left(\frac{\beta}{\alpha} + 2\gamma\right) dZ \\ \frac{aeP}{(e+N)^2(b+cP)} & \frac{abN}{(e+N)(b+cP)^2} - r - s - k - \frac{2d^2\mu^2 Z^3}{\alpha^2\lambda P^3} & -\frac{dZ}{\alpha} \\ 0 & \frac{2d^2\mu^2 Z^3}{\alpha\lambda P^3} & -dZ \end{bmatrix}.$$

The third row of $\mathbf{A}$ now has two non-zero terms, and further analysis of the stability is not viable.

Our analytical deductions concerning the local behaviour about the three-way transcritical bifurcation at $\Phi = 0$ can be summarised as:

- $\Phi < 0$ – $(N_0, 0, 0)$ stable, $({N_1}^*, {P_1}^*, 0)$ ecologically unrealistic $({P_1}^* < 0)$, (N^*, P^*, Z^*) undetermined;
- $\Phi > 0$ – $(N_0, 0, 0)$ unstable, $({N_1}^*, {P_1}^*, 0)$ realistic and unstable, (N^*, P^*, Z^*) undetermined;

and we know that $({N_1}^*, {P_1}^*, 0)$ and (N^*, P^*, Z^*) pass through $(N_0, 0, 0)$ as Φ goes through zero.

We now illustrate, in Figure 3.1, how the steady states $(N_0, 0, 0)$, $({N_1}^*, {P_1}^*, 0)$ and (N^*, P^*, Z^*) intersect at the three-way transcritical bifurcation. This is done by setting all of the parameters to their default values given in Table 2.1, calculating the values and stabilities of the steady states, and then computing how these properties of the steady states change as the respiration rate, r, is varied. The parameter r is chosen since it appears in the definition of Φ, and thus at some value will give $\Phi = 0$, where the three-way transcritical bifurcation occurs. Any of the other parameters

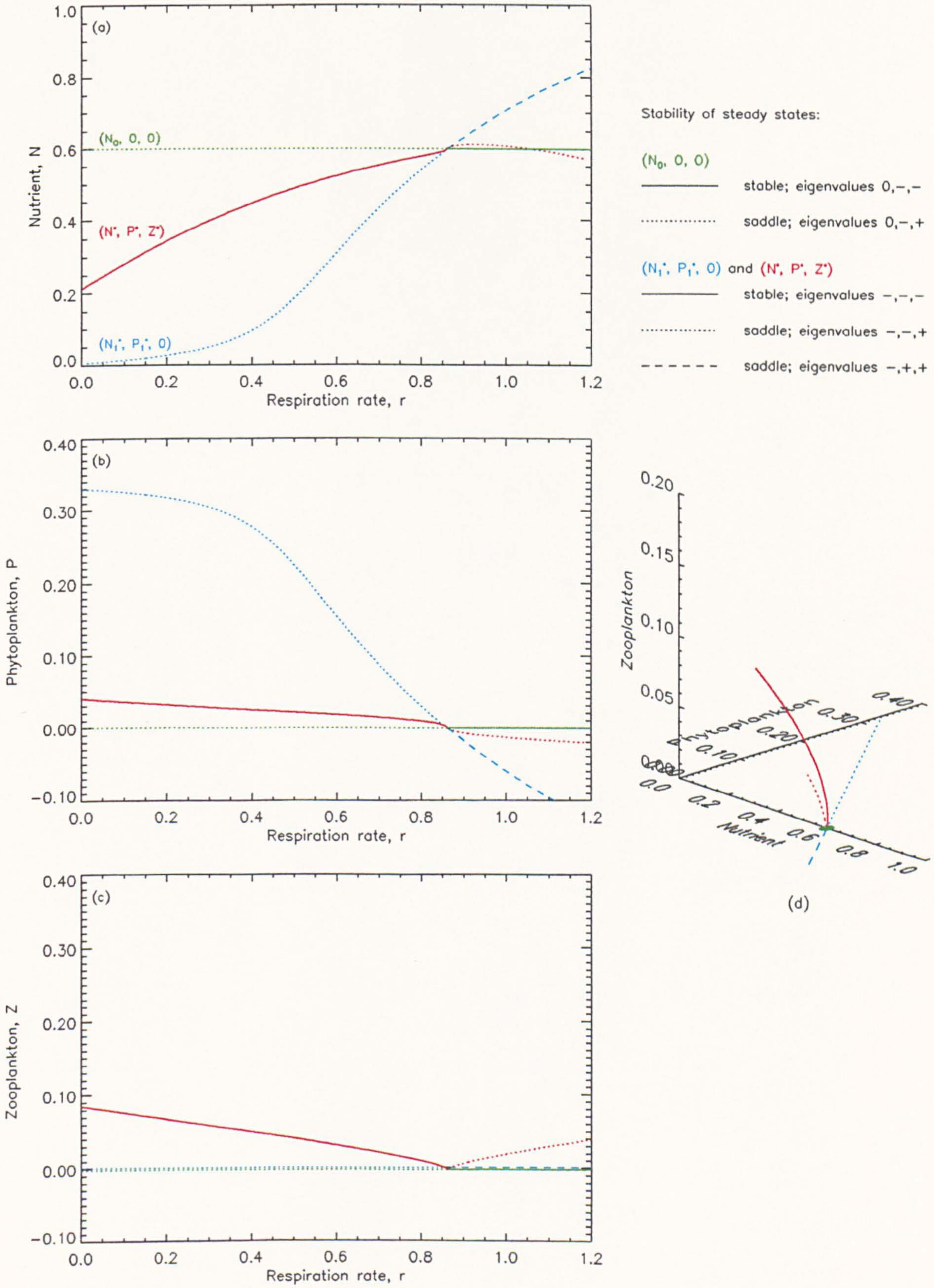

Figure 3.1: Location and stability of $(N_0, 0, 0)$, $({N_1}^*, {P_1}^*, 0)$ and (N^*, P^*, Z^*) as r is varied. The key indicates the signs of the real parts of the eigenvalues, plus the corresponding stabilities. The three-way transcritical bifurcation occurs at $r = 0.86$.

that appear in the definition of Φ could equivalently have been used. The default value of r is 0.15, for which $\Phi > 0$ when all of the other parameters are fixed at their default values. The realistic range of r given in Table 2.1 was 0.05-0.15. $\Phi = 0$ occurs when $r = 0.86$ (to two decimal places), clearly out of the biologically realistic range, but in Figure 3.1 we plot r from 0 to 1.2 as we wish to show what happens when $\Phi > 0$, $\Phi = 0$ and $\Phi < 0$. As mentioned in the analysis, $\Phi > 0$ always holds when any one of the parameters in the definition of Φ is varied over its biologically realistic range, but $\Phi = 0$ can occur if two of the parameters are set to extreme realistic values or the mixed layer deepens, and so the three-way transcritical bifurcation is an ecological possibility as well as a mathematical curiosity. The numerical calculations were performed using the bifurcation package LOCBIF (Khibnik *et al.*, 1992), and the graphics package IDL was used to produce the diagrams.

The three steady states are colour-coded - $(N_0, 0, 0)$ is green, $({N_1}^*, {P_1}^*, 0)$ is blue and (N^*, P^*, Z^*) is red. Solid, dotted and dashed lines are used to indicate the stability of the steady states and the signs of the real parts of the eigenvalues (of the Jacobian at the steady states), as indicated by the key in Figure 3.1.

Consider firstly the green line in Figure 3.1(a), which indicates how the N value and stability of the steady state $(N_0, 0, 0)$ change as r is varied. This behaviour is simply deduced from the analysis. The default value of N_0 is 0.6, so clearly $(N_0, 0, 0)$=$(0.6, 0, 0)$ for all values of r; hence the green line is horizontal. The default value of r is 0.15, for which $\Phi > 0$, and so we know from the analysis that $(N_0, 0, 0)$ has eigenvalues with signs $0, -, +$ and is unstable; this is indicated by the green line being dotted at $r = 0.15$. As r is increased, Φ remains positive, and so $(N_0, 0, 0)$ remains unstable, until $\Phi = 0$ at $r = 0.86$. At $r = 0.86$ the three-way transcritical bifurcation thus occurs, and for $r > 0.86$, $\Phi < 0$ and $(N_0, 0, 0)$ is stable, the solid line indicating this stability, and indicating that the real parts of the eigenvalues have signs $0, -, -$ (the analysis shows that the eigenvalues are real, and the stability is determined by a centre manifold analysis). The green lines in Figures 3.1(b) and (c) represent the P and Z value of $(N_0, 0, 0)$ respectively, and are thus simply at $P = 0$ and $Z = 0$. (The green and blue curves in Figure 3.1(c) are slightly offset from zero for clarity). Figure 3.1(d) shows how the steady states move about in three-dimensional $N - P - Z$ phase space as r varies; the green point indicates that $(N_0, 0, 0)$ just sits in the same location.

The blue curves in Figure 3.1 show the behaviour of the steady state $(N_1{}^*, P_1{}^*, 0)$ as r varies. At $r = 0.15$ it is a saddle point with one eigenvalue having positive real part, as indicated by the dotted line. As r is increased, $N_1{}^*$ increases and $P_1{}^*$ decreases, and $(N_1{}^*, P_1{}^*, 0)$ passes through $(N_0, 0, 0)$ at $r = 0.86$. For $r > 0.86$, $P_1{}^* < 0$, and $(N_1{}^*, P_1{}^*, 0)$ has two eigenvalues with positive real part, as indicated by the dashed line. Figure 3.1(d) shows how $(N_1{}^*, P_1{}^*, 0)$ moves in a straight line, as given by 3.5, and leaves the positive octant through $(N_0, 0, 0)$, whilst remaining in the plane $Z = 0$.

The red curves indicate the behaviour of (N^*, P^*, Z^*). It is stable for $r < 0.86$, losing stability at the three-way transcritical bifurcation. As (N^*, P^*, Z^*) passes through the bifurcation, P^* becomes negative. This leaves $(N_0, 0, 0)$, which is now stable, as the only biologically feasible steady state. (N^*, P^*, Z^*) is the only steady state for which the zooplankton are not extinct, and because its stability cannot be feasibly determined analytically, we focus on this steady state for the main numerical investigation.

With the aid of Figure 3.1, it thus appears that the full local behaviour about the three-way transcritical bifurcation at $\Phi = 0$ is:

- $\Phi < 0$ – $(N_0, 0, 0)$ stable, $(N_1{}^*, P_1{}^*, 0)$ ecologically unrealistic ($P_1{}^* < 0$), (N^*, P^*, Z^*) ecologically unrealistic ($P^* < 0$);
- $\Phi > 0$ – $(N_0, 0, 0)$ unstable, $(N_1{}^*, P_1{}^*, 0)$ realistic and unstable, (N^*, P^*, Z^*) realistic and stable;

with the exchange of stability occurring at $\Phi = 0$.

3.3 Time series and phase portraits

In Figure 3.2(a) we show the time series and the trajectory in $N-P-Z$ space of the system from the initial condition $(N, P, Z) = (0.4, 0.1, 0.05)$, with all of the parameters fixed at their default values. It is seen that N, P and Z all settle down to steady-state values of $(N, P, Z) = (0.31, 0.034, 0.072)$ after a transient time of about 50 days. The initial large rise in P is due to the excitable nature of the system (see Truscott and Brindley, 1994), which can be partly deduced from the two-dimensional nullsurfaces. Starting from a range of other initial conditions, trajectories converge to the same steady state, the transient time remains roughly the same, and the actual nature of the transient trajectories depends upon the position of the initial points with respect to the nullsurfaces. By substituting the default parameters into equations (3.1), (3.2) and (3.3) and numerically solving the tenth-order polynomial discussed in Section 3.2, it can be shown that this steady state is the only steady state with strictly positive values of N, P and Z.

In Figure 3.2(b) we increase the value of the higher predation on zooplankton, d, from the default value of 1.0 to 1.5, and re-run the system from the same initial conditions. It is seen that the system now settles down to a periodic orbit, or limit cycle, after a short transient time. Again, this behaviour is independent of the initial conditions. The cycles show large amplitude fluctuations in N, but at values remaining lower than the steady-state value for $d = 1.0$. The minimum cyclic value of P is roughly the same as the $d = 1.0$ steady-state value, while Z undergoes small oscillations about the $d = 1.0$ steady-state value. The oscillations have a period of 35 days, which is consistent with the observational data and output of large ecosystem models discussed in Chapter 1. The fact that we find such oscillations and our model has a quadratic zooplankton mortality term contrasts with the results of Steele and Henderson (1992), and motivates us to now investigate the nature of the oscillations, using d as the primary bifurcation parameter.

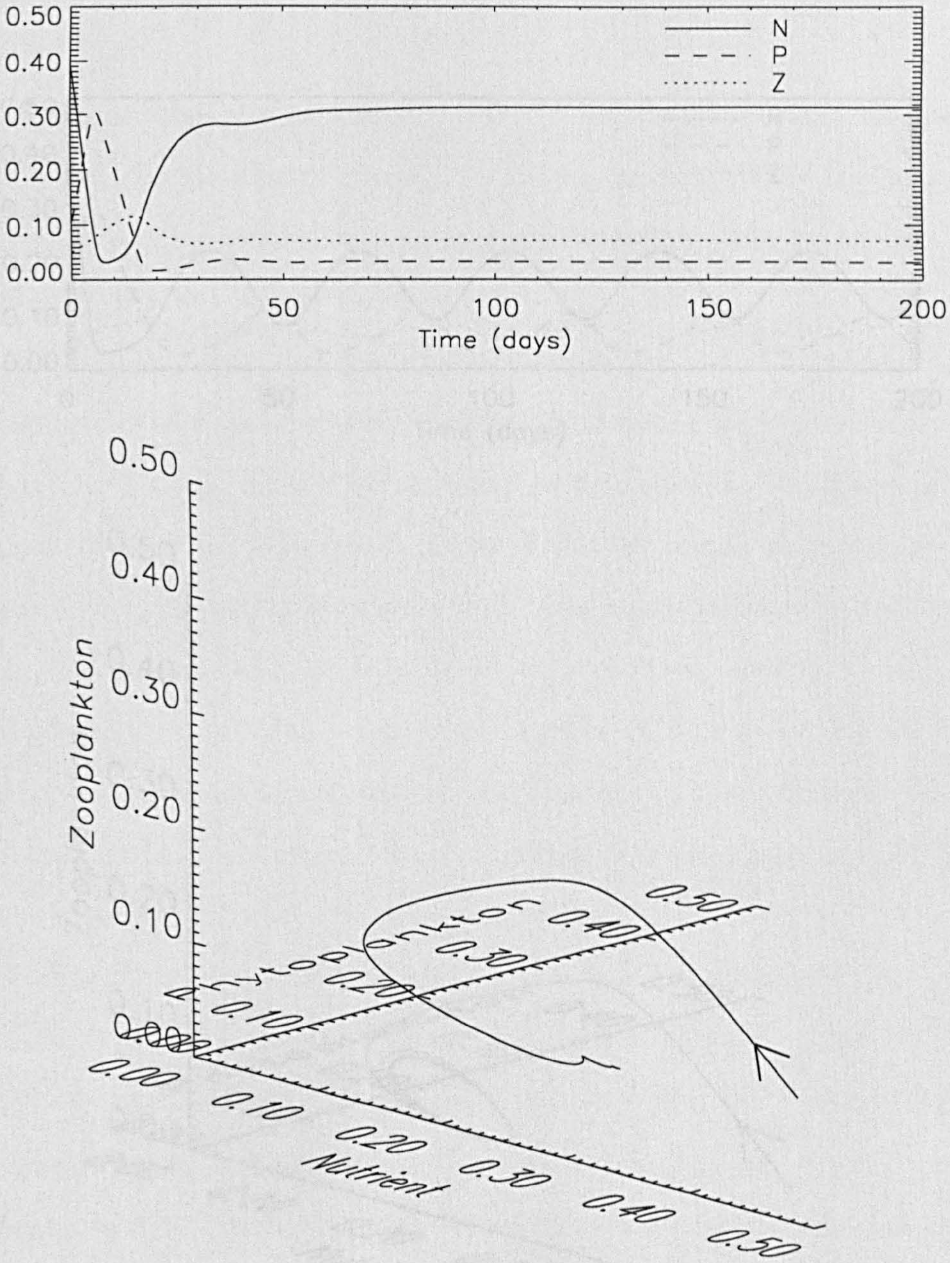

(a) $d = 1.0$ - N, P and Z settle down to steady-state values after a short transient.

Figure 3.2: The time series and phase-space trajectory at (a) $d = 1.0$ and (b) $d = 1.5$ (next page), with all of the other parameters fixed at their default values. Units of N, P and Z for all diagrams are $g\ C\ m^{-3}$, as used in the equations for the model.

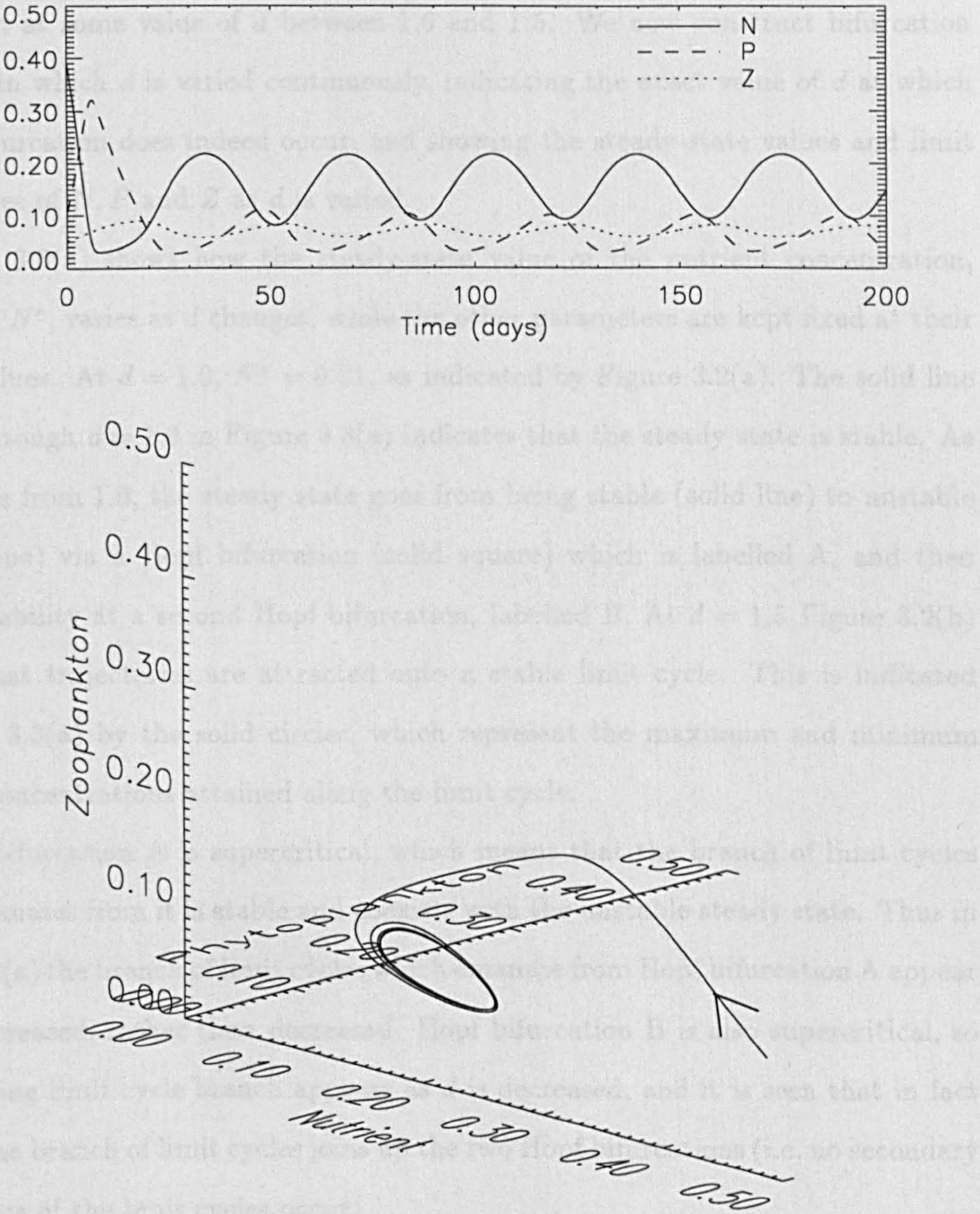

(b) $d = 1.5$ - the system settles down to a stable limit cycle.

3.4 One-parameter bifurcation behaviour

Clearly there is a qualitative difference between Figures 3.2(a) and 3.2(b); the change from a steady state to oscillatory behaviour suggests that there has been a Hopf bifurcation at some value of d between 1.0 and 1.5. We now construct bifurcation diagrams in which d is varied continuously, indicating the exact value of d at which a Hopf bifurcation does indeed occur, and showing the steady-state values and limit cycle ranges of N, P and Z as d is varied.

Figure 3.3(a) shows how the steady-state value of the nutrient concentration, defined as N^*, varies as d changes, while the other parameters are kept fixed at their default values. At $d = 1.0$, $N^* = 0.31$, as indicated by Figure 3.2(a). The solid line passing through $d = 1.0$ in Figure 3.3(a) indicates that the steady state is stable. As d increases from 1.0, the steady state goes from being stable (solid line) to unstable (dashed line) via a Hopf bifurcation (solid square) which is labelled A, and then regains stability at a second Hopf bifurcation, labelled B. At $d = 1.5$ Figure 3.2(b) showed that trajectories are attracted onto a stable limit cycle. This is indicated in Figure 3.3(a) by the solid circles, which represent the maximum and minimum nutrient concentrations attained along the limit cycle.

Hopf bifurcation A is supercritical, which means that the branch of limit cycles which emanates from it is stable and coexists with the unstable steady state. Thus in Figure 3.3(a) the branch of limit cycles which emanate from Hopf bifurcation A appear as d is increased, rather than decreased. Hopf bifurcation B is also supercritical, so the resulting limit cycle branch appears as d is decreased, and it is seen that in fact just the one branch of limit cycles joins up the two Hopf bifurcations (i.e. no secondary bifurcations of the limit cycles occur).

Figures 3.3(b) and 3.3(c) are the equivalent diagrams for phytoplankton and zooplankton, which have default steady-state values of $P^* = 0.034$ and $Z^* = 0.072$. Although d is the predation rate on Z, the stable-steady state concentration Z^* (Figure 3.3(c)) remains fairly constant for all except low d. A proportion γ (default value 0.5) of the higher predation is directly recycled into the system as the $+\gamma dZ^2$ term

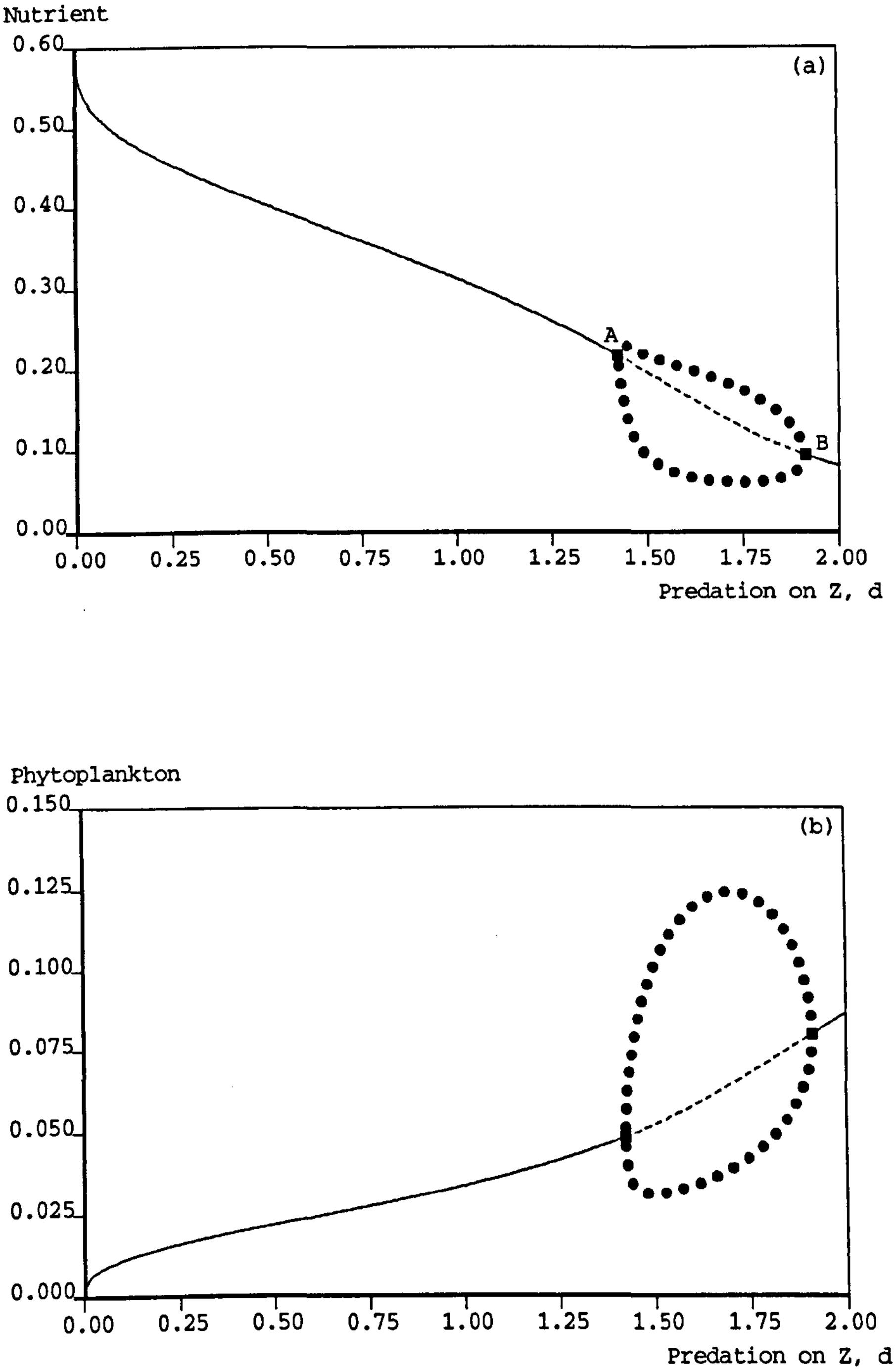

Figure 3.3: Variations in the steady-state values of (a) nutrient, (b) phytoplankton and (c) zooplankton as d, the higher predation on the zooplankton, is changed. A solid line is a stable steady state, a dashed line is an unstable steady state, a solid square is a Hopf bifurcation and solid circles indicate the maximum and minimum values of the stable limit cycles. The Hopf bifurcations are labelled A and B.

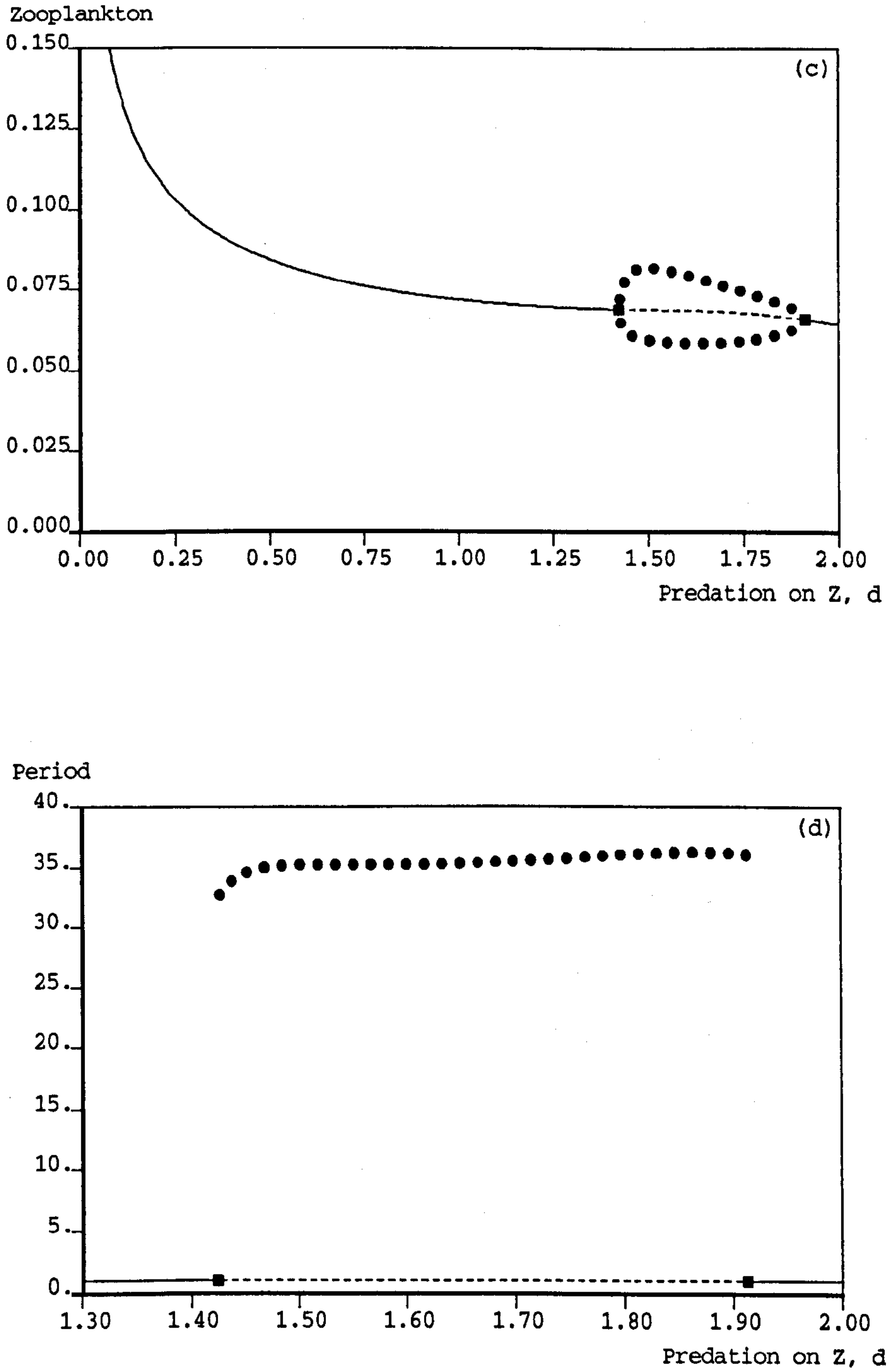

(c) The zooplankton bifurcation diagram. (d) The period of the limit cycles (solid circles) remains virtually constant throughout the region of oscillatory behaviour; the corresponding stability of the steady state is indicated by the horizontal line.

of the dN/dt equation (3.1), but increasing d actually causes the steady-state level N^* to decrease (Figure 3.3(a)), due to the increase in P^* (Figure 3.3(b)). Increasing predation on zooplankton would not *directly* cause the phytoplankton population to increase, and any definitive 'cause and effect' consequences cannot be deduced, due to the recycling effects propagating through the system.

During the oscillations, the value of P reaches levels far higher than those attained by any steady-state value, and for $d \in (1.48, 1.73)$ the maximum P value along the limit cycle is over three times the minimum value; the variations in the amplitude of Z are much smaller.

Figure 3.3(d) shows how the period of the limit cycles changes as d varies between the values at which the Hopf bifurcations occur (the only relevant range of d). It is clearly seen that the period is very insensitive to the value of d, remaining at the previously discussed value of 35 days across the whole range.

3.5 Two-parameter bifurcation behaviour

Figure 3.4 shows how the location of the two Hopf bifurcations changes as each of the other parameters is independently varied across the range reported in Table 2.1. The axis range plotted for each parameter is from zero to (approximately) its maximum reported value. Figure 3.4 thus indicates how the qualitative nature of the steady-state bifurcation diagrams depicted in Figure 3.3 will change as one other parameter is varied.

For each parameter the bifurcation diagram from Figure 3.3 is shown as a horizontal line at the default value of the parameter, since the parameter was held constant in Figure 3.3. A solid horizontal line represents a stable equilibrium, a dashed horizontal line is unstable, and squares represent the Hopf bifurcations, as for Figure 3.3. In the region of d where the equilibrium is unstable, limit cycles occur, as was illustrated in Figure 3.3. In Figure 3.4 the positions of the two Hopf bifurcations are tracked as both d and one other parameter are varied. A (non-horizontal) solid line shows the location of a supercritical Hopf bifurcation, and where it becomes dashed

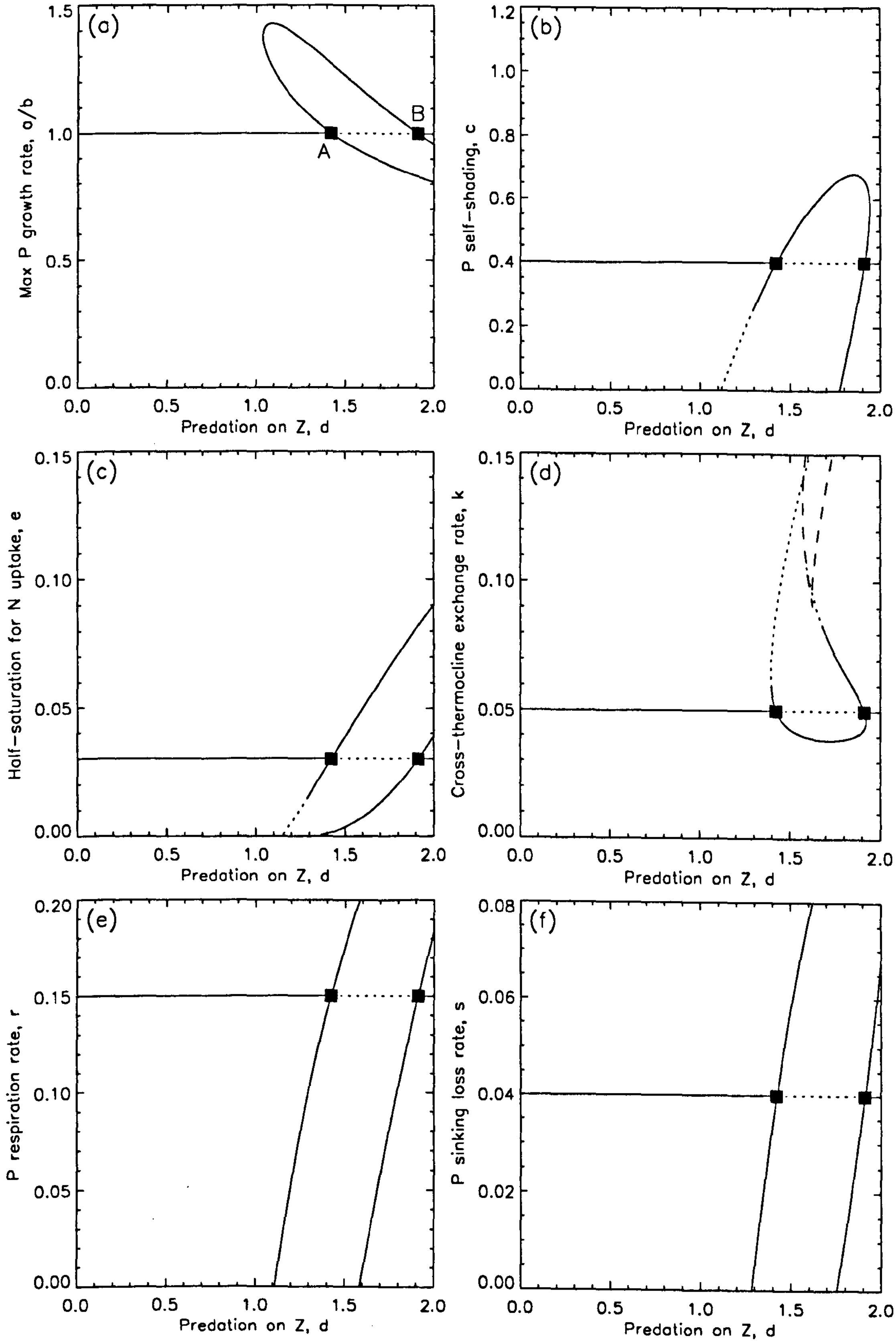

Figure 3.4: Two-parameter bifurcation diagrams showing how the positions of the Hopf bifurcations in Figure 3.3 change as each other parameter, together with d, is independently varied from its default value. The steady-state stabilities from Figure 3.3 are shown as a horizontal line at each default parameter value. Hopf A and (ctd.)

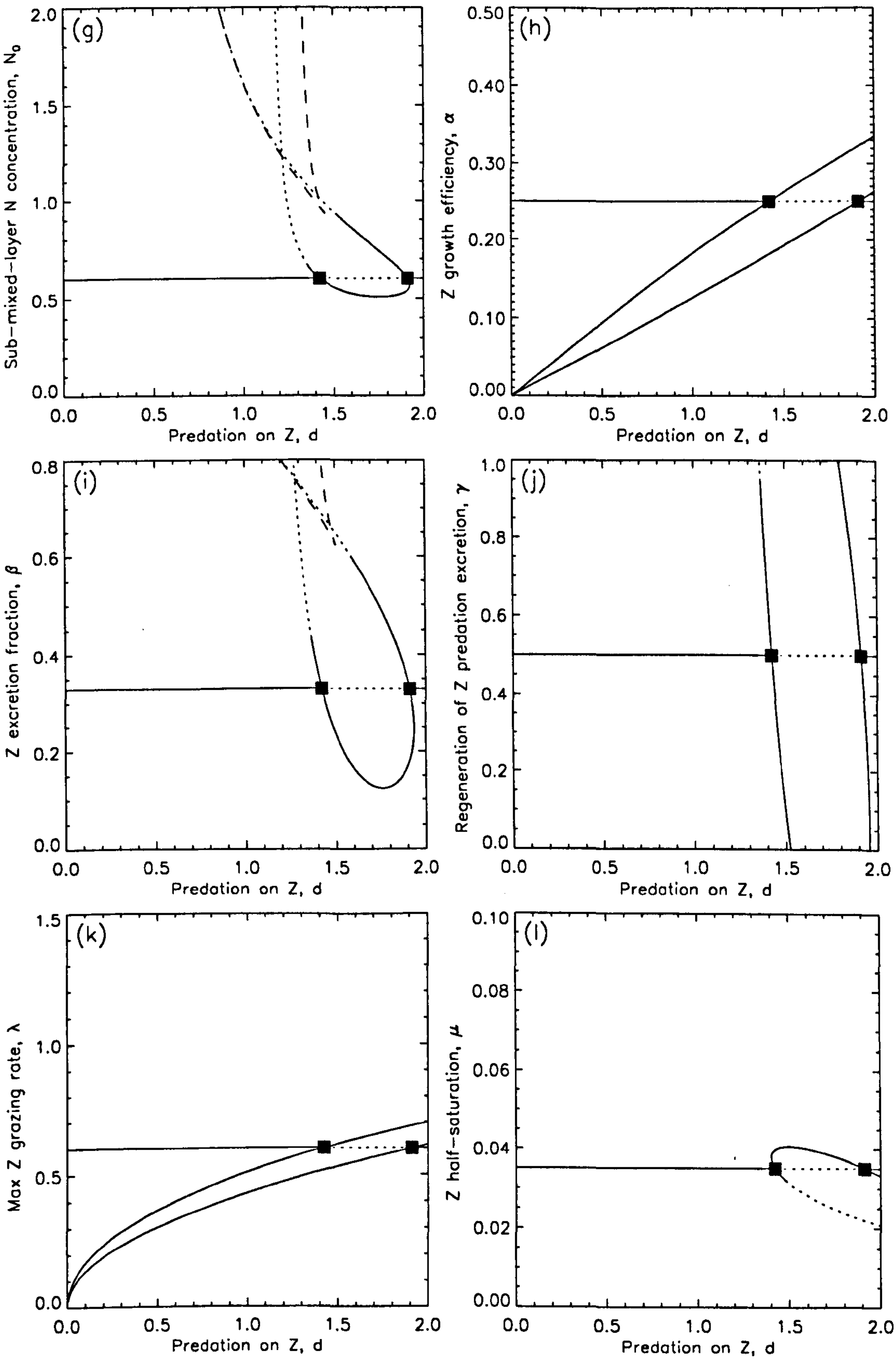

Hopf B are indicated in (a). Non-horizontal solid curves starting from the original Hopf bifurcations (the squares) indicate supercritical Hopf bifurcations, and non-horizontal curves of short dashes show where Hopf bifurcations are subcritical. In (d), (g) and (i), curves of long dashes indicate fold bifurcations of the steady state.

indicates that the Hopf bifurcation has become subcritical (meaning that the branch of periodic orbits emanating from it will be unstable and will coexist with the stable steady state). The curve of long dashes in Figures 3.4(d), (g) and (i) represent a fold bifurcation of the steady state. The effects of variations in a and b have been combined as a/b in a single diagram for the maximum phytoplankton growth rate, so that there are 12 distinct bifurcation diagrams.

Figure 3.4(a) shows that an increase in a/b causes the two Hopf bifurcations A and B from Figure 3.3 to remain supercritical, but to coalesce at $a/b = 1.43$. Above this value the steady state remains stable for all values of d, and does not undergo a Hopf bifurcation. A decrease in a/b causes the Hopf bifurcations to increase their d values, and eventually move out of the range of d which we are considering.

Figure 3.4(b) is the diagram for c, the phytoplankton self-shading parameter, against d. It is seen that an increase in c causes the Hopf bifurcations to remain supercritical and coalesce, as occurred in Figure 3.4(a). As c is decreased from the default value, Hopf A becomes subcritical (dashed line), but at a value which is below 0.3, the minimum reported value of c. Thus across the reported range of c, as d is varied, the steady state can either undergo two supercritical Hopf bifurcations, which are joined by a branch of stable limit cycles as in Figure 3.3, or it simply remains stable.

The diagram for e, the half-saturation constant for nutrient uptake, Figure 3.4(c), is qualitatively similar to that for c, but the Hopf bifurcations coalesce at a high value of d which is outside of our range. Thus increasing e from the default value causes the region of stable limit cycles in the original diagram, Figure 3.3, to shift to the right and move out of our range of d, as occurred in Figure 3.4(a), resulting in just a single stable steady state for high e.

Figure 3.4(d) for k, the cross-thermocline exchange rate, shows that increasing k causes Hopf A, and then Hopf B, to become subcritical. Figure 3.5(a) shows how the branch of limit cycles can still join up the Hopf bifurcations when $k = 0.07$ (for which Hopf A has become subcritical whilst Hopf B has remained supercritical). We wish to demonstrate qualitative effects, and so only the nutrient value is shown, and

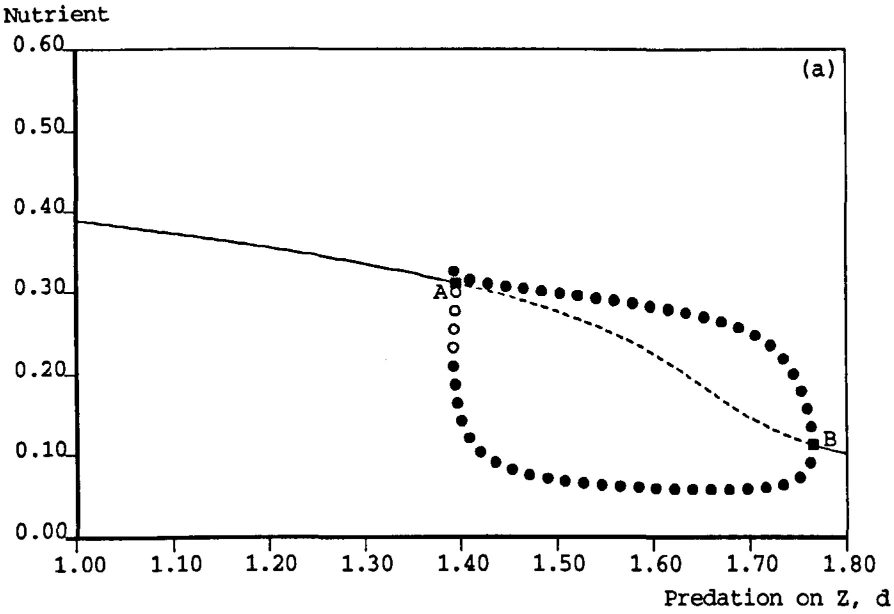

(a) $k = 0.07$ - Hopf A has become subcritical. The limit cycle branch undergoes a fold bifurcation and still joins up the two Hopf bifurcations. The open circles corresponding to the maximum nutrient values cannot actually be seen due to the close proximity of the fold bifurcation and Hopf bifurcation at $d \simeq 1.40$.

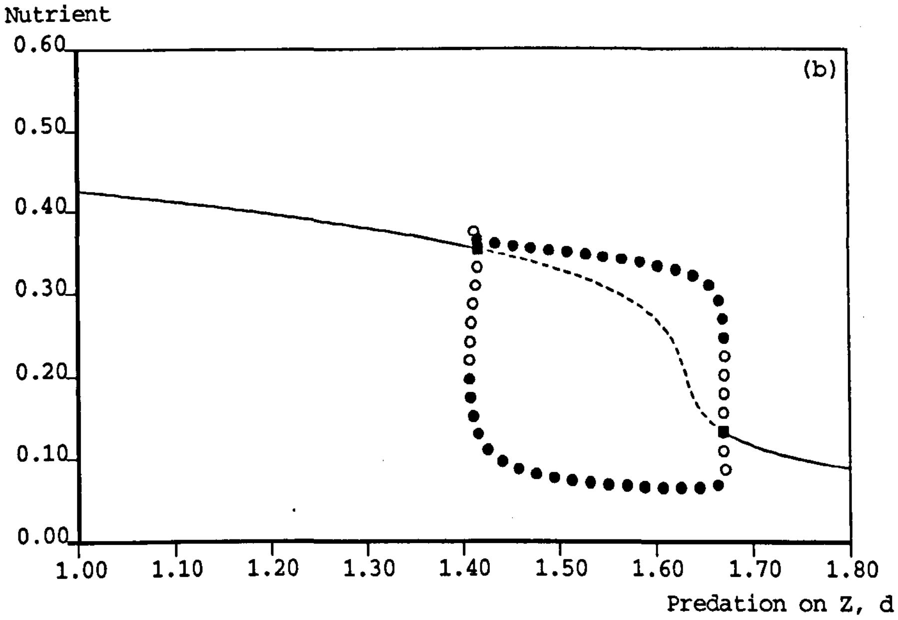

(b) $k = 0.085$ - both Hopf bifurcations are subcritical and the limit cycle branch becomes stable via fold bifurcations close to each Hopf bifurcation.

Figure 3.5: The original Figure 3.3(a) diagram of N against d changes as k is increased. Open circles represent the maximum and minimum nutrient values for unstable cycles.

the d scale is chosen to illustrate the region in question. Figure 3.5(a) is thus to be interpreted in the same way as Figure 3.3(a). Solid circles still represent the maximum and minimum nutrient values for stable limit cycles, and the open circles represent the values for unstable cycles. The four open circles in Figure 3.5(a) indicate the minimum nutrient value of the unstable cycle at the corresponding values of d. The maximum values cannot be seen on the diagram due to the proximity of the maximum stable limit cycle values to the Hopf bifurcation.

The stable limit cycle branch emanating from the supercritical Hopf B persists as d is decreased, and then undergoes a fold bifurcation at $d = 1.394$, and the resulting unstable cycles join up to the subcritical Hopf A at $d = 1.397$. A fold bifurcation of a limit cycle is similar to a fold bifurcation of a steady state - two cycles (of dissimilar stability) coexist for a particular parameter value, and as this parameter is decreased their orbits become closer together and then annihilate each other at the fold bifurcation; at values of the parameter below the fold bifurcation neither cycle exists. For clarity fold bifurcations of limit cycles are not shown in Figure 3.4; we discuss bifurcations of limit cycles in Section 3.8. Thus for the narrow region $d \in (1.394, 1.397)$ the stable steady state and stable limit cycle coexist, but for the remainder of the diagram the situation is qualitatively equivalent to Figure 3.3(a), and in this case the fact that Hopf A has become subcritical as k has increased is fairly insignificant.

Figure 3.5(b) shows what happens when $k = 0.085$, for which both Hopf bifurcations are now subcritical. The unstable branch from the subcritical Hopf B undergoes a fold bifurcation to become stable. This stable branch persists as d is decreased and undergoes another fold bifurcation to join up to Hopf A, in the same manner as for $k = 0.07$. So for $k = 0.085$ there are two narrow regions of d for which a stable limit cycle and stable steady state coexist. For $k > 0.091$ the steady state undergoes fold bifurcations (indicated by the curve of long dashes in Figure 3.4(d)), and for $k > 0.11$ only one Hopf bifurcation occurs; the consequent limit cycle behaviour shall be shown in Section 3.6 for an equivalent region in the N_0 diagram.

The diagrams for independent changes in phytoplankton respiration rate, r, phytoplankton sinking rate, s, and the regeneration of excretion by the predators on the zooplankton, γ, Figures 3.4(e), (f) and (j), respectively, are qualitatively very similar. Both Hopf bifurcations remain supercritical across the entire feasible ranges of each parameter, and furthermore the length of the interval of d for which the limit cycle behaviour occurs remains virtually constant in each case. Thus the model can be said to be insensitive to changes in these parameters, in the sense that varying each of them independently will cause hardly any change in the qualitative behaviour of the system. We note that r and γ represent recycling effects in the system (as illustrated by Figure 2.1), but the model appears insensitive to the level (or absence) of such recycling. Furthermore, FDM90 found that their specific linear phytoplankton loss parameter (essentially $r + s$ in our model) was the most sensitive, and most difficult to determine, parameter in their system, whereas in our model such a loss is among the least sensitive parameters.

Figure 3.4(g) for the sub-mixed-layer nutrient concentration, N_0, shows that increasing N_0 causes both Hopf bifurcations to become subcritical and then cross over (in terms of their d values). A curve of fold bifurcations of the steady state also arises (shown as a curve of long dashes). The Hopf B bifurcation curve terminates at the fold curve, at $N_0 = 1.97$, at a point known as a Bogdanov-Takens bifurcation point, which shall be discussed in Section 3.8. The qualitative changes in behaviour as N_0 is increased through this region are demonstrated in Figure 3.6, and are discussed in Section 3.6. Qualitatively similar behaviour also occurs when β is varied, Figure 3.4(i). Now, β represents a recycling term, but its bifurcation picture is not as simple as those for the other recycling terms r and γ. Instead, it is similar to k and N_0. Although k affects both nutrient input and phytoplankton loss, as shown in Figure 2.1, it would appear that changes in k have, in some sense, more influence as a nutrient input. This is because the k diagram is similar to the N_0 diagram and not to the s one - s and N_0 only appear once each in the model and thus have only one direct influence on the system. So k and β have similar pictures to N_0, implying that k and β have most influence as an input to the nutrient compartment. Similarly, r is both a linear loss from the P equation and an input to the N equation, and seemingly 'behaves' more like s than N_0. However, this tentatively constructed view does not extend to the results to be shown in Section 3.7 concerning the periods of the oscillations.

Figures 3.4(h) and (k) show that increasing α, the zooplankton assimilation efficiency, or λ, the maximum zooplankton grazing rate, causes the Hopf bifurcations to move out of the d range, as occurred for a decrease in a/b. Decreasing α or λ causes the Hopf bifurcations to be shifted towards $d = 0$.

Finally, Figure 3.4(l), for the zooplankton grazing half-saturation coefficient, μ, is similar to Figure 3.4(a) for a/b, except that Hopf A becomes subcritical as μ is decreased, before it moves out of the range of d.

3.6 Bifurcation behaviour at different levels of N_0

As an example of the behaviour associated with the various regions of parameter space investigated in Section 3.5, we now discuss the behaviour of the system as N_0 is increased. At each fixed value of N_0, the single bifurcation diagram of nutrient against d is shown in Figure 3.6. Figure 3.6 thus indicates how the original bifurcation diagram in Figure 3.3(a) changes as we increase N_0 through Figure 3.4(g); each Figure 3.6 picture can therefore be considered as a horizontal slice through Figure 3.4(g). Figure 3.4(g) only gives information about the bifurcations of the steady states; in Figure 3.6 we also demonstrate the qualitative changes in limit cycle behaviour as N_0 is increased. Such changes can affect both the transient and asymptotic behaviour of the system. From these computations we then, in Section 3.8, sketch the complete bifurcation diagram of N_0 against d, adding the bifurcations of limit cycles to the steady-state bifurcations already shown in Figure 3.4(g). The scales of the Figure 3.6 diagrams are not all the same, since they are chosen in order to highlight the qualitative changes that occur as N_0 is increased.

Figure 3.6(a), for $N_0 = 0.75$, shows essentially the same behaviour as Figure 3.5(a) for $k = 0.07$, whereby Hopf A is subcritical and Hopf B is supercritical, and the limit cycle branch undergoes a fold bifurcation close to Hopf A. Figure 3.6(b), for $N_0 = 1.0$, shows that the limit cycle branch joins up the two Hopf bifurcations in

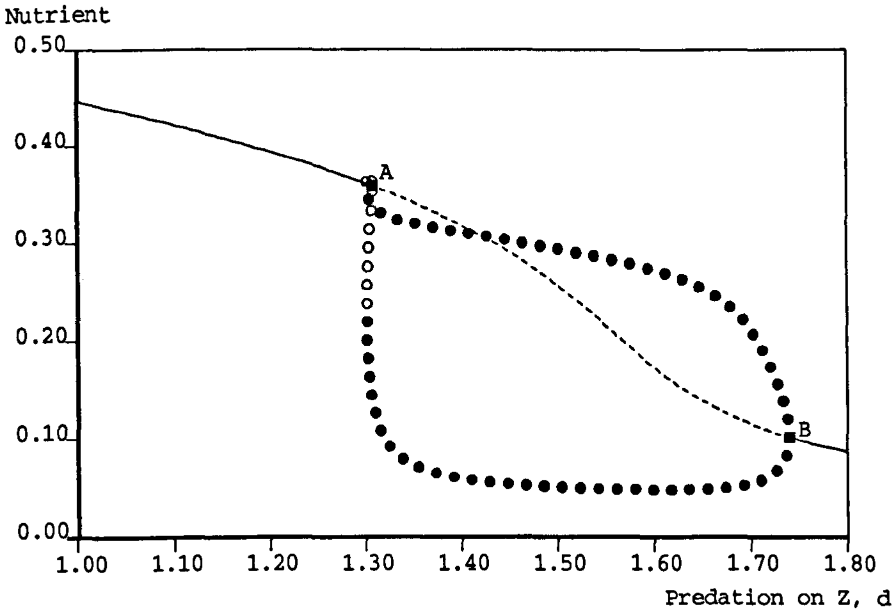

(a) $N_0 = 0.75$ - Hopf A has become subcritical and the limit cycle branch is qualitatively the same as Figure 3.5(a).

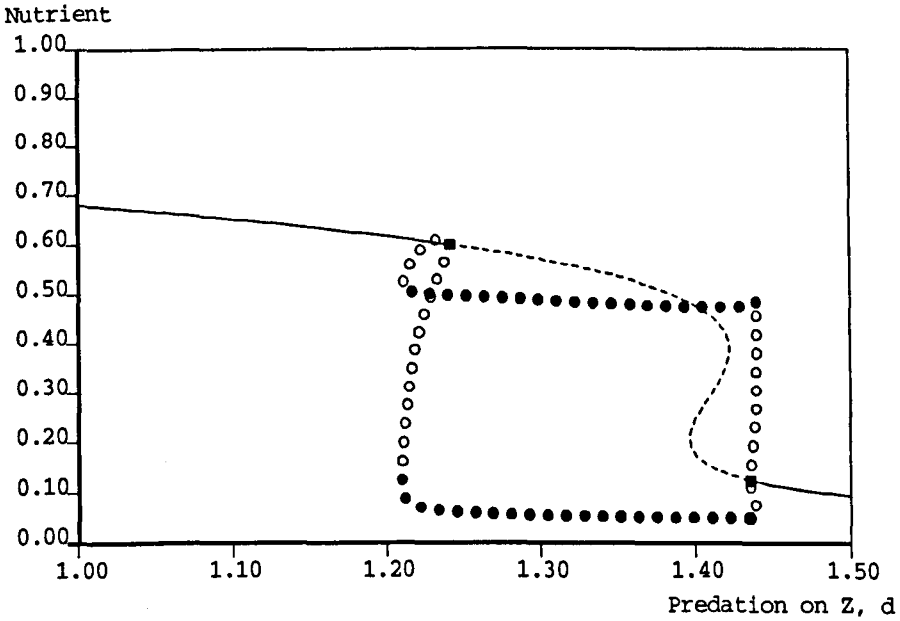

(b) $N_0 = 1.0$ - a region of multiple unstable steady states exists, and a branch of limit cycles connects the two Hopf bifurcations.

Figure 3.6: The Figure 3.3(a) diagram changes dramatically as N_0 is increased (ctd.)

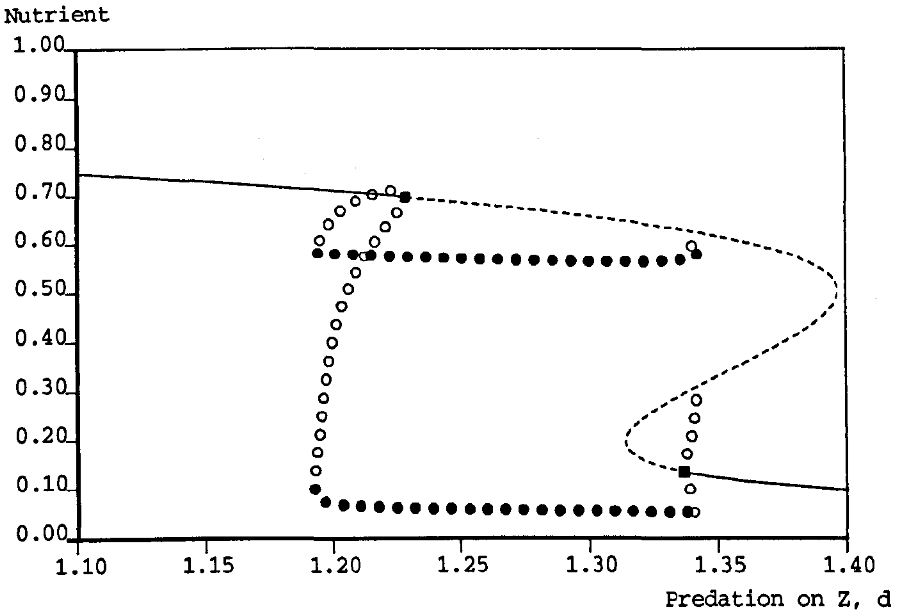

(c) $N_0 = 1.1$ - the unstable cycles near Hopf B now become homoclinic to the saddle point, and the Hopf bifurcations are no longer connected by a continuous branch of limit cycles.

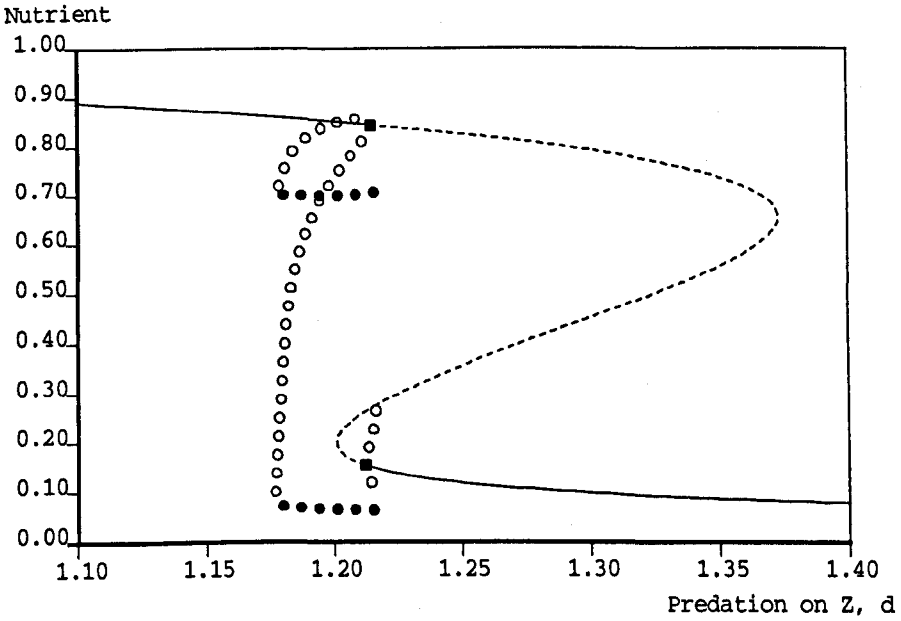

(d) $N_0 = 1.25$ - the stable steady states exhibit hysteresis, and thus for $d \in (1.2123, 1.2145)$ a stable limit cycle coexists with two stable steady states. The stable limit cycle branch still terminates at the right-hand end at a fold bifurcation - this is inferred semi-analytically (and not shown in the diagram) since the numerical computations become unreliable.

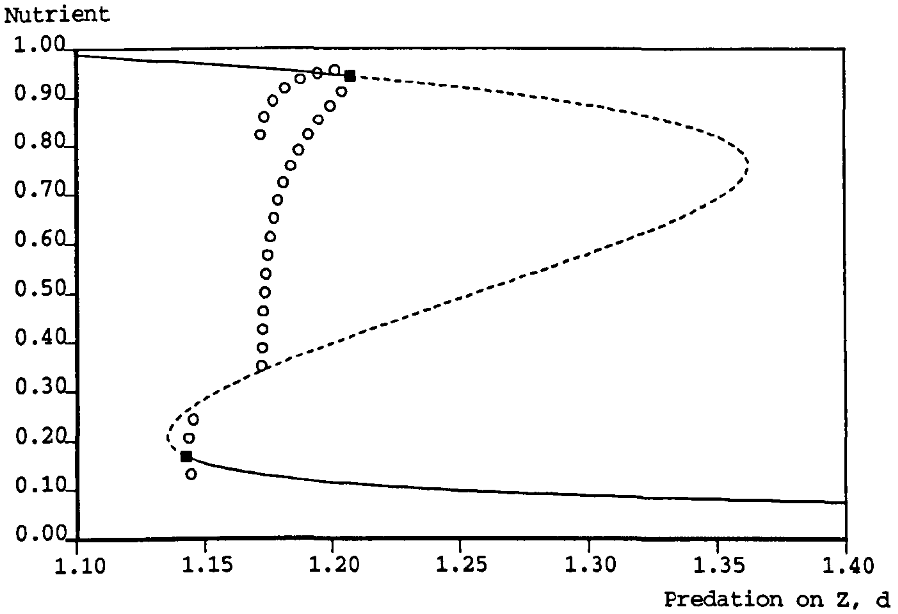

(e) $N_0 = 1.35$ - no fold bifurcations of the unstable limit cycle branch occur, thus no stable limit cycles arise and the unstable cycles become homoclinic. The region of coexistence of the steady states, now the sole attractors, is larger than in (d).

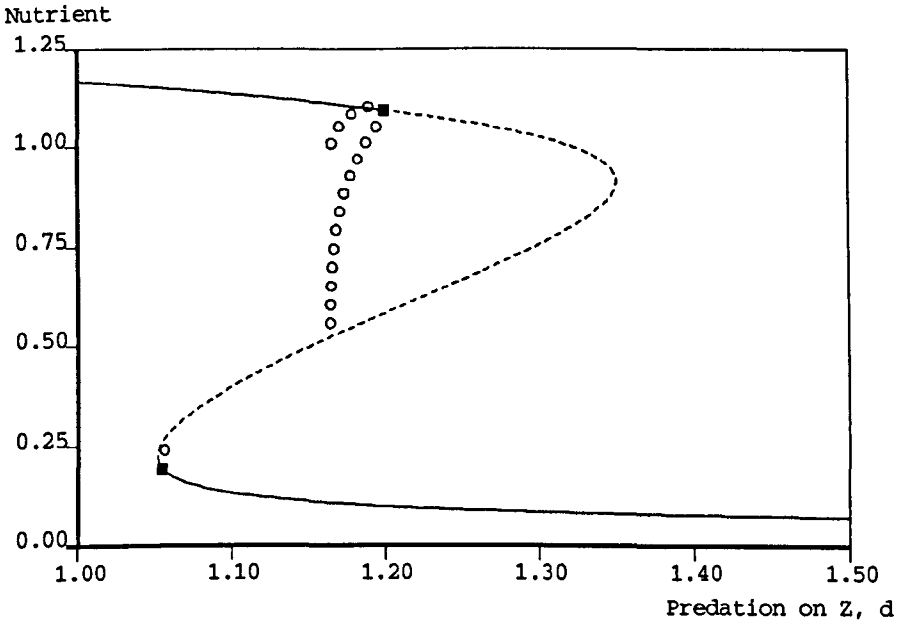

(f) $N_0 = 1.5$ - similar to (e) except that the values of d at the homoclinic connections have altered.

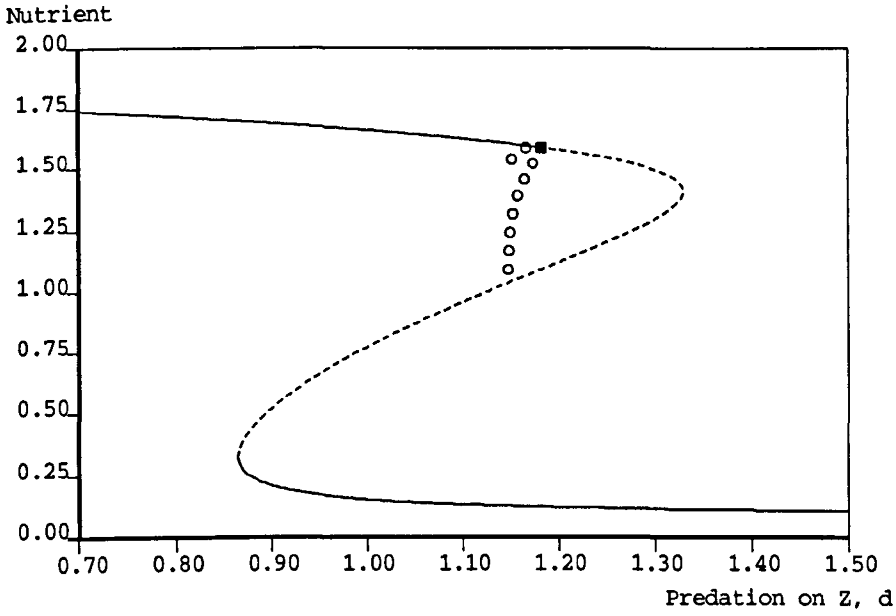

(g) $N_0 = 2.0$ - Hopf A has now become a fold bifurcation.

the same way as in Figure 3.5(b) for $k = 0.085$, but the unstable steady-state branch now undergoes two fold bifurcations; however it does not regain stability in-between the two Hopf bifurcations, and hence no new attractors appear. On Figure 3.4(g) Hopf B becomes subcritical at $N_0 = 0.92$ and the fold bifurcations of the steady state appear (at a cusp point) at $N_0 = 0.93$; since these values are so close we do not show the intermediate one-parameter bifurcation diagram in Figure 3.6 (i.e. that for which Hopf B is subcritical and the steady state does not undergo a fold bifurcation, as in Figure 3.5(b)).

Figure 3.6(c), for $N_0 = 1.1$, shows that the limit cycles now no longer form a single branch connecting up the two Hopf bifurcations. A region of stable limit cycles arises from Hopf A in the same manner as for $N_0 = 1.0$. This branch again undergoes a fold bifurcation (as d increases), but the resulting unstable branch then becomes homoclinic (as d then decreases) to the saddle point on the middle steady-state branch, rather than joining up to Hopf B. In other words, the cycle in $N-P-Z$ space approaches the saddle point, leading ultimately to a homoclinic connection in which the unstable manifold of the saddle point joins up in a loop (formerly the cycle) with its own stable manifold; see Thompson and Stewart (1986), Wiggins (1988, 1990) or Kuznetsov (1995) for further details. The unstable branch which arises from Hopf B also terminates at a homoclinic connection to the saddle point (at a different d value). The behaviour of the stable attractors has not qualitatively changed from $N_0 = 1.0$.

In Figure 3.6(d), for $N_0 = 1.25$, Hopf A now occurs at a slightly higher value of d than Hopf B, as illustrated by the crossing of the Hopf bifurcation curves at $N_0 = 1.24$ in Figure 3.4(g). The system can therefore exhibit hysteresis in moving between the two stable steady states coexisting at the same value of d.

At the right-hand endpoint of the branch of stable limit cycles the numerical computations become unreliable. Resorting to computing trajectories in time, we find that a stable limit cycle exists at $d = 1.21761$, and is close in $N - P - Z$ space to the saddle point of the middle branch of Figure 3.6(d). Increasing d to 1.21762 yields no stable cycle, even starting from a range of initial conditions, including values at and close to points which were part of the stable cycle at $d = 1.21761$. In Section 3.8 we prove that the stable limit cycle branch cannot terminate at a homoclinic connection, but rather that it (almost certainly) undergoes a fold bifurcation, and it is the resulting unstable branch that terminates at a homoclinic connection, as in Figure 3.6(c). In Edwards and Brindley (1996), which was published before the work in Section 3.8 had been done, we mistakenly thought that the stable limit cycle branch does actually terminate at the homoclinic connection - this was a perfectly valid interpretation of the available numerical evidence.

The stable limit cycle branch coexists with at least one of the stable steady states; for the (rather pathological) narrow region $d \in (1.2123, 1.2145)$ there are three coexisting stable attractors, namely two stable steady states plus a stable limit cycle. As d increases from this region, one steady state becomes unstable at Hopf A, and then the stable limit cycle branch undergoes the aforementioned fold bifurcation, and the lowest steady-state branch becomes the sole attractor.

At $N_0 = 1.35$, Figure 3.6(e), the fold bifurcation of the unstable limit cycle branch from Hopf A no longer occurs and this branch does not become stable; instead it becomes homoclinic to a saddle point (as does the branch from Hopf B) and no stable limit cycles exist. The system undergoes hysteresis, indicated by the region of coexisting stable steady states. Figure 3.6(f), for $N_0 = 1.5$, shows that Hopf B has got closer to the fold of the steady state, and that the homoclinic connections of the unstable limit cycle branches have shifted slightly along the saddle point branch. Figure 3.6(g), for $N_0 = 2.0$, shows that Hopf B has disappeared and the steady state now loses stability due to a fold bifurcation, since the Hopf bifurcation curve in Figure 3.4(g) terminates at $N_0 = 1.97$ when it joins up with the fold curve at a Bogdanov-Takens point, to be discussed in Section 3.8.

3.7 Dependence of the period of oscillations on the parameter values

In Figure 3.2(b) we showed that, when $d = 1.5$ and the other parameters are set to their default values, N, P and Z settle down to oscillations with a period of about 35 days. Figure 3.3(d) then showed that this period remains fairly constant as d is varied across the region of oscillations, i.e. between the two Hopf bifurcations. We now investigate how the period of the oscillations changes with respect to each of the other parameters in the model.

In Figure 3.7 we plot 'contours', or isochrones, of constant period, within the regions of oscillatory behaviour defined in Figure 3.4. The numbered curves are the contours, along which the period takes the constant value, in days, specified by the number. Contours are plotted at increments of 5 days. The key for the remaining features of these diagrams is the same as for Figure 3.4 - the solid squares show the Hopf bifurcations at the default parameter values; the un-numbered curves passing through the squares indicate how the positions of the Hopf bifurcations change as each parameter is varied, with solid curves again representing supercritical and dotted curves representing subcritical Hopf bifurcations; and curves of long dashes indicate

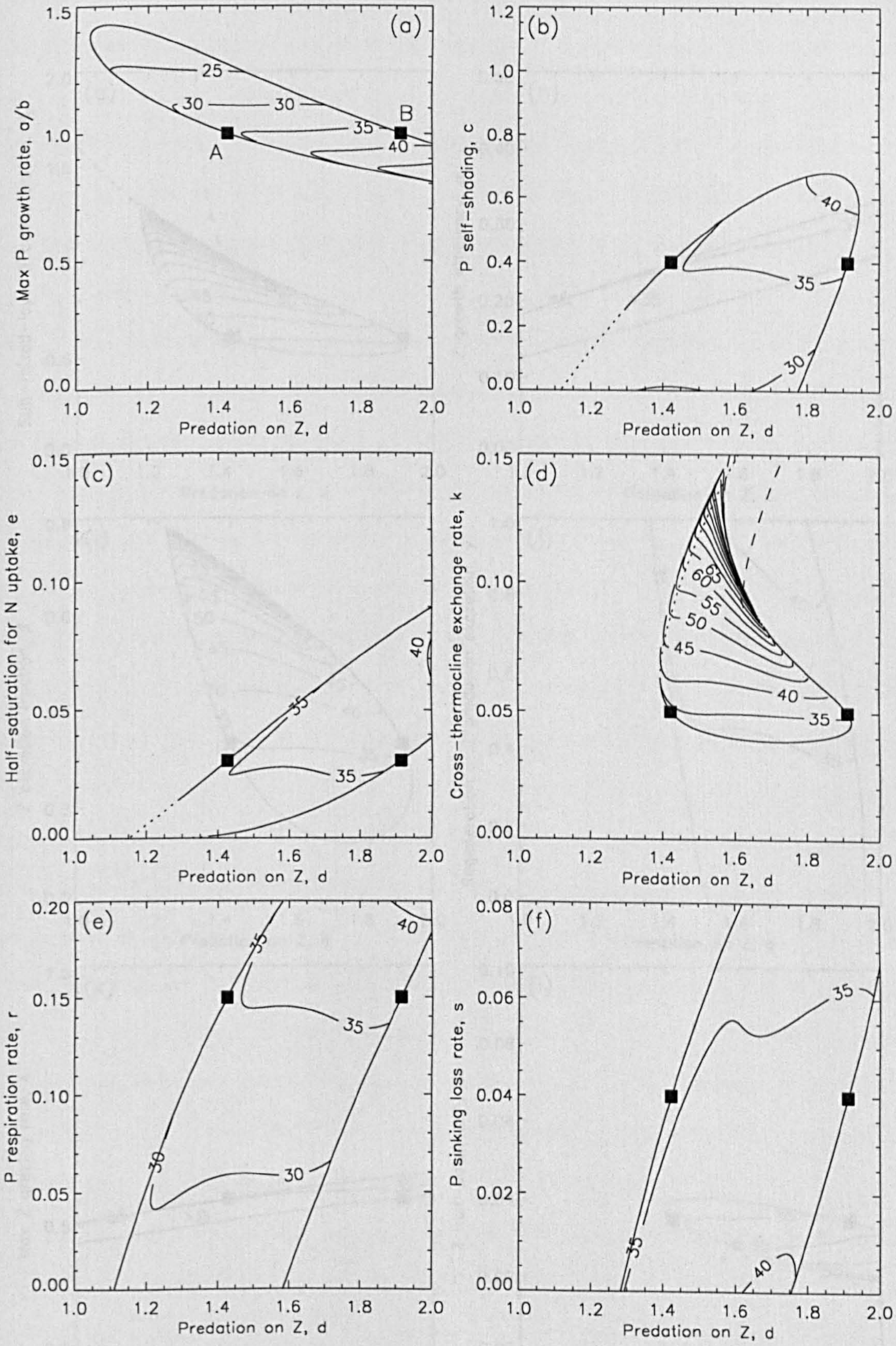

Figure 3.7: The steady-state bifurcation diagrams of Figure 3.4 are reproduced, and within the regions of oscillations the variations in period of stable limit cycles are indicated by contours of constant period. The numbers indicate the period, in days, along each contour.

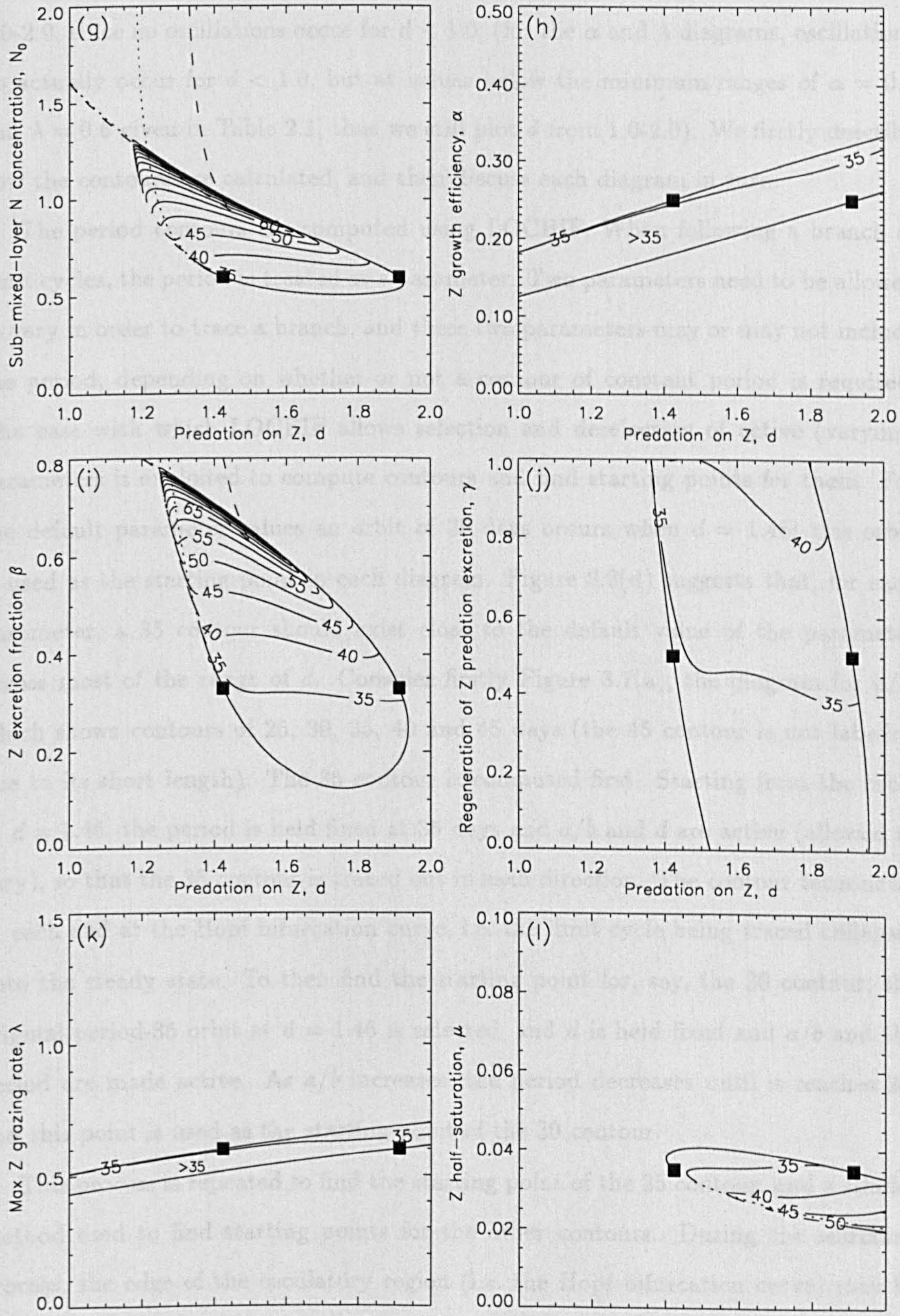

Figure 3.7 (ctd.)

fold bifurcations of the steady state. The range of d shown in each diagram is now 1.0-2.0, since no oscillations occur for $d < 1.0$; (for the α and λ diagrams, oscillations do actually occur for $d < 1.0$, but at values below the minimum ranges of $\alpha = 0.2$ and $\lambda = 0.6$ given in Table 2.1, thus we still plot d from 1.0-2.0). We firstly describe how the contours are calculated, and then discuss each diagram in turn.

The period contours are computed using LOCBIF. When following a branch of limit cycles, the period is treated as a parameter. Two parameters need to be allowed to vary in order to trace a branch, and these two parameters may or may not include the period, depending on whether or not a contour of constant period is required. The ease with which LOCBIF allows selection and deselection of active (varying) parameters is exploited to compute contours and find starting points for them. For the default parameter values an orbit of 35 days occurs when $d = 1.46$; this orbit is used as the starting point in each diagram. Figure 3.3(d) suggests that, for each parameter, a 35 contour should exist close to the default value of the parameter across most of the range of d. Consider firstly Figure 3.7(a), the diagram for a/b, which shows contours of 25, 30, 35, 40 and 45 days (the 45 contour is not labelled due to its short length). The 35 contour is computed first. Starting from the orbit at $d = 1.46$, the period is held fixed at 35 days and a/b and d are active (allowed to vary), so that the 35 contour is traced out in each direction. The contour terminates at each end at the Hopf bifurcation curve, i.e. the limit cycle being traced collapses onto the steady state. To then find the starting point for, say, the 30 contour, the original period-35 orbit at $d = 1.46$ is selected, and d is held fixed and a/b and the period are made active. As a/b increases, the period decreases until it reaches 30, and this point is used as the starting point of the 30 contour.

This process is repeated to find the starting point of the 25 contour, and a similar method used to find starting points for the other contours. During the searching process, the edge of the oscillatory region (i.e. the Hopf bifurcation curve) may be reached before the period has reached the next required value. This occurs, for example, when starting from $d = 1.46$ on the 35 contour and decreasing a/b in order to find a period-40 orbit to start the 40 contour. This is overcome by simply fixing a/b

at a point just above the Hopf curve, and then increasing d until a period-40 orbit is reached. Thus, extending this process, by keeping one of the two parameters fixed we can trace along limit cycles branches by moving vertically and horizontally through the oscillatory region until each required period is reached. Moving horizontally, with a/b fixed, and d and the period varying, is just what we did in Figure 3.3(d) when a/b was fixed at its default value.

We now show that no contours of 20 days can start from the Hopf bifurcation curve in the a/b diagram. By definition, two of the eigenvalues of the Jacobian of the steady state at a Hopf bifurcation exist as a complex and conjugate pair with zero real part, which we denote as $\pm\omega i$. The period of a limit cycle which emanates from a Hopf bifurcation is then given, sufficiently close to the Hopf bifurcation, by $2\pi/\omega$ (see, for example, Wiggins (1990), page 272). The contour of 35 days therefore terminates on the Hopf bifurcation curve at (or at least arbitrarily close to) the locations where $\omega = 2\pi/35$. Thus, by noting the values of ω as we move along the Hopf bifurcation curves we can determine, prior to actually calculating any limit cycles, where the contours will terminate, and what the minimum and maximum contours which terminate on the Hopf bifurcation curve will be. For the a/b curve, the maximum value of ω is 0.303, corresponding to a minimum period of 20.7 days, and is reached on the upper-left portion of the curve. This does not quite guarantee that no 20 contours will exist at all, since a contour could form an isolated closed loop (inside which the period is less than 20). But this seems unlikely given the decreasing nature of the period as we move towards the upper-left point of the oscillatory region. Indeed, tracing limit cycles by moving horizontally and vertically through the upper left region does not find any orbits with a period of 20 days, virtually verifying that no closed-loop 20 contours exist.

LOCBIF computes the Floquet multipliers of limit cycles, and detects local bifurcations of limit cycles such as fold, period doubling or Naimark-Sacker bifurcations. No such bifurcations were found along any of the contours in the a/b diagram (and hence the limit cycles are always stable), or indeed in the diagrams for any of the parameters except for k, N_0, β and μ for which fold bifurcations occur; in these diagrams the contours only represent the period of stable orbits. The contour diagrams will now be discussed in turn.

Figure 3.7(a) shows that an increase in a/b, due perhaps to increased sunlight, tends to decrease the period of the oscillations. Thus a higher maximum phytoplankton growth rate gives faster oscillations, as might be expected since the phytoplankton can respond to events more quickly. The contours are fairly horizontal, implying that at various levels of a/b the period remains insensitive to the value of d, as occurred for Figure 3.3(d), for which $a/b = 1$. Figure 3.3(d) showed that most variation of the period occurs close to Hopf A. This explains why the contours tend to double back on themselves just before terminating at Hopf A. So, if a/b is fixed and d is decreased, the period stays fairly constant, but drops slightly just before Hopf A is reached.

Figure 3.7(b) shows that the period tends to increase as the phytoplankton self-shading, c, increases. An increase in c reduces the phytoplankton growth term

$$\frac{N}{e+N}\frac{a}{b+cP}P,$$

and would be expected to have the same effect as a reduction in a/b. This is confirmed by the behaviour of the period, which increases as either c increases or a/b decreases. Similarly, increasing e reduces the growth term, and Figure 3.7(c) shows that increasing e tends to increase the period. However, the 40 contour shows that if $d = 2.0$, then increasing e from 0.05 will initially increase the period to above 40, but then decrease it to below 40. The 'doubling back' of the 40 contour thus does not occur as close to the Hopf curve as was the case in Figure 3.7(a). (Note that Hopf A becomes subcritical at low c and e values, thus stable cycles must undergo fold bifurcations in these regions, but none of the contours actually demonstrate this).

The diagrams for k, N_0 and β, Figures 3.7(d), (g) and (i) respectively, are very similar. We describe in detail the N_0 diagram, since in Figure 3.6 we have already shown the one-parameter bifurcation diagrams of nutrient versus d, at increasing fixed levels of N_0.

The contours computed are at intervals of 5 days up to the 100-day contour, and then the 125 contour is shown. There is no noticeable difference on the diagrams between the (unlabelled) 100 and 125 contours. When the Hopf bifurcations are subcritical, as shown by the lines of short dashes in Figure 3.7(g) and seen more clearly in the original Figure 3.4(g), unstable cycles emanate from the Hopf bifurcations and can become stable at fold bifurcations. Figure 3.6(b), for $N_0 = 1.0$, shows how the fold bifurcation of the limit cycles near Hopf A must occur at a d value to the left of Hopf A. In Figure 3.7(g) the fold of the limit cycle branch is indicated by the terminations of the contours, since we do not plot the contours for points where the cycles are unstable, and these terminations occur to the left of the curve of subcritical bifurcations. It is seen that the region of coexistence of stable limit cycles and stable steady states, which is bounded by the subcritical Hopf curve and the termination of the contours, is fairly small, and that the oscillations occur in a region which is only slightly larger than the region bounded by the Hopf bifurcation curves.

Figures 3.6(d) and (e) suggest that, at some N_0 value between 1.25 and 1.35, the fold bifurcations of the limit cycles disappear, most likely by coming together at a cusp point (on a diagram of N_0 against d) - this will be discussed in Section 3.8. For N_0 values above this cusp point no stable cycles, and hence no period contours, exist.

Figures 3.6(c)-(g) show that the unstable cycles can terminate at homoclinic connections to saddle points. As a cycle approaches a homoclinic connection its period tends to infinity. Along a branch of cycles the period changes continuously, even through a fold bifurcation. This helps explain why we find stable cycles with relatively large period in the N_0 diagram - in Figures 3.6(c) and (d) the fold bifurcations of stable limit cycles occur very close to where the subsequent unstable cycles go homoclinic. The diagrams for k, N_0 and β are the only ones for which we find fold bifurcations of steady states, and subsequent homoclinic behaviour, and this helps explain why these are the only diagrams exhibiting stable cycles with a period greater than 50 days.

Figure 3.7(e) shows that the period increases as r is increased, whilst Figure 3.7(f) shows that the period decreases as s is increased. Now, s is purely a linear loss of phytoplankton whilst r appears in the equations as both a linear phytoplankton loss and as a nutrient input. The bifurcation diagrams (without the contours) for r and s are very similar, and this was interpreted in Section 3.5 as implying that r behaves more like s, as a phytoplankton loss, than as, say, N_0, a nutrient input. But this is contradicted by the contour pictures - the period behaves more like N_0, increasing with increased r or N_0, even though the actual bifurcation picture is different. The increase in period for r is not as dramatic as that for N_0. Since the sensitivity of the period to s is actually quite weak, the consequence of an increase in r acting as a nutrient input is to pull the period up, overcoming the much weaker reduction due to its behaviour as a phytoplankton loss (like s). However, such interpretations should be treated with caution, since the actual loss is rP, and increasing r could actually cause rP, averaged over one cycle or taken at equilibrium, to decrease, a counter-intuitive but feasible notion. Figure 3.7(j) shows that the γ picture is similar to the r picture, which agrees with the notion of r being considered more as a nutrient input.

Figures 3.7(h) and (k) show that α and λ have similar minor influences on the period. Neither the 30 or 40 contours were reached in the region shown, and a decrease in either parameter increases the period slightly. So increasing the maximum zooplankton grazing rate, λ, has the opposite effect on the period to increasing the maximum phytoplankton growth rate, a/b.

Finally, Figure 3.7(l) shows that decreasing the zooplankton half-saturation constant, μ, increases the period. A decrease in μ will directly increase the grazing function $\lambda P^2 Z/(\mu^2 + P^2)$, but this (tentatively) has an opposite effect on the period to that of increasing λ, which will also increase the grazing function. For μ, the 50 contour is reached. Excepting k, N_0 and β, which exhibited homoclinic behaviour, this is the only parameter variation for which the period reaches 50 days.

The overall picture that emerges is that, except for the homoclinic cases of k, N_0 and β, as parameters are independently varied the period is confined to roughly the range 25-50 days, only reaching 25 in one case and 50 in one other. The insensitivity to d, originally illustrated in Figure 3.3(d), seems to persist, since the contours tend to remain fairly horizontal. The large periods reached for k, N_0 and β are explained by the presence of homoclinicity.

3.8 Limit cycle bifurcations - the complete picture for N_0

For mathematical completeness we now present the complete bifurcation diagram of N_0 against d, adding the bifurcations of limit cycles to the steady-state bifurcation diagram shown in Figure 3.4(g). The one-parameter diagrams of Figure 3.6 plus the N_0 contour diagram 3.7(g) together suggest how the complete bifurcation picture looks. We take Figure 3.4(g), and onto it sketch the bifurcations of limit cycles, namely curves of fold bifurcations and of homoclinic connections. Only parts of the fold curves could be numerically traced; the remainder are deduced approximately from theory and numerics. The resulting bifurcation diagram is shown in Figure 3.8. We shall firstly briefly discuss the diagram, and then explain in detail how it has been constructed.

The key for the curves of steady-state bifurcations remains as for Figure 3.4, namely solid squares are the default Hopf bifurcations, unlabelled solid curves are supercritical Hopf bifurcations, curves of short dashes are subcritical Hopf bifurcations and curves of long dashes are fold bifurcations. All bifurcations of limit cycles are represented by labelled solid curves. The two points labelled BB are Bautin bifurcations, and occur where each of the Hopf bifurcations changes criticality. From each of the Bautin bifurcations arises a curve of fold bifurcations of limit cycles, labelled FC1 and FC2, which then join up at a cusp point (FC2 is sketched, and thus the cusp point does not look definitively 'cusp-like'). BT is a Bogdanov-Takens bifurcation, where a curve of Hopf bifurcations terminates on a curve of fold bifurcations of steady states. From this point arises a curve of unstable homoclinic orbits, H1, which joins up at a cusp point with a second curve of unstable homoclinic orbits, H2. FC2, H1 and H2 could not be computed and are sketched, based on the following analytical and numerical discussion.

A point in parameter space at which a Hopf bifurcation changes from being supercritical to subcritical is called a Bautin bifurcation (Kuznetsov, 1995). Such points exist on each of the Hopf bifurcation curves, and are labelled BB in Figure 3.8. A

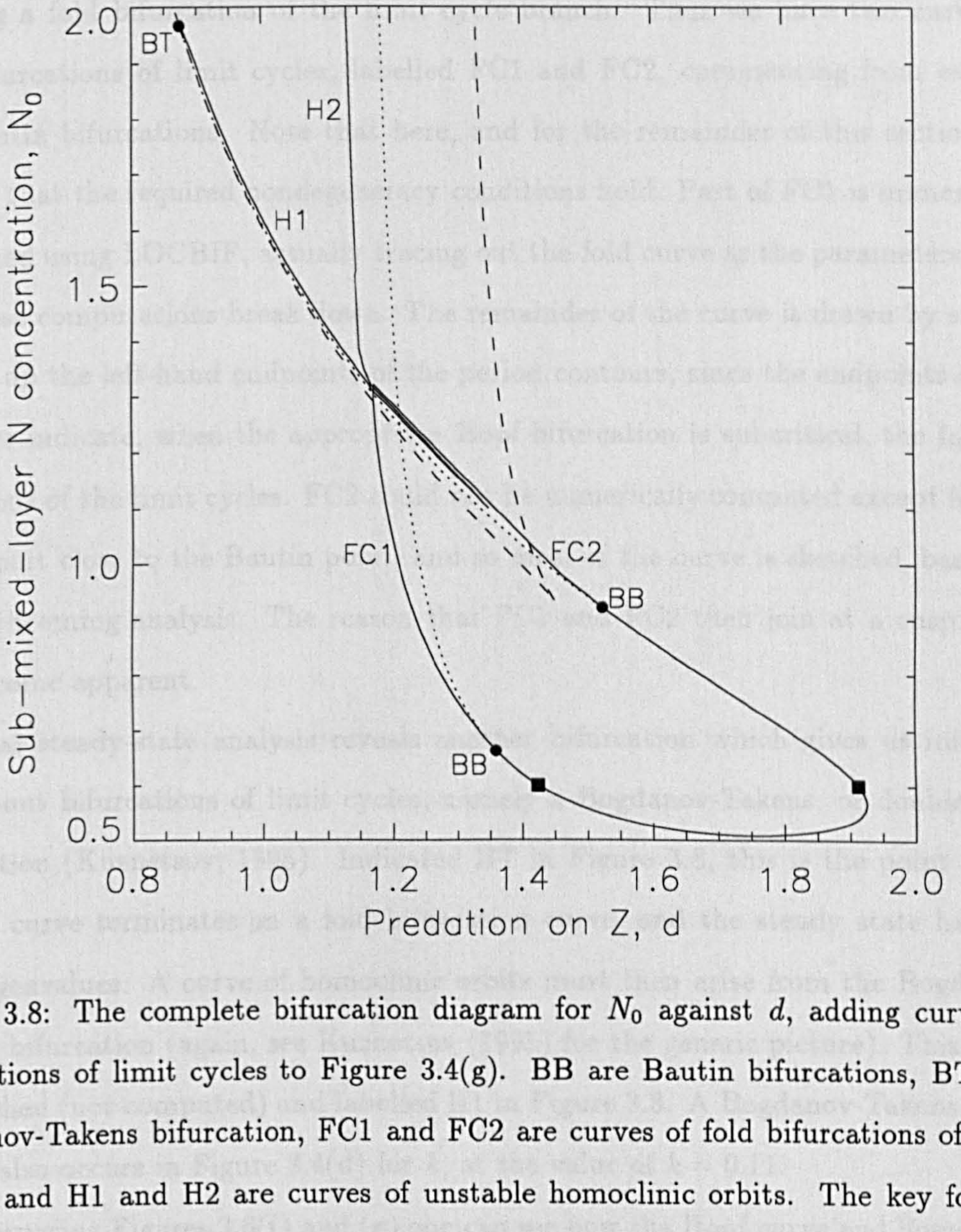

Figure 3.8: The complete bifurcation diagram for N_0 against d, adding curves of bifurcations of limit cycles to Figure 3.4(g). BB are Bautin bifurcations, BT is a Bogdanov-Takens bifurcation, FC1 and FC2 are curves of fold bifurcations of limit cycles, and H1 and H2 are curves of unstable homoclinic orbits. The key for the remaining curves is the same as that for Figure 3.4. FC1 is explicitly computed, whereas FC2, H1 and H2 are sketched, based on the numerical evidence.

curve of fold bifurcations of limit cycles must commence from a Bautin bifurcation due to the change in criticality of the Hopf bifurcation (see Kuznetsov (1995) for the generic picture). This can be seen by comparing Figures 3.3(a) and 3.6(a) - as N_0 increases from 0.6 to 0.75 Hopf A changes from being to supercritical to subcritical, yielding a fold bifurcation of the limit cycle branch. Thus we have two curves of fold bifurcations of limit cycles, labelled FC1 and FC2, commencing from each of the Bautin bifurcations. Note that here, and for the remainder of this section, we assume that the required nondegeneracy conditions hold. Part of FC1 is numerically computed using LOCBIF, actually tracing out the fold curve as the parameters vary, but these computations break down. The remainder of the curve is drawn by simply joining up the left-hand endpoints of the period contours, since the endpoints of the contours indicate, when the appropriate Hopf bifurcation is subcritical, the fold bifurcations of the limit cycles. FC2 could not be numerically computed except for the initial part close to the Bautin point, and so most of the curve is sketched, based on the forthcoming analysis. The reason that FC1 and FC2 then join at a cusp point will become apparent.

Local steady-state analysis reveals another bifurcation which gives us information about bifurcations of limit cycles, namely a Bogdanov-Takens, or double-zero, bifurcation (Kuznetsov, 1995). Indicated BT in Figure 3.8, this is the point where a Hopf curve terminates on a fold bifurcation curve, and the steady state has two zero eigenvalues. A curve of homoclinic orbits must then arise from the Bogdanov-Takens bifurcation (again, see Kuznetsov (1995) for the generic picture). This curve is sketched (not computed) and labelled H1 in Figure 3.8. A Bogdanov-Takens bifurcation also occurs in Figure 3.4(d) for k, at the value of $k = 0.11$.

Comparing Figures 3.6(f) and (g) one can see how the Hopf curve and homoclinic curve collapse onto the same point on the fold curve (in $N_0 - d$ space), and that at this point the nature of the fold bifurcation of the steady state changes. In Figure 3.6(g) the stable steady state loses stability at the fold bifurcation, whereas in (f) a saddle point changes stability at the fold bifurcation (but it remains a saddle point - the signs of the eigenvalues go from $-,+,+$ to $-,-,+$, whereas in (g) they go from $-,-,-$ to $-,-,+$). Figure 3.6(g) suggests that a second curve of homoclinic orbits passes through $N_0 = 2.0$, this is the curve H2. We now combine some theory and numerical investigation to show how the homoclinic curves H1 and H2, and the fold bifurcation curves FC1 and FC2, all fit together on Figure 3.8. We cannot say for certain that this is the picture, but the picture produced is consistent with the numerical evidence.

It is along the middle branch of saddle steady states that homoclinic connections occur in Figures 3.6(c)-(g). We now show that all such homoclinic connections involve unstable, and never stable, homoclinic orbits. The Andronov-Leontovich theorem (Kuznetsov, 1995; Glendinning and Laing, 1996) essentially states that the stability of a homoclinic orbit (and consequently the branch of cycles close to it in parameter space) is determined by the sum of the dominant eigenvalues of the saddle equilibrium point. The dominant eigenvalues, when the eigenvalues are real, are the negative eigenvalue closest to zero and the positive eigenvalue closest to zero.

Consider Figure 3.6(d), for $N_0 = 1.25$. The eigenvalues at the right-hand steady-state fold bifurcation are all real and have signs $-,0,+$. Close to the fold bifurcation, along the lower of the two branches (i.e. the middle branch of steady states when looking at the whole diagram), the eigenvalues have signs $-,-,+$, and following the notation of Glendinning and Laing (1996) we denote these eigenvalues as $\nu_2 < \nu_1 < 0 < \lambda_1$. The dominant eigenvalues are thus ν_1 and λ_1, and would be expected to vary in size as we move further along the branch (i.e. decrease d).

Now, at a homoclinic connection, the orbit, the cycle having infinite period, is stable if the dominant eigenvalues satisfy $|\nu_1| > \lambda_1$, otherwise it is a saddle cycle (we shall assume the term 'unstable cycles' to include saddle cycles). Monitoring the eigenvalues as d decreases we find that they remain real, and that $|\nu_1| < \lambda_1$ along the entire middle branch of Figure 3.6(d); therefore any homoclinic connections must involve unstable cycles. Consequently, the stable limit cycle branch, towards the right-hand end of which the numerics become unreliable, cannot become homoclinic to a saddle point.

In Section 3.6, for $N_0 = 1.25$ we found that a stable limit cycle occurs for $d =$

1.21761, but that no stable cycles exist for $d = 1.21762$. This discounts the possibility of a period doubling bifurcation or a Naimark-Sacker bifurcation, since these would both require stable cycles at $d = 1.21762$. Stable cycles can also go homoclinic to a saddle cycle rather than a saddle point (Gaspard and Wang, 1987), but we exclude this possibility since no other branch of saddle cycles appears to exist in this region (the branch from Hopf B ends at a homoclinic connection to a saddle point at $d = 1.2164$). Thus we conclude that the stable limit cycle branch undergoes a fold bifurcation, and it is the subsequent branch of unstable (saddle) cycles which terminates at a homoclinic connection, as in Figure 3.6(c) for $N_0 = 1.1$.

The fact that the negative eigenvalues remain real along the saddle-point branch, and do not coalesce to form a complex and conjugate pair, is instructive, since it means that the saddle point does not change from being a saddle node to become a saddle focus. This means that we cannot have homoclinic orbits to a saddle focus (Glendinning and Sparrow, 1984; Mullin, 1993), and eliminates the possibility of multiple homoclinic orbits exhibiting period-doubling cascades to chaos.

The eigenvalues satisfy $\nu_2 < \nu_1$ and $|\nu_2| < \lambda_1$ (together implying that $|\nu_1| < \lambda_1$) along the saddle-point branch of Figure 3.6(d) right down to $d = 1.203$; the fold then occurs at $d = 1.201$, and between these values we have $|\nu_2| > \lambda_1$, but $|\nu_1| < \lambda_1$ still holds. At $d = 1.203$ there is a neutral saddle with $|\nu_2| = \lambda_1$.

Now, returning to Figure 3.8, we find that $|\nu_2| < \lambda_1$ along the whole of the right-hand curve of fold bifurcations of the steady state (the third eigenvalue being zero), and from the cusp point up to the point where $N_0 = 1.06$ on the left-hand fold curve. At this point the eigenvalues are $\nu_2, 0, \lambda_1$, with $|\nu_2| = \lambda_1$. When $N_0 = 1.25$ and $d = 1.203$ we also have $|\nu_2| = \lambda_1$, as previously discussed. Starting from this point in $N_0 - d$ space, and varying N_0 and d, we can trace out a neutral-saddle curve, along which $|\nu_2| = \lambda_1$. This curve, which we do not display, remains close to the steady-state fold curve, reaching the fold curve at $N_0 = 1.06$ as N_0 decreases, and continuing past $N_0 = 2.0$ as N_0 increases. To the right of the curve it would seem likely that we have a large region for which $|\nu_2| < \lambda_1$. This region is bounded by the neutral-saddle curve, along which $|\nu_2| = \lambda_1$, and the parts of the fold curves with

$|\nu_2| < \lambda_1$. Providing that $\nu_2 < \nu_1$ holds throughout the region, and there is no other neutral-saddle curve with $|\nu_2| = \lambda_1$, we are guaranteed that $|\nu_1| < \lambda_1$ and thus all homoclinic orbits are unstable. Looking at the numerical values of the eigenvalues, it seems likely that these two conditions on the eigenvalues are satisfied. Indeed, by crossing the diagram horizontally at constant values of N_0 (at increments of 0.1) and monitoring the eigenvalues, we verify that $\nu_2 < \nu_1$ and $|\nu_2| < \lambda_1$ appear to hold throughout the region.

Thus the saddle point remains a saddle node, not becoming a saddle focus, and since $\nu_2 < \nu_1$ and $|\nu_2| < \lambda_1$ hold, the inequality $|\nu_1| < \lambda_1$ is satisfied, and so any homoclinic orbits that occur must be unstable. Furthermore, in the narrow region between the neutral-saddle curve and the left-hand fold curve, where $|\nu_2| > \lambda_1$, we find that $|\nu_1| < \lambda_1$ still holds.

Thus, we conclude that no stable homoclinic orbits exist. This, together with Figures 3.6(c)-(e), suggests that the curves of fold bifurcations of limit cycles, FC1 and FC2, join up at a cusp point, as drawn in Figure 3.8, and do not terminate on one of the curves of homoclinic orbits. See page 285 of Kuznetsov (1995) for an example of this latter case in a simple predator-prey system. Figures 3.6(b) and (c), plus the analysis just performed, suggest that the two homoclinic curves also terminate at a cusp point. The resultant Figure 3.8 is consistent with the one-parameter diagrams in Figure 3.6 and the contour diagram of Figure 3.7(g).

3.9 Discussion

We have systematically built up a comprehensive picture of the bifurcation behaviour of the three-component model, revealing an array of both local and global bifurcations.

The analysis of Section 3.2 showed how the steady state (N^*, P^*, Z^*), with nutrient, phytoplankton and zooplankton concentrations $N^*, P^*, Z^* > 0$, originates in the positive octant of phase space at a three-way transcritical bifurcation with two other steady states, $(N_0, 0, 0)$ and $(N_1{}^*, P_1{}^*, 0)$, which remain unstable throughout the subsequent numerical analysis.

We started with the parameters set at their default values, and showed that qualitatively different behaviour of the trajectories occurred at two distinct values of d, measuring the higher predation on zooplankton. This difference was illustrated in Figure 3.3, which showed how the steady-state values and limit cycle amplitudes of the nutrient, phytoplankton and zooplankton concentrations changed as d was varied; somewhat surprisingly the zooplankton concentrations showed the least variation, even though it was the higher predation on them which was being altered. The period of the oscillations was 35 *days*, in agreement with the oscillatory behaviour discussed by Ryabchenko *et al.* (1997).

Figure 3.4 then demonstrated how this picture can qualitatively change as a second parameter is varied, and showed that changing some of the parameters caused the oscillatory region to disappear. The parameters which, when varied, demonstrated persistence of the oscillatory behaviour across a similar range of d as in Figure 3.3, were r, s and γ. As discussed, the model may have been expected to show greater sensitivity to such parameters. We then showed how the original one-parameter bifurcation diagrams change significantly as the sub-mixed-layer nutrient level, N_0, is increased, displaying a rich array of bifurcation behaviour, including destruction of unstable cycles at homoclinic connections.

The insensitivity of the period to the value of d, Figure 3.3(d), implies that the fundamental frequency of the oscillations is controlled by some other specification of the system. This motivated calculation of the contour diagrams of Figure 3.7, showing how the period changes as each of the parameters is independently varied. Finally, we sketched the full bifurcation diagram about a Bogdanov-Takens bifurcation, to illustrate how the local and global bifurcations fit together.

The broad picture which emerges is that parameter space is divided into large regions where either a single stable equilibrium or a single attracting limit cycle exists. There are also small regions where the dynamics are more complex. These contain multiple attractors, such that, for example, two stable equilibria or a stable equilibrium plus a stable limit cycle can coexist.

Although, as is usual in bifurcational analysis, we have dwelt on the character of the asymptotic attractors (for large time) of the system, it is important to note that transient behaviour of trajectories is much affected, even for far shorter times, by that character. However, the trajectories which we have shown, in common with further simulations using other initial conditions and parameter values, indicate that the attractors are actually reached after a relatively short transient time.

The fact that we get oscillations at all with the quadratic zooplankton mortality term is important, and contrasts with the results of Steele and Henderson (1992), who found oscillations only with the linear mortality function. We re-iterate that we have not had to 'search around' parameter space in order to find oscillations, but that they occur when d is well within the range used by Steele and Henderson (1981), and the remaining parameters are set to their default parameters. An obvious question to ask is how does the bifurcation picture we have built up in this chapter change if the quadratic mortality function is replaced by the linear form. This is the focus of Chapter 4.

Chapter 4

Behaviour of model with linear zooplankton mortality

4.1 Introduction

We now investigate the NPZ system formulated in Chapter 2, but with linear, rather than quadratic, zooplankton mortality. The quadratic form dZ^2 in the equations is replaced by the linear form qZ. The two forms represent different ecological assumptions - for dZ^2, the specific (per capita) rate is dZ, which assumes that higher predators have a biomass proportional to their prey, whereas the linear qZ function assumes a constant specific higher-predation rate. The linear form is often used due to it being the most simple form, and due to the lack of data that would strongly support an alternative form. Steele and Henderson (1992), when discussing the use of the linear form, said that "There can be a strong empirical basis for this approach if nothing is known (or can be known) about the actual ecological context".

To investigate the new model, we follow the methodology of Chapter 3, in order to facilitate easy comparison between the results for the quadratic and linear zooplankton mortality cases. In Section 4.2 we explain the formulation of the new model, and obtain, from models in the literature, a default parameter value and range for q, the linear rate of zooplankton mortality. In Section 4.3 we perform an analysis of the system, and find that we can derive far more information about the location and stability of the steady states without having to invoke any specific values of the parameters, than we could for the quadratic case. We show that the three-way transcritical bifurcation calculated in Section 3.2, does not occur, but seems to have split into two separate transcritical bifurcations. We obtain conditions for stability of the steady state (N^*, P^*, Z^*) which is in the strictly positive octant, and in particular show that this is the unique steady state with $N^*, P^*, Z^* > 0$; thus the hysteresis behaviour which we found for the quadratic case cannot occur, due to the absence of coexisting positive steady states. We also calculate an invariant set, from which no trajectory can leave, and compare the nullsurfaces of the linear and quadratic systems, which illustrate clearly why the linear model cannot have coexisting positive steady states, whilst the quadratic model can.

We perform a numerical investigation into the dynamical behaviour of the system using q, the linear zooplankton mortality rate, as the primary bifurcation parameter. As discussed earlier, this parameter is a particularly difficult parameter to measure and was varied by Steele and Henderson (1981); the equivalent quadratic rate, d, was consequently used in Chapter 3 as a bifurcation parameter. Firstly, in Section 4.4, we plot the trajectories of the system when all the parameters are set at their default values, and then show that at an increased value of q the asymptotic behaviour of the system is qualitatively different, exhibiting oscillations rather than settling down to a steady state. This difference is then explained by the one-parameter bifurcation diagrams constructed in Section 4.5, where only q is varied, and the system is seen to undergo a Hopf bifurcation as q is increased. Each of the other parameters in the model is then varied in turn in Section 4.6, to produce two-parameter bifurcation diagrams which demonstrate how the default one-parameter diagrams change as the other parameters are varied. In Section 4.7 we show the explicit pictures for N_0 varying, as for the quadratic case, and in Section 4.8 we construct period-contour diagrams, illustrating how the period of the oscillations changes as each parameter is varied.

4.2 Model formulation

The three ordinary differential equations used to model the temporal changes of the concentrations of the three variables are:

$$\begin{aligned}
\frac{dN}{dt} &= -\frac{N}{e+N}\frac{a}{b+cP}P + rP + \frac{\beta\lambda P^2}{\mu^2+P^2}Z + \gamma q Z + k(N_0 - N), && (4.1)\\
\frac{dP}{dt} &= \frac{N}{e+N}\frac{a}{b+cP}P - rP - \frac{\lambda P^2}{\mu^2+P^2}Z - (s+k)P, && (4.2)\\
\frac{dZ}{dt} &= \frac{\alpha\lambda P^2}{\mu^2+P^2}Z - qZ. && (4.3)
\end{aligned}$$

The dZ^2 function used in the quadratic case is replaced by qZ, where q is the new predation rate, and has units of $days^{-1}$. This function appears in (4.3) as a zooplankton loss term due to predation by higher organisms, and as a regeneration term γqZ in (4.1), where γ is the proportion of the higher predation which is assumed to be recycled into utilisable nutrient. The food web diagram for this model is obviously the same as Figure 2.1 for the quadratic case, with dZ^2 replaced by qZ on the appropriate arrows.

Returning to the models reviewed in Chapter 2 to abstract realistic ranges for parameters, we find the following values of the daily zooplankton loss rate, q, to have been used when the linear zooplankton mortality term was considered: 0.04 day^{-1} by Wroblewski (1989), 0.05 by Fasham *et al.* (1990) and 0.07 by Evans and Parslow (1985). However, subtle differences in the equations used mean that these values cannot be simply taken at face value, as is now discussed.

Fasham *et al.* (1990) also included a linear zooplankton excretion rate of 0.1 day^{-1}, making a total loss rate of 0.15. However, our zooplankton excretion is an assumed proportion, β, of zooplankton grazing rather than a proportion of zooplankton biomass, and consequently our growth efficiency, α, has a value of 0.25, whereas the equivalent parameter in Fasham *et al.* (1990) was an assimilation efficiency with a value of 0.75. Wroblewski (1989) had an 'unassimilated fraction' of zooplankton grazing of 0.3 recycled to nutrient, with the remaining 0.7 fuelling zooplankton growth, but no zooplankton excretion. Evans and Parslow (1985) had a 'grazing efficiency' of 0.5, twice as high as our growth efficiency, and no specific excretion term. In

Fasham (1993) the Fasham *et al.* (1990) assimilation efficiency of 0.75 was retained, but the zooplankton loss term was changed from a linear form to a Michaelis-Menten (or Holling type II) function, with a maximum loss rate of 0.3 day^{-1}. This maximum was only attained in the simulations during summer at OWS "India"; for the Bermuda simulations, the loss rate peaked above 0.15 day^{-1} (the constant Fasham *et al.* (1990) total loss rate) only during April and May.

We wish to investigate the effects of substituting a linear zooplankton mortality term for the quadratic form used in Chapter 3. This substitution is a qualitative difference, and it is desirable to minimise quantitative differences. Thus, to obtain the default value and range for q, we note that Figure 3.3(c) showed a fairly constant steady state value of Z of roughly 0.075 $g\ C\ m^{-3}$, when all other parameters were set to their default values. Therefore, so that $qZ \simeq dZ^2$ (where dZ^2 is the quadratic mortality term used in Chapter 3), we take $q \simeq 0.075d$. Since d had the default value 1.0 and a range 0.25-2.0, we take the default value of q to be 0.075, with the range 0.015-0.150. This is a reasonable range to consider given the aforementioned values used by other authors and the practical difficulties in obtaining measurements for q.

4.3 Analysis

The following analysis is based on the analysis of a general class of models by Truscott and Brindley (1994). However, the incorporation of the self-shading term $b/(b+cP)$ in our model, means that their analysis cannot be explicitly used, despite what they claim. Their approach aids us in defining an invariant set for the system in Section 4.3.1. We then investigate analytically the steady states of the system and their stability, and find that the analysis can proceed further than was possible for the quadratic mortality model in Chapter 3. In Figure 4.3 we demonstrate how the transcritical bifurcations, which we have found analytically, actually occur, and this diagram allows easy comparison with the equivalent colour picture, Figure 3.1, for the quadratic case. We then plot the nullsurfaces for the default parameters. These illustrate graphically a major difference between the linear and quadratic cases, namely that the quadratic case can have more than one steady state in the strictly positive octant, whereas the linear case cannot.

4.3.1 An invariant set

We can define an invariant set for the system, from which no trajectory can leave. On the boundaries of the positive octant we have:

$$\begin{aligned}
\text{on } N &= 0, \quad \frac{dN}{dt} = rP + \frac{\beta\lambda P^2}{\mu^2+P^2}Z + \gamma q Z + kN_0 > 0,\\
\text{on } P &= 0, \quad \frac{dP}{dt} = 0,\\
\text{on } Z &= 0, \quad \frac{dZ}{dt} = 0.
\end{aligned}$$

Thus, no trajectory starting within the positive octant $\{N, P, Z \geq 0\}$ can leave it. Now consider the plane

$$N + P + Z = \xi$$
$$\text{where} \quad \xi = \max\left\{N_0, \frac{kN_0}{q(1-\gamma)}\right\},$$

which has outward normal vector $\underline{\mathrm{n}} = (1,1,1)$. Note that ξ is undefined for the special case of $\gamma = 1$ (full recycling of higher predation on zooplankton) which occurs, theoretically, for fully conservative systems; we do not consider such an extreme special case.

On the plane $N + P + Z = \xi$ we have

$$\begin{aligned}
\frac{d}{dt}\begin{pmatrix} N \\ P \\ Z \end{pmatrix} \cdot \underline{\mathrm{n}} &= \frac{d}{dt}\begin{pmatrix} N \\ P \\ Z \end{pmatrix} \cdot \begin{pmatrix} 1 \\ 1 \\ 1 \end{pmatrix}\\
&= \frac{d}{dt}(N + P + Z)\\
&= (\alpha + \beta - 1)\frac{\lambda P^2}{\mu^2 + P^2}Z + (\gamma - 1)\, qZ\\
&\qquad + k\,(N_0 - N) - (s + k)\,P\\
&\leq -(1-\gamma)\, qZ + kN_0 - kN - kP\\
&\leq 0,
\end{aligned}$$

where the last step comes from substituting $N = \xi - P - Z$ if $\xi = N_0$, or $Z = \xi - N - P$ if $\xi = kN_0/q(1-\gamma)$.

Thus no trajectories can pass through the plane in the outward direction; the plane intersects each of the N, P and Z axes at ξ, producing a tetrahedron which forms the boundary of the invariant set. The invariant set is hence given by

$$\{(N, P, Z) : N, P, Z \geq 0,\ N + P + Z \leq \xi\}.$$

Putting in the default numerical values of the parameters gives

$$\xi = \max\{0.6, 0.8\} = 0.8,$$

and so the plane $N + P + Z = 0.8$ together with the three planes $N, P, Z = 0$ define the tetrahedron enclosing the invariant set.

4.3.2 Steady states

We now calculate the steady states of the system, together with their stability. The Jacobian matrix is given by

$$\mathbf{A} = \begin{bmatrix} -\frac{aeP}{(e+N)^2(b+cP)} - k & -\frac{abN}{(e+N)(b+cP)^2} + r + \frac{2\beta\lambda\mu^2PZ}{(\mu^2+P^2)^2} & \frac{\beta\lambda P^2}{\mu^2+P^2} + \gamma q \\ \frac{aeP}{(e+N)^2(b+cP)} & \frac{abN}{(e+N)(b+cP)^2} - r - s - k - \frac{2\lambda\mu^2PZ}{(\mu^2+P^2)^2} & -\frac{\lambda P^2}{\mu^2+P^2} \\ 0 & \frac{2\alpha\lambda\mu^2PZ}{(\mu^2+P^2)^2} & \frac{\alpha\lambda P^2}{\mu^2+P^2} - q \end{bmatrix}$$

evaluated at the steady state values of N, P and Z. The steady states are solutions (N, P, Z) to $dN/dt = dP/dt = dZ/dt = 0$, i.e. solutions to the three simultaneous equations

$$\begin{aligned} 0 &= -\frac{N}{e+N}\frac{a}{b+cP}P + rP + \frac{\beta\lambda P^2}{\mu^2+P^2}Z + \gamma qZ + k(N_0 - N), && (4.4) \\ 0 &= \frac{N}{e+N}\frac{a}{b+cP}P - rP - \frac{\lambda P^2}{\mu^2+P^2}Z - (s+k)P, && (4.5) \\ 0 &= \frac{\alpha\lambda P^2}{\mu^2+P^2}Z - qZ. && (4.6) \end{aligned}$$

It is clear that solutions with $Z = 0$ will be unchanged from the quadratic zooplankton mortality case. However, their stability may change, since the third column of the Jacobian has changed; in the quadratic case this column included a term dZ, which became zero when $Z = 0$, but in the linear case this term has become q which will clearly not disappear when $Z = 0$.

Firstly, we note that adding (4.4) and (4.5), and using (4.6) to replace $\lambda P^2 Z/(\mu^2 + P^2)$ with qZ/α, yields

$$0 = -(1 - \alpha\gamma - \beta)\frac{qZ}{\alpha} - (s + k)P + k(N_0 - N), \tag{4.7}$$

which shows that all steady states with $P, Z \geq 0$ must have $N \leq N_0$ (since $(1 - \alpha\gamma - \beta) \geq 0$). Also, it is clear that no steady state with $N = 0$ and $P, Z \geq 0$ can exist, since setting $N = 0$ in (4.5) implies that $P = Z = 0$, but such a solution does not satisfy (4.4).

The steady state $(N, P, Z) = (N_0, 0, 0)$ exists for all parameter values, and the Jacobian at $(N_0, 0, 0)$ is

$$\mathbf{A} = \begin{bmatrix} -k & -\frac{aN_0}{b(e+N_0)} + r & \gamma q \\ 0 & \frac{aN_0}{b(e+N_0)} - r - s - k & 0 \\ 0 & 0 & -q \end{bmatrix}.$$

Since this matrix is upper triangular, the eigenvalues are clearly $-k$, Φ and $-q$, where Φ has the same definition as for the quadratic case in Chapter 3, namely

$$\Phi = \frac{aN_0}{b(e + N_0)} - r - s - k.$$

Thus the stability depends on the sign of Φ; for $\Phi < 0$ $(N_0, 0, 0)$ is a stable node and for $\Phi > 0$ it is a saddle point, and therefore unstable. As mentioned for the quadratic case, Φ is positive for the default parameter values, and remains positive as any one parameter is varied over its range.

We now show that for $\Phi < 0$ there are no other steady states in the positive octant $\{N, P, Z \geq 0\}$. It is clear that any steady state with $P = 0$ requires, from (4.6), that $Z = 0$, and so $(N_0, 0, 0)$ is the only such steady state. A steady state with $P > 0$ must, by definition, satisfy (4.5). Now, for $\Phi < 0$, knowing that $N \leq N_0$, (4.5) becomes

$$\begin{aligned}0 &= \frac{N}{e+N}\frac{a}{b+cP}P - rP - \frac{\lambda P^2}{\mu^2+P^2}Z - (s+k)P \\ &< \left(\frac{N_0 a}{(e+N_0)b} - r - s - k\right)P - \frac{\lambda P^2}{\mu^2+P^2}Z \\ &= \Phi P - \frac{\lambda P^2}{\mu^2+P^2}Z \\ &< 0,\end{aligned}$$

which is contradictory, and so no such steady state with $P > 0$ can exist. Thus, for $\Phi < 0$, $(N_0, 0, 0)$ is the only steady state in the positive octant, and furthermore we know that it is stable.

Setting $Z = 0$ and eliminating P from (4.4) and (4.5), results in the quadratic equation given by (3.4), namely

$$ckN^2 + \left[\frac{a(s+k)}{r+s+k} - b(s+k) + ck(e-N_0)\right]N - (b(s+k) + ckN_0)e = 0, \quad (4.8)$$

the solutions of which we denote by ${N_1}^*$ and ${N_2}^*$; they correspond to the two steady states $({N_1}^*, {P_1}^*, 0)$ and $({N_2}^*, {P_2}^*, 0)$, where ${P_1}^*$ and ${P_2}^*$ are given by

$${P_i}^* = \frac{k(N_0 - {N_i}^*)}{s+k} \quad (4.9)$$

for $i = 1, 2$. The constant term of (4.8) is negative, and so the quadratic equation has two real roots, one negative and one positive. Defining ${N_1}^*$ to be the positive root of (4.8) and ${N_2}^*$ to be the negative root, then the steady state $({N_2}^*, {P_2}^*, 0)$ can never enter the positive octant. Since ${N_1}^* > 0 > {N_2}^*$, from (4.9) we know that ${P_2}^* > 0$, and that ${P_1}^* < {P_2}^*$, since

$${P_1}^* = \frac{k(N_0 - {N_1}^*)}{s+k} < \frac{k(N_0 - {N_2}^*)}{s+k} = {P_2}^*. \quad (4.10)$$

Now, rearranging (4.9) we have

$${N_i}^* = N_0 - \left(\frac{s+k}{k}\right){P_i}^*, \quad (4.11)$$

which gives, upon substitution into (4.8) and use of the definition of Φ, the following quadratic for ${P_i}^*$,

$$\frac{c(s+k)}{k}{P_i}^{*2} - \left[c(e+N_0) + \frac{b(s+k)}{k(r+s+k)}\left(\frac{a}{b} - r - s - k\right)\right]{P_i}^* + \frac{b(e+N_0)}{r+s+k}\Phi = 0. \quad (4.12)$$

Since ${P_2}^*$ is always real and positive, and the product of two roots of a quadratic (with positive coefficient of the squared term) equals the constant term of the quadratic, the second root, namely ${P_1}^*$, will have the same sign as the constant term of (4.12). The sign of ${P_1}^*$ is thus simply the sign of Φ. As $\Phi \rightarrow 0$, we have ${P_1}^* \rightarrow 0$, and ${N_1}^* \rightarrow N_0$, i.e. $({N_1}^*, {P_1}^*, 0) \rightarrow (N_0, 0, 0)$.

A further point, that we shall need later, is that, for $\Phi > 0$, the coefficient of the linear term of (4.12) is negative, since

$$\frac{a}{b} - r - s - k > \frac{aN_0}{b(e + N_0)} - r - s - k = \Phi > 0. \tag{4.13}$$

For $\Phi > 0$, (4.12) is thus a U-shaped quadratic, with both roots being positive.

So, in common with the quadratic case, we find that ${P_1}^* > 0$ for $\Phi > 0$ and ${P_1}^* < 0$ for $\Phi < 0$, and at $\Phi = 0$ we have $({N_1}^*, {P_1}^*, 0) = (N_0, 0, 0)$, which is the previously calculated steady state.

The Jacobian at $({N_1}^*, {P_1}^*, 0)$ is given by

$$\mathbf{A} = \begin{bmatrix} -\frac{aeP}{(e+N)^2(b+cP)} - k & -\frac{abN}{(e+N)(b+cP)^2} + r & \frac{\beta\lambda P^2}{\mu^2+P^2} + \gamma q \\ \frac{aeP}{(e+N)^2(b+cP)} & \frac{abN}{(e+N)(b+cP)^2} - r - s - k & -\frac{\lambda P^2}{\mu^2+P^2} \\ 0 & 0 & \frac{\alpha\lambda P^2}{\mu^2+P^2} - q \end{bmatrix}. \tag{4.14}$$

One eigenvalue is

$$\frac{\alpha\lambda {P_1}^{*2}}{\mu^2 + {P_1}^{*2}} - q, \tag{4.15}$$

and the other two eigenvalues are the eigenvalues of the principal 2×2 submatrix $\mathbf{A}'$, the components of which we denote by R, S, T and U, using (4.5) to simplify the U term:

$$\begin{aligned} \mathbf{A}' &= \begin{bmatrix} R & S \\ T & U \end{bmatrix} \\ &= \begin{bmatrix} -\frac{aeP}{(e+N)^2(b+cP)} - k & -\frac{abN}{(e+N)(b+cP)^2} + r \\ \frac{aeP}{(e+N)^2(b+cP)} & -\frac{cP}{b+cP}(r + s + k) \end{bmatrix}. \end{aligned} \tag{4.16}$$

It can be seen from (4.16) that, for $P_1^* > 0$, i.e. $\Phi > 0$, we have $R, U < 0$, $T > 0$ and $R + T < 0$. The sign of S is undetermined, but from (4.14) we have $S + U < 0$. The trace of $\mathbf{A}'$ is clearly negative, and the determinant is positive:

$$\begin{aligned} \det\mathbf{A}' &= RU - ST \\ &= RU + TU - TU - ST \\ &= U(R+T) - T(S+U) \\ &> 0. \end{aligned}$$

Since $\mathbf{A}'$ is a 2×2 matrix with negative trace and positive determinant, both eigenvalues have negative real part, and hence the stability of $(N_1^*, P_1^*, 0)$ is determined solely by the sign of the third eigenvalue, given by (4.15). $(N_1^*, P_1^*, 0)$ is thus stable for $P_1^* > 0$ if and only if

$$\frac{\alpha\lambda P_1^{*2}}{\mu^2 + P_1^{*2}} - q < 0. \tag{4.17}$$

So at small enough values of P_1^*, $(N_1^*, P_1^*, 0)$ is stable. As $\Phi \to 0^+$, $(N_1^*, P_1^*, 0) \to (N_0, 0^+, 0)$, and for $\Phi < 0$, $P_1^* < 0$ and the steady state $(N_1^*, P_1^*, 0)$ is outside the positive octant. $(N_0, 0, 0)$ is unstable for $\Phi > 0$ and stable for $\Phi < 0$. Thus, at $\Phi = 0$ we have a transcritical bifurcation, whereby $(N_1^*, P_1^*, 0)$ exchanges stability with $(N_0, 0, 0)$. The local picture around this bifurcation can be summarised as

- $\Phi < 0$ – $(N_0, 0, 0)$ stable, $(N_1^*, P_1^*, 0)$ ecologically unrealistic ($P_1^* < 0$);
- $\Phi > 0$ – $(N_0, 0, 0)$ unstable, $(N_1^*, P_1^*, 0)$ realistic and stable.

In the numerical investigation we are going to use the higher predation on zooplankton parameter q as the primary bifurcation parameter (analogous to the quadratic case). Setting all parameters except for q to their default values, solving (4.8) and (4.9) gives the steady state

$$(N_1^*, P_1^*, 0) = (0.0196, 0.322, 0), \tag{4.18}$$

which is independent of q. However the stability does depend on q, and we can state from (4.17) that $(N_1^*, P_1^*, 0)$ is stable if and only if $q > 0.148$. Furthermore, setting only q, α and λ to their default values, we obtain the result that $(N_1{}^*, P_1{}^*, 0)$ is stable if and only if $P_1{}^* < \mu$, i.e. $P_1{}^*$ is less than the half-saturation constant for zooplankton grazing.

For the quadratic mortality case analysed in Chapter 3, we showed that the steady state $(N_1{}^*, P_1{}^*, 0)$, which had the same definition as in the current linear case, could not become stable. This difference can be seen by looking at the dZ/dt equation for each case. For quadratic mortality, we can write dZ/dt as

$$\frac{dZ}{dt} = \left(\frac{\alpha\lambda P^2}{\mu^2 + P^2} - dZ\right) Z.$$

If $P > 0$ and the bracketed function is negative, so that Z is decreasing, then the bracketed function will become positive at some small Z value, and it is clear that Z cannot reach zero whilst P remains non-zero. Thus the zooplankton cannot die out if the phytoplankton do not, and so $(N_1{}^*, P_1{}^*, 0)$ can never be stable. The zooplankton can only become extinct if the phytoplankton do, and hence $(N_0, 0, 0)$ can be stable.

For the linear case we have

$$\frac{dZ}{dt} = \left(\frac{\alpha\lambda P^2}{\mu^2 + P^2} - q\right) Z,$$

and if the bracketed term is negative then the zooplankton will die out exponentially. This can occur with persistence of P, and so $(N_1{}^*, P_1{}^*, 0)$ can be stable.

Furthermore, we note that the steady state $(N_1{}^*, P_1{}^*, 0)$ cannot undergo a Hopf bifurcation since two of its eigenvalues always have negative real parts. This is unlike the simple three-species food chain of Hastings and Powell (1991), for which McCann and Yodzis (1995) showed that the steady state with zero top predator undergoes a Hopf bifurcation. The resulting limit cycle, which lies in the plane $Z = 0$, can then, via a transcritical bifurcation of cycles, allow a cycle that previously existed in the octant $\{N, P > 0, Z < 0\}$ to enter the strictly positive octant $\{N, P, Z > 0\}$, (note that we use N, P, Z for ease of comparison with our model, although the Hastings and Powell model is not specifically a plankton model). This cycle then coexists with a second cycle in the positive octant, which arises from a Hopf bifurcation of a steady state of the form (N^*, P^*, Z^*). The interaction of two different oscillatory frequencies leads to the chaotic 'tea-cup' attractor.

Such a route to chaos is thus not possible in our system, since we cannot have a planar limit cycle arising from a Hopf bifurcation of $(N_1{}^*, P_1{}^*, 0)$. It would be instructive to be able to show that no limit cycles at all can exist in the $Z = 0$ plane. Bendixson's criteria (Perko, 1993) gives conditions which prove that no limit cycle can lie entirely within a planar region, but these conditions cannot quite be met, and so limit cycles may occur. We do know that $P_1{}^* > 0$ if and only if $\Phi > 0$, and so for $\Phi < 0$ no planar cycles can occur, since any such cycle must contain at least one steady state, by virtue of Poincaré index calculation (Glendinning, 1994).

For steady-state solutions of the form (N^*, P^*, Z^*) with $Z^* \neq 0$, (4.6) gives

$$P^* = \sqrt{\frac{q}{\alpha\lambda - q}}\,\mu, \tag{4.19}$$

where the positive root is taken. The steady state obtained from the negative root will have a negative P value for all parameter values, and so can never enter the positive octant. P^* clearly exists if and only if

$$q < \alpha\lambda. \tag{4.20}$$

The value of P^* depends only on parameters which are associated with zooplankton, and not on the phytoplankton growth term or the other phytoplankton losses.

For the default values of $\alpha = 0.25$ and $\lambda = 0.6$, such a steady state with non-zero Z does not exist for $q \geq 0.15$, and $(N_0, 0, 0), (N_1{}^*, P_1{}^*, 0)$ and $(N_2{}^*, P_2{}^*, 0)$ are the only steady states (and since $N_2{}^* < 0$ only the first two are biologically plausible), with solely $(N_1{}^*, P_1{}^*, 0)$ being stable since $\Phi > 0$.

There is a significant qualitative difference here from the quadratic mortality case, for which we had

$$Z = \frac{\alpha\lambda P^2}{d(\mu^2 + P^2)}, \tag{4.21}$$

preventing P^* from being found analytically; further substitution into the other equations led to an analytically intractable tenth order polynomial.

However for the linear case, discounting the extreme case of $1 - \alpha\gamma - \beta = 0$ (which only occurs for the complete recycling situation $\alpha + \beta = \gamma = 1$), we can rearrange

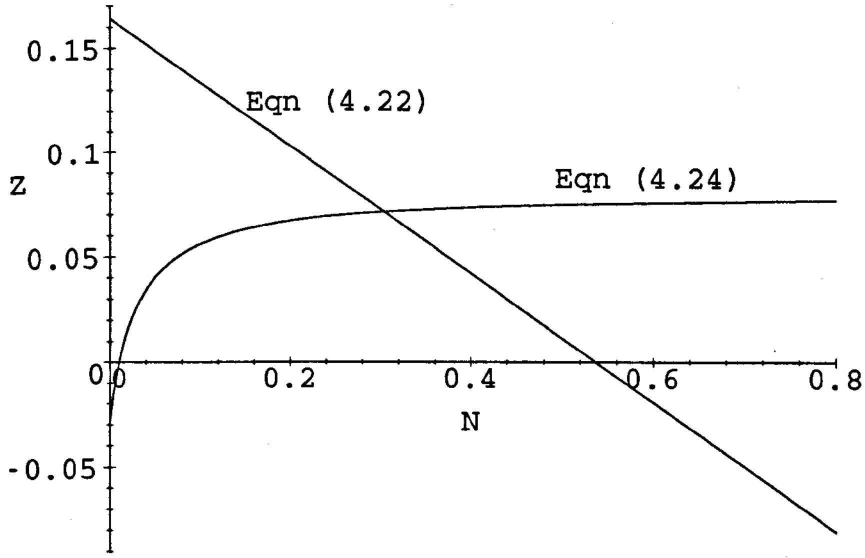

Figure 4.1: The straight line and curve defined by (4.22) and (4.24) intersect once when all of the parameters are set to their default values, and so there is exactly one steady state in $\{N, P, Z > 0\}$.

(4.7) to give

$$Z = \frac{\alpha}{q(1-\alpha\gamma-\beta)}\left[k(N_0-N)-(s+k)P^*\right], \tag{4.22}$$

which expresses Z as a function of N, with the value of P^* already known. For this equation, Z is always defined, and $Z > 0$ if and only if

$$P^* < \frac{k(N_0-N)}{s+k}. \tag{4.23}$$

From (4.5) and (4.6) we can obtain a second equation for Z in terms of N, namely

$$Z = \frac{\alpha}{q}\left[\frac{N}{e+N}\frac{aP^*}{b+cP^*}-(r+s+k)P^*\right]. \tag{4.24}$$

Now, for $N > 0$, (4.22) is a decreasing linear function of N, and (4.24) is a monotonically increasing function of N; thus the two curves have at most one intersection with $N > 0$. There is hence at most one steady state with $N, P, Z > 0$. In Figure 4.1 we plot the two curves given by (4.22) and (4.24), when all of the parameters are set at their default values. The curves intersect, and this point thus defines the N^* and Z^* values of the steady state (N^*, P^*, Z^*), with P^* defined by (4.19).

Rearranging (4.22) to make N the subject, and substituting this into (4.24), results in the following quadratic for Z^*:

$$\begin{aligned}0=&\left[\frac{q^2}{k\alpha^2}(1-\alpha\gamma-\beta)\right]Z^{*2}\\&+\left[-\frac{q}{k\alpha}(1-\alpha\gamma-\beta)\left[\frac{a}{b+cP^*}-(r+s+k)\right]P^*-\left(N_0-\frac{(s+k)}{k}P^*\right)\frac{q}{\alpha}-\frac{q}{\alpha}e\right]Z^*\\&+\left[\left(N_0-\frac{(s+k)}{k}P^*\right)\left[\frac{a}{b+cP^*}-(r+s+k)\right]-(r+s+k)e\right]P^* \qquad (4.25)\end{aligned}$$

The constant term of this quadratic can be written as

$$\begin{aligned}const &= \left\{\frac{c(s+k)}{k}P^{*2}-\left[c(e+N_0)+\frac{b(s+k)}{k(r+s+k)}\left(\frac{a}{b}-r-s-k\right)\right]P^*\right.\\&\qquad\qquad\left.+\frac{b(e+N_0)}{r+s+k}\Phi\right\}\frac{(r+s+k)P^*}{b+cP^*}\\&\equiv \left\{\Gamma\right\}\frac{(r+s+k)P^*}{b+cP^*}, \qquad (4.26)\end{aligned}$$

defining Γ as the term within the curly brackets.

Now, since $P^* > 0$, the term multiplying Γ is positive. We see that Γ is a quadratic in P^*; this quadratic is the same as the quadratic (4.12) for P_i^*. We only need to consider $\Phi > 0$, since we know that for $\Phi < 0$, $(N_0, 0, 0)$ is the only steady state in the positive octant. For $\Phi > 0$ we already know that (4.12) is a U-shaped quadratic with two positive real roots, and thus Γ is also a U-shaped quadratic, and has the same roots as (4.12). Therefore the roots of Γ are P_1^* and P_2^*, and so the zeroes of *const* are P_1^* and P_2^* (plus zero, but we know that $P^* > 0$). In Figure 4.2 we plot *const* as a function of P^*, with all of the parameters set to their default values, but without calculating the value of P^*, which is specified by (4.19); (in fact the parameters q, α, λ and μ which define P^* in (4.19) do not appear elsewhere in the definition of *const*). The two positive roots of *const* are P_1^* and P_2^*, where we know from (4.10) that $P_1^* < P_2^*$. Figure 4.2 shows that *const* > 0 if $P^* < P_1^*$, and *const* < 0 if $P_1^* < P^* < P_2^*$. We do not need to consider the region $P^* > P_2^*$, since $P_2^* > kN_0/(s+k)$, and so for $P^* > P_2^*$, (4.23) is violated, and Z^* would not be positive.

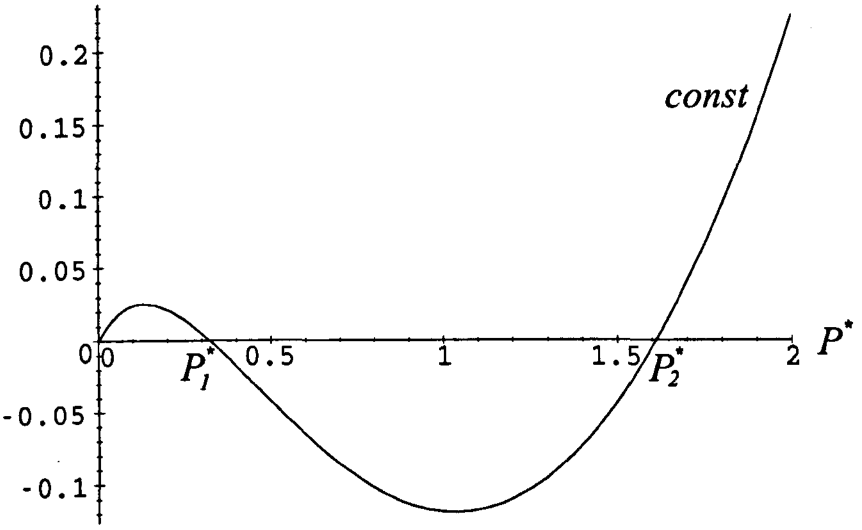

Figure 4.2: The value of *const*, defined by (4.26), is plotted as a function of P^*, with all of the parameters set to their default parameters. We know from the analysis that the positive solutions to *const* $= 0$ are ${P_1}^*$ and ${P_2}^*$, and see that *const* > 0 for $P^* < {P_1}^*$, and *const* < 0 for ${P_1}^* < P^* < {P_2}^*$, ($P^* > {P_2}^*$ need not be considered). When *const* > 0, we show that (N^*, P^*, Z^*) is in the positive octant.

If *const* > 0, then, from the way that *const* is expressed in (4.25), the signs of the two expressions

$$\left(N_0 - \frac{(s+k)}{k}P^*\right) \quad \text{and} \quad \left[\frac{a}{b+cP^*} - (r+s+k)\right] \tag{4.27}$$

must be the same, since their product must be positive. Suppose that the second of these is negative, then (4.5) is

$$\begin{aligned} 0 &= \frac{N^*}{e+N^*}\frac{a}{b+cP^*}P^* - rP^* - \frac{\lambda P^{*2}}{\mu^2+P^{*2}}Z^* - (s+k)P^* \\ &< \frac{a}{b+cP^*} - (r+s+k) - \frac{\lambda P^*}{\mu^2+P^{*2}}Z^* \\ &< 0, \end{aligned}$$

which is a contradiction, and so both expressions of (4.27) must be positive, which in turn implies that the linear coefficient of Z^* in (4.25) is negative. This means that the two roots of (4.25) have positive real parts, and are either a complex and conjugate pair or are both real. The fact that the first term of (4.27) is positive implies that the straight line given by (4.22) satisfies $Z > 0$ at $N = 0$, and since the curve defined by (4.24) satisfies $Z < 0$ at $N = 0$, the line and the curve definitely cross at some point with $N > 0$, due to their monotonicities, and so (4.25) has a real solution. Thus, (4.25) must have two positive real solutions, one of which corresponds to the positive steady state (N^*, P^*, Z^*), with $P^* < P_1{}^*$.

If parameters are varied such that $P^* \longrightarrow P_1{}^*$, then *const* $\longrightarrow 0$, as illustrated by Figure 4.2. Equivalently, we can talk of (alternative) parameters varying such that *const* $\longrightarrow 0$, which in turn will imply that $P_1{}^* \longrightarrow P^*$. Either way, we arrive at the case $P^* = P_1{}^*$, *const* $= 0$, for which $Z^* = 0$ solves (4.25), and $(N^*, P^*, Z^*) = (N_1{}^*, P_1{}^*, 0)$. If, $P^* > P_1{}^*$ we see that *const* < 0 (ignoring the unrequired case of $P^* > P_2{}^*$).

For *const* < 0, (4.25) has one positive real root and one negative real root. One root corresponds to a steady state with $N < 0$, and the corresponding Z value cannot equal zero at *const* $= 0$ since the linear coefficient of (4.25) is non-zero at *const* $= 0$ (we have shown that it is negative), and so the Z value for the steady state with $N < 0$ must remain positive. The second root of (4.25) is Z^*, which satisfies $Z^* > 0$ for *const* > 0, and $Z^* = 0$ when *const* $= 0$, and by continuity must satisfy $Z^* < 0$ for *const* < 0. Since *const* remains negative for $P_1{}^* < P^* < P_2{}^*$, Z^* remains negative in this region.

So, when $P^* < P_1{}^*$, where P^* is defined by (4.19), and $P_1{}^*$ is the smallest root of (4.12), (N^*, P^*, Z^*) is in the strictly positive octant $\{N, P, Z > 0\}$, and then as parameters are varied continuously such that $P^* = P_1{}^*$ and then $P^* > P_1{}^*$, (N^*, P^*, Z^*) leaves the strictly positive octant, by passing through the steady state $(N_1{}^*, P_1{}^*, 0)$. The surface in parameter space described by $P^* = P_1{}^*$ is equivalent to *const* $= 0$, and is even more concisely expressed by $\Omega = 0$, where Ω is defined using the form of the constant term in (4.25), taking out a factor of P^*:

$$\Omega = \left(N_0 - \frac{(s+k)}{k} P^*\right) \left[\frac{a}{b + cP^*} - (r + s + k)\right] - (r + s + k)e. \tag{4.28}$$

The steady state $(N_1{}^*, P_1{}^*, 0)$ is stable if and only if condition (4.17) is satisfied.

For $\alpha\lambda \leq q$ it is always satisfied, otherwise we can rearrange (4.17) as

$$P_1{}^* < \sqrt{\frac{q}{\alpha\lambda - q}}\,\mu = P^*. \tag{4.29}$$

Hence, the condition for stability of $(N_1{}^*, P_1{}^*, 0)$ is the same as the condition for (N^*, P^*, Z^*) to be outside the strictly positive octant; $(N_1{}^*, P_1{}^*, 0)$ is stable if and only if $P_1{}^* < P^*$, or equivalently $\Omega < 0$. This suggests that a transcritical bifurcation of $(N_1{}^*, P_1{}^*, 0)$ and (N^*, P^*, Z^*) takes place at $\Omega = 0$, and we now prove this to be the case.

The Jacobian at the positive steady state (N^*, P^*, Z^*) can be simplified and is given by

$$\mathbf{A} = \begin{bmatrix} -\frac{aeP}{(e+N)^2(b+cP)} - k & -\frac{abN}{(e+N)(b+cP)^2} + r + \frac{2\beta q^2\mu^2 Z}{\alpha^2\lambda P^3} & \left(\frac{\beta}{\alpha} + \gamma\right) q \\ \frac{aeP}{(e+N)^2(b+cP)} & \frac{abN}{(e+N)(b+cP)^2} - r - s - k - \frac{2q^2\mu^2 Z}{\alpha^2\lambda P^3} & -\frac{q}{\alpha} \\ 0 & \frac{2q^2\mu^2 Z}{\alpha\lambda P^3} & 0 \end{bmatrix}.$$

This is slightly simpler than the equivalent matrix for the quadratic zooplankton mortality case, for which the (3,3) term was non-zero, and no further analysis could be performed. For this case, however, we can partly follow the analysis of Truscott and Brindley (1994). Writing $\mathbf{A}$ as

$$\mathbf{A} = \begin{bmatrix} N_N & N_P & N_Z \\ P_N & P_P & P_Z \\ 0 & Z_P & 0 \end{bmatrix},$$

where each coefficient represents the terms given above, all except two of the signs of the coefficients are known, as follows:

$$\mathbf{A} = \begin{bmatrix} - & ? & + \\ + & ? & - \\ 0 & + & 0 \end{bmatrix},$$

We can also see that $N_N + P_N < 0$ and $N_P + P_P < 0$. The characteristic polynomial of $\mathbf{A}$, calculated by $0 = \det(\mathbf{A} - \omega\mathbf{I})$, where ω represents the eigenvalues and $\mathbf{I}$ is the 3×3 identity matrix, is

$$0 = \omega^3 - (N_N + P_P)\omega^2 + (N_N P_P - N_P P_N - P_Z Z_P)\omega + (N_N P_Z - N_Z P_N) Z_P.$$

The Routh-Hurwitz conditions (Murray 1989) state that for a characteristic polynomial of the form

$$0 = \omega^3 + a_1\omega^2 + a_2\omega + a_3,$$

then $\mathrm{Re}(\omega) < 0$ for all ω, if and only if

$$a_1, a_3 > 0 \quad \text{and} \quad a_1a_2 - a_3 > 0.$$

Now,

$$\begin{aligned} a_3 &= [N_N P_Z - N_Z P_N]\, Z_P \\ &= \left[\frac{aeqP}{\alpha(e+N)^2(b+cP)}(1-\alpha\gamma-\beta) + \frac{kq}{\alpha}\right] Z_P \\ &> 0, \end{aligned}$$

and

$$\begin{aligned} a_1a_2 - a_3 &= (N_N + P_P)(-N_N P_P + N_P P_N + P_Z Z_P) - (N_N P_Z - N_Z P_N) Z_P \\ &= (N_N + P_P)(-N_N P_P + N_P P_N) + (N_Z P_N + P_P P_Z) Z_P \\ &= (N_N + P_P)\Big[-(N_N + P_N)P_P + (N_P + P_P)P_N\Big] + (N_Z P_N + P_P P_Z) Z_P. \end{aligned}$$

Only the signs of N_P and P_P are undetermined. If we consider $P_P < 0$, then using the facts that $N_N + P_N < 0$ and $N_P + P_P < 0$, we have $a_1a_2 - a_3 > 0$. Furthermore, $P_P < 0$ also ensures that $a_1 > 0$, and the Routh-Hurwitz conditions are satisfied, and so (N^*, P^*, Z^*) is stable. Considering $P_P \geq 0$ leads nowhere, and so we now seek conditions for $P_P < 0$.

Using (4.5) we can write

$$\frac{abN}{(e+N)(b+cP)^2} = \frac{b}{b+cP}\left(r + s + k + \frac{\lambda PZ}{\mu^2 + P^2}\right),$$

which, together with

$$\frac{q^2(\mu^2 + P^2)^2}{\alpha^2\lambda^2 P^4} = 1,$$

(which simply comes from (4.19)), enables P_P to be written as

$$P_P = -\frac{cP}{b+cP}(r+s+k) + \frac{\lambda PZ}{(b+cP)(\mu^2+P^2)^2}\left(bP^2 - 2c\mu^2 P - b\mu^2\right), \quad (4.30)$$

where $P = P^*$. If

$$P^* \ < \ \max\left\{\mu, \frac{2c\mu^2}{b}\right\}, \tag{4.31}$$

then the final bracketed term of (4.30) is negative, so that $P_P < 0$ and the Routh-Hurwitz conditions are satisfied. So if P^* satisfies (4.31) then (N^*, P^*, Z^*) is stable.

This inequality is by no means a necessary condition for stability, and even if it is violated by a significant amount the steady state can remain stable. But we note that, in particular, if the steady state value P^* is below the zooplankton half grazing coefficient μ (condition (4.31)), then the steady state will be stable. Since the steady state is the unique steady state in the strictly positive octant $\{N, P, Z > 0\}$, then it can only lose stability (whilst remaining strictly positive) via a Hopf bifurcation.

For the default parameter values, $\mu = 0.035$ and $2\mu^2 c/b = 0.0049$, and if any one parameter is varied over its range given in Table 2.1 we still have $\mu < 2\mu^2 c/b$ (but if more than one parameter is varied then we can have $\mu > 2\mu^2 c/b$). In the numerical investigation we shall vary at most just one of b, c and μ at a time, and so (4.31) becomes $P^* < \mu$. Substituting for P^* from (4.19), we obtain

$$q < \frac{\alpha\lambda}{2}. \tag{4.32}$$

So when at least two of b, c and μ are set to their default values, (and the third one is within its realistic range), then if $q < \alpha\lambda/2$ the steady state (N^*, P^*, Z^*) is stable. For the default values of α and λ this gives $q < 0.075$, where 0.075 coincidently happens to be the default value of q.

We can also see that for small enough positive values of Z^*, from (4.30) we have $P_P < 0$, and hence (N^*, P^*, Z^*) will be stable. When $Z^* < 0$, $Z_P < 0$ and the term a_3 of the characteristic polynomial is negative, so the Routh-Hurwitz conditions are not satisfied, and so (N^*, P^*, Z^*) is unstable when $Z^* < 0$. Thus, the stability of (N^*, P^*, Z^*) changes as it passes through $({N_1}^*, {P_1}^*, 0)$, and we have a transcritical bifurcation, since we have already shown that the stability of $({N_1}^*, {P_1}^*, 0)$ also changes. (N^*, P^*, Z^*) passes through $({N_1}^*, {P_1}^*, 0)$ as Ω passes through zero, and the local behaviour around this transcritical bifurcation is summarised as

- $\Omega < 0$ – $({N_1}^*, {P_1}^*, 0)$ stable, (N^*, P^*, Z^*) ecologically unrealistic ($Z^* < 0$);
- $\Omega > 0$ – $({N_1}^*, {P_1}^*, 0)$ unstable, (N^*, P^*, Z^*) realistic and stable.

We shall discuss the regions of parameter space for which $\Omega < 0$ and $\Omega > 0$ in connection with the bifurcation diagrams of Sections 4.5 and 4.6, and we graphically demonstrate the nature of the two transcritical bifurcations occurring at $\Phi = 0$ and $\Omega = 0$ in Figure 4.3, which is to be discussed shortly.

Recall that P^* is defined only if $\alpha\lambda - q > 0$. If we start from a location in parameter space where (N^*, P^*, Z^*) is in the strictly positive octant (and hence $\alpha\lambda - q > 0$ and $P^* < {P_1}^*$), and vary α, λ and/or q continuously such that $\alpha\lambda - q \to 0^+$, then $P^* \to \infty$. Thus at some point with $\alpha\lambda - q > 0$ we reach $P^* = {P_1}^*$. This is the transcritical bifurcation, and so (N^*, P^*, Z^*) leaves the positive octant before P^* asymptotes to infinity. So we know that $\alpha\lambda - q$ can only reach zero if $Z^* < 0$, and thus if we start from a point in parameter space for which $Z^* > 0$, and continuously vary the parameters, we will reach the transcritical bifurcation, and (N^*, P^*, Z^*) will leave the positive octant, before we reach a point with $\alpha\lambda - q = 0$. Thus we will not need to worry about the situation $\alpha\lambda - q = 0$ arising in the numerical investigation when we trace the location of steady states as parameters vary, since this will only occur when $Z^* < 0$.

In Figure 4.3 we show the bifurcational behaviour of the three steady states as the phytoplankton respiration rate, r, is varied, with all of the other parameters set to their default values. These numerical computations graphically illustrate the analytical results. Figure 4.3 is constructed in the same way as Figure 3.1 for the quadratic case, and has the same colour coding and axes scales. The stability of $(N_0, 0, 0)$ is exactly the same as for the quadratic case. At low values of r, (N^*, P^*, Z^*) is in the positive octant and is stable, as shown by the solid red line, and we have $\Phi > 0$ and $\Omega > 0$. As r increases, N^* increases, P^* remains constant and Z^* decreases, passing through zero when $\Omega = 0$, which occurs at $r = 0.80$. Looking at Figure 4.2, as r is increased from its default value of 0.15 the value of P^* remains fixed (at 0.035), but the curve *const* moves such that ${P_1}^* \to P^*$ as $r \to 0.80$. At $r = 0.80$ stability

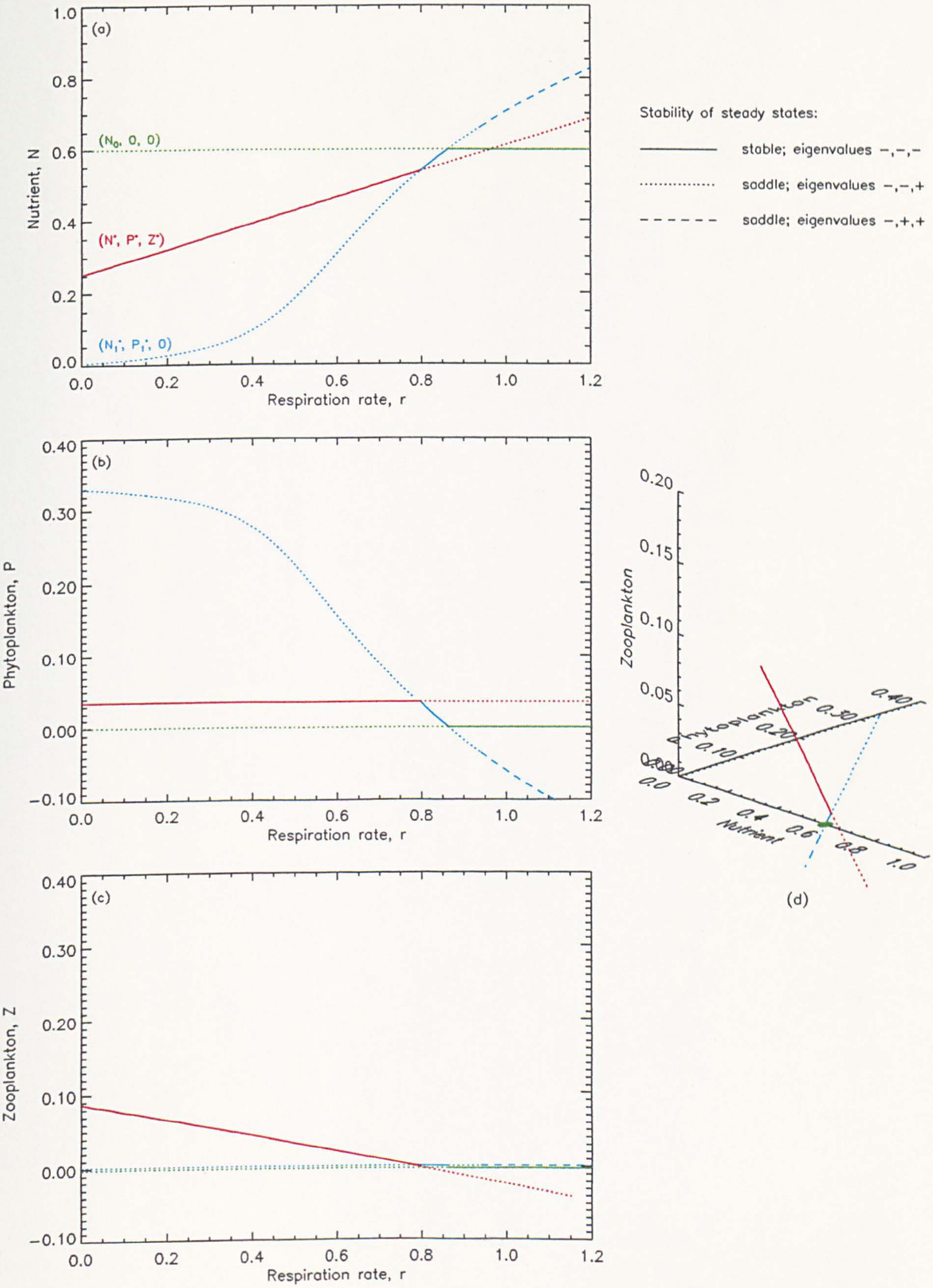

Figure 4.3: Location and stability of $(N_0, 0, 0)$, $({N_1}^*, {P_1}^*, 0)$ and (N^*, P^*, Z^*) as r is varied. The key indicates signs of the real parts of the eigenvalues and corresponding stabilities. Transcritical bifurcations occur at $r = 0.80$ $(\Omega = 0)$ and $r = 0.86$ $(\Phi = 0)$.

is transferred, via the transcritical bifurcation, to $(N_1{}^*, P_1{}^*, 0)$. $(N_1{}^*, P_1{}^*, 0)$ remains stable (solid blue line) until $r = 0.86$, which corresponds to $\Phi = 0$. At this point the second transcritical bifurcation occurs, and stability is transferred to $(N_0, 0, 0)$, which remains stable for $r > 0.86$.

Comparing the above analysis with that for the quadratic case, plus the corresponding Figures 3.1 and 4.3, it appears that the three-way transcritical bifurcation for the quadratic case has split into two transcritical bifurcations, allowing $(N_1{}^*, P_1{}^*, 0)$ to have a region of stability. In both cases (N^*, P^*, Z^*) loses stability as it leaves the positive octant $\{N, P, Z > 0\}$, but this occurs in different ways. For the quadratic case (N^*, P^*, Z^*) passes through the N-axis (which has $P = 0$ and $Z = 0$), whereas for the linear case it passes through the $Z = 0$ plane with $P \neq 0$, as is most clearly seen in the three-dimensional Figures 3.1(d) and 4.3(d).

Figure 4.3(b) shows how the phytoplankton steady-state value P^* remains constant as r varies, even though r is a direct phytoplankton loss rate. This is known from (4.19), which shows that P^* is independent of all of the parameters which do not appear in the dZ/dt equation, including r and the other loss terms, as well as the growth terms. This is a consequence of the linear zooplankton mortality term, and does not occur for the quadratic case.

It is seen that, at $r = 0.94$, the eigenvalues of $(N_1{}^*, P_1{}^*, 0)$ change from having real parts with signs $-, -, +$ to $-, +, +$ (which implies that they must all be real), as indicated by the blue line changing from dotted to dashed. This is due to $(N_1{}^*, P_1{}^*, 0)$ undergoing a third transcritical bifurcation, this time with the steady state $(N_-{}^*, P_-{}^*, Z_-{}^*)$ which arises from using the negative root, $P_-{}^*$, of (4.19). Since this steady state can never enter the positive octant its nature was not considered further in the analysis, and for clarity it is not drawn in Figure 4.3.

Comparing the red lines in Figure 4.3 and Figure 3.1, it can be seen that, whilst (N^*, P^*, Z^*) remains in the positive octant, the quantitative nature of Z^* differs less than that of N^* and P^* between the two cases, despite it being solely the zooplankton mortality that differs between the two models.

4.3.3 Nullsurfaces

In Figure 4.4 we show how the (non-trivial) nullsurfaces for the linear zooplankton mortality case differ from those for the quadratic case. An N nullsurface is defined as a surface in $N-P-Z$ space on which $dN/dt = 0$; P and Z nullsurfaces are defined similarly. If the N, P and Z nullsurfaces all intersect at a particular point, then this point is a steady state of the system (since $dN/dt = dP/dt = dZ/dt = 0$). Clearly, from (4.5) and (4.6), $P = 0$ is a P nullsurface and $Z = 0$ is a Z nullsurface for all parameter values; we refer to these as the trivial nullsurfaces and do not plot them.

For a two-dimensional system modelling, say, P and Z, one can draw the P nullclines and the Z nullclines, which are, respectively, the lines in the two dimensional $P-Z$ space for which $dP/dt = 0$ and $dZ/dt = 0$. At intersections of the nullclines exist steady states, and drawing all of the nullclines on one (two-dimensional) graph is instructive in elucidating the behaviour of the system. However, drawing all of the nullsurfaces of a three-dimensional system on one (three-dimensional) graph results in an unsightly mess, and so we plot the (non-trivial) nullsurfaces on separate graphs.

The nullsurfaces are most useful in comparing the two cases of linear and quadratic zooplankton mortality. The lines indicated on the surfaces in Figure 4.4 are at intervals of 0.05 in Z. All of the parameters are set at their default values. The N nullsurfaces for each case are qualitatively similar. The P nullsurfaces are the same, since the dP/dt equations do not depend on the form of zooplankton mortality and so are the same for each model. At a P value larger than that shown, the P nullsurface curves down again (i.e. Z decreases), in a similar fashion to the nullclines of PZ systems (for example, see Steele and Henderson (1992)). The Z nullsurfaces do, however, show a qualitative difference, as is seen by solving $dZ/dt = 0$ in each case, giving the surfaces defined, for the linear and quadratic cases respectively, by

$$P = \sqrt{\frac{q}{\alpha\lambda - q}}\,\mu, \tag{4.33}$$

and

$$Z = \frac{\alpha\lambda P^2}{d(\mu^2 + P^2)}. \tag{4.34}$$

Linear zooplankton mortality Quadratic zooplankton mortality

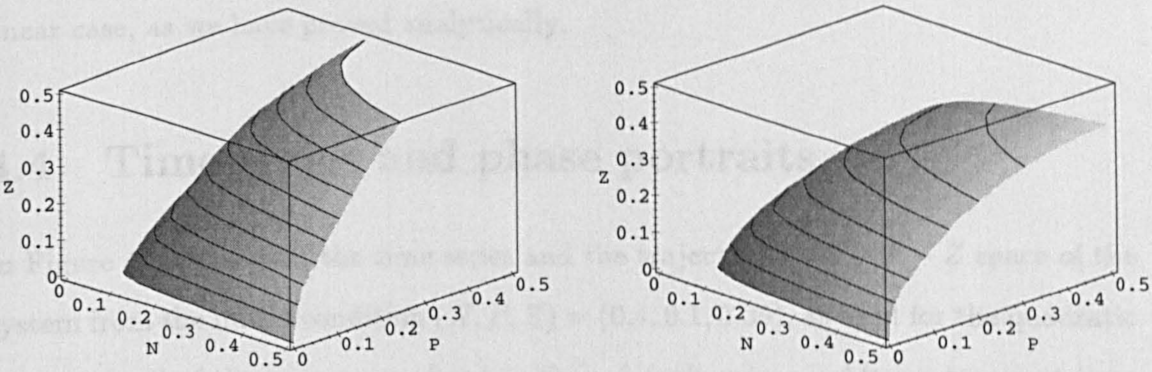

(a) N nullsurface (d) N nullsurface

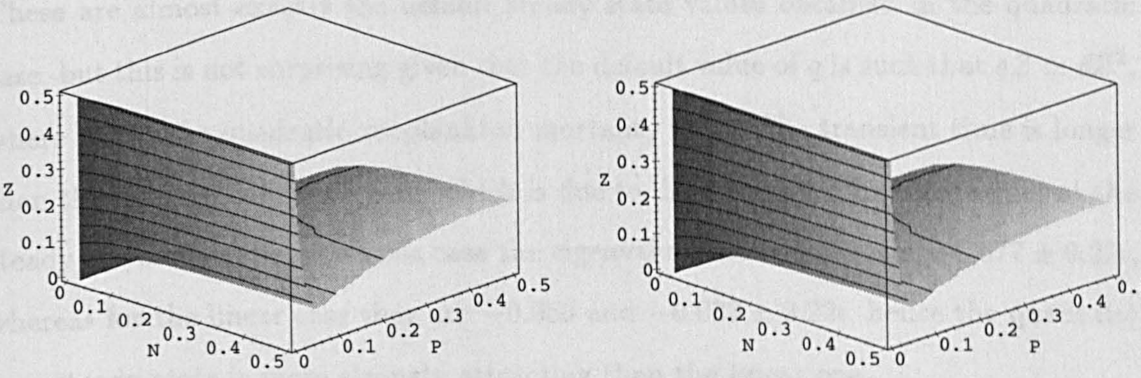

(b) P nullsurface (e) P nullsurface

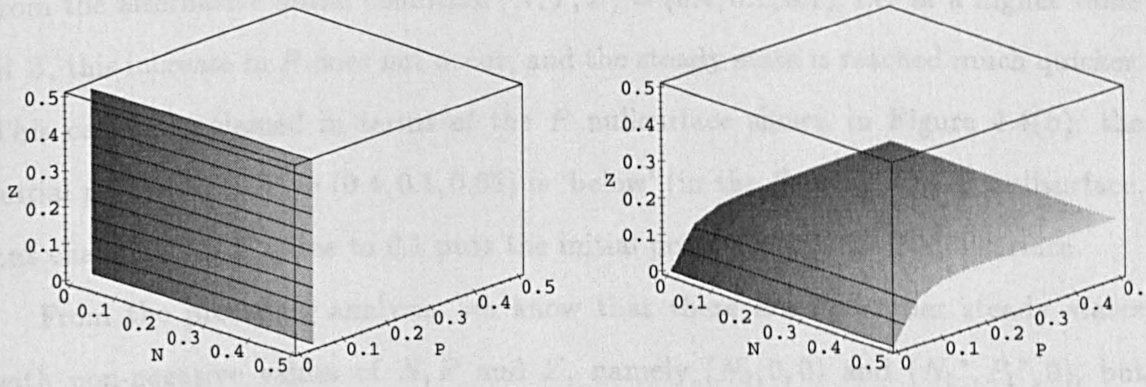

(c) Z nullsurface (f) Z nullsurface

Figure 4.4: Nullsurfaces for linear Z mortality (left column) and quadratic Z mortality (right column), for the default parameter values. The P nullsurface is the same for both cases, and the qualitative difference between the Z nullsurfaces illustrates how multiple steady states cannot occur for linear Z mortality.

This graphically shows how multiple coexisting steady states can occur for quadratic mortality (as was demonstrated in Sections 3.5 and 3.6), but cannot occur for the linear case, as we have proved analytically.

4.4 Time series and phase portraits

In Figure 4.5(a) we plot the time series and the trajectory in $N-P-Z$ space of the system from the initial condition $(N,P,Z) = (0.4, 0.1, 0.05)$, as used for the quadratic case, with all of the parameters fixed at their default values. After a transient time N, P and Z settle down to steady-state values of $(N,P,Z) = (0.30, 0.035, 0.071)$. These are almost exactly the default steady state values obtained in the quadratic case, but this is not surprising given that the default value of q is such that $qZ \simeq dZ^2$, where dZ^2 is the quadratic zooplankton mortality term. The transient time is longer than that for the quadratic case, which is due to differences in the eigenvalues at the steady states. For the quadratic case the eigenvalues are -0.055 and $-0.077 \pm 0.22i$, whereas for the linear case they are -0.050 and $-0.032 \pm 0.22i$, hence the quadratic case steady state is more strongly attracting than the linear one.

The initial large increase in P is due to the excitable nature of the system; starting from the alternative initial condition $(N,P,Z) = (0.4, 0.1, 0.1)$, i.e. at a higher value of Z, this increase in P does not occur, and the steady state is reached much quicker. This can be explained in terms of the P nullsurface shown in Figure 4.4(b); the initial point $(N,P,Z) = (0.4, 0.1, 0.05)$ is 'below' (in the Z sense) the P nullsurface, but changing the Z value to 0.1 puts the initial point 'above' the P nullsurface.

From the preceding analysis, we know that there are two other steady states with non-negative values of N, P and Z, namely $(N_0, 0, 0)$ and $(N_1{}^*, P_1{}^*, 0)$, but that these are both unstable at the default parameter values. We also know that $(N,P,Z) = (0.30, 0.035, 0.071)$ is the unique steady state in the strictly positive octant $\{N, P, Z > 0\}$. The analysis showed that if q is then decreased from its default value of 0.075, then (N^*, P^*, Z^*) will stay in the strictly positive octant and remain stable (although the actual values of N, P and Z will obviously change).

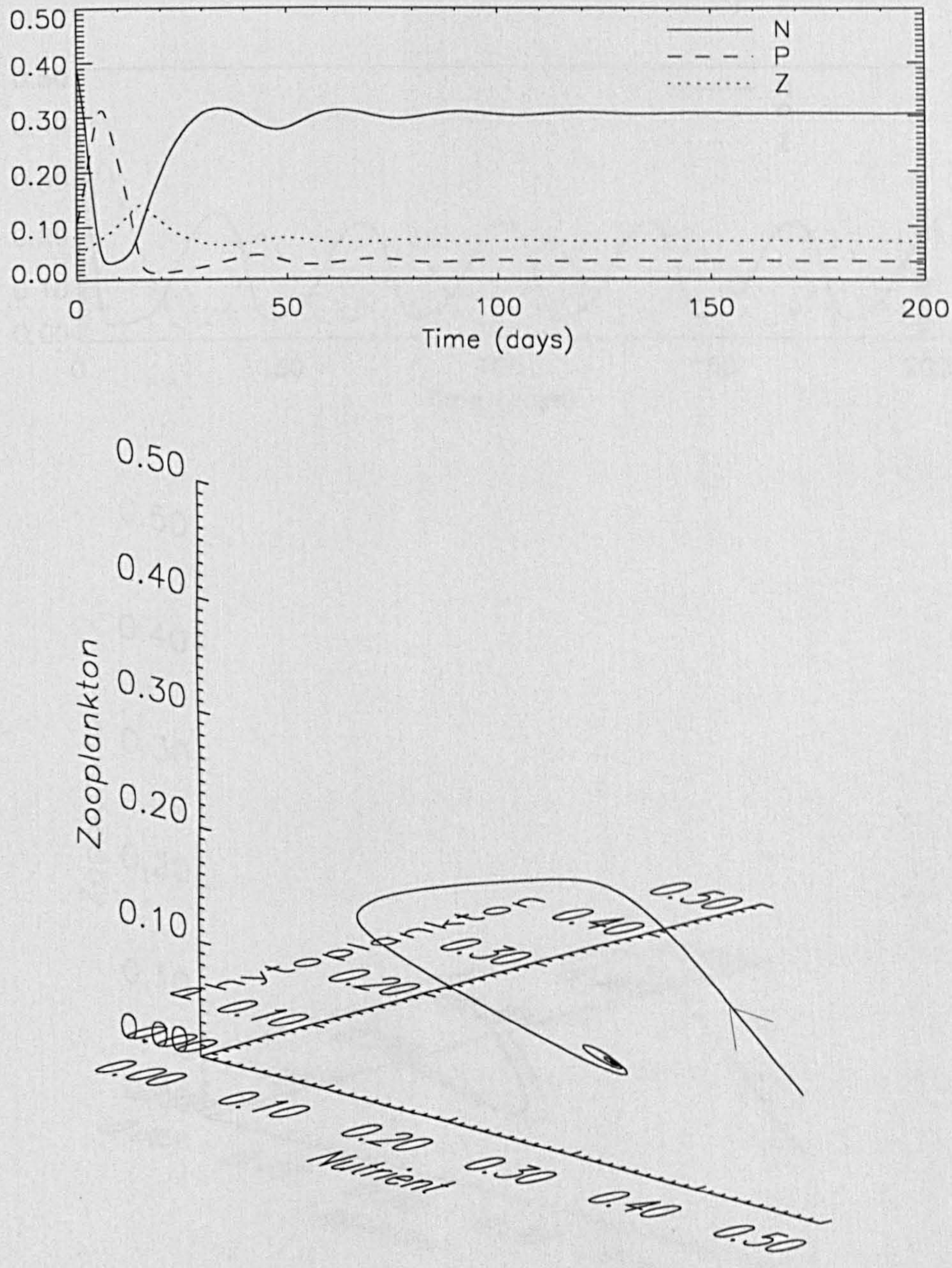

(a) $q = 0.075$ - N, P and Z settle down to steady-state values.

Figure 4.5: The time series and phase-space trajectory at (a) $q = 0.075$ and (b) $q = 0.11$ (next page), with all of the other parameters fixed at their default values.

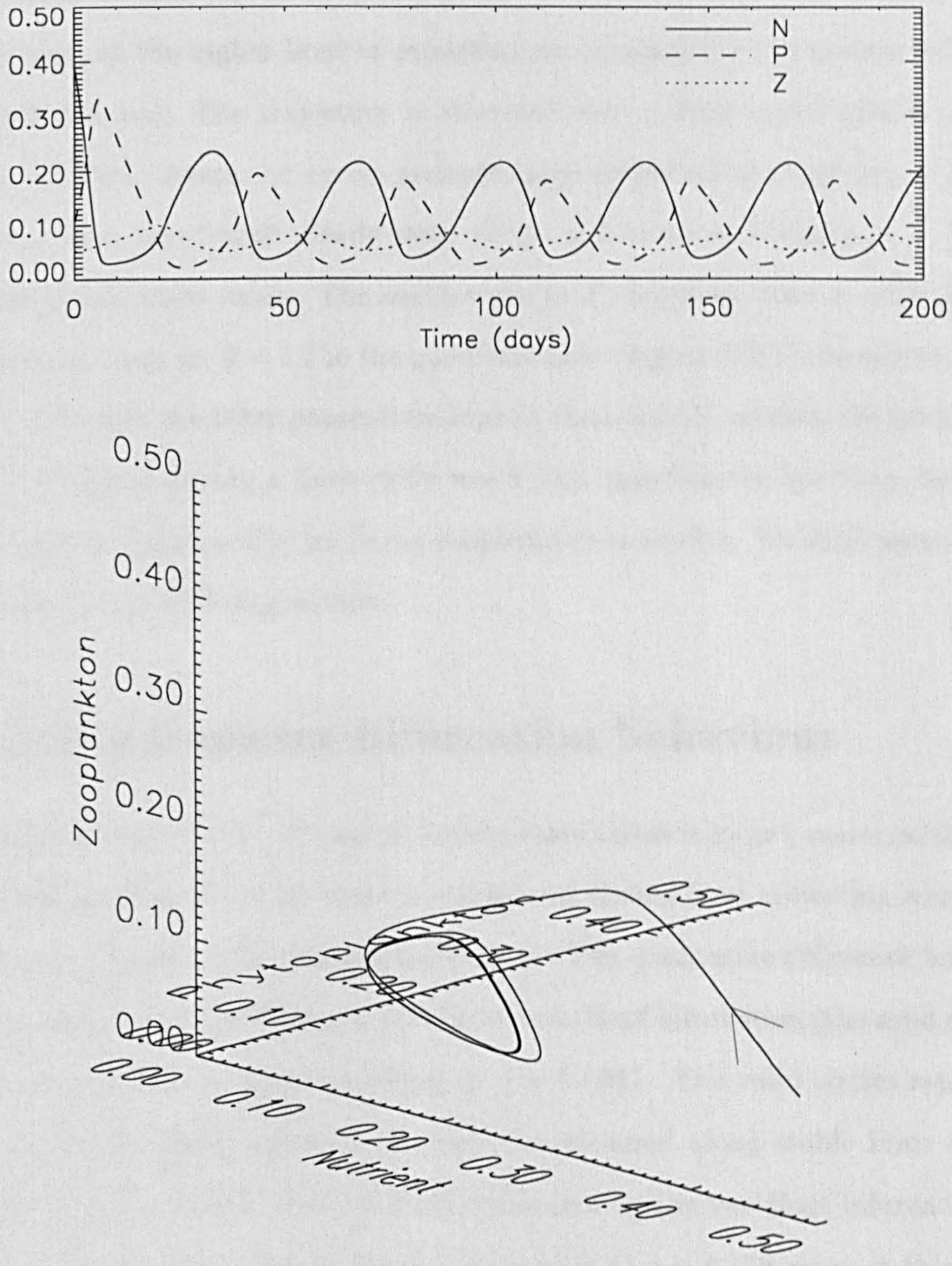

(b) $q = 0.11$ - the system settles down to a stable limit cycle.

In Figure 4.5(b) the value of q is increased to 0.11, and the system integrated from the same initial conditions. The value $q = 0.11$ was chosen since it is (to two significant figures) one and a half times the default value of 0.075, and for the quadratic case we showed the trajectories for $d = 1.0$ and $d = 1.5$. As for the quadratic case, at the higher level of predation on zooplankton the system exhibits oscillatory behaviour. The trajectory is attracted onto a limit cycle, with a period of roughly 35 days. Again the cycles undergo large amplitude fluctuations in N, at values lower than the default steady-state value, and small oscillations in Z about the default steady-state value. The oscillations in P, however, have a much larger amplitude than those for $d = 1.5$ in the quadratic case. Figure 3.3(b) showed that, for any value of d (with the other parameters kept at their default values), the maximum value of P attained during a limit cycle was 0.125, significantly less than the 0.18 value attained in Figure 4.5(b) for linear zooplankton mortality. We shall pursue this point further in the following section.

4.5 One-parameter bifurcation behaviour

Figure 4.6 shows how the N^*, P^* and Z^* steady-state values vary as q varies, with solid lines indicating when the steady state is stable, and dashed lines indicating when it is unstable, as in Figure 3.3 for the quadratic case. The qualitative difference between the trajectories at $q = 0.075$ and $q = 0.11$ is due to a Hopf bifurcation (the solid square labelled A) of the steady state occurring at $q = 0.0841$. The solid circles represent minimum and maximum values of the variables attained along stable limit cycles, and it is seen that a branch of stable limit cycles join up the two Hopf bifurcations A and B. The steady-state curve in Figure 4.5(a) ends at $q = 0.148$ since at this point Z^* passes through zero, because Ω, as defined by (4.28), reaches zero. This point is the transcritical bifurcation calculated in Section 4.3.2, and stability is transferred to $({N_1}^*, {P_1}^*, 0)$, which remains stable for $q > 0.148$.

The bifurcational behaviour is very similar to the quadratic case; the Hopf bifurcations, and consequent limit cycles, still occur. Comparing Figures 3.3 and 4.6, the

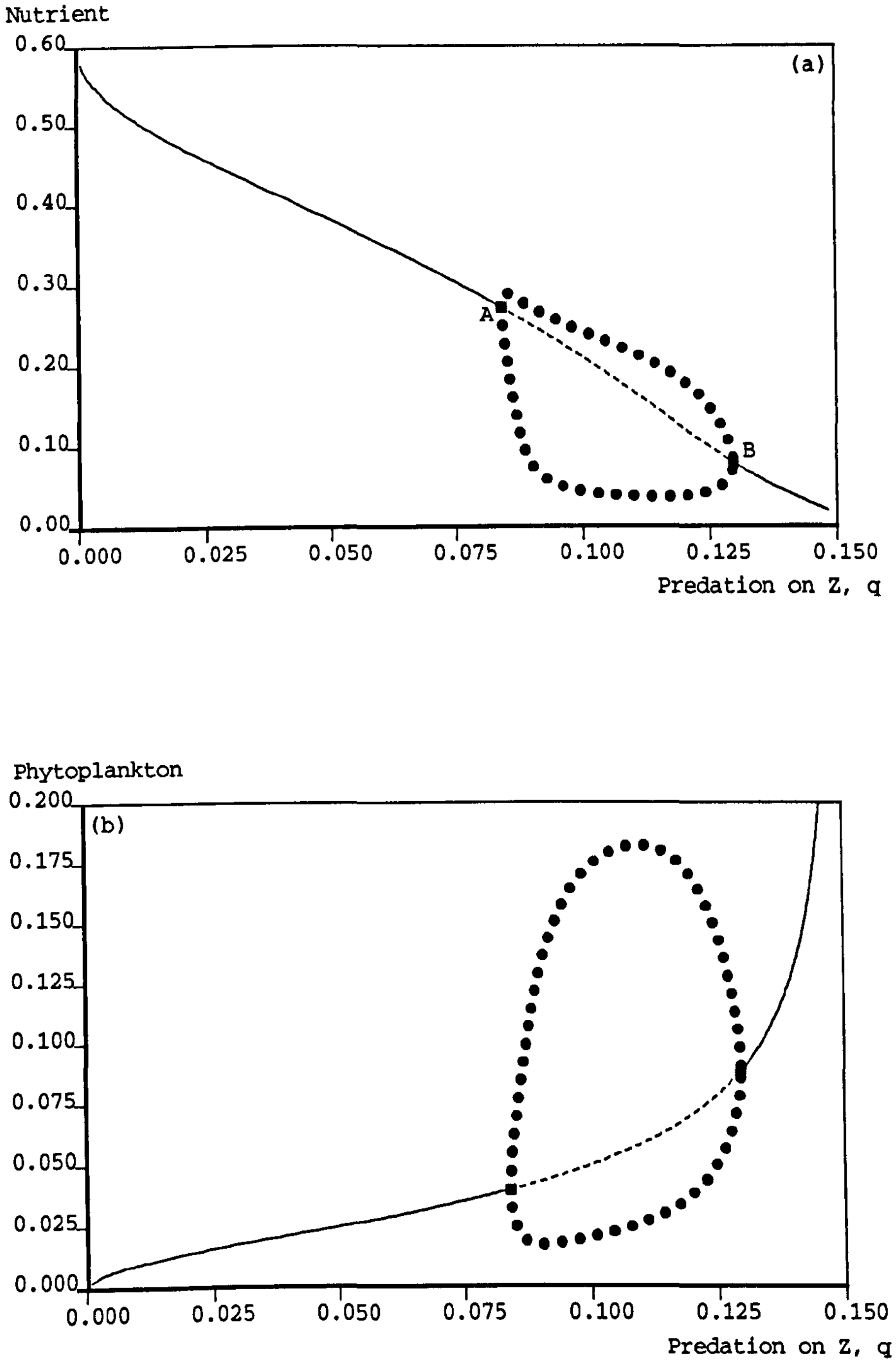

Figure 4.6: Variations in the steady-state values of (a) nutrient, (b) phytoplankton and (c) zooplankton as q, the higher predation on the zooplankton, is changed. A solid line is a stable steady state, a dashed line is an unstable steady state, a solid square is a Hopf bifurcation and solid circles indicate the maximum and minimum values of the stable limit cycles. The Hopf bifurcations are labelled A and B.

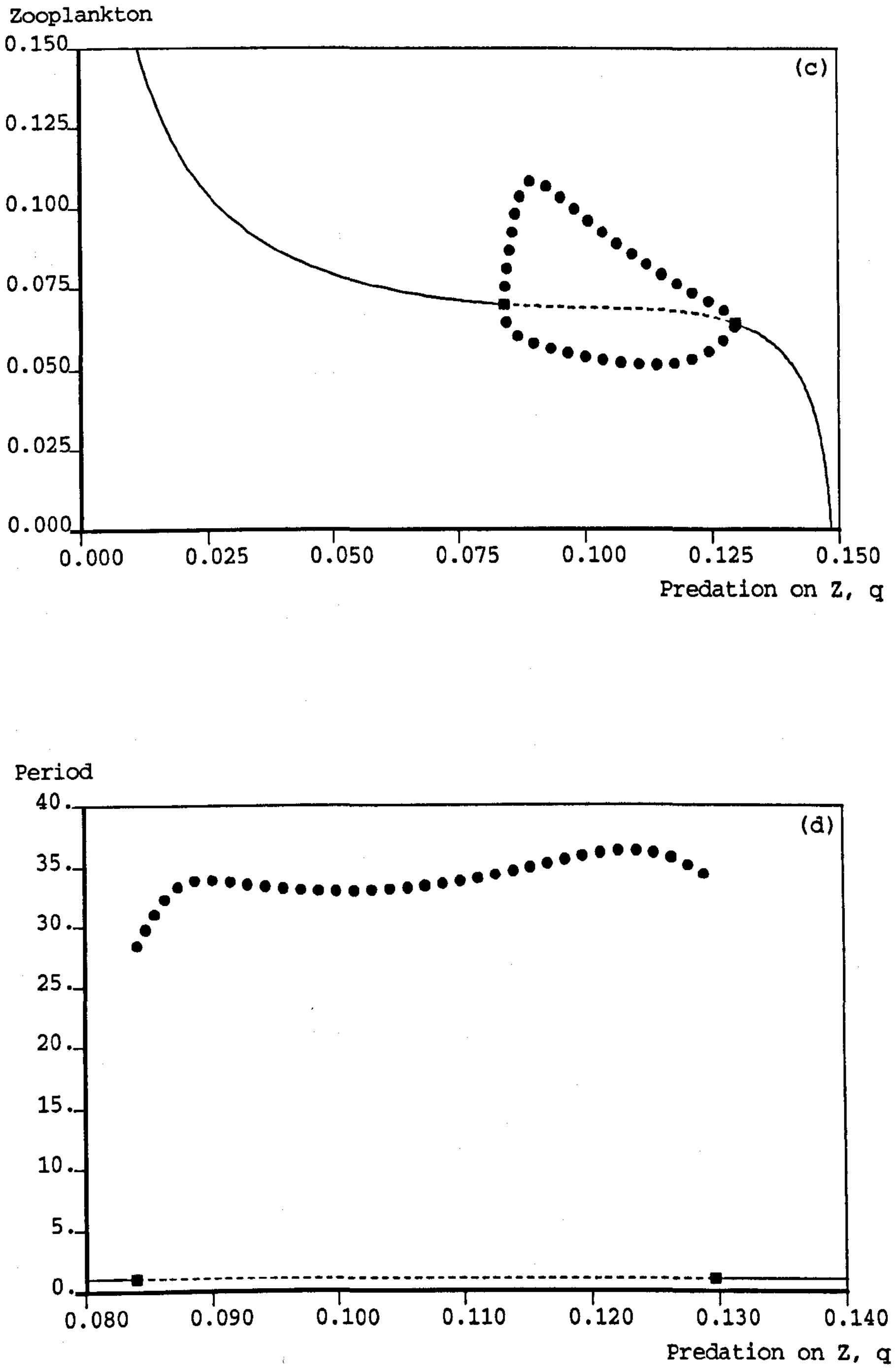

(c) The zooplankton bifurcation diagram. (d) The period of the limit cycles (solid circles) remains virtually constant throughout the region of oscillatory behaviour; the corresponding stability of the steady state is indicated by the horizontal line.

oscillations occur across a wider range of q than the corresponding relative range of d. The amplitudes of the cycles are greater for the linear case than the quadratic case, with all three variables reaching higher maximum and lower minimum values than for the linear case (note the increased scale of Figure 4.6(b), where P goes up to 0.2 to show the full amplitude of the cycles; the other scales remain the same as for the quadratic case). The amplitude of fluctuations in Z for the quadratic case were relatively small, but for the linear case they are much more pronounced. Apart from at high q values, the Z^* steady-state pictures for the two cases are similar. Since the default value and range of q are taken such that $qZ \simeq dZ^2$, this similarity may not seem too surprising, but on the other hand there is a qualitative difference in the way in which Z^* is calculated from the equations, and so such similarity between the linear and quadratic cases may be slightly unexpected.

The period of the oscillations, Figure 4.6(d), shows slightly more variance than for the quadratic case, but again remains close to 35 days. The sensitivity of the period to each of the parameters shall be shown by period-contour diagrams in Section 4.8.

4.6 Two-parameter bifurcation behaviour

In Figure 4.7 we show how the location of the two Hopf bifurcations changes as each of the parameters is independently varied. The axes have the same scales as in Figure 3.4 for the quadratic case, whereby the nature of (N^*, P^*, Z^*), as demonstrated in Figure 4.6, is represented as a horizontal line at the default value of each parameter, a solid line indicates that the steady state is stable, and a dashed line that it is unstable. The non-horizontal lines show the locations of the Hopf bifurcations, with solid lines indicating supercritical Hopf bifurcations, and dashed lines indicating subcritical. Unlike the quadratic case, there are no fold bifurcations of the steady state, a fact which was proved in the analysis of Section 4.3.

In the analysis we have shown that, unlike in the quadratic case, $(N_1{}^*, P_1{}^*, 0)$ can become stable; a transcritical bifurcation transfers stability from (N^*, P^*, Z^*) to $(N_1{}^*, P_1{}^*, 0)$ as (N^*, P^*, Z^*) leaves the positive octant, as illustrated in Figure 4.3.

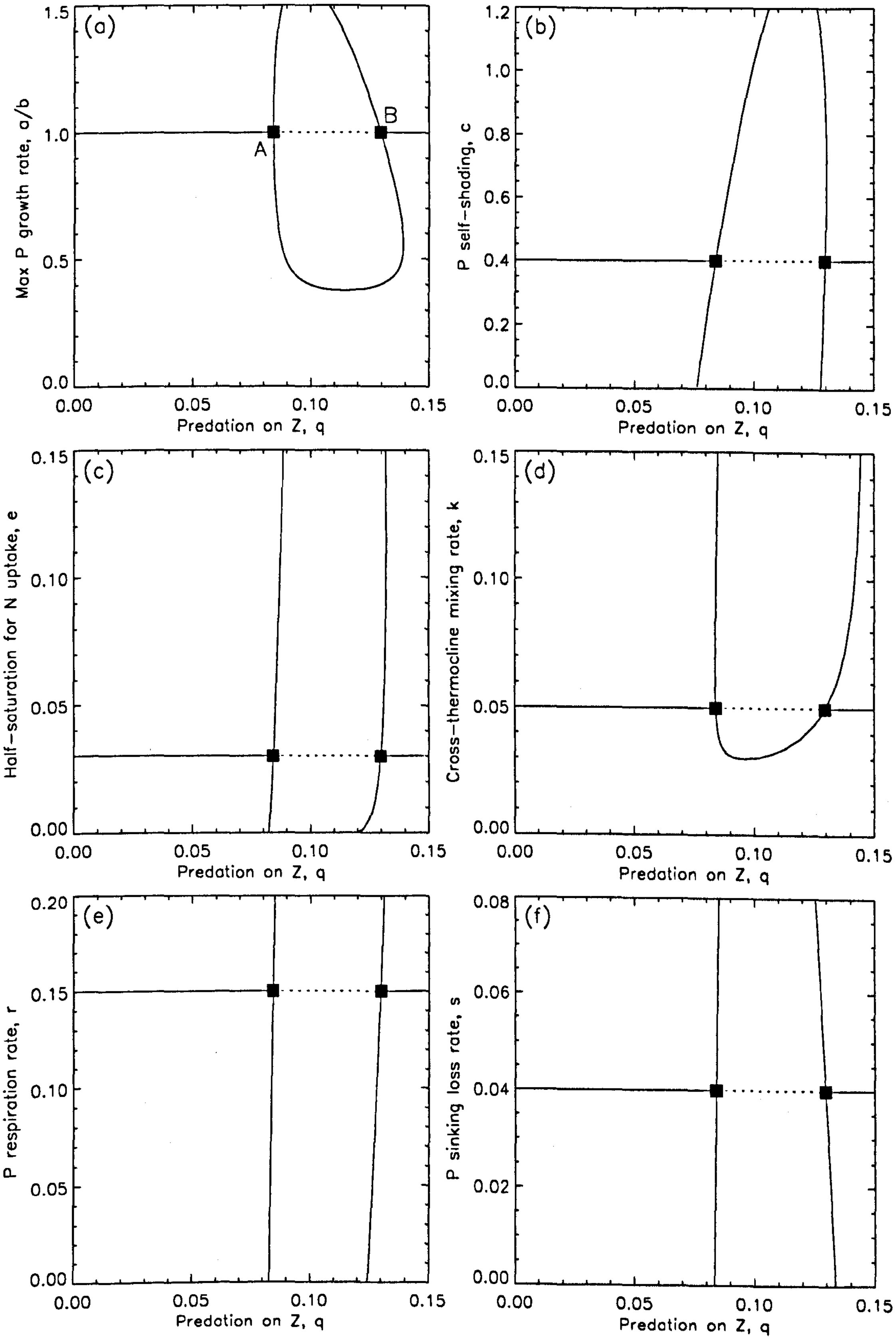

Figure 4.7: Two-parameter bifurcation diagrams showing how the positions of the Hopf bifurcations in Figure 4.6 change as each other parameter, together with q, is independently varied from its default value. The steady-state stabilities from Figure 4.6 are shown as a horizontal line at each default parameter value. Hopf A and (ctd.)

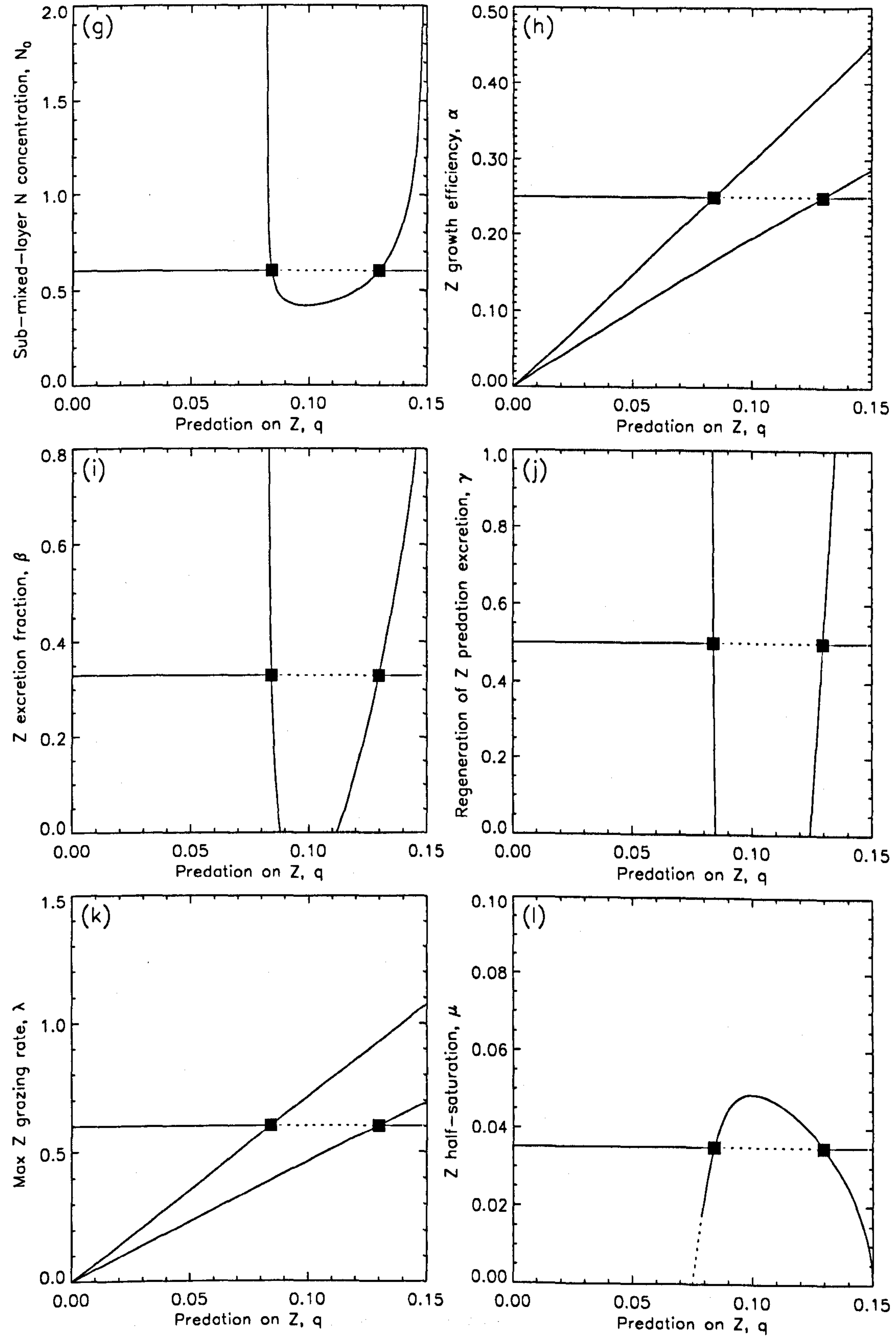

Hopf B are indicated in (a). Non-horizontal solid curves starting from the original Hopf bifurcations (the squares) indicate supercritical Hopf bifurcations, and non-horizontal curves of short dashes show where Hopf bifurcations are subcritical. No fold bifurcations of the steady state occur.

This transcritical bifurcation occurs when Ω reaches zero, and in the locality of the bifurcation we have shown that (N^*, P^*, Z^*) is stable for $\Omega > 0$, and $({N_1}^*, {P_1}^*, 0)$ is stable for $\Omega < 0$. Figure 4.6(c) indicates that $\Omega = 0$ when $q = 0.148$ (and all other parameters are set to their default values), and $({N_1}^*, {P_1}^*, 0)$ is stable for $q > 0.148$. Thus in the two-parameter diagrams it will not be the case, as it was for the quadratic model, that (N^*, P^*, Z^*) is the only steady state that can be stable across the realistic parameter ranges. The transcritical bifurcation at $q = 0.148$ will vary in location as other parameters are varied; such variation depends on how significant each of the parameters is in the definition of Ω. We will show how the transcritical bifurcation varies in Figure 4.8, but for clarity and ease of comparison with Figure 3.4 we do not show it in Figure 4.7. The horizontal line in each diagram of Figure 4.7, representing the stability of (N^*, P^*, Z^*) at the default parameter values, terminates at $q = 0.148$, although this can only be clearly seen in Figure 4.7(i) for β, due to the location of tick marks on the right-hand axis in the other diagrams.

In the analysis we have shown that when at least two of b, c and μ are set to their default values, which is always true in the two-parameter diagrams of Figure 4.7, then, if $q < \alpha\lambda/2$ (inequality (4.32)), (N^*, P^*, Z^*) is stable. The default values of α and λ give $\alpha\lambda/2 = 0.075$, and so in all except the α and λ diagrams of Figure 4.7, we know that (N^*, P^*, Z^*) will not undergo a Hopf bifurcation in the region $q < 0.075$, which is the left half of each picture. For the α and λ diagrams we know this to be true for the region $q < \alpha\lambda/2$, which shall be indicated in Figure 4.8.

We now compare the linear and quadratic two-parameter diagrams, firstly looking at the whole picture, and secondly comparing the individual diagrams for each parameter in turn.

The most striking difference between Figure 4.7, for the linear case, and Figure 3.4, for the quadratic case, is that the steady steady state is unstable, and hence oscillations occur, across a larger range of parameters for the linear case. Oscillations occur across the full ranges of six of the parameters, namely c, e, r, s, β and γ, in the linear case, but this occurred for only r, s and γ in the quadratic case. In the linear case, a Hopf bifurcation becomes subcritical only when μ is varied, Figure 4.7(l), and the Hopf bifurcations remain supercritical as each other parameter is varied, whereas subcritical Hopf bifurcations were common in the quadratic case, occurring for six of the parameters. This, together with the absence of fold bifurcations of steady states, makes the linear diagrams appear altogether simpler than the quadratic diagrams. However, expecting this to imply that the limit-cycle behaviour will be simpler turns out to be foolhardy, as will be demonstrated by the contours of constant period to be discussed in Section 4.8.

The Hopf curves are, on the whole, fairly 'vertical', and so the Hopf bifurcations will, when they occur, tend to be at the same values of q as for the default values, i.e. at the values of $q = 0.084$ and $q = 0.130$ shown in Figure 4.6. There do exist broad similarities between the linear and quadratic diagrams, in that the linear diagrams can, in some sense, be seen to be stretched versions of the quadratic ones. The absence of fold bifurcations in the linear case means that the Hopf bifurcation curves cannot cross over each other, since there are never co-existing steady states in the strictly positive octant. We now compare and discuss the diagrams for each parameter in turn.

Figure 4.6(a) shows that oscillatory behaviour occurs for a larger range of a/b values than in Figure 3.5(a) for the quadratic case. In a topological sense both pictures are the same, with the Hopf bifurcations remaining supercritical, and the curves of the bifurcations forming a closed loop, although part of the loop is outside of the plotted range in each case.

Figure 4.6(b) shows that the oscillations persist across the full range of c, unlike the quadratic case where the Hopf bifurcations came together at $c = 0.68$, above which (N^*, P^*, Z^*) was stable.

As e varies, Figure 4.7(c) shows that the q values of the Hopf bifurcations remain fairly constant, with the curves of bifurcations practically vertical. For the quadratic case, however, as e increases the Hopf bifurcations occur at higher values of predation on zooplankton, d, since the Hopf curves move to the right, out of the plotted range of d.

For k, Figure 4.7(d) is much simpler than the corresponding figure for the quadratic case, due to the absence of the fold bifurcations of the steady state. This absence prevents the Hopf curves from crossing over, since co-existing steady states cannot occur. The Hopf bifurcations remain supercritical, and oscillations occur for all except low k values.

Figures 4.7(e), (f) and (j), the respective diagrams for r, s and γ, show the Hopf bifurcations to be very insensitive to the values of each of these parameters. This is similar to the quadratic situation, although for the linear case the Hopf curves are almost vertical, and so the q values of the Hopf bifurcations are virtually independent of r, s and γ. We note that γ multiplies the qZ or dZ^2 functions, the only terms to differ between the linear and quadratic cases, but that the γ bifurcation diagrams are practically identical.

Similarly to the k situation, Figure 4.7(g) for N_0 shows a much simpler picture than in the quadratic case, due to the absence of the fold bifurcations. The consequent homoclinicity and detailed bifurcation structure shown in Figure 3.8 will thus not occur. This is because there can be no Bogdanov-Takens bifurcation, as there are no fold bifurcations of steady states. The Bogdanov-Takens bifurcation is where a curve of homoclinic orbits originates, and so the absence of such a bifurcation precludes homoclinic orbits from arising in this way.

The α and λ pictures, Figures 4.7(h) and (k), are similar, as for the quadratic case, and show a larger region of oscillations than in the quadratic case. The Hopf bifurcations persist across the full range of β, Figure 4.7(i), whereas for the quadratic case the picture was similar to the k and N_0 pictures.

The μ picture, Figure 4.7(l), differs from the quadratic case in that the oscillations persist as μ decreases, but is similar in that an increase causes the Hopf bifurcations to combine and disappear. The quadratic picture looks as though it may be qualitatively the same as the linear picture, and just be shifted along, but in actual fact, for the quadratic case fold bifurcations of the steady state occur at d values above the range shown; two curves of fold bifurcations exist with a minimum d value of 2.29 (with $\mu = 0.0219$), where they terminate at a cusp point. The Hopf bifurcations then cross over at a slightly higher d value, giving a rotated version of the quadratic N_0 picture,

Figure 3.4(g), although neither Hopf curve terminates at a Bogdanov-Takens point on a fold curve, as discussed for N_0 in Section 3.8. One Hopf curve passes through $\mu = 0$, whilst the other asymptotes to $\mu = 0$ as d gets large. For the linear case, the asymptotic behaviour does not occur. As mentioned previously, μ is the only parameter for which a Hopf bifurcation becomes subcritical in the linear case.

In Figure 4.8 we indicate where (N^*, P^*, Z^*) and $({N_1}^*, {P_1}^*, 0)$ exchange stability at the transcritical bifurcation. The location of the transcritical bifurcation in parameter space is defined by $\Omega = 0$, which is shown as a curve of long dashes in each diagram.

A second transcritical bifurcation occurs at $\Phi = 0$, where $({N_1}^*, {P_1}^*, 0)$ exchanges stability with $(N_0, 0, 0)$; in the locality of the bifurcation we have shown that $(N_0, 0, 0)$ is stable for $\Phi < 0$, and $({N_1}^*, {P_1}^*, 0)$ is stable for $\Phi > 0$. As mentioned in Chapter 3, $\Phi > 0$ when all of the parameters are set to their default values, and Φ remains positive as any one of the parameters in its definition is varied within its realistic range given in Table 2.1. For a/b and N_0, the solutions to $\Phi = 0$ (with all other parameters set to their default values) are $a/b = 0.25$ and $N_0 = 0.0095$, which lie within the ranges plotted in the two-parameter diagrams (but are below the realistic ranges given in Table 2.1). So, for completeness, we plot the horizontal lines corresponding to $\Phi = 0$, shown as a line of long and short dashes, for the a/b and N_0 diagrams, Figures 4.8(a) and (g), although the N_0 line is barely noticeable as it is as such a low value. For the other parameters in the definition of Φ, namely e, r, s and k, the lines $\Phi = 0$ occur at much higher values than the realistic ranges (the solutions to $\Phi = 0$ are $e = 1.9, r = 0.86$ (as illustrated in Figure 4.3), $s = 0.75$ and $k = 0.76$). For the quadratic case, $({N_1}^*, {P_1}^*, 0)$ can never be stable, and (N^*, P^*, Z^*) loses stability to $({N_1}^*, {P_1}^*, 0)$ at a three-way transcritical bifurcation at $\Phi = 0$, and since $\Phi = 0$ always occurs outside of the realistic ranges of the two-parameter diagrams, we did not indicate it.

Inequality (4.32) of Section 4.3.2 gives a sufficient condition for (N^*, P^*, Z^*) to be stable, namely that (N^*, P^*, Z^*) is stable if $q < \alpha\lambda/2$. When α and λ are fixed at their default values, we have $\alpha\lambda/2 = 0.075$. Thus, in all of the diagrams of Figure 4.8, except for (h) and (k) for α and λ, we know that (N^*, P^*, Z^*) is stable for $q < 0.075$.

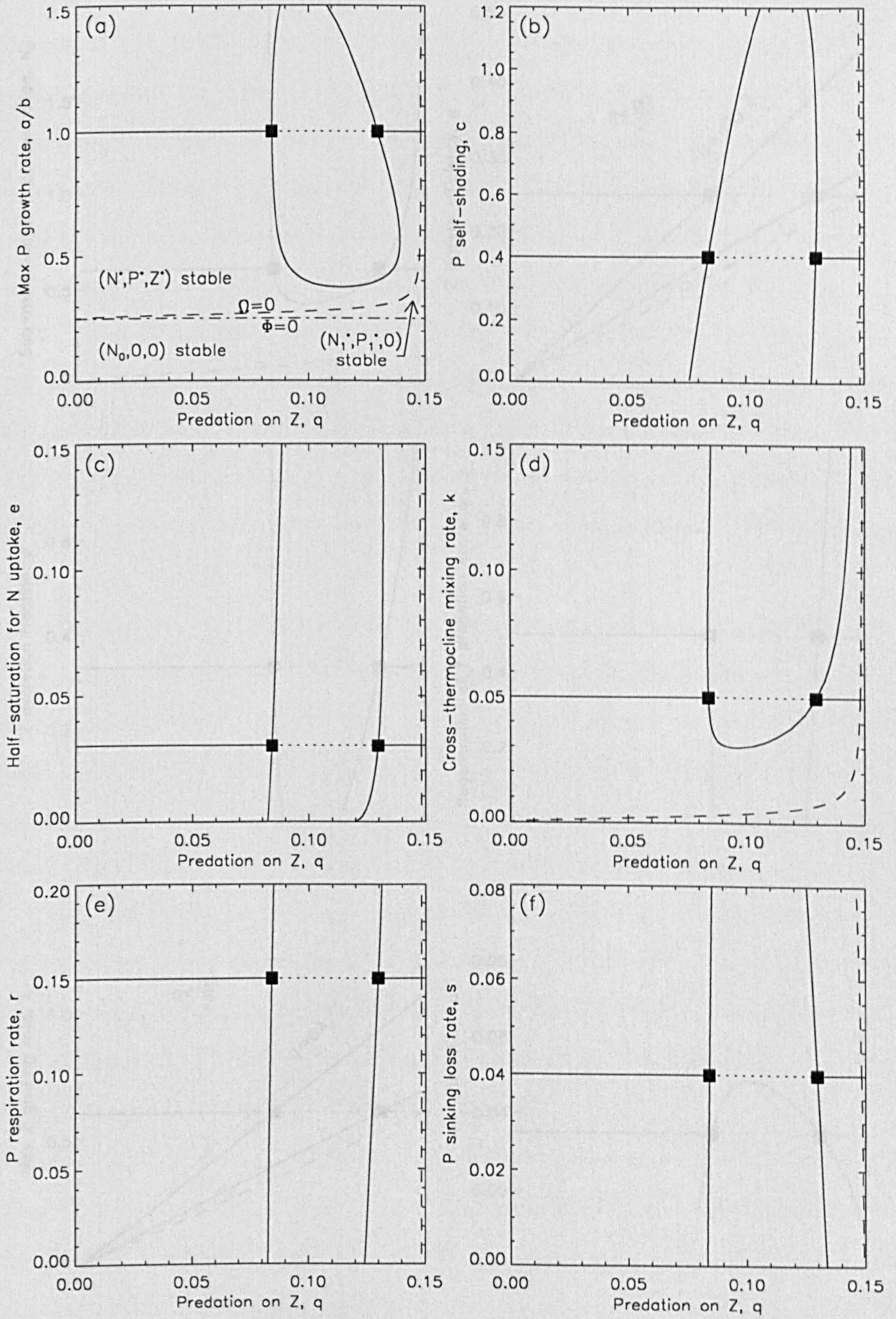

Figure 4.8: The curve $\Omega = 0$, on which the transcritical bifurcation of (N^*, P^*, Z^*) and $({N_1}^*, {P_1}^*, 0)$ occurs, is plotted as a curve of long dashes onto the bifurcation diagrams from Figure 4.7. To the right of $\Omega = 0$, (N^*, P^*, Z^*) has $Z^* < 0$, and $({N_1}^*, {P_1}^*, 0)$ is stable. (ctd.)

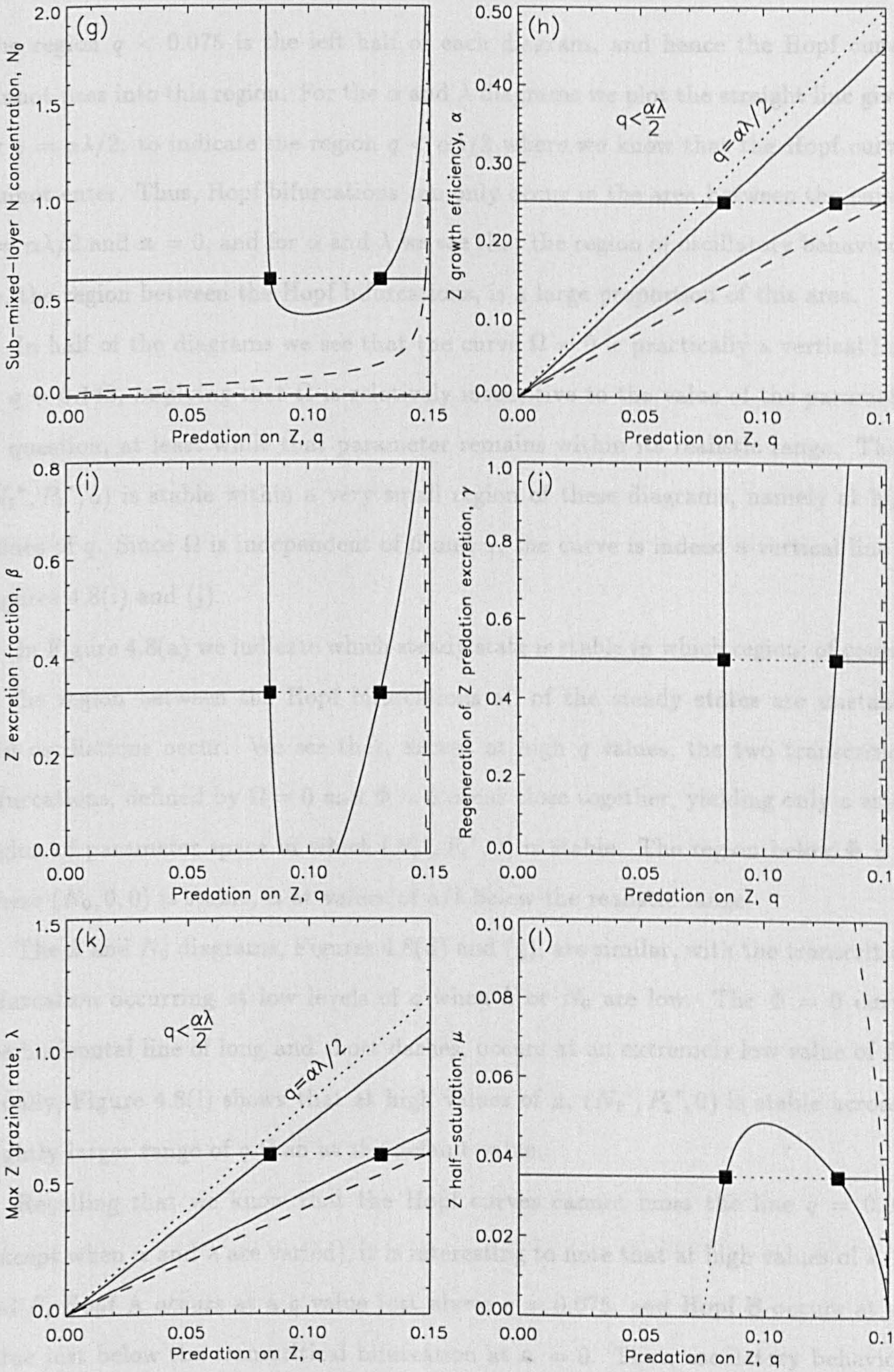

For a/b and N_0, (a) and (g), $\Phi = 0$ is shown as a horizontal line of long and short dashes; this line is the location of the transcritical bifurcation between $(N_1{}^*, P_1{}^*, 0)$ and $(N_0, 0, 0)$. On (h) and (k) we also show the line $q = \alpha\lambda/2$, to the left of which (N^*, P^*, Z^*) must be stable.

The region $q < 0.075$ is the left half of each diagram, and hence the Hopf curves cannot pass into this region. For the α and λ diagrams we plot the straight line given by $q = \alpha\lambda/2$, to indicate the region $q < \alpha\lambda/2$ where we know that the Hopf curves cannot enter. Thus, Hopf bifurcations can only occur in the area between the curves $q = \alpha\lambda/2$ and $\Lambda = 0$, and for α and λ we see that the region of oscillatory behaviour, i.e. the region between the Hopf bifurcations, is a large proportion of this area.

In half of the diagrams we see that the curve $\Omega = 0$ is practically a vertical line, at $q = 0.148$, implying that Ω is relatively insensitive to the value of the parameter in question, at least while that parameter remains within its realistic range. Thus, $(N_1^*, P_1^*, 0)$ is stable within a very small region of these diagrams, namely at high values of q. Since Ω is independent of β and γ, the curve is indeed a vertical line in Figures 4.8(i) and (j).

In Figure 4.8(a) we indicate which steady state is stable in which region; of course, in the region between the Hopf bifurcations all of the steady states are unstable, and oscillations occur. We see that, except at high q values, the two transcritical bifurcations, defined by $\Omega = 0$ and $\Phi = 0$ occur close together, yielding only a small region of parameter space in which $(N_1^*, P_1^*, 0)$ is stable. The region below $\Phi = 0$, where $(N_0, 0, 0)$ is stable, is at values of a/b below the realistic range.

The k and N_0 diagrams, Figures 4.8(d) and (g), are similar, with the transcritical bifurcation occurring at low levels of q when k or N_0 are low. The $\Phi = 0$ curve, the horizontal line of long and short dashes, occurs at an extremely low value of N_0. Finally, Figure 4.8(l) shows that at high values of μ, $(N_1^*, P_1^*, 0)$ is stable across a slightly larger range of q than at the default value.

Recalling that we know that the Hopf curves cannot cross the line $q = 0.075$ (except when α and λ are varied), it is interesting to note that at high values of k, N_0 and β, Hopf A occurs at a q value just above $q = 0.075$, and Hopf B occurs at a q value just below the transcritical bifurcation at $\Lambda = 0$. Thus, oscillatory behaviour occurs across practically the largest permissible range of q, since we know that the Hopf bifurcations must occur above $q = 0.075$ and below $\Lambda = 0$. This is also true at low values of μ.

For regions in which $q < \alpha\lambda$ does not hold (inequality (4.20)), (N^*, P^*, Z^*) does not exist since a solution P^* is undefined. In the analysis we showed that, when we start from (N^*, P^*, Z^*) with $Z^* > 0$, and vary parameters, we must reach the transcritical bifurcation at $\Omega = 0$ before we reach $q = \alpha\lambda$. For the α and λ diagrams, the straight line $q = \alpha\lambda$ (which is not shown) lies very close, and just to the right of, the $\Omega = 0$ curve. For the other diagrams, $q = \alpha\lambda$ is the vertical line $q = 0.15$.

4.7 Bifurcation behaviour at different levels of N_0

For the quadratic case we showed, in Figures 3.6(a)-(g), how the one-parameter bifurcation diagram of N against zooplankton predation rate, d, changes as N_0 is set to progressively higher values. The values of N_0 shown were 0.75, 1.0, 1.1, 1.25, 1.35, 1.5 and 2.0, since the bifurcation diagrams are qualitatively different at each of these values (except for 1.35 and 1.5). For the linear case, we know, from Figure 4.7(g), that both Hopf bifurcations persist and remain supercritical as N_0 is increased up to 2.0, and so no Bautin bifurcations occur whereby a Hopf bifurcation becomes subcritical (as illustrated in Figure 3.8 for the quadratic case). This means that, locally at least, the branch of limit cycles emanating from each Hopf bifurcation is stable. The absence of coexisting positive steady states suggests that we will not find the homoclinic behaviour seen in the quadratic case, and with no fold bifurcations occurring there can be no Bogdanov-Takens bifurcation providing a source for homoclinic orbits. Thus, we might expect that, at increasing values of N_0, the bifurcation picture remains qualitatively the same as that for $N_0 = 0.6$.

For $N_0 = 0.75$, we find that a simple continuous branch of stable limit cycles connects the two Hopf bifurcations. Since this behaviour is the same as that for the default value of $N_0 = 0.6$, i.e. the bifurcation diagram is qualitatively the same as 4.6(a), we do not show it here.

However, for $N_0 = 1.0$, the behaviour does change, as shown in Figure 4.9(a). We see that the branch of stable limit cycles becomes unstable at the point labelled PD1, and then restabilises at PD2. These points are period-doubling bifurcations, a

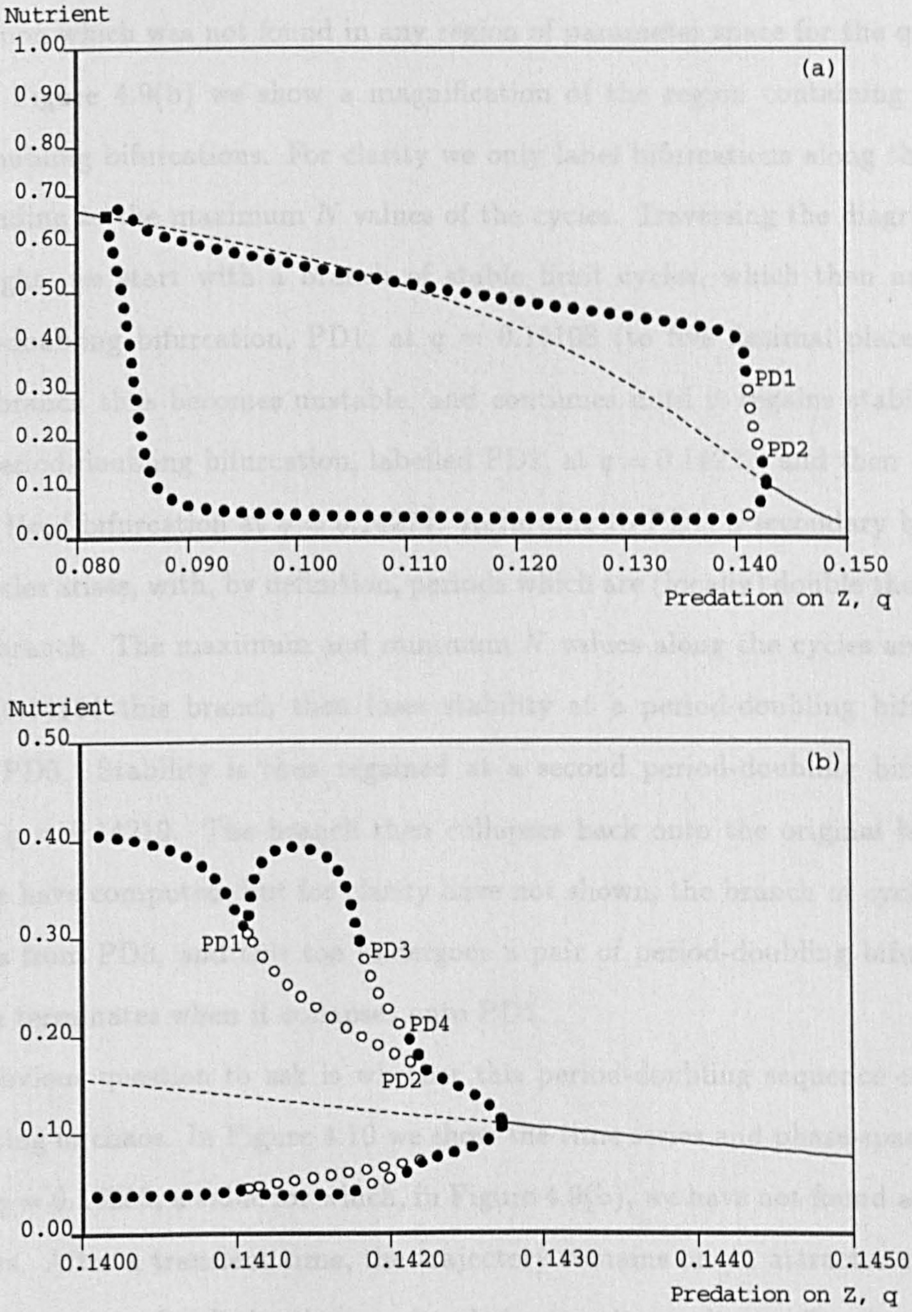

Figure 4.9: (a) At $N_0 = 1.0$ the stable limit cycle branch loses stability at two period-doubling bifurcations, labelled PD1 and PD2; such bifurcations are not present in Figure 4.6(a) for $N_0 = 0.6$, and were not found at all for the quadratic mortality model. (b) A magnification of the region containing the period-doubling bifurcations. The period-doubled branch of limit cycles arising from PD1 is shown. This branch loses and then regains stability at period-doubling bifurcations PD3 and PD4, and then collapses onto the original branch at PD2. The branch which then arises from PD3 is not shown, but also undergoes period-doubling bifurcations.

phenomenon which was not found in any region of parameter space for the quadratic case. In Figure 4.9(b) we show a magnification of the region containing the two period-doubling bifurcations. For clarity we only label bifurcations along the circles corresponding to the maximum N values of the cycles. Traversing the diagram from left to right, we start with a branch of stable limit cycles, which then undergoes a period-doubling bifurcation, PD1, at $q = 0.14108$ (to five decimal places). The original branch thus becomes unstable, and continues until it regains stability at a second period-doubling bifurcation, labelled PD2, at $q = 0.14222$, and then collapses onto the Hopf bifurcation at $q = 0.14274$. Returning to PD1, a secondary branch of stable cycles arises, with, by definition, periods which are (locally) double those of the original branch. The maximum and minimum N values along the cycles are shown. At $q = 0.14184$ this branch then loses stability at a period-doubling bifurcation, labelled PD3. Stability is then regained at a second period-doubling bifurcation, PD4, at $q = 0.14210$. The branch then collapses back onto the original branch at PD2. We have computed, but for clarity have not shown, the branch of cycles which emanates from PD3, and this too undergoes a pair of period-doubling bifurcations, and then terminates when it collapses onto PD4.

An obvious question to ask is whether this period-doubling sequence continues, culminating in chaos. In Figure 4.10 we show the time series and phase-space trajectory for $q = 0.14200$, a value for which, in Figure 4.9(b), we have not found any stable attractors. After a transient time, the trajectory remains on an attractor which appears to be chaotic; for clarity the transient behaviour is not shown. For the quadratic model, recall that no chaotic orbits were found in any region of parameter space.

The period-doubling bifurcations persist as N_0 is increased further, and the bifurcational behaviour is similar at $N_0 =1.1$, 1.25, 1.35, 1.5 and 2.0, which were the values shown for the quadratic case. To verify this we show only the diagram for $N_0 = 2.0$, in Figure 4.11.

The stable limit cycle branch is unstable between period-doubling bifurcations at $q = 0.14824$ and $q = 0.14834$, and so the region of instability is much smaller than that for $N_0 = 1.0$. Nevertheless, by computing trajectories at intermediate values

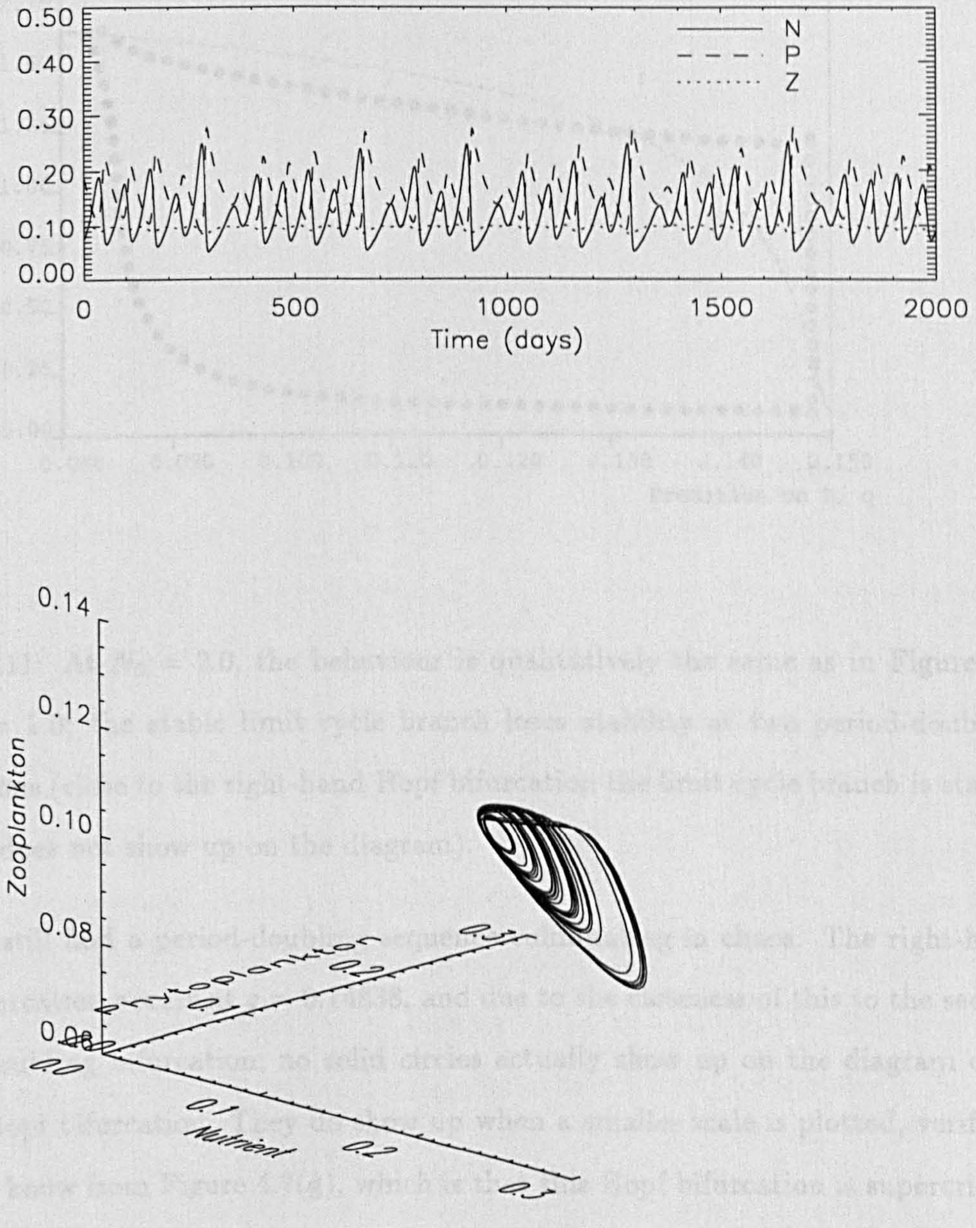

Figure 4.10: The time series and phase-space trajectory for $N_0 = 1.0$ and $q = 0.14200$. The transient behaviour is not shown, and the trajectory is attracted onto an attractor which appears to be chaotic. No chaotic behaviour was found at all in the quadratic model.

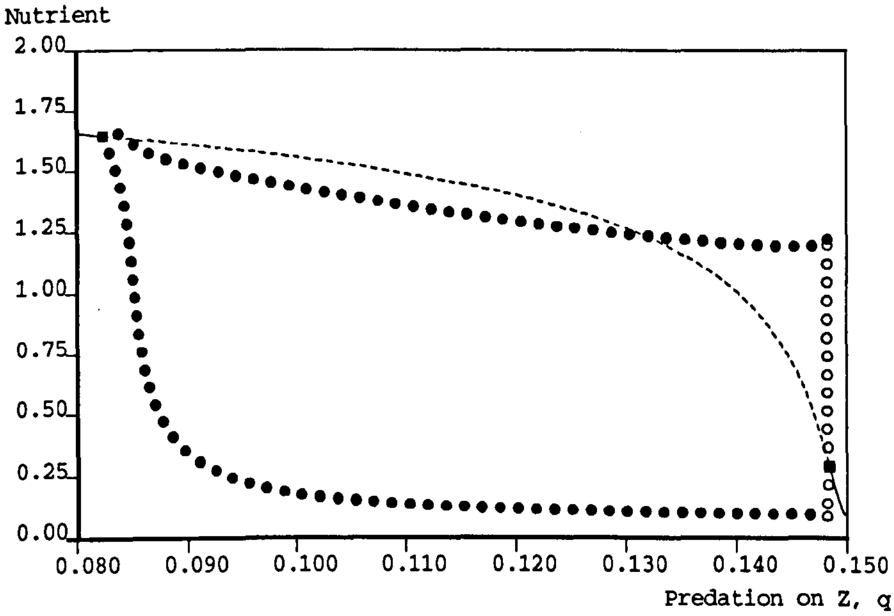

Figure 4.11: At $N_0 = 2.0$, the behaviour is qualitatively the same as in Figure 4.9 for $N_0 = 1.0$; the stable limit cycle branch loses stability at two period-doubling bifurcations (close to the right-hand Hopf bifurcation the limit cycle branch is stable, but this does not show up on the diagram).

of q, we still find a period-doubling sequence culminating in chaos. The right-hand Hopf bifurcation occurs at $q = 0.14838$, and due to the closeness of this to the second period-doubling bifurcation, no solid circles actually show up on the diagram close to this Hopf bifurcation. They do show up when a smaller scale is plotted, verifying what we know from Figure 4.7(g), which is that this Hopf bifurcation is supercritical and so the branch of limit cycles which emanates from it is stable. Continuation of the branch in the narrow region where cycles are unstable becomes unreliable, due to differences in the value of q as small as 10^{-7} showing qualitative changes in behaviour, which we have discovered by computing trajectories.

4.8 Dependence of the period of oscillations on the parameter values

In Figure 4.12 we plot contours of constant period, within the regions of oscillatory behaviour shown in Figure 4.7. The contours are computed using the same technique as that described for the quadratic case, and the range of q shown is 0.075-0.15, which is from the default value to the maximum value, as plotted for the quadratic case.

As a contour is traced out, if a period-doubling bifurcation is reached (i.e. a Floquet multiplier leaves the unit circle through -1), then we continue computation of the contour, but do not plot it when the cycles in question are unstable (i.e. whilst the Floquet multiplier remains outside of the unit circle). In most cases we find that the cycles then restabilise at a second period-doubling bifurcation (i.e. the Floquet multiplier re-enters the unit circle through -1, as occurs at PD2 in Figure 4.9(b)), and the remainder of the contour corresponds to stable cycles, and is thus plotted. We find that period-doubling bifurcations only occur for k, N_0, β and μ, Figures 4.12(d), (g), (i) and (l) respectively. So in these diagrams we see small regions of gaps in some of the contours, the edges of these regions indicating the locations of the period-doubling bifurcations. These occur at high q values in each picture, and are most clearly seen in Figure 4.12(i) for β. In all diagrams, we plot contours at increments of five days, up to and including the 100-day contour (where applicable), and then show the 125, 150 and 175 contours, except for Figure 4.12(a) for a/b where we show the 105, 110, 115 and 120 contours.

Comparing each corresponding diagram in Figures 3.7 and 4.12 for the quadratic and linear models, we find that, for each parameter, the general tendency of an increase in that parameter to either increase or decrease the period, is the same for the two models. For example, Figure 3.7(e) and Figure 4.12(e) show that an increase in r will increase the period of the oscillations in both of the models.

In Figure 4.12(a) we see that at low values of a/b the period can reach as high as 120 days, much higher than the maximum of 45 days reached for a/b in the quadratic case. Such high periods for the quadratic case only occurred within the presence

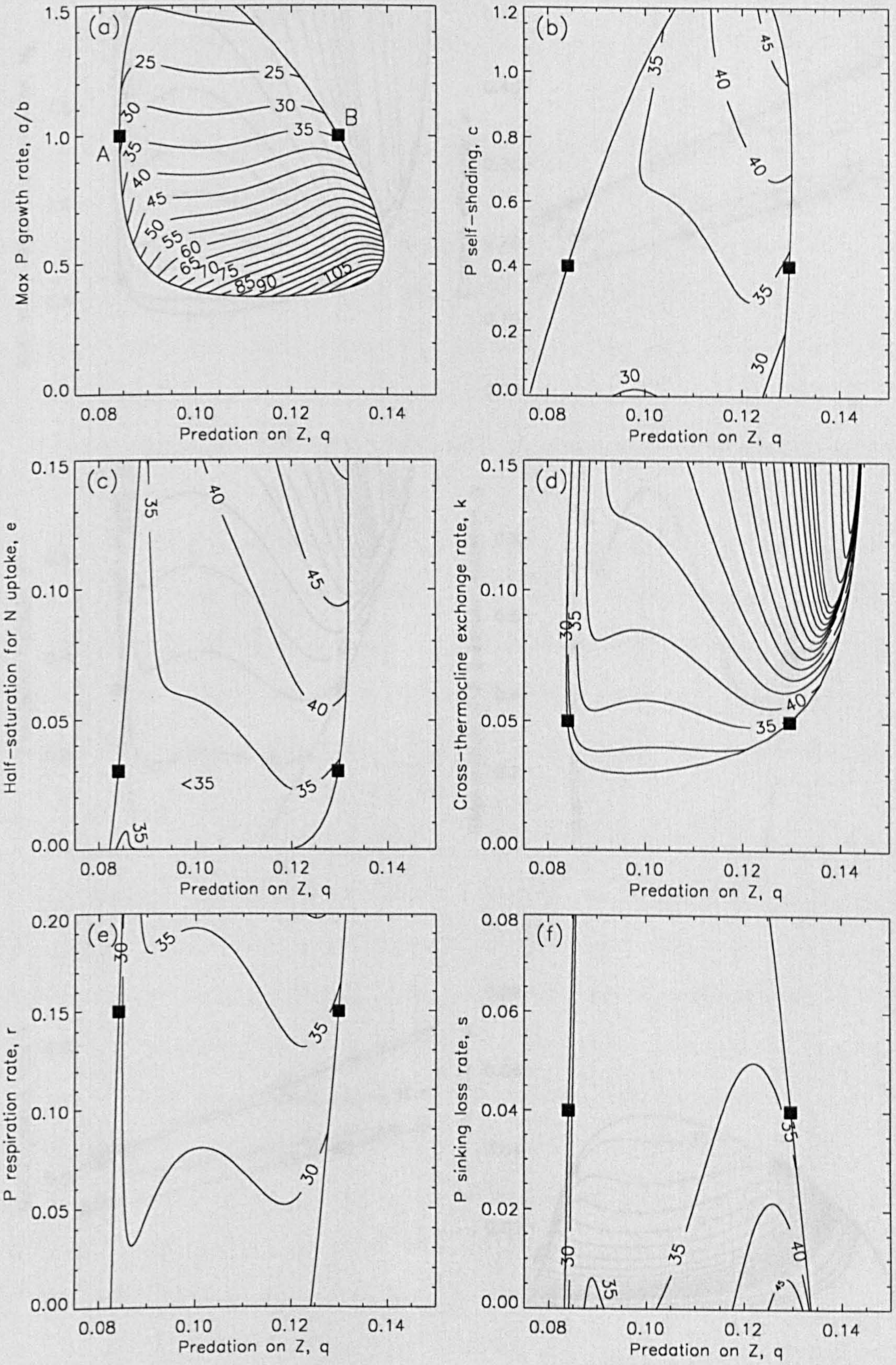

Figure 4.12: Within the regions of oscillations given by Figure 4.7, the variations in period of stable limit cycles are indicated by contours of constant period. The numbers indicate the period, in days, along contours, which are plotted at increments of five days up to 100 days, and then the 125, 150 and 175 contours are (ctd.)

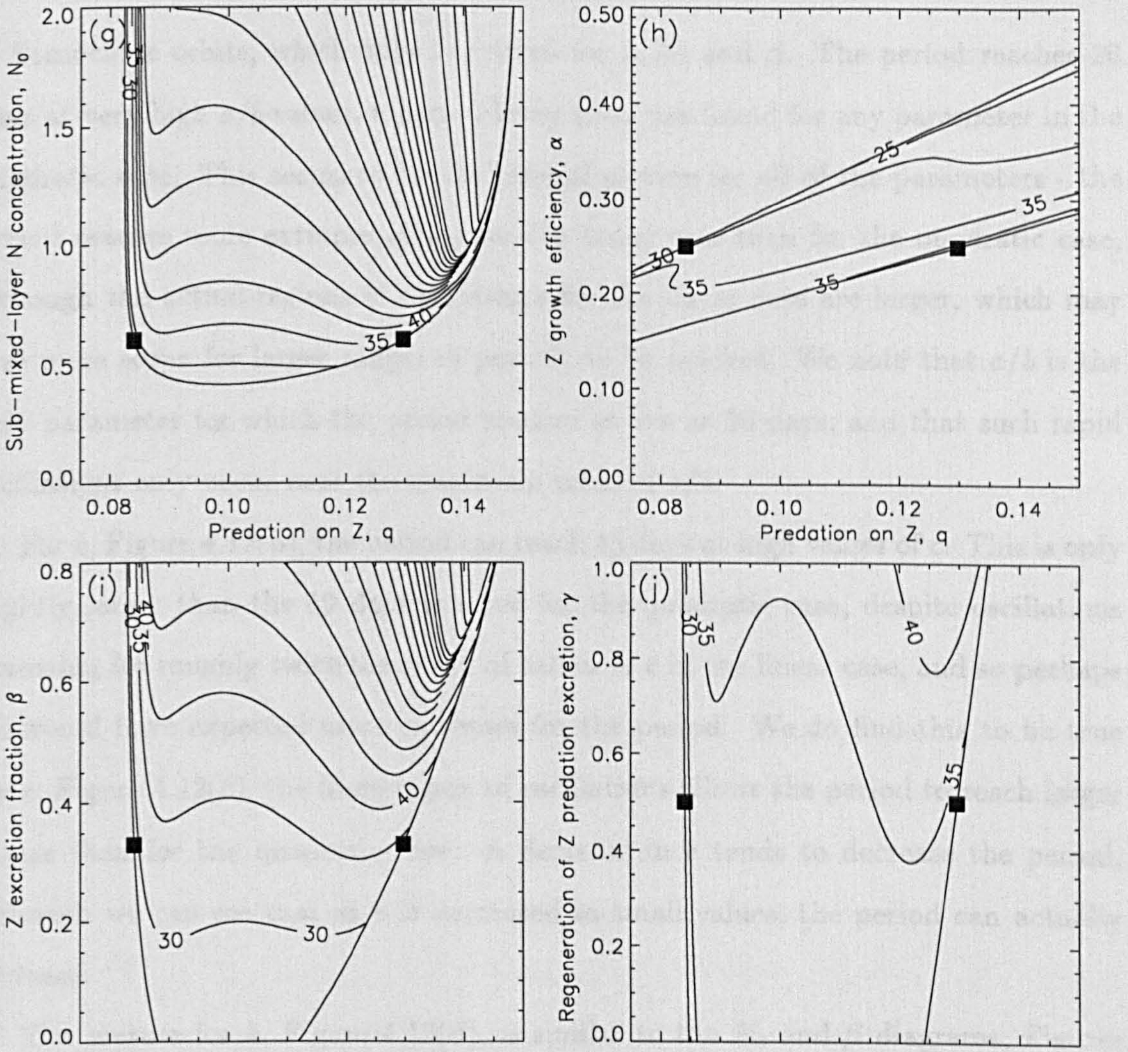

shown (except for a/b where we continue at five-day intervals). For k, N_0, β and μ, diagrams (d), (g), (i) and (l) respectively, period-doubling bifurcations occur; these are indicated by gaps in the contours (see text). Overall we find more variation in the period than occurred for the quadratic case.

of homoclinic orbits, which only happened for k, N_0 and β. The period reaches 20 days at very high a/b values, a period lower than was found for any parameter in the quadratic case. This seems to be the general picture for all of the parameters - the period reaches more extreme values for the linear case than for the quadratic case, although the actual regions of oscillations for the linear case are larger, which may give more scope for larger ranges of periods to be reached. We note that a/b is the only parameter for which the period reaches as low as 20 days, and that such rapid oscillations only occur near the maximum value of a/b.

For c, Figure 4.12(b), the period can reach 45 days at high values of c. This is only slightly larger than the 40 days reached for the quadratic case, despite oscillations occurring for roughly twice the range of values of c in the linear case, and so perhaps we would have expected more extremes for the period. We do find this to be true for e, Figure 4.12(c); the large region of oscillations allows the period to reach larger values than for the quadratic case. A decrease in e tends to decrease the period, although we can see that as e is decreased to small values, the period can actually increase.

The picture for k, Figure 4.12(d), is similar to the N_0 and β diagrams, Figures 4.12(g) and (i), with contours of 175 days reached (we do not compute any higher values), and period-doubling bifurcations occurring, as shown by the gaps in some of the contours. For the quadratic case, the diagrams for these parameters were also similar, all showing high periods, but this was due to homoclinicity, which does not occur in the linear case. So the tendency to produce long periods carries over from the quadratic case, despite the qualitative differences in bifurcational behaviour. The lowest contour for which a period-doubling bifurcation occurs for each of k, N_0 and β is the 55 contour. A period-doubled cycle resulting from such a bifurcation will then, by definition, have a period of 110 days, and will take the form of a double-loop, with each 'loop' having a period of roughly 55 days. In a similar way, it takes about 60 days to get round each 'loop' of the chaotic attractor shown in Figure 4.10, where a loop can be defined as, say, from one maximum value of N to the next. So the actual time between the local maxima of each variable for a period-doubled cycle, will be, at least close to a period-doubling bifurcation, similar to the period of the original un-doubled cycle, but there will be two local maxima.

For the N_0 diagram, we additionally find fold bifurcations of cycles, but only on the 150 and 175 contours. We now explain this, by tracing along the 150-day contour, the second-highest contour plotted, starting from the point at $q = 0.138$, $N_0 = 2.0$, and moving down the contour, decreasing N_0. We reach a minimum value of N_0, as for most of the other contours, and then N_0 increases as q increases. When we reach $N_0 = 1.311$ a fold bifurcation of cycles occurs (i.e. a Floquet multiplier leaves the unit circle through $+1$). As we continue (since the cycles are unstable they are not plotted in this intermediate region), the multiplier then re-enters the unit circle through $+1$ at $N_0 = 1.555$, and hence the cycles become stable again. We then plot this stable section of the contour, but the aforementioned multiplier carries on decreasing along the real axis, and shoots through -1; this is a period-doubling bifurcation, and occurs at $N_0 = 1.566$. Therefore the 150-day cycles have only become stable for the small interval $N_0 \in (1.555, 1.566)$, as shown by the very short line in Figure 4.12(g). The multiplier does then re-enter the unit circle through -1, but this occurs at a value of N_0 higher than the range plotted. Throughout these wild excursions of the Floquet multiplier, the second multiplier is quite content to remain very close to zero, apparently untempted to venture around the complex plane (or at least along the real line) like its associate. The third multiplier, by definition, remains equal to $+1$. The multipliers behave in a similar fashion along the 175-day contour, although the stable portion between fold and period-doubling bifurcations is so short that it does not show up on the diagram (the multiplier rapidly decreases through $+1$ and then -1 as the parameters increase slightly).

The r, s and γ diagrams, Figures 4.12(e), (f) and (j), are fairly similar to the ones for the quadratic case, with an increase in r again having the opposite effect on the period to an increase in s, despite them both being linear phytoplankton losses. The s and γ diagrams both have a 30 contour running close to Hopf A across their whole parameter ranges.

The α and λ diagrams, Figures 4.12(h) and (k), both show similar behaviour to the quadratic case, but exhibit a larger range of periods.

Finally, the μ diagram, Figure 4.12(l), is very different to the quadratic case, although given that the actual region of oscillations looks very different, it is hard to make a comparison of the nature of the period contours. The diagram exhibits very high periods at low values of μ, plus period-doubling bifurcations on the contours from 50 upwards. Hopf A becomes subcritical at low values of μ, the only parameter for which we have found subcritical Hopf bifurcations in the linear case, although the narrow region of coexistence of a stable steady state with a stable limit cycle cannot clearly be seen in Figure 4.12(l). The behaviour of the contours near to the region of period-doubling bifurcations is not quite as simple as for k, N_0 and β.

For example, following the 85 contour as q increases, we find that a Floquet multiplier leaves the unit circle through -1, producing a period-doubling bifurcation. But then instead of it re-entering the unit circle and re-stabilising the cycles, the second multiplier, which in the N_0 diagram had been content to sit near to the origin, becomes restless and inquisitive, and heads off along the real line. It leaves the unit circle through -1, yielding a period-doubling bifurcation of the saddle cycles; these cycles had lost stability at the first period-doubling bifurcation. As we continue along the contour, the two multipliers then coalesce and become a complex and conjugate pair, and venture away from the real line, undertaking the following journey. The magnitude of the imaginary part of the multipliers increases to a value greater than one, then the real part increases, and the pair move to the right in the complex plane, remaining outside of the unit circle. The real part is then greater than one, and the pair come together again on the positive real axis to become a pair of real multipliers, and one of them then re-enters the unit circle through $+1$, when μ reaches zero. Such an elaborate excursion by the multipliers does not occur for k, N_0 and β, or for any other parameters, or indeed at all in the quadratic case.

4.9 Discussion

We have investigated the behaviour of the three-component model formulated in Chapter 2, but with linear, rather than quadratic, zooplankton mortality to represent different ecological assumptions. More results can be deduced analytically, without using any explicit parameter values, than could be obtained for the quadratic case in Chapter 3. In particular, the expression for the steady-state (N^*, P^*, Z^*), with positive values of all three variables, requires the solving of a quadratic equation, rather than the infeasible tenth-order polynomial obtained for the quadratic case. The three-way transcritical bifurcation of the steady-states $(N_0, 0, 0)$, $(N_1{}^*, P_1{}^*, 0)$ and (N^*, P^*, Z^*) no longer occurs, but has split into two transcritical bifurcations between $(N_0, 0, 0)$ and $(N_1{}^*, P_1{}^*, 0)$, and between $(N_1{}^*, P_1{}^*, 0)$ and (N^*, P^*, Z^*), as graphically illustrated in Figure 4.3. (N^*, P^*, Z^*) was analytically shown to be the unique steady state in the strictly positive octant, a fact which precludes fold bifurcations and hysteresis from occurring; such bifurcations were found for the quadratic case.

The numerical investigation followed the same approach as for the quadratic case. Again we found the system to settle down to a stable steady state for the default parameter values, and then to undergo oscillations when the zooplankton mortality is increased. The one-parameter bifurcation diagrams show the same qualitative behaviour as for the quadratic case, but with the oscillations occurring over a relatively larger range of zooplankton mortality, and having larger amplitudes. The period again is around 35 days. The two-parameter diagrams show that oscillations occur across a wider range of the parameter space investigated than for the quadratic case, and the absence of fold bifurcations makes the diagrams simpler. Unlike the quadratic case, the zooplankton can die out for some small realistic regions of parameter space, namely the regions where $(N_1{}^*, P_1{}^*, 0)$ is stable.

The existence of a homoclinic connection would be sufficient to produce cycles with periods taking values up to infinity. So in the absence of any homoclinic connections, it may have been expected that the high periods of limit cycles reached for the quadratic mortality case would not occur here. However, the period-contour diagrams show that high periods do indeed occur. Furthermore we find period-doubling bifurcations, and subsequent cascades to chaos, whereas no such bifurcations or chaotic behaviour were found for the quadratic case.

A question worth asking is whether the fact that we have found chaotic behaviour for the linear model, but not for the quadratic model, is due to the differences in the model structures. In other words, is there something fundamental that keeps the model with quadratic zooplankton mortality from exhibiting chaos, or have we just not examined a region of parameter space which could give chaos for the quadratic model?

Recent work by Caswell and Neubert (1997) shows that this is not true for the simple three-species food chain model of Hastings and Powell (1991). The Hastings and Powell model consists of a top predator, species Z, which feeds on intermediate species Y, which in turn feeds on basal species X. Species X undergoes logistic growth, the two feeding relationships are Holling type II functions, and the mortalities of species Y and Z are modelled with linear functions. Hastings and Powell (1991) demonstrated the existence of a chaotic 'tea-cup' attractor. Caswell and Neubert (1997) have shown that if a quadratic function replaces the linear function for mortality of the top predator, Z, then a chaotic tea-cup attractor still occurs. Thus quadratic mortality of the top predator does not exclude the possibility of chaos in three-species models in general.

Perhaps there does exist chaotic behaviour for our quadratic mortality model investigated in Chapter 3, but we have just not been in the right region of parameter space to observe it. However, we did not find any period-doubling bifurcations of limit cycles (these would have been detected during the construction of the period-contour diagrams), and in Section 3.8 we found that along the relevant branch, the saddle point remains a saddle node and does not become a saddle focus. This latter fact eliminates the possibility of multiple homoclinic orbits exhibiting period-doubling cascades to chaos, and the former finding means that we do not find a bifurcation to initiate a conventional period-doubling cascade of limit cycles. So, we do not even find the starting points for two routes to chaos, suggesting that if a region of chaos does occur, we are not close to it in parameter space.

In these last two chapters we have investigated our NPZ model with quadratic and linear functions for zooplankton mortality, finding limit cycles to occur widely for both forms. This contrast with the results of Steele and Henderson (1992) prompts us to now re-examine their work in Chapter 5.

Chapter 5

Comparison with Steele and Henderson (1992)

5.1 Introduction

The results of Steele and Henderson (1992), in their paper entitled 'The role of predation in plankton models', are often considered by modellers when formulating plankton models, e.g. Fasham (1993, 1995). Indeed, this influential paper has inspired the work in this thesis, and has been cited over 40 times in the five years since its publication. By performing a limited number of numerical integrations of an NPZ model, Steele and Henderson (1992) found oscillations to occur when zooplankton mortality is modelled using a linear form, but not with a quadratic form. This contrasts with our findings of Chapter 3, where limit cycles were shown to occur across wide ranges of parameter space in our NPZ model with the quadratic mortality term. We now investigate the reasons for these differences. (Steele and Henderson actually forced their model with an annual cycle, but the oscillations we refer to are short-term oscillations that are not due to the forcing, as we demonstrate in Section 5.5).

Steele and Henderson (1992), hereafter SH92, firstly took a two-compartment PZ model, without nutrient limitation, and 'normalised' the two ordinary differential equations to concentrate on the effects of changes in the rate of zooplankton mortality. They then introduced nutrient limitation, adding a third variable, N, and a third ordinary differential equation to the model. The NPZ model is very similar to that of Steele and Henderson (1981), and hence to our NPZ models, which are based on the Steele and Henderson (1981) model. SH92 then normalised the new three-component model in the same way as for the two-component model. However, in Section 5.4 we show that this is not valid. The normalisation, which is essentially a nondimensionalisation of a dimensional system, results in a nondimensional three-component model which is inconsistent with the original dimensional model.

In Section 5.2 we describe the dimensional PZ model of SH92, and then in Section 5.3 show how their 'normalisation' is equivalent to a unique nondimensionalisation of the equations. In Section 5.4 we show that, contrary to what SH92 assumed, the NPZ model cannot be normalised, or nondimensionalised, in the same way as for the PZ model. We show that an extra parameter is needed in the nondimensional NPZ model, and then in Section 5.5 recompute the simulations of SH92, with the corrected form of the equations. We find that, in general, the results of SH92 are not greatly affected by the anomaly in their equations, and where differences do occur, we explain these by constructing bifurcation diagrams. In the numerical simulations we do not find limit cycles to occur for quadratic zooplankton mortality, in agreement with the findings of SH92. In Section 5.6 we therefore investigate how the differences in our NPZ model and that of SH92 leads to the apparent contradiction. We find that oscillations do occur in the NPZ model of SH92 with quadratic zooplankton mortality when parameters are changed. SH92 did not witness them since they only varied the zooplankton mortality parameter, and none of the other parameters. This is not a criticism of SH92, since they were not specifically looking for such oscillations. Rather, by changing the zooplankton mortality, the system, when seasonally forced, was shown to simulate the qualitative differences in N, P and Z between the general situation in the North Pacific and the North Atlantic Oceans.

SH92 also found that the nutrient steady-state value was less than the nutrient uptake half-saturation constant, $N^* < e$ in our notation, for linear zooplankton mortality, but that $N^* > e$ for quadratic zooplankton mortality. In Section 5.7 we discuss how our results from Chapters 3 and 4 contradict this finding. Finally, in Section

5.8 we discuss the results of this chapter in relation to Chapters 3 and 4, and specify exactly the differences between the formulations of our NPZ model and that of SH92.

5.2 The dimensional SH92 PZ system

In Steele and Henderson (1992), PZ and NPZ models with and without forcing were studied. The dimensional two-component unforced PZ system has the form

$$\frac{dP}{dt} = \beta P\left(1-\frac{P}{\gamma}\right) - \frac{\lambda P^n}{\mu^n + P^n}Z, \tag{5.1}$$

$$\frac{dZ}{dt} = \alpha\frac{\lambda P^n}{\mu^n + P^n}Z - \alpha\delta Z^m, \tag{5.2}$$

where P and Z represent the phytoplankton and zooplankton concentrations, t is time, and all parameters are positive. The value of m equals one to represent linear zooplankton mortality, and two to represent quadratic zooplankton mortality, and n takes the values one or two to represent Holling type II or III grazing functions. Parameters β and γ are the intrinsic growth rate and carrying capacity of the logistic phytoplankton growth term. Parameters α, λ and μ have the same definitions as for our models (see Chapter 2), and $\alpha\delta$ equals our q or d parameters, depending on whether $m = 1$ or 2. Note that SH92 actually have $\mu + P^n$, but this must be a misprint and it should be $\mu^n + P^n$ (the form used in Steele and Henderson (1981)), so that μ has the same definition and dimensions for both n=1 and n=2.

These equations were then 'normalised' by taking $\beta = \lambda = \mu = 1$, so that at equilibrium, the new rescaled P and Z, which we shall call p and z for clarity, satisfy

$$p\left(1-\frac{p}{c}\right) = \frac{p^n}{1+p^n}z, \tag{5.3}$$

$$az^{m-1} = \frac{p^n}{1+p^n}, \tag{5.4}$$

where $c = \gamma/\mu$, and a depends on δ. This is equivalent to rescaling the equations by a unique nondimensionalisation, which we derive below. SH92 implicitly calculated the new time units, and stated that, assuming an average doubling time for P of 2 days, the new time units are O(3) days, giving 100 time units ≈ 1 year. They then added a nutrient equation to the PZ system, and stated that the new system can be rescaled in the same way as for the NPZ system. However, we show here that this cannot be done, and that an extra parameter needs to be introduced into the nondimensional equations.

5.3 Nondimensionalising the PZ system

The setting of $\beta = \lambda = \mu = 1$ by SH92 in order to normalise (5.1) and (5.2) is a rescaling of P, Z and t, such that the new equations have the form

$$\frac{dp}{d\tau} = p\left(1 - \frac{p}{c}\right) - \frac{p^n}{1 + p^n}z, \tag{5.5}$$

$$\frac{dz}{d\tau} = \hat{\alpha}\frac{p^n}{1 + p^n}z - \hat{\alpha}az^m, \tag{5.6}$$

where τ is non-dimensional time and c, $\hat{\alpha}$ and a are non-dimensional parameters. Setting $\beta = \lambda = \mu = 1$ in (5.1) and (5.2) thus gives equations of the form of (5.5) and (5.6).

This transformation can be made explicit by defining the new nondimensional variables p and z, plus nondimensional time, τ, as

$$\tau = \frac{t}{T}, \qquad p = \frac{P}{\tilde{P}}, \qquad z = \frac{Z}{\tilde{Z}}, \tag{5.7}$$

and finding expressions for T, $\tilde{P}$ and $\tilde{Z}$. This gives

$$\frac{d}{dt} = \frac{d\tau}{dt}\frac{d}{d\tau} = \frac{1}{T}\frac{d}{d\tau}, \tag{5.8}$$

and substitution into (5.1) leads to

$$\frac{dp}{d\tau} = \beta Tp\left(1 - \frac{\tilde{P}p}{\gamma}\right) - \frac{\lambda\tilde{Z}T}{\tilde{P}}\,\frac{\tilde{P}^n p^n}{\mu^n + \tilde{P}^n p^n}z. \tag{5.9}$$

To make this into the form of (5.5) uniquely requires

$$T = \frac{1}{\beta}, \qquad \tilde{P} = \mu, \qquad \tilde{Z} = \frac{\beta\mu}{\lambda}. \tag{5.10}$$

Defining $c = \gamma/\mu$ gives the required equation (5.5). The transformations (5.7) therefore become

$$\tau = \beta t, \qquad p = \frac{P}{\mu}, \qquad z = \frac{\lambda Z}{\beta\mu}. \tag{5.11}$$

Using these substitutions, (5.2) becomes

$$\frac{dz}{d\tau} = \frac{\alpha\lambda}{\beta}\frac{p^n}{1+p^n}z - \frac{\alpha\delta}{\beta}\cdot\left(\frac{\beta\mu}{\lambda}\right)^{m-1} z^m, \tag{5.12}$$

and so to obtain the form (5.6) requires $\hat{\alpha}$ and a to be defined as

$$\hat{\alpha} = \frac{\lambda\alpha}{\beta}, \qquad a = \frac{\delta\beta^{m-1}\mu^{m-1}}{\lambda^m}. \tag{5.13}$$

The rescalings, or nondimensionalisations, (5.11) and (5.13) are unique in that they are the only transformations that will turn equations (5.1) and (5.2) into the required forms (5.5) and (5.6).

In the nondimensional system one unit of time, τ, is equivalent to $1/\beta$ days (the old time scale was days). SH92 took an average doubling time for the phytoplankton of 2 days, which means that $\beta = ln2/2$. Thus one new unit of time $= 2/ln2 = 2.88$ days, and so 100 new time units is approximately equal to 1 year.

5.4 Nondimensionalising the *NPZ* system

The full three-component system considered by SH92 has the original dimensional form

$$\frac{dN}{dt} = -\beta\frac{N}{k+N}P\left(1-\frac{P}{\gamma}\right) + (1-\alpha)\frac{\lambda P^2}{\mu^2+P^2}Z + S(N_0 - N), \tag{5.14}$$

$$\frac{dP}{dt} = \beta\frac{N}{k+N}P\left(1-\frac{P}{\gamma}\right) - \frac{\lambda P^2}{\mu^2+P^2}Z, \tag{5.15}$$

$$\frac{dZ}{dt} = \alpha\frac{\lambda P^2}{\mu^2+P^2}Z - \alpha\delta Z^m, \tag{5.16}$$

where S is the cross-thermocline exchange rate, N_0 is the nutrient concentration below the mixed layer and k is the half-saturation coefficient for nutrient uptake. In the numerical simulations to be discussed shortly, SH92 only considered the Holling Type III grazing function, and so we have set $n = 2$ in the grazing expressions $\lambda P^n/(\mu^n + P^n)$. SH92 then expressed the three equations in the following form, and stated that (5.18) and (5.19) had been normalised in the same way as for the two-component system:

$$\frac{dn}{d\tau} = -\frac{n}{\bar{k}+n}p\left(1-\frac{p}{c}\right) + (1-\hat{\alpha})\frac{p^2}{1+p^2}z + s\left(n_0 - n\right), \tag{5.17}$$

$$
\begin{aligned}
\frac{dp}{d\tau} &= \frac{n}{\tilde{k}+n}p\left(1-\frac{p}{c}\right)-\frac{p^2}{1+p^2}z, && (5.18)\\
\frac{dz}{d\tau} &= \hat{\alpha}\frac{p^2}{1+p^2}z-\hat{\alpha}az^m, && (5.19)
\end{aligned}
$$

where s, n_0 and $\tilde{k}$ are new nondimensional parameters, and n is the nondimensionalised nutrient variable.

Since (5.18) and (5.19) have been normalised, (5.17) must clearly have been rescaled in the same way, so that the units of time, p and z are consistent in all three equations. However, we now show that equations (5.14), (5.15) and (5.16) cannot be rescaled into exactly the form of (5.17), (5.18) and (5.19) using the same nondimensionalisations as those used for the two-component system.

Using the substitutions for t, P and Z given by (5.11), and defining n as

$$
n=\frac{N}{\tilde{N}}, \qquad (5.20)
$$

the three dimensional equations, (5.14), (5.15) and (5.16) become

$$
\begin{aligned}
\frac{dn}{d\tau} &= -\mu\frac{n}{k+\tilde{N}n}p\left(1-\frac{p}{c}\right)+(1-\alpha)\frac{\mu}{\tilde{N}}\frac{p^2}{1+p^2}z+\frac{S}{\beta}\left(\frac{N_0}{\tilde{N}}-n\right), && (5.21)\\
\frac{dp}{d\tau} &= \frac{\tilde{N}n}{k+\tilde{N}n}p\left(1-\frac{p}{c}\right)-\frac{p^2}{1+p^2}z, && (5.22)\\
\frac{dz}{d\tau} &= \hat{\alpha}\frac{p^2}{1+p^2}z-\hat{\alpha}az^m. && (5.23)
\end{aligned}
$$

The zooplankton equation (5.23) is the same as (5.19). We also require that (5.21) and (5.22) are in the same form as (5.17) and (5.18). In order for the phytoplankton uptake terms to be the same in the nutrient and phytoplankton equations (the first terms in (5.21) and (5.22)) requires $\tilde{N}=\mu$. Note that N and P must be scaled by the same factor, namely μ, since the uptake terms have the same form in the dimensional dN/dt and $dPdt$ equations, plus have the same form in the nondimensional $dn/d\tau$ and $dp/d\tau$ equations. The definitions $s=S/\beta$, $n_0=N_0/\mu$ and $\tilde{k}=k/\mu$ are clearly required.

This only leaves the regeneration term, the penultimate term in (5.21), not in the required form given in (5.17). In (5.21) there is a $(1-\alpha)$ term ($\tilde{N}=\mu$, so $\mu/\tilde{N}=1$) but in (5.23) we have $\hat{\alpha}$, which is given by $\hat{\alpha}=\lambda\alpha/\beta$. This shows that equations

(5.17), (5.18) and (5.19) are inconsistent, since they have $(1-\hat{\alpha})$ for the regeneration in (5.17), and $\hat{\alpha}$ in (5.19), but we have just shown that it cannot be the same 'alpha' in both equations. The value of β used by SH92 was $\ln 2/2 = 0.35$, and they did not actually give a value for λ (because it became 'normalised'), but in an earlier paper (Steele and Henderson, 1981) they used 0.6, and so $\lambda/\beta \neq 1$ and $\hat{\alpha} \neq \alpha$.

The full consistent nondimensional equations are therefore

$$\begin{aligned}
\frac{dn}{d\tau} &= -\frac{n}{\tilde{k}+n}p\left(1-\frac{p}{c}\right)+(1-\alpha)\frac{p^2}{1+p^2}z+s\left(n_0-n\right), && (5.24)\\
\frac{dp}{d\tau} &= \frac{n}{\tilde{k}+n}p\left(1-\frac{p}{c}\right)-\frac{p^2}{1+p^2}z, && (5.25)\\
\frac{dz}{d\tau} &= \hat{\alpha}\frac{p^2}{1+p^2}z-\hat{\alpha}az^m, && (5.26)
\end{aligned}$$

and contain both α and $\hat{\alpha}$. Since α is a dimensionless constant, the equations are nondimensional and consistent.

For their numerical simulations, SH92 used $\alpha = 0.5$ in the (incorrect) equations (5.17), (5.18) and (5.19), which is equivalent to setting $\alpha = \hat{\alpha} = 0.5$ in the corrected system given by (5.24), (5.25) and (5.26). Setting $\alpha = 0.5$ in (5.24) is equivalent to setting $\alpha = 0.5$ in (5.14), the original dimensional dN/dt equation. Setting $\hat{\alpha} = 0.5$ in (5.26), means that the corresponding α in (5.16), the dimensional dZ/dt equation, is given by $\beta\hat{\alpha}/\lambda$. With $\beta = 0.35$ and $\lambda = 0.6$ this gives $\alpha = 0.29$. So the SH92 value of $\alpha = 0.5$ in their normalised equations (5.17), (5.18) and (5.19), corresponds to setting $\alpha = 0.5$ in (5.14), but $\alpha = 0.29$ in (5.16). This means that a proportion 0.29 of zooplankton grazing fuels zooplankton growth, a proportion 0.5 ($= 1 - 0.5$) is recycled as nutrient, and the remaining 0.21 is lost from the system. This is similar to our NPZ model, formulated in Chapter 2, where the respective proportions are 0.25, 0.33 and 0.42. But the way that SH92 wrote their original dimensional equations (5.14), (5.15) and (5.16), with the same 'alpha' in (5.14) and (5.16), implies that they intended a proportion α of zooplankton grazing to fuel zooplankton growth, with the remaining proportion $1-\alpha$ to be recycled into nutrient, with no external loss from the system. But the values of the nondimensional parameters that they used does give a loss, due to the inconsistencies in the nondimensionalisation, giving a slight structural difference to their original dimensional model.

5.5 Simulations

We now ask whether or not the anomaly in the model of SH92 affects their results. The three-component model used in the numerical simulations presented by SH92 in their Figures 5 and 6, is the model given by equations (5.17), (5.18) and (5.19). This model is equivalent to equations (5.24), (5.25) and (5.26), with $\alpha = \hat{\alpha}$, and from now on we shall refer to these equations. In the simulations SH92 actually forced the phytoplankton growth rate, which had been normalised to one, to represent seasonal changes through the year. They used a sinusoidal forcing function with a period of 100 time units ($\simeq$ 1 year). The precise function used was

$$\text{forcing} = 1 + \frac{1}{2}\sin\frac{2\pi\tau}{100}.$$

The parameter values used by SH92 for their Figure 5B, which we consider as the default case, were:

$$\begin{aligned} s &= 0.1, & \alpha = \hat{\alpha} &= 0.5, \\ n_0 &= 4, & m &= 1, \\ \tilde{k} &= 0.5, & a &= 0.7, \\ c &= 10. \end{aligned}$$

Figure 5A of SH92 is a simulation of the *pz* system, equations (5.5) and (5.6), which contains $\hat{\alpha}$ but not α, and so the anomaly is irrelevant. For Figure 5B the full *npz* model was used, and so we now need to calculate a correct value of α to be used in equation (5.24). The value $\hat{\alpha} = 0.5$ was used by SH92 for both the *pz* and *npz* models, and so we take this to be the 'correct' value, and then work out what the correct value of α should be. From our nondimensionalisation, we know that this will be given by $\alpha = \beta\hat{\alpha}/\lambda$. SH92 did not explicitly state values for the dimensional parameters, but as mentioned earlier, we know that $\beta = 0.35$, and we take $\lambda = 0.6$, as this value was used by the same authors in an earlier paper (Steele and Henderson,

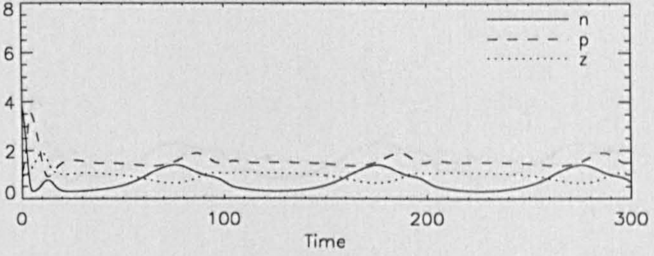

(a) SH92 Figure 5B

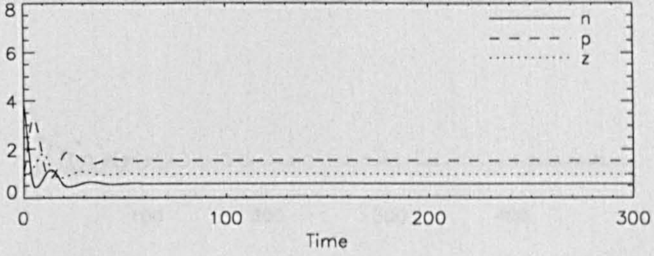

(b) SH92 Figure 5B without forcing

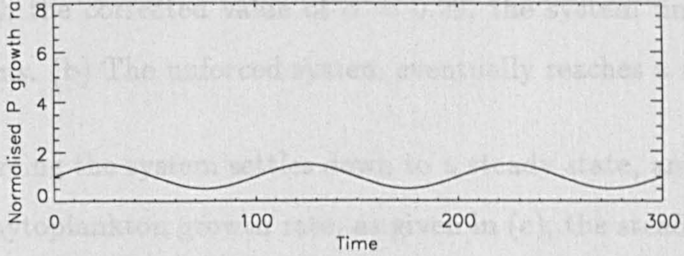

(c) Sinusoidal forcing function

Figure 5.1: (a) Figure 5B of SH92 shows that n, p and z vary slowly when the system is forced. (b) Without forcing the system settles down to a steady state. (c) The sinusoidal forcing function (100 time units $\equiv$ 1 year).

1981). These values give $\alpha = 0.29$ (to two decimal places). So we now recompute the simulations given by SH92, for the following two situations:

i) $\hat{\alpha} = \alpha = 0.5$ - the (incorrect) SH92 values,

ii) $\hat{\alpha} = 0.5$ and $\alpha = 0.29$,

to see whether the difference in the value of α is important.

5.5.1 Linear zooplankton mortality

Firstly, SH92 had $m = 1$, representing linear mortality, for their Figures 5B and 5C. In Figure 5.1(a) we recompute Figure 5B of SH92, and in (b) show what happens when the forcing is switched off. The initial conditions, as used by SH92, are $(n, p, z) =$

(a) Using the corrected value α=0.29

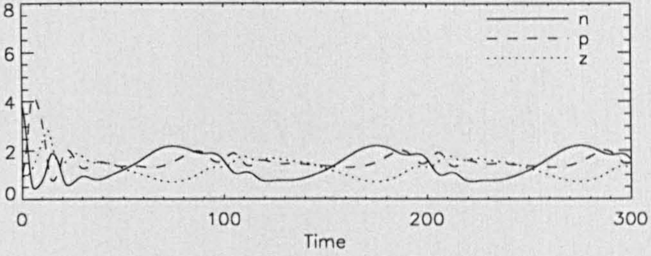

(b) With α=0.29 but unforced

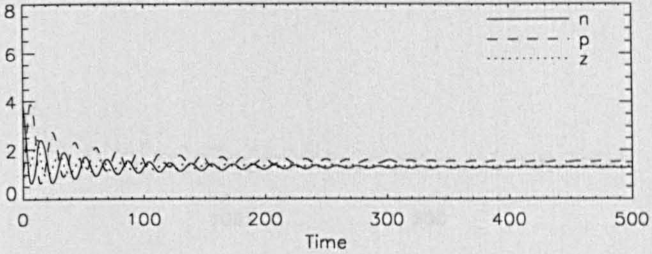

Figure 5.2: (a) With the corrected value of $\alpha = 0.29$, the system undergoes extra short-term oscillations. (b) The unforced system eventually reaches a steady state.

$(4, 1, 1)$. Without forcing the system settles down to a steady state, and with forcing of the normalised phytoplankton growth rate, as given in (c), the steady-state values of n, p and z vary slowly, with a frequency (or period) the same as that of the forcing.

In Figure 5.2(a) we set $\alpha = 0.29$, and see that the variables undergo larger variations than they did for $\alpha = 0.5$. Furthermore, there are extra small oscillations with frequencies incommensurate with the forcing frequency. These occur just after 100 and 200 time steps. These short-term oscillations suggest that the unforced system may exhibit oscillations, in contrast to Figure 5.1(b). In Figure 5.2(b) we see that the unforced system does, however, settle down to a steady state again, but after a much longer transient time than in Figure 5.1(b). Note that we have extended the time axis, but the steady state is still not quite reached in this time. Thus there is a difference between the $\alpha = 0.5$ and $\alpha = 0.29$ cases. The gradual spiralling in of the trajectory to the steady state in Figure 5.1(b) suggests that we are close to a Hopf bifurcation.

Indeed, if we reduce α only by a small amount, to $\alpha = 0.27$, we see in Figure 5.3 that the trajectory of the forced system is very similar to that for $\alpha = 0.29$, but

(a) α=0.27 is similar to α=0.29

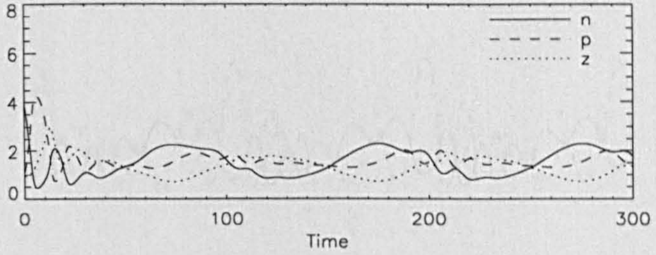

(b) α=0.27 unforced settles onto a limit cycle

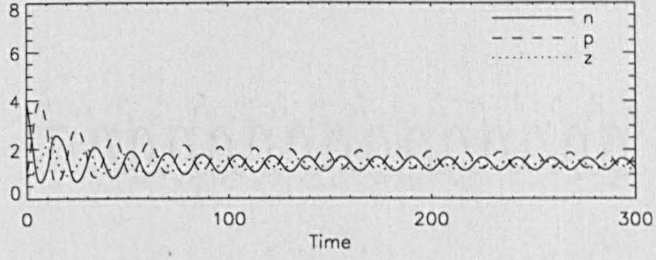

Figure 5.3: (a) With $\alpha = 0.27$, the forced system is similar to $\alpha = 0.29$. (b) However, the unforced system now settles onto a limit cycle.

that the trajectory of the unforced system settles down to a limit cycle, rather than a steady state. This suggests that a Hopf bifurcation has occurred, and indeed there is one at $\alpha = 0.274$, which we have computed using LOCBIF. The values of p, which SH92 commented on, remain at relatively low values ($\simeq 2$) throughout the oscillations for each of the α values used.

SH92 then increased the mixing rate s from 0.1 to 0.3, producing their Figure 5C which is shown in Figure 5.4(a). With this higher mixing rate, the system exhibits large oscillations, at a frequency of roughly five cycles per year. The unforced system shown in Figure 5.4(b) demonstrates larger amplitude oscillations than when we had $s = 0.1$ and $\alpha = 0.27$ in Figure 5.3(b). When we use the corrected value of $\alpha = 0.29$, with $s = 0.3$, there is little difference to Figure 5.4 for $\alpha = 0.5$. The limit cycles have a slightly larger amplitude, but we do not show them here.

So, with linear zooplankton mortality the α anomaly does give a qualitative difference in trajectories at the original low mixing rate of $s = 0.1$, as shown by comparing Figures 5.1, 5.2 and 5.3. But the small-amplitude short-term oscillations seen in the latter two figures are by no means as dramatic as what happens when the mixing rate

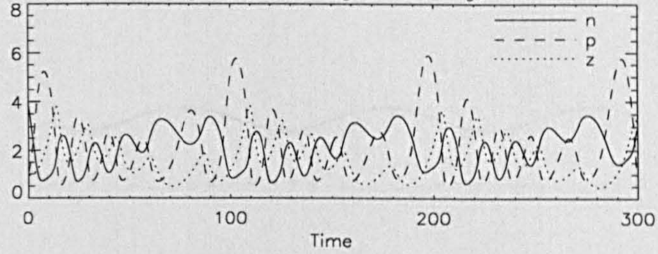
(a) SH92 Figure 5C – higher mixing rate s=0.3

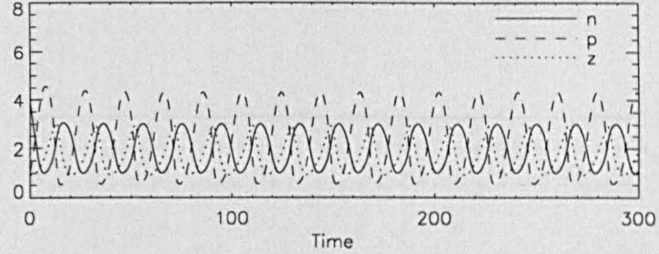
(b) s=0.3 without forcing

Figure 5.4: (a) With a higher mixing rate of $s = 0.3$, (previously $s = 0.1$), the forced system undergoes large-amplitude oscillations. (b) The unforced system settles onto a large-amplitude limit cycle.

is increased and large-amplitude oscillations occur, as shown in Figure 5.4. Thus we have found that decreasing α causes the unforced system to undergo oscillations, by taking the steady state through a Hopf bifurcation. This is equivalent to increasing the zooplankton excretion recycling parameter β in our NPZ models of Chapters 3 and 4. From Figures 3.4(i) and 4.7(i), we see that an increase in our β from low values can, for both the quadratic and linear zooplankton mortality models, take the system through a Hopf bifurcation, into a region of oscillations. This does, however, depend on the value of zooplankton mortality, d or q, and for the linear mortality case we find that the oscillations can occur at low values of recycling.

More pronounced oscillations were found by SH92 when they increased the mixing rate s, as demonstrated in Figure 5.4. For both of our previous models, Figures 3.4(d) and 4.7(d) show that an increase in the mixing rate, k, can also take our systems into a region of oscillations.

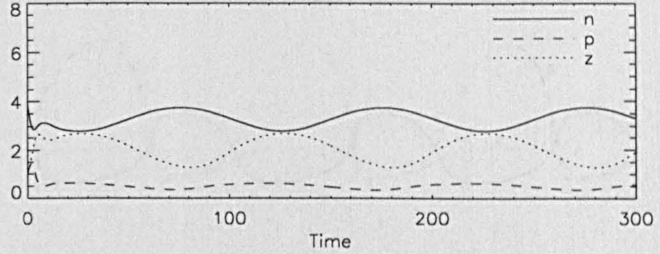
(a) SH92 Figure 6A, where a=0.1

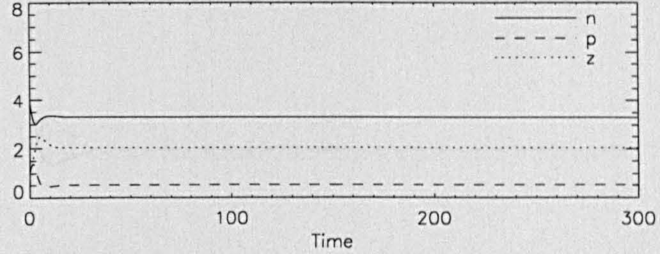
(b) SH92 Figure 6A without forcing

Figure 5.5: (a) Figure 6A of SH92 shows that with quadratic zooplankton mortality ($m = 2$) at a rate of $a = 0.1$, the forced system has fairly constant low p values, and slowly oscillating n and z, which is the general situation for the Pacific Ocean. (b) The unforced system settles down to a steady state.

5.5.2 Quadratic zooplankton mortality

In their Figure 6, SH92 set $m = 2$, to investigate the effects of using quadratic zooplankton mortality. They retained the higher mixing rate of $s = 0.3$. In Figure 5.5(a) we reproduce Figure 6A of SH92, for which they set $a = 0.1$, where a is the zooplankton mortality parameter. The forced system shows fairly constant low phytoplankton values, higher zooplankton values which oscillate with the forcing, and high nutrient values. This corresponds to the general situation in the Pacific Ocean, shown in Figure 2 of SH92. If we omit the forcing, the system quickly reaches a steady state, with low p and high n and z, as shown in Figure 5.5(b). When forced, the system thus simply tracks the steady state, which is moved around due to the forcing. If we then use the corrected value of $\alpha = 0.29$, the forced and unforced pictures change very little to those in Figure 5.5 (for which $\alpha = 0.5$), and so we do not plot them here.

SH92 then increased the value of a to 0.5, to give their Figure 6B, which we

(a) SH92 Figure 6B, where a=0.5

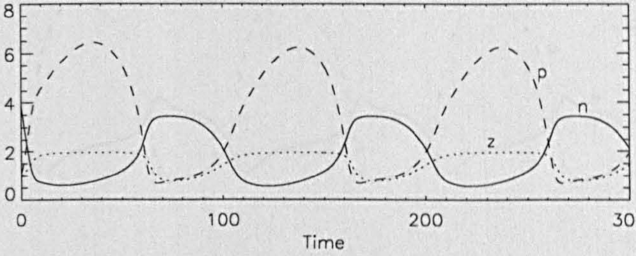

(b) SH92 Figure 6B without forcing

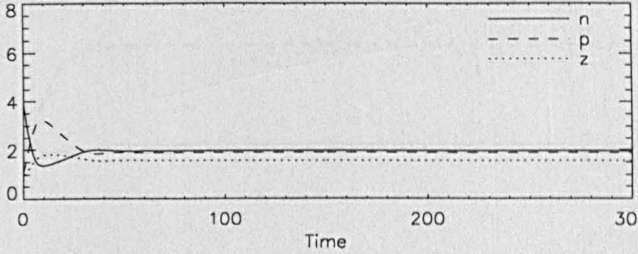

Figure 5.6: (a) Figure 6B of SH92 shows that with an increase in the rate of zooplankton mortality, $a = 0.5$, p undergoes large-amplitude fluctuations, and n gets close to the value of the half-saturation constant $\tilde{k}$, corresponding to the situation in the Atlantic Ocean. (b) The unforced system settles down to a steady state.

reproduce in Figure 5.6(a). We see that p undergoes large-amplitude fluctuations, and the minima of n are close to the value of the half-saturation constant $\tilde{k} = 0.5$. This situation corresponds to the Atlantic Ocean. For the unforced system we see that the system settles down to a steady state, with n, p and z all taking similar values. The steady-state value of p is much less than the average of the p values throughout the cycles of the forced system. This is unlike Figure 5.5 for $a = 0.1$, where the average of p in the forced system equals the unforced steady-state value. We elaborate on this shortly.

When we use the corrected value of $\alpha = 0.29$, we obtain the picture for the forced system given in Figure 5.7(a). We see that p reaches much higher values than for $\alpha = 0.5$, Figure 5.6(a), and that n only gets as low as 1.0, twice the value of the half-saturation constant. The behaviour of z is practically identical to that for $\alpha = 0.5$. Also we note that the maxima and minima of n are not as 'smooth' as for $\alpha = 0.5$. For the unforced system, Figure 5.7(b), we find a three-fold increase in the steady-state

(a) a=0.5 with α=0.29

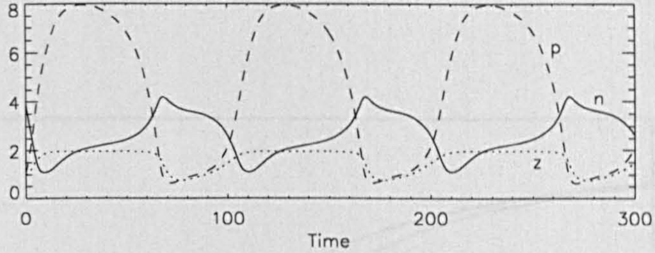

(b) a=0.5 and α=0.29 without forcing

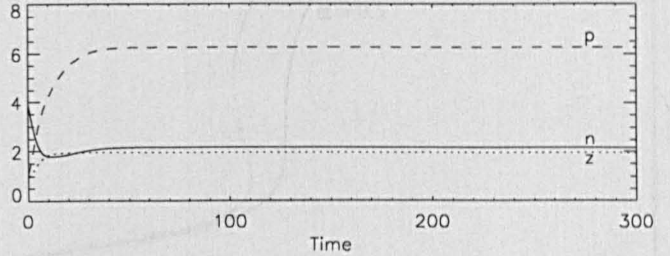

Figure 5.7: (a) With the corrected $\alpha = 0.29$, and $a = 0.5$, p reaches higher values than for $\alpha = 0.5$. (b) The steady-state value of p is three times that for $\alpha = 0.5$, explaining why the forced system shows higher p values.

value of p, compared to Figure 5.6(b) for $\alpha = 0.5$. The n value increases marginally, and the z value actually increases by a third, despite showing no change for the forced equations. So the α anomaly does, in this case, make a difference.

In Figure 5.8 we show how the steady-state value of p for the unforced system, changes in magnitude as we vary a, the predation on the zooplankton. We plot the curves for both $\alpha = 0.5$ and $\alpha = 0.29$. The situations that we have just discussed are for $a = 0.1$, Figure 5.5, and then $a = 0.5$, Figures 5.6 and 5.7. On Figure 5.8 we see that at $a = 0.1$, the steady-state value of p is the same for both $\alpha = 0.5$ and $\alpha = 0.29$, at the value shown in Figure 5.5. In Figure 5.8 we see that at $a = 0.5$, the steady-state value of p is just below two for $\alpha = 0.5$ and just above six for $\alpha = 0.29$. This explains the large difference in p values that we found in Figures 5.6 and 5.7. The reason for the difference is that the $\alpha = 0.29$ curve in Figure 5.8 shows a hysteresis effect, which is due to two fold bifurcations of the steady state occurring. The dashed line indicates where the steady state is unstable, and so the two fold bifurcations occur where the dashed line becomes solid. For $\alpha = 0.5$ the hysteresis does not occur, although high

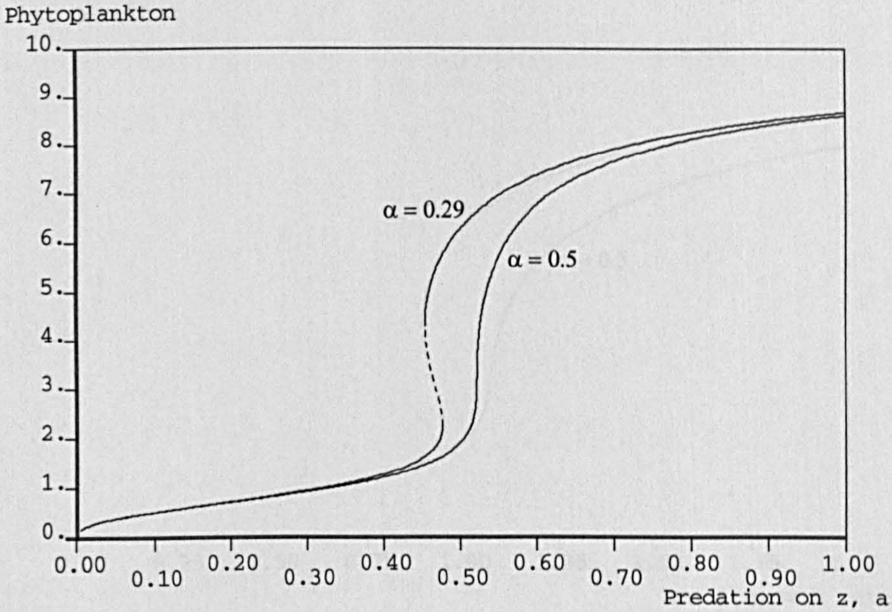

Figure 5.8: The phytoplankton steady-state value changes as the predation on zooplankton, a, is increased. The solid line indicates where the steady state is stable, and the dashed line where it is unstable. Hysteresis occurs for $\alpha = 0.29$, but not for $\alpha = 0.5$. At $a = 0.1$ the p values are the same for both values of α, but at $a = 0.5$, the $\alpha = 0.29$ value is much higher than for $\alpha = 0.5$, explaining the difference between Figures 5.6 and 5.7.

p values are reached at higher a values. For example, if $a = 0.7$, then $\alpha = 0.5$ and $\alpha = 0.29$ again have similar p steady-state values.

In Figure 5.9 we show how the steady-state value of p for the unforced system changes as the maximum growth rate of p is varied, with a set to 0.5. The maximum growth rate, which has been 'normalised' to one and is not specified explicitly as a parameter, is what is forced in the preceding diagrams. In the unforced diagrams, it equals 1.0, and when forced it ranges from 0.5 to 1.5, because the forcing function is given by

$$\text{forcing} = 1 + \frac{1}{2}\sin\frac{2\pi\tau}{100}.$$

When the maximum growth rate equals 1.0, we have the same steady-state values for

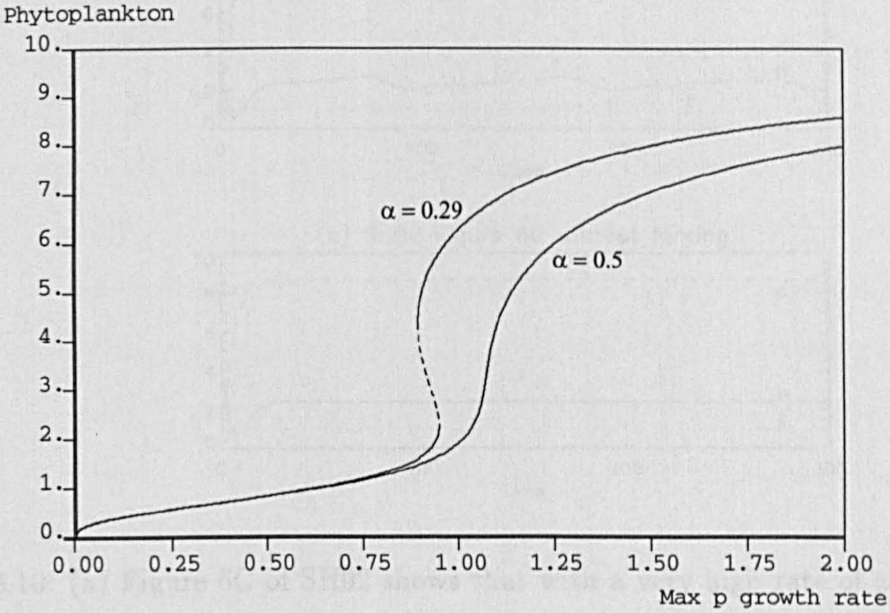

Figure 5.9: In the unforced system, the maximum phytoplankton growth rate is set to 1.0, but in the forced system it varies sinusoidally between 0.5 and 1.5. This diagram (for which $a = 0.5$) shows that for $\alpha = 0.5$, the forcing pushes the system into a region where the steady-state value of p is much higher than in the unforced system, thus explaining the large peaks of p, relative to the unforced steady-state value, reached in Figure 5.6(a). For $\alpha = 0.29$, the unforced steady-state is already at a high value of p.

p as we have at $a = 0.5$ in Figure 5.8. Again we find hysteresis for $\alpha = 0.29$ but not for $\alpha = 0.5$. As the forcing increases the growth rate, we see that, for $\alpha = 0.5$, this pushes up the steady-state value of p to values much greater than when the growth rate equals 1.0. This explains why, in Figure 5.6, for $\alpha = 0.5$, the average value of p during the forced cycles, Figure 5.6(a), is much greater than the unforced steady-state value shown in Figure 5.6(b). The forcing pushes the system through a region where p increases sharply, namely the near vertical part of the $\alpha = 0.5$ curve in Figure 5.9.

For their final numerical simulation, SH92 set a to the high value of 1.0, to produce their Figure 6C, which we reproduce in Figure 5.10(a). Throughout the cycles, p

(a) SH92 Figure 6C, where a=1.0

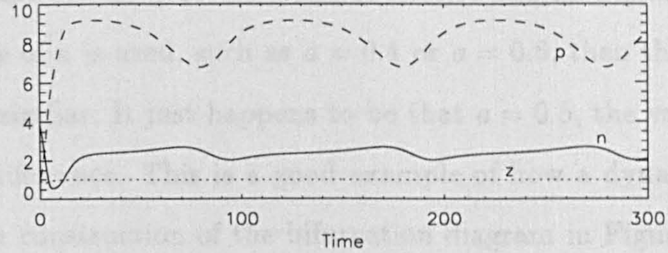

(b) SH92 Figure 6C without forcing

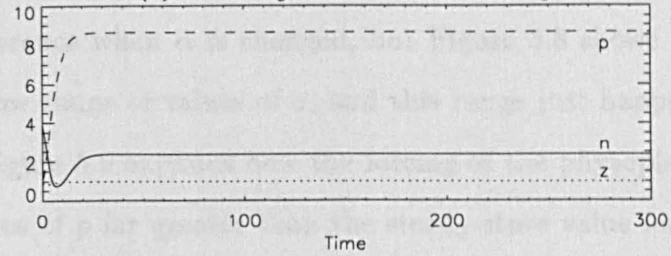

Figure 5.10: (a) Figure 6C of SH92 shows that with a very high rate of zooplankton mortality, $a = 0.5$, p remains large and fairly close to the carrying capacity ($c = 10$), and z remains low and constant. (b) The unforced system settles down to a steady state with a high p value, as predicted by the bifurcation diagram of Figure 5.8.

remains fairly high. In Figure 5.10(b) we see that the unforced system settles down to a steady state with a high p value. We actually already know this - it is given by the point with $a = 1.0$ on the bifurcation diagram of Figure 5.8. If we set $\alpha = 0.29$, then the forced and unforced diagrams are very similar to Figures 5.10(a) and 5.10(b) for $\alpha = 0.5$, and so we do not plot them here.

Thus we have recomputed the numerical simulations of SH92 with the corrected value of $\alpha = 0.29$. For linear zooplankton mortality we find that with the low mixing rate of $s = 0.1$, the system does exhibit unforced oscillations, as shown in Figures 5.2 and 5.3, whereas SH92 thought that the higher mixing rate was required to produce oscillations. But the oscillations with the higher mixing rate, Figure 5.4, are much larger in amplitude than those shown for the low mixing rate, although the small oscillations are due to being close to the Hopf bifurcation which occurs at $\alpha = 0.274$. For quadratic zooplankton mortality, when $a = 0.5$ the 'alpha' anomaly does make a difference, as shown by Figures 5.6 and 5.7 which show different p values for $\alpha = 0.5$

and $\alpha = 0.29$. In Figure 5.8 we show that this difference can be explained, and that if an alternative value of a is used, such as $a = 0.4$ or $a = 0.6$, then the steady-state values of p would be similar. It just happens to be that $a = 0.5$, the value chosen by SH92, gives a large difference. This is a good example of how a dynamical systems approach, namely the construction of the bifurcation diagram in Figure 5.8, is more powerful than simple computation of trajectories. The time series of Figures 5.6 and 5.7 show a large difference when α is changed, but Figure 5.8 shows that this only occurs within a narrow range of values of a, and this range just happens to contain the value $a = 0.5$. Figure 5.9 explains how the forcing of the phytoplankton growth rate can lead to values of p far greater than the steady-state value for the unforced system. Overall it appears that the results of SH92 are not drastically altered when the 'alpha' anomaly is corrected.

5.6 Do oscillations occur for the SH92 model with quadratic zooplankton mortality?

We have not found any unforced oscillations when quadratic zooplankton mortality is used, which agrees with the findings of SH92. But in Chapter 3 we showed that oscillations occur across wide ranges of parameter values in our NPZ model, which has the quadratic zooplankton mortality. So, is this difference due to slight differences in the structure of the SH92 model and our model? Or is it the case that the SH92 model can exhibit oscillations, but we have just been in an area of parameter space that does not give them?

To investigate these questions, we continue using the corrected nondimensionalised SH92 model, as given by equations (5.24), (5.25) and (5.26), but use our default parameter values from Chapter 2. These parameter values are equivalent to the following values for the dimensional parameters of the dimensional SH92 model, given by equations (5.14), (5.15) and (5.16):

$$S = 0.05, \qquad \alpha = 0.25,$$
$$N_0 = 0.6, \qquad \lambda = 0.6,$$
$$k = 0.03, \qquad \mu = 0.035,$$
$$\beta = 1, \qquad \delta = 4,$$
$$\gamma = 1.$$

These parameters therefore have the same units as those for our model in Chapter 2. Most of the parameters have equivalent definitions to parameters in our model. But in our model we have the phytoplankton growth rate, excluding nutrient limitation, as the function $aP/(b+cP)$, whereas in the SH92 model it is the logistic form $\beta P(1 - P/\gamma)$. We thus equate β to our maximum specific phytoplankton growth rate, $a/b = 1$. The half-saturation constant in $aP/(b + cP)$ is b/c, and for $\beta P(1 - P/\gamma)$ half of the maximum specific growth rate is reached when $P = \gamma/2$, and so we set $\gamma = 2b/c$.

These values result in the following parameters (to two significant figures) for the nondimensionalised model, as given by equations (5.24), (5.25) and (5.26):

$$s = 0.05, \qquad \alpha = 0.25,$$
$$n_0 = 17, \qquad \hat{\alpha} = 0.15,$$
$$\tilde{k} = 0.86, \qquad a = 0.39,$$
$$c = 29.$$

As we have just shown, SH92 considered different levels of zooplankton mortality, a, in their numerical simulations. We thus treat a as a bifurcation parameter. This was the case in Chapter 3, where the equivalent dimensional parameter, d, had a default value of 1.0 and a maximum of 2.0. We therefore use a default value of $a = 0.39$ (which corresponds to $d = 1.0$), and take a maximum of double this value, namely 0.78.

In Figure 5.11 we show the bifurcation diagram of nutrient values against a. For the default value of $a = 0.39$ there is a stable steady state with $n = 4.22$. As a is decreased, the steady state loses stability at a fold bifurcation at $a = 0.30$. A second fold bifurcation occurs at $a = 0.38$, but the steady state does not regain stability until

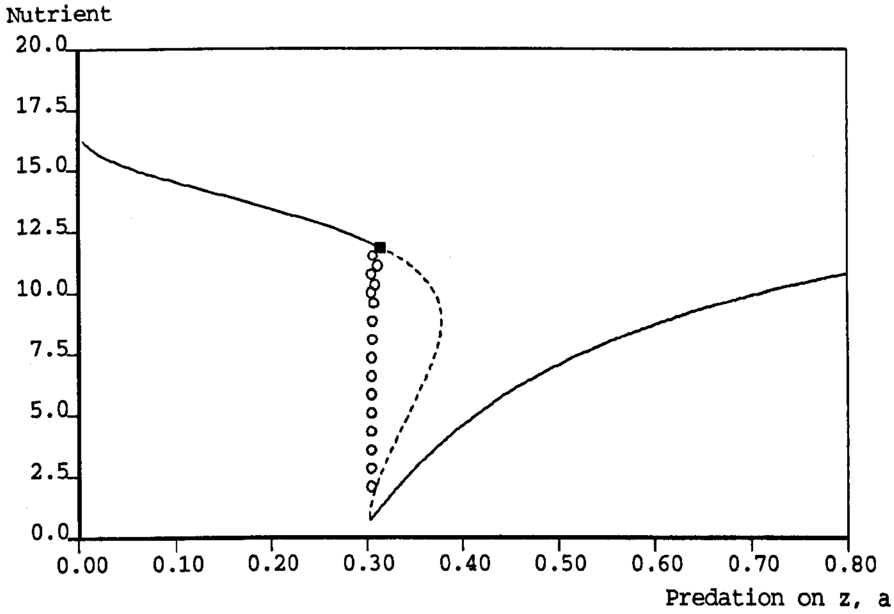

Figure 5.11: Bifurcation diagram of nutrient against a, for the SH92 model with the default parameter values from our NPZ model of Chapter 3. The solid and dashed lines represent stable and unstable steady states respectively, and the solid square is a Hopf bifurcation. The resulting branch of cycles is unstable; the maximum and minimum nutrient values along cycles are given by the circles, which are open to indicate instability. This picture is similar to Figure 3.6(g) for our NPZ model.

a Hopf bifurcation. The Hopf bifurcation is subcritical, and so the limit cycles close to it are unstable. The branch of limit cycles does not become stable, but terminates at a homoclinic connection with the saddle point near to the fold bifurcation. Now, apart from at high values of a, this picture is similar to Figure 3.6(g) for our NPZ model with quadratic zooplankton mortality. Figure 3.6(g) has a blown-up horizontal scale, whereas Figure 5.11 gives the full range of a. Both Figures show a subcritical Hopf bifurcation with a branch of unstable cycles which terminates at a homoclinic connection, plus two fold bifurcations of the steady state. Figure 3.6(g) was for high values of the sub-mixed-layer nutrient concentration, N_0, and so this suggests that if we reduce the value of n_0, we may find a similar scenario to lower values of N_0 for

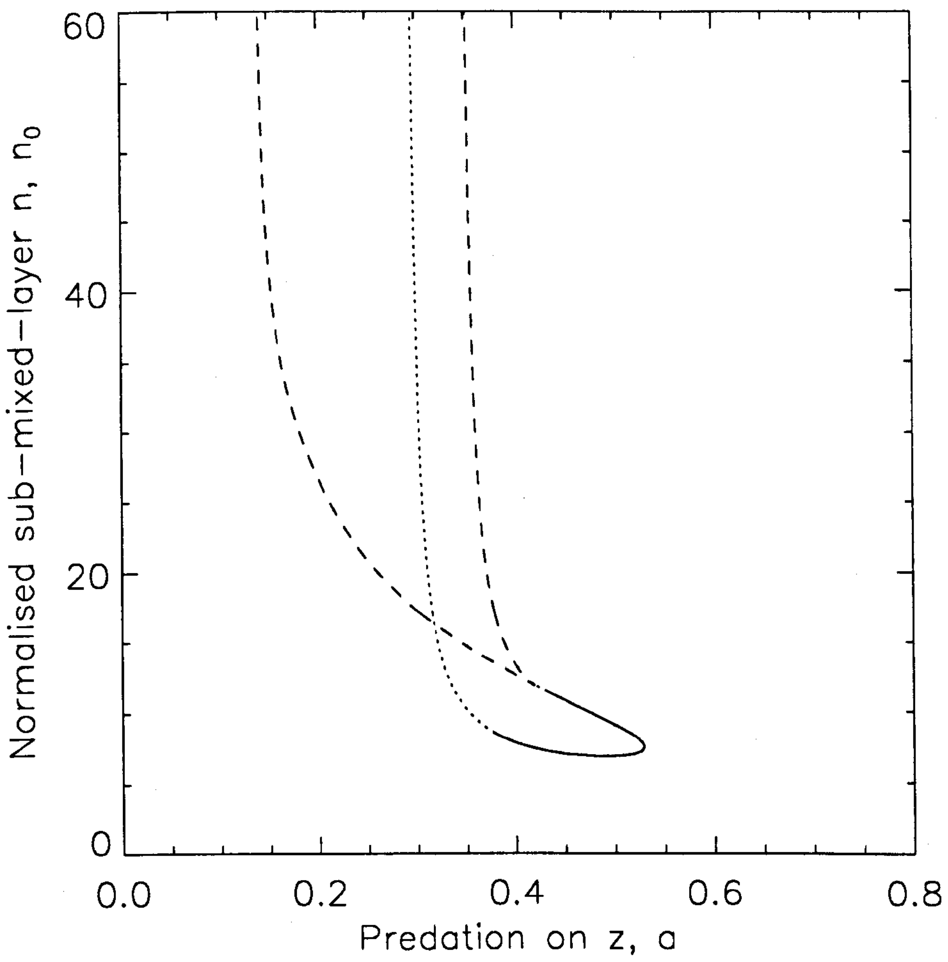

Figure 5.12: Two-parameter bifurcation diagram of n_0 against a, showing a qualitatively similar picture to Figure 3.4(g) for our *NPZ* model. Solid lines represent supercritical Hopf bifurcations, dotted lines are subcritical Hopf bifurcations and dashed lines are fold bifurcations.

our *NPZ* model. Despite the current value of n_0 being based on the default value of N_0, the differences in model structure may have caused the bifurcation picture to have been shifted.

In Figure 5.12 we therefore compute how the bifurcations of steady states in Figure 5.11 change as n_0 is varied. The resulting picture is qualitatively similar to Figure 3.4(g) for the *NPZ* model, implying that the bifurcation structure found for the *NPZ* model also occurs for the SH92 model. Since the Hopf bifurcations in Figure 5.12 become supercritical, at the points where the dotted lines become dashed, we

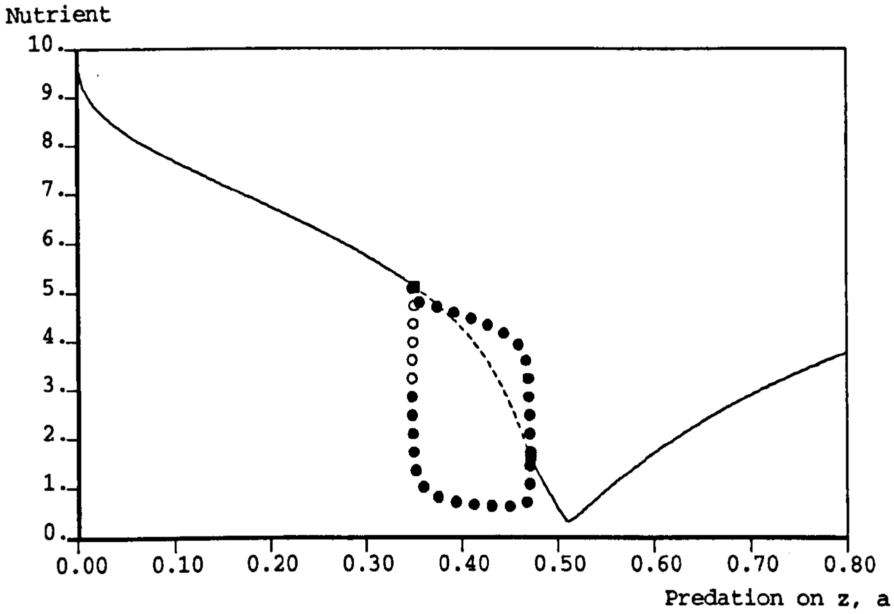

Figure 5.13: For $n_0 = 10$, we have stable limit cycles, as shown by the solid circles. Thus oscillations do occur in the SH92 model. This picture is qualitatively similar to Figure 3.6(a), which, for our *NPZ* model, has $N_0 = 0.75$ and all of the other parameters set to their default values.

know that there are stable limit cycles in the SH92 model. The detailed structure of Figure 3.4(g) was investigated more thoroughly in Figure 3.8, which also indicates bifurcations of limit cycles. On Figure 3.8 the Bogdanov-Takens bifurcation is clearly marked, which is the point at which a Hopf bifurcation curve terminates on the curve of fold bifurcations of the steady state. This also occurs in Figure 5.12, at the point $a = 0.409, n_0 = 12.3$, which is at a relatively lower value of n_0 than the high N_0 of Figure 3.8.

Figure 5.12 therefore proves the existence of oscillations in the SH92 model. To illustrate this, in Figure 5.13 we plot the bifurcation diagram of nutrient against a, with $n_0 = 10$. From Figure 5.12 we see that at this level of n_0, the fold bifurcations of the steady state no longer occur, and two Hopf bifurcations occur, one of which is supercritical, and therefore yields stable limit cycles. The stable limit cycles are indicated by the solid circles. Figure 5.12 is similar to Figure 3.6(a) for the NPZ model, for which $N_0 = 0.75$. Plotting the equivalent bifurcation diagram for a slightly lower value of n_0 where both Hopf bifurcations are supercritical, say 0.8 or 0.7, results in a diagram which is qualitatively the same as Figure 3.3(a), the original nutrient against d diagram for the NPZ model, when N_0 (and all other parameters except d) are fixed at their default values.

5.7 Nutrient steady-state values compared to the half-saturation constant

SH92 looked at the nutrient steady-state values, N^*, and nutrient uptake half-saturation constant, e, in five models from the literature, and concluded that

$$\begin{array}{ll} N^* < e & \text{for linear } Z \text{ mortality,} \\ N^* > e & \text{for quadratic } Z \text{ mortality.} \end{array}$$

However, comparing our Figures 3.3(a) and 4.6(a), which show N^* against zooplankton mortality for the quadratic zooplankton case and linear case respectively, we see that the values of N^* are similar for both models. In both cases, $N^* > e$, where e is at the default value of 0.03, is satisfied (except that $N^* < 0.03$ in the tiny interval $q \in (0.144, 0.148)$ for the linear case).

Furthermore, all of our other one-parameter bifurcation diagrams which have shown values of N^*, namely Figures 3.5(a) and (b), 3.6(a)-(g), 4.9 and 4.11, show N^* to be larger, usually much larger, than 0.03, the value of e, for both linear and quadratic mortality. Even during limit cycles, the nutrient concentration seems to remain above the half-saturation value of 0.03.

Figures 3.6(a)-(g), for progressively higher values of N_0, with quadratic zooplankton mortality, suggest that at high values of the quadratic zooplankton mortality rate, d, N^* may reach 0.03. We have computed the value of N^* with d fixed at its maximum value of $d = 2.0$ and N_0 set to to its maximum value of $N_0 = 2.0$, and found $N^* > e$ still holds. Then, allowing N_0 to decrease, keeping $d = 2.0$, we find

$N^* > e$ holds right down until $N_0 = 0.15$, which is close to its minimum realistic value of 0.1 given in Table 2.1. For $N_0 < 0.15$ we then have $N^* < e$, in contrast to SH92 who found $N^* < e$ only for linear zooplankton mortality.

Thus we find $N^* > e$ to hold for almost all of the parameter values we have investigated, for both forms of mortality. And we have found that $N^* < e$ can occur for quadratic zooplankton mortality. This has been achieved by only changing the zooplankton mortality function between our two models. The SH92 conclusions may be due to other differences between the five models that they considered, which ranged from their 1981 NPZ model to the ten-equation model of Hofmann and Ambler (1988).

5.8 Discussion

In this chapter we have examined the results of SH92, since our results of Chapters 3 and 4 have shown oscillations to occur when either the quadratic or the linear zooplankton mortality functions are used, in contrast to the findings of SH92. Firstly, we have found an anomaly in the 'normalisation' of the NPZ model by SH92. We have recomputed the simulations of SH92 with the corrected equations, and found the results to generally not be affected. By constructing bifurcation diagrams, we have shown that where major quantitative differences do occur, these are confined to small parameter ranges. The SH92 model does exhibit oscillations when quadratic zooplankton mortality is used, which we have shown by using our default parameter values. Finally, we have discussed how our results from Chapters 3 and 4 contradict the hypothesis of SH92 that the nutrient steady-state values, N^*, tends to be larger than nutrient uptake half-saturation constant, e, when the quadratic zooplankton mortality function is used, but smaller when the linear form is used.

Comparing the two-parameter bifurcation diagrams of Figures 3.4 and 4.7 we see that oscillations occur across larger ranges of parameters for our linear mortality model than for our quadratic model. Therefore, if we pick arbitrary parameter values for our models, we would be more likely to find oscillations for the linear model than for the quadratic one. This is consistent with the situation that Steele and Henderson found, and it would be surprising if they had found the converse to be true.

In addition to the difference in the growth-rate formulations used in the SH92 model and our model, as formulated in Chapter 2, there are other differences between the two models. Comparing our NPZ model, as given by (2.1), (2.2) and (2.3), and the original dimensional NPZ model of SH92, equations (5.14), (5.15) and (5.16), the differences are as follows, where parameter definitions are those for our model. For the SH92 model:

- there is no phytoplankton respiration or natural mortality, rP;
- there is no phytoplankton sinking term, sP;
- the phytoplankton are not lost from the mixed layer due to diffusive mixing - the kP term in our dP/dt equation (2.2);
- regeneration of excretion from the higher predators on zooplankton, γ, is omitted;
- the recycling of zooplankton excretion is a proportion $1-\alpha$ of zooplankton grazing, but a proportion $\beta \leq 1-\alpha$ in our model.

The first two differences correspond to setting $r = 0$ and $s = 0$ in our model. The two-parameter diagrams of Figures 3.4(e) and (f) show that setting $r = 0$ and (independently) $s = 0$ retains the oscillatory behaviour in our model, shifting the region of oscillations to a lower range of d values. Omitting the kP mixing term from our dP/dt equation (2.2) would no doubt give the same result; this is not simply equivalent to setting $k = 0$, since k also appears in the dN/dt equation (2.1). The default values of $s = 0.04$ and $k = 0.05$ suggest that setting $s = 0$ is practically equivalent to omitting kP from (2.2), since s only appears once in all of the equations, namely as a linear phytoplankton loss.

Omitting the regeneration of excretion of the higher predators means setting $\gamma = 0$ in our model. Figure 3.4(j) shows that setting $\gamma = 0$ retains the oscillations. So none of the terms in our model that are omitted in the SH92 model affect whether or not the oscillations exist in our model (at least when they are omitted independently). Furthermore, r, s and γ show the least effect on the oscillations of all the parameters shown in the two-parameter diagrams of Figure 3.4. Thus, Steele and Henderson seemingly omitted the least important terms of their 1981 model when they constructed their 1992 model.

The final difference between the models is in the recycling of zooplankton excretion. This is a proportion β of zooplankton grazing in our model, but is set to $1 - \alpha$ in the SH92 model. We used our value of $\alpha = 0.25$ in Section 5.6, and so this is equivalent to setting $\beta = 0.75$ in our NPZ model of Chapter 3. Now, Figure 3.4(i) shows that setting $\beta = 0.75$ in our model gives fold bifurcations and subcritical Hopf bifurcations, in a similar fashion to setting N_0 high. This is almost precisely what we have found in Figure 5.12. At $n_0 = 17$, which corresponds to our default value of $N_0 = 0.6$, we have fold bifurcations of the steady state, but this difference from the $N_0 = 0.6$ situation in our model can be explained because of the higher recycling rate of 0.75 - setting $\beta = 0.75$ in our model produces the same situation, as shown by Figure 3.4(i). Reducing n_0 in the SH92 model, thus compensating for the high regeneration, then gives the situation that we found for the default parameters in our model. This demonstrates the value of our two-parameter bifurcation diagrams of Figure 3.4 in predicting the consequences of omitting or changing certain features of a model.

Chapter 6

Modelling detritus: dynamics of a four-component model

6.1 Introduction

We now add a fourth variable, representing detritus, to our NPZ model, and assess whether or not the dynamical behaviour of the NPZ model is preserved in the four-component model. Detritus consists of faecal pellets of zooplankton, plus dead phytoplankton and zooplankton, as defined by Fasham *et al.* (1990). Attached bacteria can break the detritus down into utilisable nutrient, a process known as remineralisation (Totterdell *et al.*, 1993), giving a simple representation of the microbial loop. Detrital particles can aggregate together and sink out of the mixed layer, a process which plays an important part in exporting carbon to the deep ocean. Detritus is also lost from the mixed layer due to diffusive mixing processes with the sub-mixed-layer water, as occurs for the non-motile nutrient and phytoplankton. The final possible fate of detritus is that it can be consumed by zooplankton. This depends upon the species composition of the zooplankton, and is included in some models where zooplankton and detritus are explicitly modelled (Fasham *et al.*, 1990; Fasham, 1993), but excluded from others (Hood and Olson model in Davis and Steele, 1994; Fasham, 1995).

Since the addition of the detrital component presents a major difference to the structure of the model, compared to the original NPZ model, we do not allow zooplankton to graze on detritus in the model for this chapter, but do consider such grazing in Chapter 7. This is so that we add complexity to the models one step at a time, making it clear which particular amendment brings about any change in dynamical behaviour.

In Section 6.2 we formulate the $NPZD$ model. We consider only quadratic zooplankton mortality, and so all results shall be compared directly to the results in Chapter 3 (and it is to this chapter that we are referring to when we talk about the NPZ model). We then investigate this new model in the same way as for the NPZ model. Firstly, in Section 6.3, we proceed as far as possible analytically. This analysis suggests that a three-way transcritical bifurcation between steady states occurs at the same parameter values as for the NPZ model, and by numerically constructing the colour bifurcation diagram of Figure 6.2 we illustrate this to be so. In Section 6.4 two time series are shown, the first demonstrates the system settling down to a steady state, and the second demonstrates oscillations of the variables. This behaviour, which is the same as that of the NPZ model, prompts investigation of the bifurcations of the system in Sections 6.5 and 6.6. We find the bifurcational behaviour of the NPZ system to be remarkably preserved in the $NPZD$ system. In Section 6.7 we discuss how the period of the oscillations changes with each of the parameters, and finally all of the results are discussed in Section 6.8.

6.2 Model formulation

In Figure 6.1 we show the structure of the four component $NPZD$ model, where D represents the concentration of detritus in the mixed layer. We measure D in $g\ C\ m^{-3}$, the same units as used for N, P and Z. The term $(1-\alpha-\beta)G_1$, where G_1 is just the grazing term $\lambda P^2 Z/(\mu^2+P^2)$, represents faecal pellets from zooplankton grazing on phytoplankton, and thus enters the detritus compartment. In the NPZ model such pellets were assumed to immediately sink out of the mixed layer; now they are treated explicitly as detritus. The sinking term is $-\psi D$, where the sinking rate ψ has units of

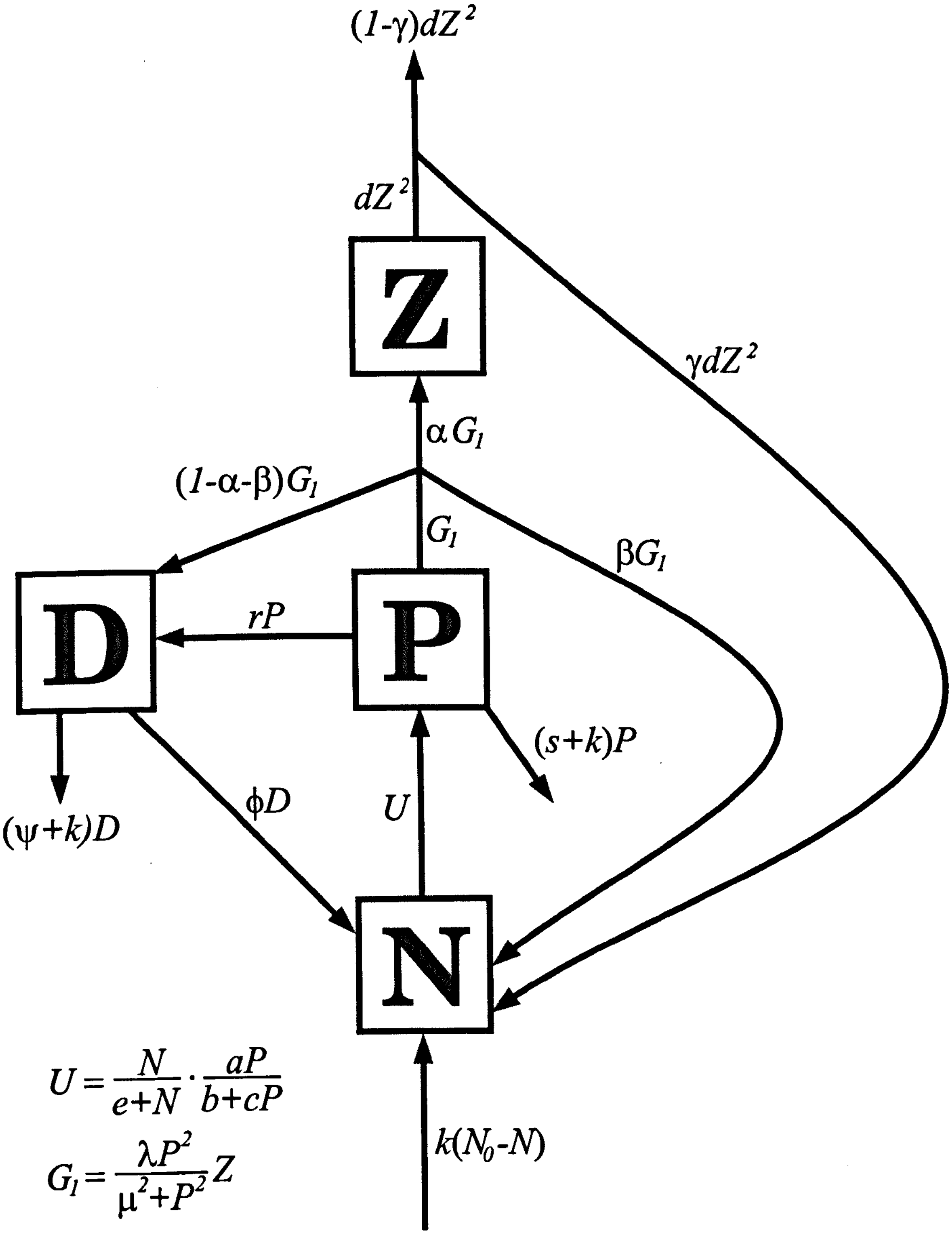

Figure 6.1: The addition of the detritus compartment, D, represents remineralisation more realistically than in the NPZ model. Detritus comes from zooplankton faecal pellets, $(1-\alpha-\beta)G_1$, and the phytoplankton loss rP. Detritus is converted into nutrient at a rate ϕ, and is lost due to sinking at a rate ψ and diffusive mixing at a rate k.

day^{-1}. The other input to the detritus compartment is from phytoplankton natural mortality, which is included in the rP term. Previously, this was recycled directly into utilisable nutrient; now this process occurs via remineralisation of detritus by (unmodelled) bacteria. This remineralisation is modelled as a flow of ϕD converting detritus into nutrient, where the remineralisation rate ϕ has units of day^{-1}. Detritus will also leave the mixed layer due to diffusive mixing with sub-mixed-layer water; as we had for nutrient and phytoplankton, this linear loss rate is parameterised by k.

The resulting equations are:

$$\frac{dN}{dt} = -\text{uptake} + Z \text{ excretion} + Z \text{ predation excretion} + D \text{ remineralisation} + \text{mixing},$$
$$\frac{dP}{dt} = \text{uptake} - \text{respiration} - \text{grazing by } Z - \text{sinking} - \text{mixing},$$
$$\frac{dZ}{dt} = \text{growth} - \text{higher predation},$$
$$\frac{dD}{dt} = P \text{ respiration} + Z \text{ faecal pellets} - \text{remineralisation} - \text{sinking} - \text{mixing}.$$

The specific functional forms used are:

$$\frac{dN}{dt} = -\frac{N}{e+N}\frac{a}{b+cP}P + \frac{\beta\lambda P^2}{\mu^2+P^2}Z + \gamma dZ^2 + \phi D + k(N_0 - N), \quad (6.1)$$
$$\frac{dP}{dt} = \frac{N}{e+N}\frac{a}{b+cP}P - rP - \frac{\lambda P^2}{\mu^2+P^2}Z - (s+k)P, \quad (6.2)$$
$$\frac{dZ}{dt} = \frac{\alpha\lambda P^2}{\mu^2+P^2}Z - dZ^2, \quad (6.3)$$
$$\frac{dD}{dt} = rP + (1-\alpha-\beta)\frac{\lambda P^2}{\mu^2+P^2}Z - (\phi+\psi+k)D. \quad (6.4)$$

Fasham *et al.* (1990) quoted the review of breakdown rates of dead organic matter by Jones and Henderson (1986), who found a range of 0.004-0.18 day^{-1}. Fasham *et al.* (1990) used the value of 0.05 day^{-1} for breakdown of detritus into dissolved organic nitrogen, which can then be utilised by phytoplankton via uptake by bacteria. Mike Fasham (personal communication) suggested a range for ϕ in our model of 0.01-0.1 day^{-1}. The Hood and Olson closed $NPZD$ model in Davis and Steele (1994) has a value of 0.2 day^{-1}. To include all these values, we thus take a range for ϕ of 0.004-0.2, with a default at the average value of $\phi = 0.1$ day^{-1}.

Fasham *et al.* (1990) used two detritus sinking velocities, of 1 and 10 m day^{-1}. Since we have a relatively shallow mixed-layer depth of 12.5m, we use the lower value for our default sinking velocity. Dividing the sinking velocity by the mixed-layer depth gives a default value of $\psi = 0.08\ day^{-1}$, and a range of $0.08 - 0.8$.

6.3 Analysis

We now calculate the steady states of the system, plus, where possible, their stability. The stability of a steady state is given by the eigenvalues of the Jacobian matrix evaluated at that steady state; the Jacobian for a general steady state is given by

$$\mathbf{A} =$$

$$\begin{bmatrix} -\frac{aeP}{(e+N)^2(b+cP)} - k & -\frac{abN}{(e+N)(b+cP)^2} + \frac{2\beta\lambda\mu^2 PZ}{(\mu^2+P^2)^2} & \frac{\beta\lambda P^2}{\mu^2+P^2} + 2\gamma dZ & \phi \\ \frac{aeP}{(e+N)^2(b+cP)} & \frac{abN}{(e+N)(b+cP)^2} - r - s - k - \frac{2\lambda\mu^2 PZ}{(\mu^2+P^2)^2} & -\frac{\lambda P^2}{\mu^2+P^2} & 0 \\ 0 & \frac{2\alpha\lambda\mu^2 PZ}{(\mu^2+P^2)^2} & \frac{\alpha\lambda P^2}{\mu^2+P^2} - 2dZ & 0 \\ 0 & r + \frac{2(1-\alpha-\beta)\lambda\mu^2 PZ}{(\mu^2+P^2)^2} & \frac{(1-\alpha-\beta)\lambda P^2}{\mu^2+P^2} & -\phi - \psi - k \end{bmatrix}$$

evaluated at the steady-state values of N, P, Z and D. The 3×3 submatrix obtained by deleting the fourth column and the fourth row from $\mathbf{A}$, is identical to the Jacobian for the NPZ system, except that the second entry in the first row does not have the term $+r$. This is because the rP term, representing phytoplankton respiration and natural mortality, now enters the detritus compartment before being recycled into nutrient. Note that D does not appear explicitly in $\mathbf{A}$, since it only appears linearly in the model equations (6.1), (6.2), (6.3) and (6.4).

The steady states of the system are obtained by solving the four simultaneous equations

$$0 = -\frac{N}{e+N}\frac{a}{b+cP}P + \frac{\beta\lambda P^2}{\mu^2+P^2}Z + \gamma dZ^2 + \phi D + k(N_0 - N), \tag{6.5}$$

$$0 = \frac{N}{e+N}\frac{a}{b+cP}P - rP - \frac{\lambda P^2}{\mu^2+P^2}Z - (s+k)P, \tag{6.6}$$

$$0 = \frac{\alpha\lambda P^2}{\mu^2+P^2}Z - dZ^2, \tag{6.7}$$

$$0 = rP + (1-\alpha-\beta)\frac{\lambda P^2}{\mu^2+P^2}Z - (\phi+\psi+k)D. \tag{6.8}$$

Considering only the biologically realistic solutions, for which the steady-state values satisfy $N, P, Z, D \geq 0$, we can see from (6.8) that a solution with $D = 0$ must also have $P = Z = 0$. This leads to the steady state $(N_0, 0, 0, 0)$, which is analogous to the $(N_0, 0, 0)$ steady state for the NPZ model. The Jacobian at $(N_0, 0, 0, 0)$ is

$$\mathbf{A} = \begin{bmatrix} -k & -\frac{aN_0}{b(e+N_0)} & 0 & \phi \\ 0 & \frac{aN_0}{b(e+N_0)} - r - s - k & 0 & 0 \\ 0 & 0 & 0 & 0 \\ 0 & r & 0 & -\phi - \psi - k \end{bmatrix}.$$

One eigenvalue is $-k$ (since it is the first term in the first column, and the remaining terms of the first column are zero). The 3×3 submatrix obtained by deleting the first row and the first column is lower triangular, and so the remaining three eigenvalues are the three diagonal terms. Thus, the four eigenvalues are $-k$, Φ, 0 and $-\phi - \psi - k$, where, as for the NPZ model,

$$\Phi = \frac{aN_0}{b(e+N_0)} - r - s - k.$$

The occurrence of a zero eigenvalue means that centre manifold analysis would be required to deduce the stability of $(N_0, 0, 0, 0)$, but numerical simulations suggest that $(N_0, 0, 0, 0)$ is unstable for $\Phi > 0$, and stable for $\Phi < 0$, in agreement with the stability of $(N_0, 0, 0)$ for the NPZ model.

Looking for solutions with $Z = 0$, we have, from (6.8),

$$D = \frac{r}{\phi + \psi + k} P, \tag{6.9}$$

which is then substituted into (6.5) to give, from the sum of (6.5) and (6.6),

$$P = \frac{k(N_0 - N)}{\Sigma + s + k},$$
$$\text{where} \quad \Sigma = \frac{(\psi + k)r}{\phi + \psi + k}.$$

Substituting the expression for P into (6.6), results in the following quadratic equation in N:

$$ckN^2 + \left[\frac{a(\Sigma + s + k)}{r + s + k} - b(\Sigma + s + k) + ck(e - N_0)\right] N - \Big(b(\Sigma + s + k) + ckN_0\Big) e = 0. \tag{6.10}$$

Denoting the solutions of (6.10) by ${N_1}^*$ and ${N_2}^*$, results in the two steady states $({N_1}^*, {P_1}^*, 0, {D_1}^*)$ and $({N_2}^*, {P_2}^*, 0, {D_2}^*)$, where

$$P_i^* = \frac{k(N_0 - N_i^*)}{\Sigma + s + k}, \tag{6.11}$$

$$D_i^* = \frac{r}{\phi + \psi + k} P_i^*, \tag{6.12}$$

for $i = 1, 2$. The constant term of the quadratic (6.10) is negative, and so it has two real roots, one negative and one positive. Defining ${N_1}^*$ to be the positive root and ${N_2}^*$ to be the negative root, it is clear that $({N_2}^*, {P_2}^*, 0, {D_2}^*)$ can never enter the region $\{N, P, Z, D \geq 0\}$, and thus is not considered any further. For the NPZ model, the region $\{N, P, Z \geq 0\}$ of phase space is called the positive octant; for the $NPZD$ model we hereby define the equivalent ecologically realistic region $\{N, P, Z, D \geq 0\}$ to be the 'positive hexadectant', since it is a sixteenth of the entire phase space. Rearranging (6.11) and substituting for N_i^* into (6.6), results in a quadratic in P_i^*. The constant term of this quadratic is a positive multiple of Φ, and since ${P_1}^*$ and ${P_2}^*$ are real and ${P_2}^* > 0$ (this comes from (6.11) because ${N_2}^* < 0$), ${P_1}^*$ must have the same sign as Φ. As $\Phi \to 0$, we have ${P_1}^* \to 0$, ${D_1}^* \to 0$ and ${N_1}^* \to N_0$, i.e. $({N_1}^*, {P_1}^*, 0, {D_1}^*) \to (N_0, 0, 0, 0)$.

This behaviour is clearly analogous to that for both of the three-component models analysed in Chapters 3 and 4, for which we equivalently had $({N_1}^*, {P_1}^*, 0) \to (N_0, 0, 0)$ as $\Phi \to 0$. In fact the only differences between the quadratic equations for N_i^*, namely (3.4) for the three-component model with quadratic zooplankton mortality (the linear mortality case in Chapter 4 is the same) and (6.10) here, is the appearance of Σ in (6.10) and (6.11). Setting $\Sigma = 0$ results in the same values of N_i^* and P_i^* as for the three-component models. This is because the only difference in the dN/dt and dP/dt equations between the NPZ and $NPZD$ models, is that the term $+\phi D$ replaces $+rP$ in the dN/dt equation. In the expression for P_i^*, r does not appear in the denominator for the NPZ models, equation (3.5), because the rP terms cancel when $dN/dt = 0$ and $dP/dt = 0$ are added. For the $NPZD$ model, the addition of $dN/dt = 0$ and $dP/dt = 0$ has a component

$$\phi D - rP = \frac{\phi r}{\phi + \psi + k} P - rP$$

$$\begin{aligned} &= -\frac{(\psi+k)}{\phi+\psi+k} rP \\ &= -\Sigma P, \end{aligned}$$

which is how the definition of Σ originally arises. Now, if $\phi D - rP = 0$, then $\Sigma = 0$. Having $\phi D - rP = 0$ means replacing ϕD by rP in (6.5), resulting in exactly the same $dN/dt = 0$ and $dP/dt = 0$ equations as for the NPZ model. Looking at the food-web diagrams of Figures 2.1 and 6.1 makes it clear to see that if $Z = 0$, and the input to D, namely rP, equals the output ϕD, then the other loss, $(\psi + k)D$ must equal zero, and we could just draw the rP arrow from P straight into N, forgetting about D, which is what we had for the NPZ model. If $\psi + k = 0$ then $\Sigma = 0$, confirming the notion of $\Sigma = 0$ being equivalent to the NPZ model for $Z = 0$ steady states. Note that $\psi + k$ cannot actually equal zero in our model, since all parameters are positive, but having a 'negative sinking rate' of $\psi = -k$, would mean that the remineralisation ϕD is the only loss from the D compartment.

The third row of the Jacobian at $({N_1}^*, {P_1}^*, 0, {D_1}^*)$ is

$$\begin{pmatrix} 0 & 0 & \dfrac{\alpha\lambda {P_1}^{*2}}{\mu^2 + {P_1}^{*2}} & 0 \end{pmatrix}.$$

The third term is thus an eigenvalue, and since it is always positive, for ${P_1}^* \neq 0$, the steady state $({N_1}^*, {P_1}^*, 0, {D_1}^*)$ can never be stable. In Chapter 3, we showed in a similar fashion that the steady state $({N_1}^*, {P_1}^*, 0)$ for the NPZ model with quadratic zooplankton mortality could also never become stable.

We have thus found steady states by setting $D = 0$, and setting $Z = 0$. Setting $N = 0$ results in no steady states with $P, Z, D \geq 0$, as can be seen from (6.5), and setting $P = 0$ gives $Z = D = 0$ from (6.7) and (6.8), and gives us the steady state $(N_0, 0, 0, 0)$. Thus, we now look for solutions (N^*, P^*, Z^*, D^*) with non-zero values of all the variables.

From (6.7) and (6.8) we can express Z and D in terms of P, as

$$Z = \frac{\alpha\lambda P^2}{d(\mu^2 + P^2)}, \tag{6.13}$$

$$D = \frac{1}{\phi+\psi+k}\left(rP + \frac{(1-\alpha-\beta)\alpha\lambda^2 P^4}{d(\mu^2+P^2)^2}\right). \tag{6.14}$$

Adding (6.5) to (6.6) and using (6.7) results in the following expression for N, which is in terms of P when (6.13) and (6.14) are substituted:

$$N = N_0 - \frac{(1-\alpha\gamma-\beta)dZ^2}{k\alpha} + \frac{\phi D}{k} - \frac{(r+s+k)P}{k}. \tag{6.15}$$

Putting all these into (6.6) results, upon rearrangement, in a tenth-order polynomial for P. Writing the polynomial such that the coefficient of P^{10} is one, the constant term of the polynomial is given by Ψ, where

$$\Psi = \frac{bk\mu^8(e+N_0)(\phi+\psi+k)\Phi}{c\left[(s+k)(\phi+\psi+k)+r(\psi+k)\right](r+s+k)}.$$

As for Chapter 3, we see that Ψ is a positive multiple of Φ, and so $\Psi \to 0$ as $\Phi \to 0$, and at $\Phi = 0$, $P = 0$ becomes a solution of the tenth-order polynomial. An (N^*, P^*, Z^*, D^*) solution thus degenerates to $(N_0, 0, 0, 0)$ at $\Phi = 0$, suggesting that, as for the NPZ model, we have a three-way transcritical bifurcation. Setting all of the parameters to their default values, we find only one solution of the form (N^*, P^*, Z^*, D^*) with strictly positive values of all of the variables.

The Jacobian at (N^*, P^*, Z^*, D^*) can be simplified slightly from the general form of $\mathbf{A}$ given earlier, but has too many non-zero terms to make investigation of the eigenvalues feasible.

In Figure 6.2 we show how the three-way transcritical bifurcation occurs. The axes scales are the same as for Figure 3.1 for the NPZ model, and we have an extra figure which shows the value of detritus at the steady states. The extra eigenvalue in the $NPZD$ model remains negative, and so the solid, dotted and dashed lines indicate equivalent stability of the steady states as in Figure 3.1.

The stability of $(N_0, 0, 0, 0)$ is the same as for the NPZ model, as expected from the analysis, with $(N_0, 0, 0, 0)$ unstable for $r < 0.86$, and stable for $r > 0.86$. Recall that $r = 0.86$ is the location of the three-way transcritical bifurcation, given by $\Phi = 0$, but is at a value of r which is much higher than is ecologically realistic.

The behaviour of $({N_1}^*, {P_1}^*, 0, {D_1}^*)$ is similar to that of $({N_1}^*, {P_1}^*, 0)$ for the NPZ model, with $({N_1}^*, {P_1}^*, 0, {D_1}^*)$ leaving the positive hexadectant at the three-way transcritical bifurcation. As r increases, the value of ${P_1}^*$ falls faster for the $NPZD$ model

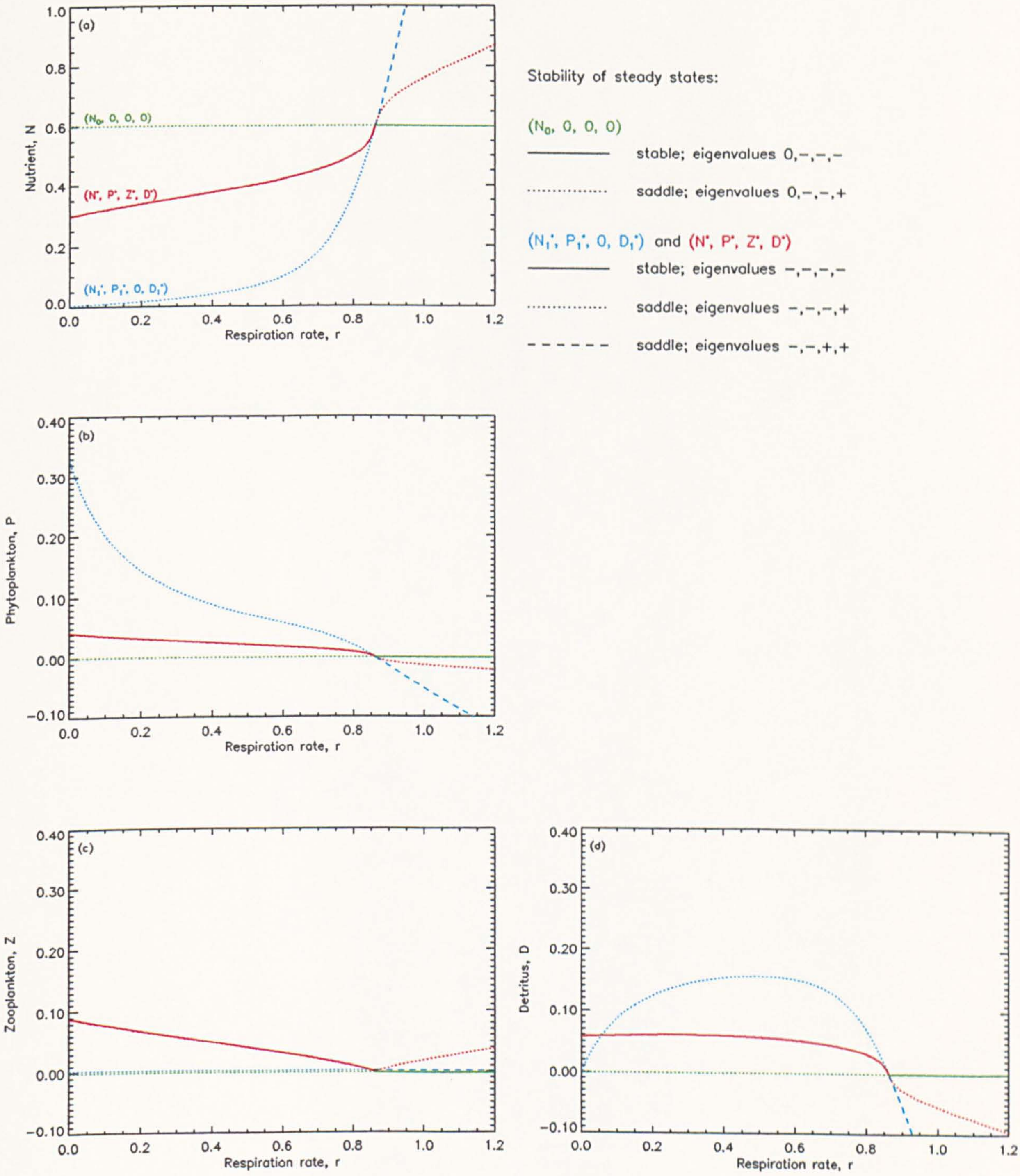

Figure 6.2: Location and stability of the steady states $(N_0, 0, 0, 0)$, $(N_1{}^*, P_1{}^*, 0, D_1{}^*)$ and (N^*, P^*, Z^*, D^*) as r is varied. The key indicates the signs of the real parts of the four eigenvalues, plus the corresponding stabilities. The three-way transcritical bifurcation occurs at $r = 0.86$.

than for the NPZ model. The value of ${D_1}^*$ increases with r, and then falls to zero as the bifurcation is reached. This differing behaviour of ${P_1}^*$ is to be expected. Although the steady states $({N_1}^*, {P_1}^*, 0, {D_1}^*)$ and $({N_1}^*, {P_1}^*, 0)$ are never stable in their full systems, analysing their nature is still insightful. If we restrict ourselves to considering $Z = 0$, then we can just think of the NPZ and $NPZD$ systems as respectively being an NP system and an NPD system. The corresponding steady state given by $({N_1}^*, {P_1}^*)$ is stable in the NP system, (since the two-dimensional stable manifold of $({N_1}^*, {P_1}^*, 0)$ for the NPZ system lies in the $Z = 0$ plane), at least when the two eigenvalues have negative real parts; this is true for $r < 0.86$, as indicated by the fact that the blue line is dotted, rather than dashed, in this region in Figure 3.1. Since $({N_1}^*, {P_1}^*, 0)$ and $({N_1}^*, {P_1}^*, 0, {D_1}^*)$ are stable in the respective plane and hyperplane given by $Z = 0$, it is worth commenting on their quantitative nature. The introduction of the detritus compartment delays the regeneration of natural mortality and respiration of phytoplankton, rP, as can be seen by ignoring the Z compartment and corresponding arrows in Figure 6.1. The equivalent steady state $({N_1}^*, {P_1}^*, {D_1}^*)$ in the NPD system is also stable for $r < 0.86$, and, as expected, the value of ${P_1}^*$ is higher for the NP model than for the NPD model.

The steady state (N^*, P^*, Z^*, D^*) behaves in the same qualitative way as (N^*, P^*, Z^*) for the NPZ model, being stable for $r < 0.86$, and leaving the positive hexadectant at the three-way transcritical bifurcation. Figure 6.2 shows that P^* and D^* become negative at the bifurcation. Quantitatively, P^* and Z^* are very similar to P^* and Z^* for the NPZ model, and N^* approaches the bifurcation in a slightly different way than for the NPZ model. D^* remains fairly constant as r is increased, until the bifurcation is approached. D^* is expressed, in (6.14), as an increasing function of P^*. However, r also appears in (6.14), which explains why D^* may remain constant despite the fact that P^* is decreasing. The decrease in P^* is offset by the increase in r, until we are close to the bifurcation.

6.4 Time series and phase portraits

In Figure 6.3(a) we show the time series of the system from the initial condition $(N, P, Z, D) = (0.4, 0.1, 0.05, 0.08)$, with all of the parameters fixed at their default values. The three-dimensional picture shows the N, P and Z values of the trajectory, for comparison with the NPZ model. This picture is the projection onto $N-P-Z$ space of the full trajectory, which exists in four-dimensional $N-P-Z-D$ space; plotting the fourth dimension on the same picture is obviously unfeasible. The N, P and Z initial condition values are the same as for the NPZ model, and the D value is chosen arbitrarily. The system settles down to steady-state values of $(N, P, Z, D) = (0.33, 0.034, 0.072, 0.060)$; starting from a variety of other initial conditions it does likewise. This steady state is the unique steady state with $N, P, Z, D > 0$, which we know by setting the parameters to their default values and solving the tenth-order polynomial for P^*, plus (6.13), (6.14) and (6.15), as derived in the preceding analysis. The default steady-state of the NPZ model is $(N, P, Z) = (0.31, 0.034, 0.072)$, and so, to two significant figures, the P and Z values for the $NPZD$ model are the same, and the N value is marginally higher.

Figure 6.3(b) shows that when d, the higher predation on zooplankton, is increased to 1.5, the system is attracted onto a limit cycle. This is what happened for the NPZ model, and the period of the oscillations is 34 days, virtually the same as the 35-day period of the NPZ model. It is seen that the peaks and troughs of D lag slightly behind those of P. The amplitudes of the cycles for the two models are more easily compared by using the one-parameter bifurcation diagrams which we now construct in Section 6.5.

6.5 One-parameter bifurcation behaviour

Figure 6.4 shows that the behaviour of the system as d is varied is very similar to that for the NPZ model. Supercritical Hopf bifurcations A and B occur at $d = 1.43$ and $d = 1.84$ respectively, compared with $d = 1.42$ and $d = 1.91$ for the NPZ model.

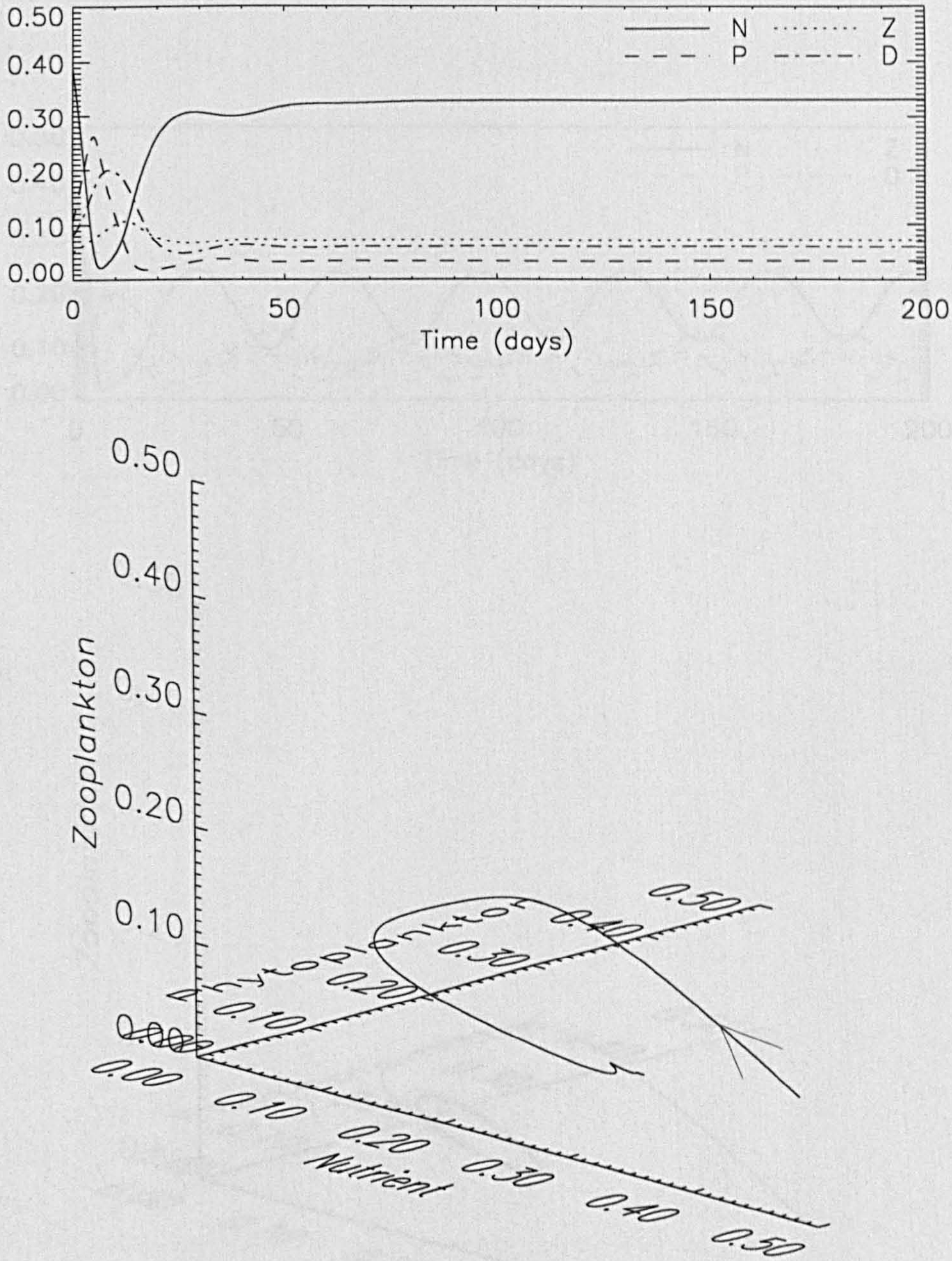

(a) $d = 1.0$ - N, P, Z and D settle down to steady-state values.

Figure 6.3: The time series and trajectory at (a) $d = 1.0$ and (b) $d = 1.5$ (next page), with all of the other parameters fixed at their default values. The trajectory is shown as the NPZ projection of the full $NPZD$ phase space for comparison with the three-component model.

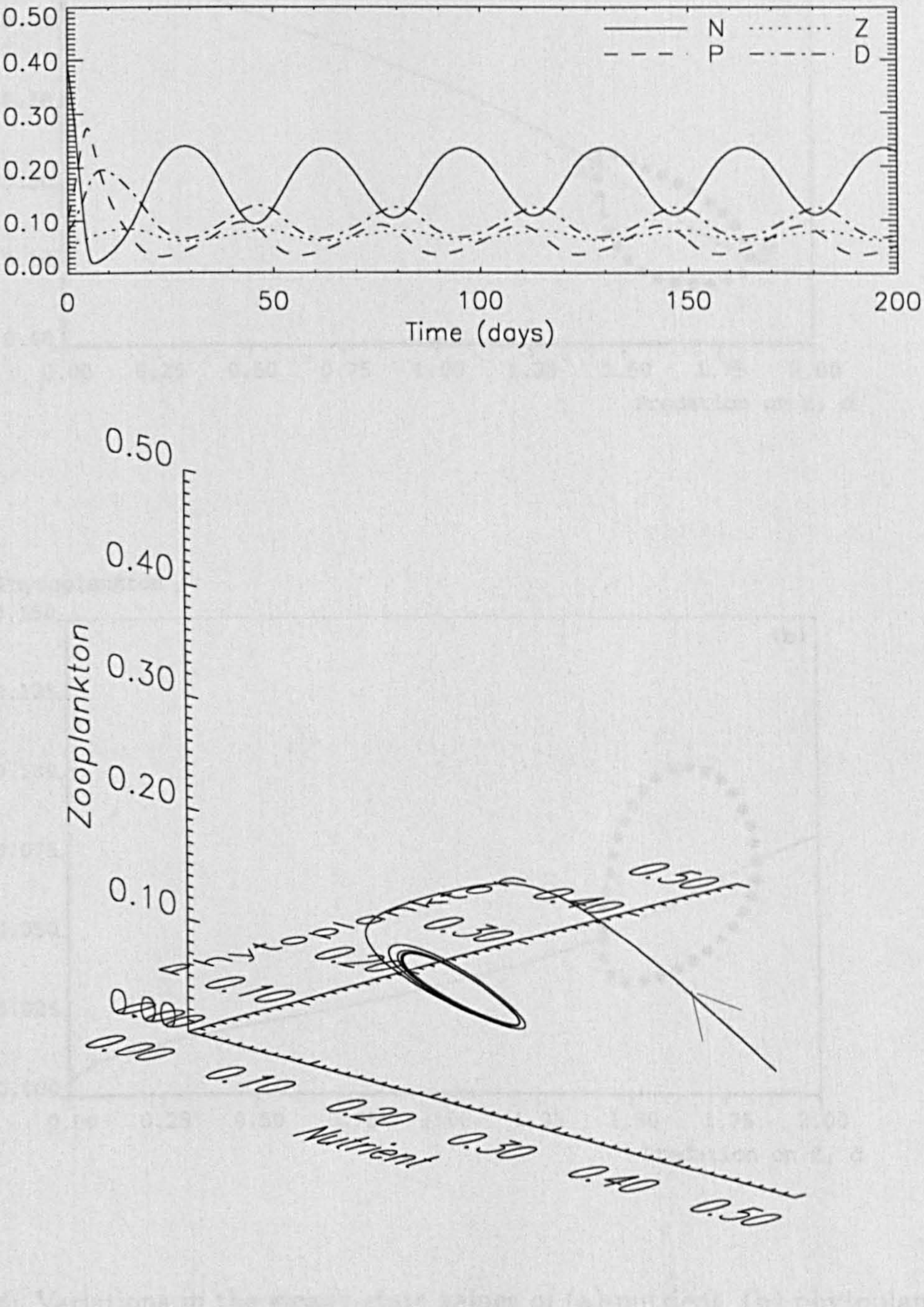

(b) $d = 1.5$ - the system settles down to a stable limit cycle.

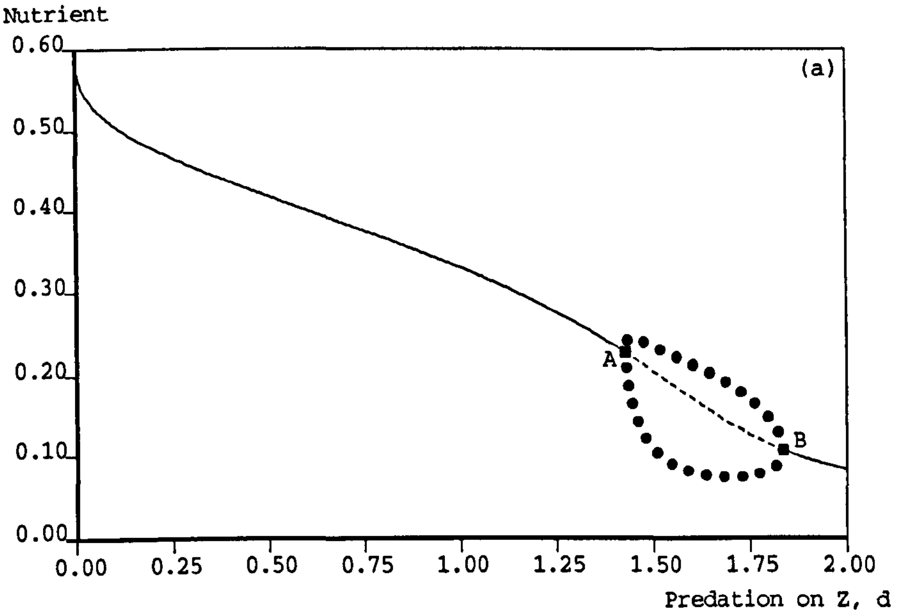

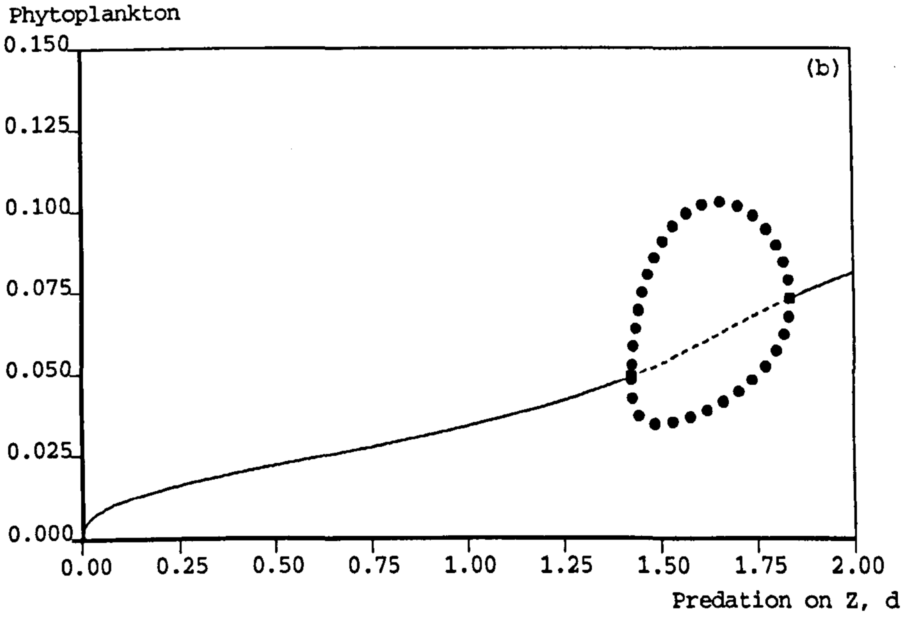

Figure 6.4: Variations in the steady-state values of (a) nutrient, (b) phytoplankton, (c) zooplankton and (d) detritus as d, the higher predation on the zooplankton, is changed. A solid line is a stable steady state, a dashed line is an unstable steady state, a solid square is a Hopf bifurcation and solid circles indicate the maximum and minimum values of the stable limit cycles. The Hopf bifurcations are labelled A and B.

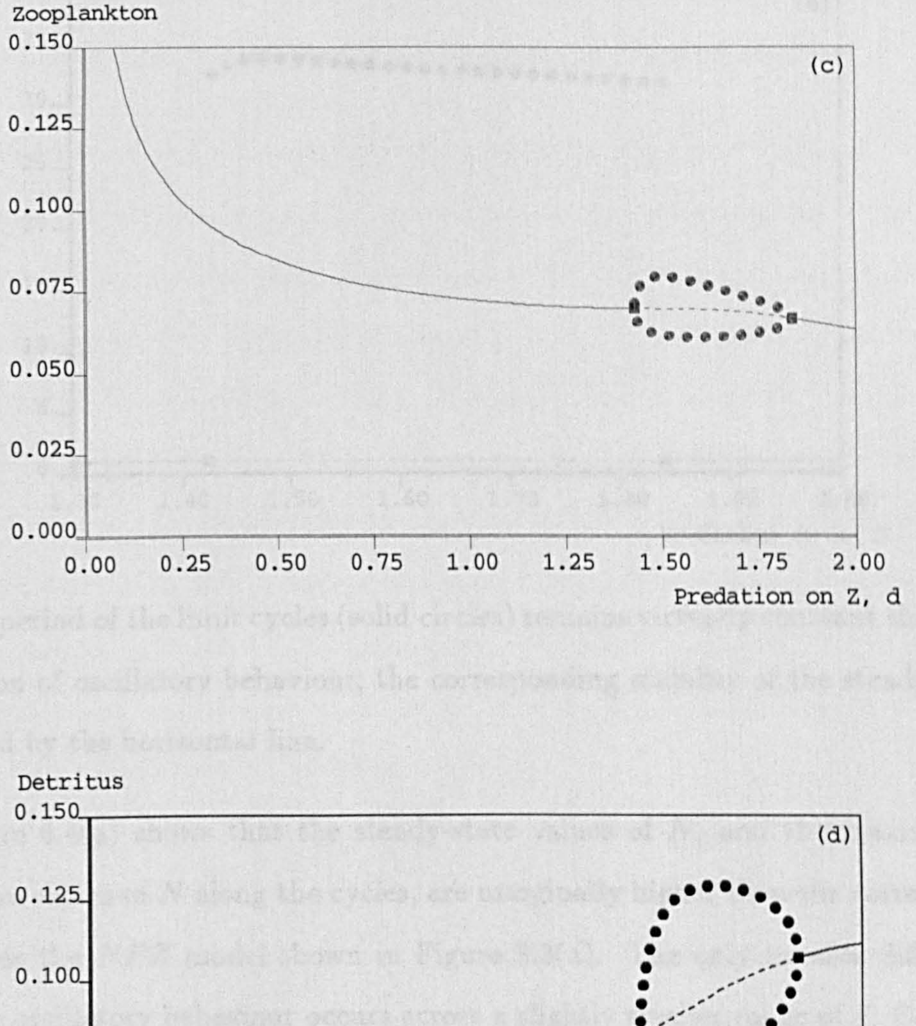

(c) The zooplankton bifurcation diagram. (d) The detritus steady-state and limit cycle values correlate to the phytoplankton values.

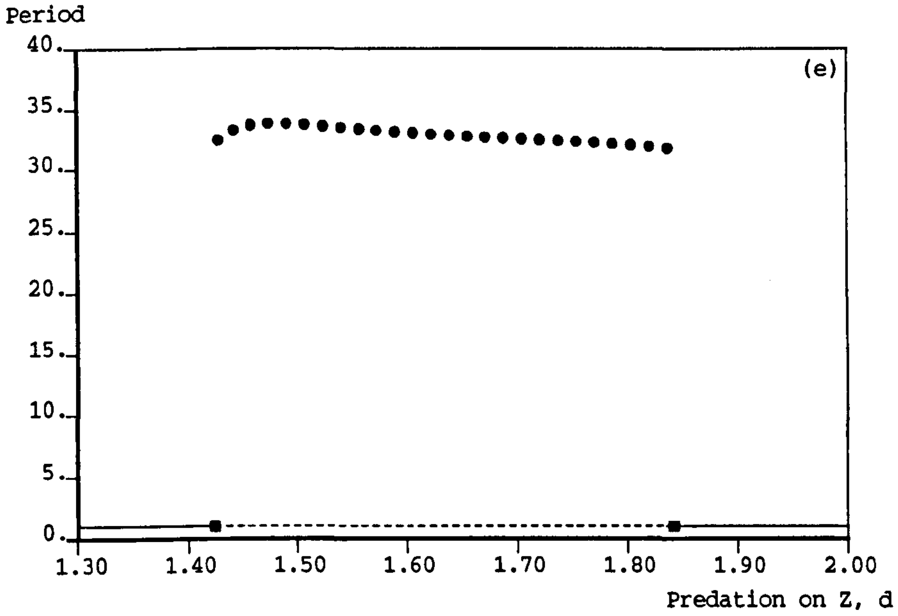

(e) The period of the limit cycles (solid circles) remains virtually constant throughout the region of oscillatory behaviour; the corresponding stability of the steady state is indicated by the horizontal line.

Figure 6.4(a) shows that the steady-state values of N, and the maximum and minimum values of N along the cycles, are marginally higher than the corresponding values for the NPZ model shown in Figure 3.3(a). The only notable difference is that the oscillatory behaviour occurs across a slightly smaller range of d. Comparing Figures 6.4(b) and 3.3(b), we see that the P steady-state values are virtually identical, but that the oscillations in the $NPZD$ model do not reach as high or as low P values as the oscillations in the NPZ model. The Z bifurcation diagrams, Figures 6.4(c) and 3.3(c), are practically identical, with the amplitude of Z in the $NPZD$ model being slightly smaller than that in the NPZ model.

For the $NPZD$ model we have an extra diagram, that of D against d, Figure 6.4(d). This shows that values of D are correlated with the P values. This would be expected, since as d increases, P steady-state values increase, whilst Z steady-state values remain fairly constant, and so both inputs to the D compartment increase as d increases. The amplitudes of the D cycles are comparable to those of the P cycles.

The period of the oscillations remains fairly insensitive to the value of d, as shown in Figure 6.4(e), taking slightly lower values than for the NPZ model.

6.6 Two-parameter bifurcation behaviour

In Figure 6.5 we plot the two-parameter bifurcation diagrams, which show how the Hopf bifurcations move as each of the parameters is independently varied. The axes have the same scales as in Figure 3.4 for the NPZ model, and there are two extra diagrams, namely Figures 6.5(m) and (n), for the two extra parameters ϕ and ψ which appear in the $NPZD$ model. The key is the same as for the NPZ model - the nature of (N^*, P^*, Z^*, D^*), as demonstrated in Figure 6.4, is represented as a horizontal line at the default value of each parameter, a solid line indicates that the steady state is stable, and a dashed line that it is unstable. The non-horizontal lines show the locations of the Hopf bifurcations, with solid lines indicating supercritical Hopf bifurcations, and dashed lines indicating subcritical. The curves of long dashes indicate fold bifurcations of the steady state.

The striking conclusion of Figure 6.5 is that the overall bifurcational picture presented by Figure 3.4 for the NPZ model, is remarkably preserved in the $NPZD$ model. The addition of the detritus equation to the NPZ system appears to make very little difference to the location in parameter space of the Hopf and fold bifurcations. Certainly, the differences we found in Chapter 4 were far more significant, implying that changing the zooplankton mortality term from quadratic to linear has more of an effect on the dynamical behaviour of the system than adding the detritus equation to the NPZ model. The addition of the detritus equation introduces an extra eigenvalue to the story, but, despite its potential to alter the behaviour of the system, this eigenvalue apparently does not cause any extra bifurcations - it seems to remain negative and not pass through zero. For each diagram in turn, we have searched for further bifurcations of the steady state. This was done for each parameter by setting $d = 1.0$ and increasing and decreasing the parameter across its full range, and then repeating this at a low and a high value of d. Then the parameter

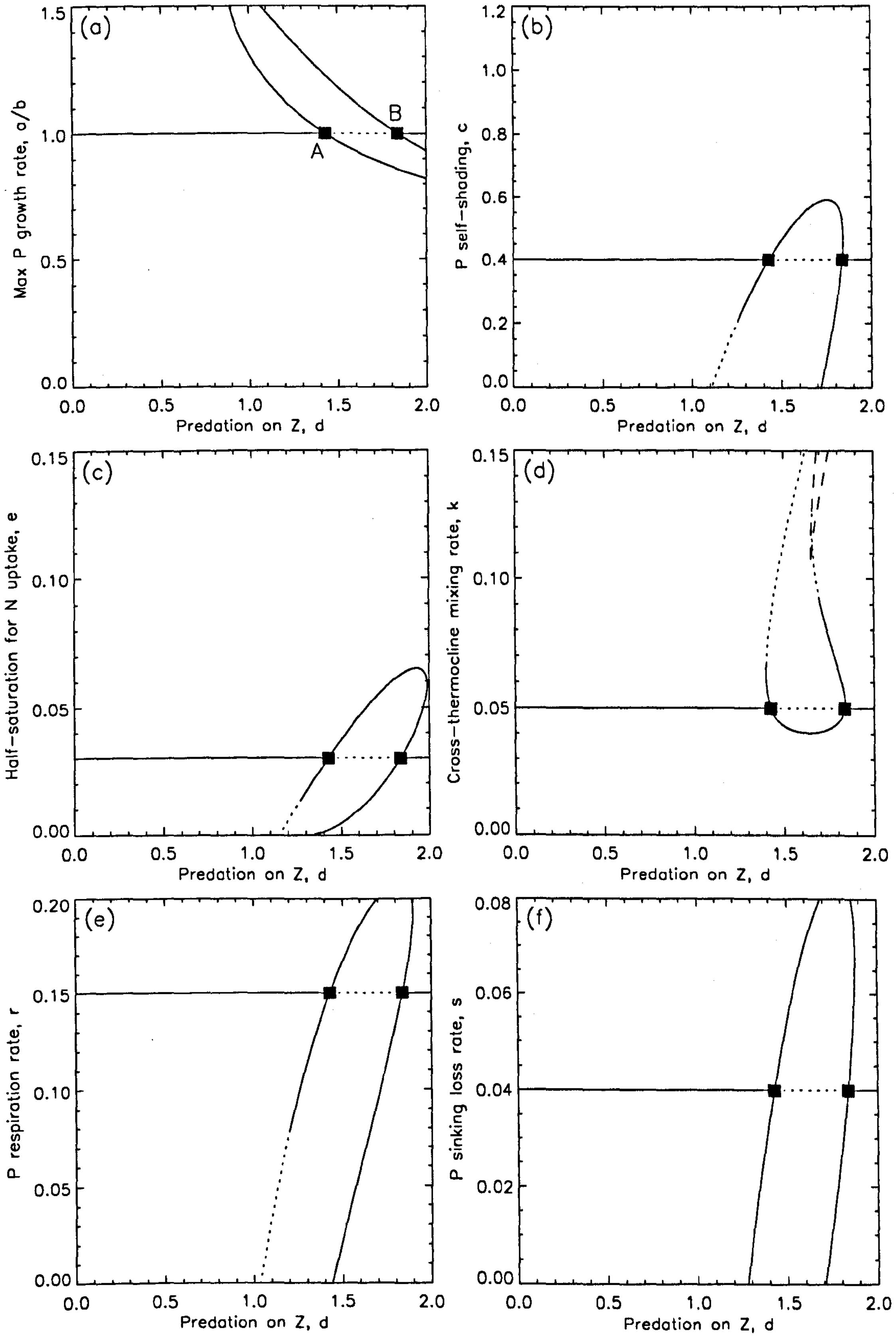

Figure 6.5: Two-parameter bifurcation diagrams showing how the positions of the Hopf bifurcations in Figure 6.4 change as each other parameter, together with d, is independently varied from its default value. The steady-state stabilities from Figure 6.4 are shown as a horizontal line at each default parameter value. Hopf A and (ctd.)

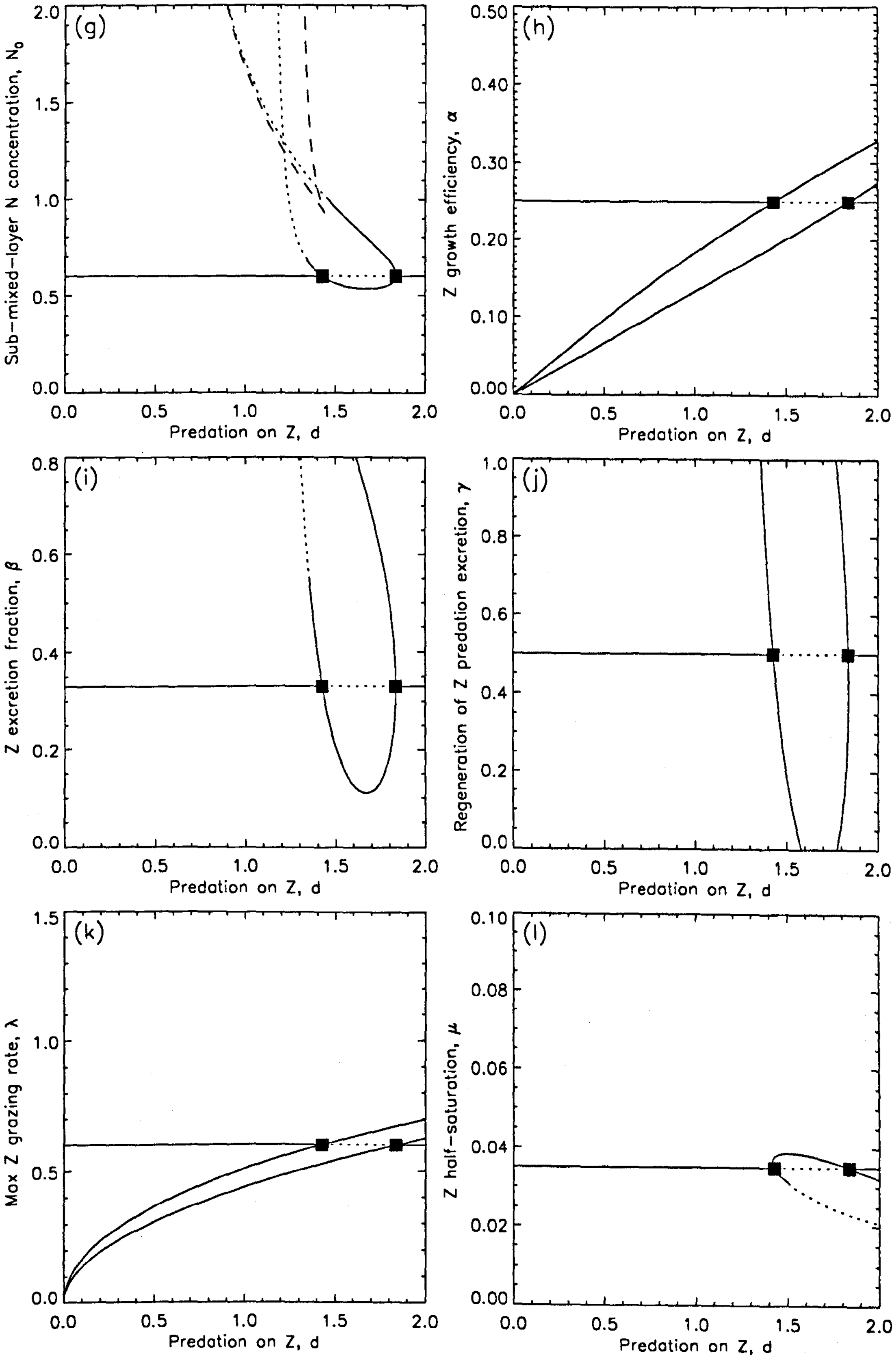

Hopf B are indicated in (a). Non-horizontal solid curves starting from the original Hopf bifurcations (the squares) indicate supercritical Hopf bifurcations, and non-horizontal curves of short dashes show where Hopf bifurcations are subcritical. In (d) and (g), curves of long dashes indicate fold bifurcations of the steady state. (ctd.)

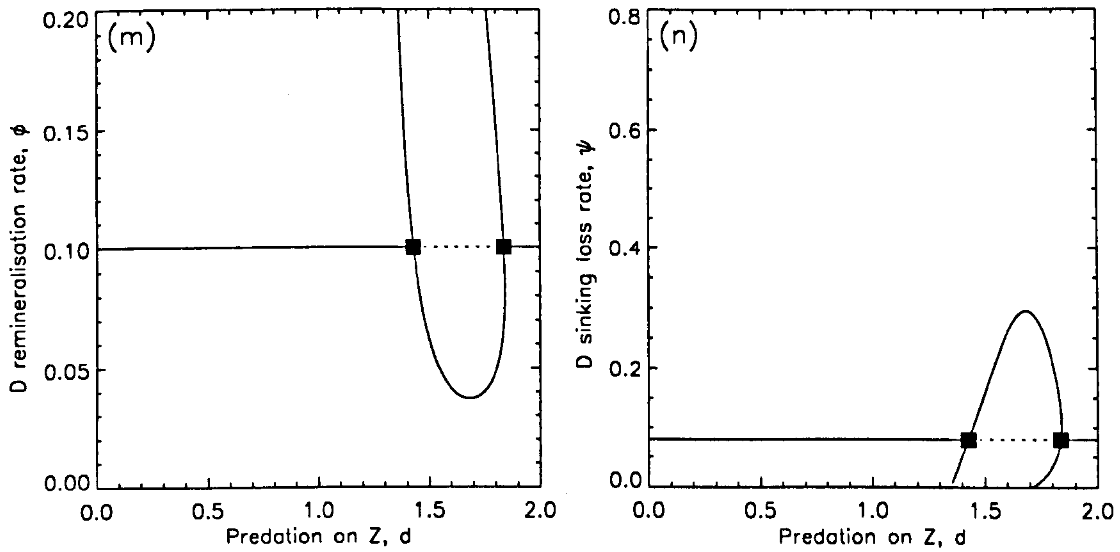

Diagrams (m) and (n) correspond to the two parameters ϕ and ψ which do not occur in the *NPZ* model.

was fixed at a high then a low value, and d varied across its range. No other bifurcations were found, implying that the Hopf and fold bifurcations plotted are the only bifurcations occurring in the realistic region of parameter space.

For the two extra parameters, Figure 6.5(m) shows that oscillations occur across most of the range of the detritus remineralisation rate ϕ, and Figure 6.5(n) shows that oscillations occur only at the lower values of the detritus sinking rate ψ.

Figure 6.5(i), for β, does not show any fold bifurcations of the steady state, unlike for the *NPZ* model. The fold bifurcations do actually still exist, but they terminate at a cusp point at $\beta = 0.86$, outside the range plotted. Note that such a high value of β is ecologically unrealistic, since it gives $\alpha + \beta > 1$, violating conditions on the definitions of α and β (they must sum to less than one).

For N_0 the Bogdanov-Takens bifurcation which occurs for the *NPZ* model and was discussed in Section 3.8 still occurs, but at the value of $N_0 = 2.54$, which is above the plotted range of N_0 in Figure 6.5(g). For the *NPZ* model a Bogdanov-Takens bifurcation occurs as k is varied, at the value $k = 0.11$. For the *NPZD* model the bifurcation occurs at the higher value of $k = 0.13$, where the dotted curve representing

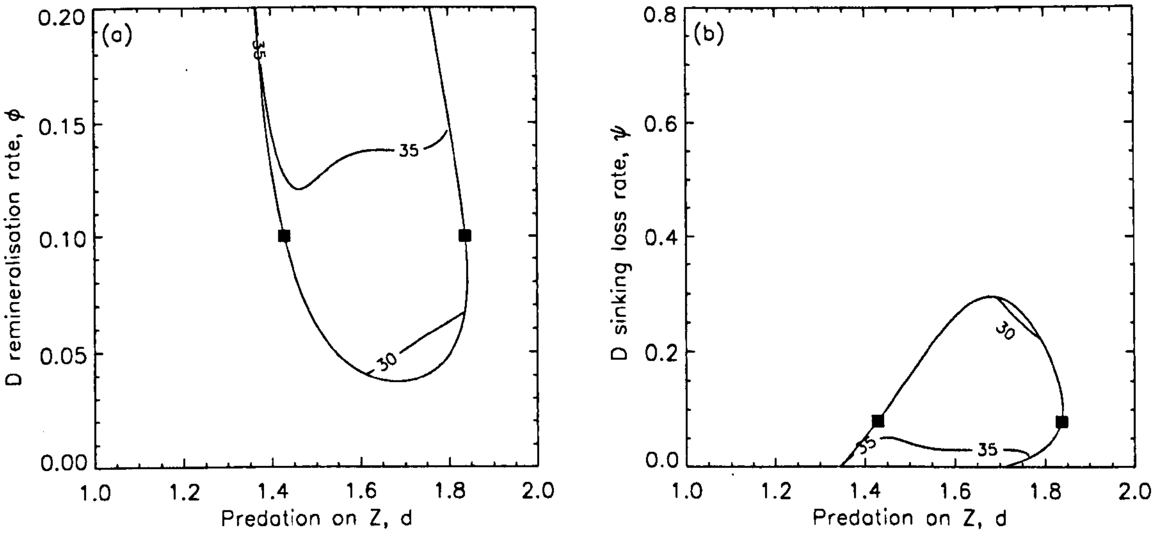

Figure 6.6: The two period-contour diagrams for the two parameters ϕ and ψ which do not occur in the *NPZ* model. The period is not greatly affected by changes in ϕ and ψ.

subcritical Hopf bifurcation B terminates on the curve of fold bifurcations in Figure 6.5(d).

6.7 Dependence of the period of oscillations on the parameter values

In Figure 6.6 we plot the contour diagrams of constant period, for the two parameters that appear in the *NPZD* model but not in the *NPZ* model. We see that the period can range from just below 30 days to values which are less than 40 days, as ϕ or ψ are varied (the 40-day contour lies above the realistic range of ϕ). Thus, the values of ϕ and ψ do not greatly affect the period of the oscillations. Simulations of a different *NPZD* model formulated by Ken Denman (Institute of Ocean Sciences, British Columbia, personal communication), also exhibit oscillations which show a decrease in period as ψ increases, in agreement with Figure 6.6(b).

No bifurcations of the limit cycles were found along the contours, despite the presence of an extra Floquet multiplier, compared to the NPZ model.

We have investigated whether or not the effect on the period of varying each of the other 12 parameters is the same as for the NPZ model. To do this we used, as a starting point, the limit cycle that occurs for $d = 1.6$ with all of the other parameters set to their default values - this cycle has a period of 33.1 days. For parameter c, as an example, we kept d fixed at 1.6 and tracked the branch of limit cycles as c increases, until the edge of the oscillatory region, defined by the Hopf bifurcations in Figure 6.5(b), was reached. We found that as c increases, the period of the oscillations increases. This agrees with Figure 3.7(b) which showed that for the NPZ model the period increases as c increases. Similarly, decreasing c leads to a decrease in the period for the $NPZD$ model, also in agreement with the NPZ model.

This process was repeated for each parameter in turn. For e, and most of the other parameters, we had to criss-cross the oscillatory region, given by Figure 6.5(c), to fully investigate the behaviour of the period. At the top-right corner of the oscillatory region for e (high values of d) the period is 35 days - a 35-day contour was actually computed, and it just cuts across the corner in question. A 33-day contour starts at $e \simeq 0.04$ on the Hopf curve close to the default value of Hopf B, and runs down towards $d \simeq 1.3$ at $e = 0$. So it appears that the period tends to be slightly higher at high values of e. This agrees with Figure 3.7(c) for the NPZ model, but the changes in period are much smaller in magnitude. The situation for s was slightly inconclusive, with the period remaining roughly between 32 and 34 days throughout the oscillatory region - for the NPZ model the 40-day contour only just crept in at low values of d, also indicating little variation in the period as s varies.

However, for the remaining parameters the period does change fairly conclusively in the same manner as for the NPZ model, as given by the contour diagrams in Figure 3.7. Even when the actual region of oscillations is fairly narrow, as in Figures 6.5(h) and (k) for α and λ, by criss-crossing the region we have found the period variations to agree with those for the NPZ model. In general the period remains within a narrower range for the $NPZD$ model than for the NPZ model, as explained for s.

Finally, we mention that for $\beta = 0.75$, the maximum allowed value of β (so that $\alpha + \beta = 1$), the period remains below 50 days across the range of d, whereas Figure 3.7(i) shows that the period reaches much higher values for the NPZ model at this value. However, these high values are explained in terms of homoclinic behaviour which, as for k and N_0, arises from a Bogdanov-Takens bifurcation. For the NPZ model such a bifurcation occurs at the ecologically unrealistic value of $\beta = 0.96$. But the cusp of fold bifurcations in the $NPZD$ model occurs at $\beta = 0.86$, much higher than for the NPZ model, and the Bogdanov-Takens bifurcation has been shifted all the way up to $\beta = 1.85$ (this value is even more unrealistic, since β by definition must be a fraction no greater than one). Thus, for the $NPZD$ model, the homoclinic behaviour associated with the Bogdanov-Takens bifurcation has been shifted to a high value of β, and consequently so has the region of high periods. This explains why the period has not yet attained 50 days when we reach $\beta = 0.75$ in the $NPZD$ model.

During this process of tracing limit cycles, no bifurcations of limit cycles were found, except for the fold bifurcations which must occur when a Hopf bifurcation is subcritical. So, as for the NPZ model, no period-doubling bifurcations or Naimark-Sacker bifurcations were found anywhere within the oscillatory regions.

6.8 Discussion

The clear conclusion from this chapter is that the explicit addition of detritus to the NPZ model investigated in Chapter 3 does not significantly affect the nature of the bifurcations. The analysis of the steady states in Section 6.3 shows that the three-way transcritical bifurcation is preserved. The subsequent numerical investigation involving computation of time series, one- and two-parameter bifurcation diagrams and period-contour diagrams, demonstrates that the general bifurcational structure of the NPZ model is retained.

This implies that if an ecosystem is considered to be expressed by the food web shown in Figure 6.1, and knowledge of the actual level of detritus is not explicitly required, then the dynamics of the food web may be modelled by considering just the NPZ system.

With hindsight it may be unsurprising that the addition of the detritus compartment to the NPZ model does not greatly affect the dynamics, because D only appears linearly in the equations for the model. However, it would not be possible to have predicted, *a priori*, that this should be the case. Rather, once the investigation has been performed, the fact that D only appears linearly in the equations offers a plausible explanation for the unaltered dynamics.

Chapter 7

Consequences of zooplankton grazing on both detritus and phytoplankton

7.1 Introduction

We now modify the *NPZD* model investigated in Chapter 6 to allow zooplankton to graze on detritus in addition to phytoplankton. This is a feature of the seven-component models of Fasham *et al.* (1990) and Fasham (1993), but is not considered in the six-component model of Fasham (1995) or the Hood and Olson *NPZD* model in Davis and Steele (1994).

In Section 7.2 we formulate the multiple-grazing model. This adds extra interactions to the food web, and requires modifying the zooplankton grazing function of the previous *NPZD* model to incorporate consumption of the two alternative food sources, phytoplankton and detritus. In Section 7.3 we proceed analytically, but find that explicitly calculating a positive steady state of the form (N^*, P^*, Z^*, D^*) is even more difficult than in Chapter 6, for which an intractable tenth-order polynomial for P^* was obtained. However, the numerically-computed colour bifurcation diagrams of Figure 7.2 show that the three-way transcritical bifurcation still occurs. The time series of Section 7.4, together with the one-parameter diagrams of Section 7.5, show oscillations to occur, but not at exactly the same values of d as for the previous $NPZD$ model, and with longer periods. In Section 7.6 we show how the oscillations persist as each parameter is independently varied, and in Section 7.7 we investigate the changes in the periods of the oscillations.

7.2 Model formulation

Allowing zooplankton to graze on detritus adds some extra pathways to the food-web picture, and requires a new formulation of zooplankton grazing. Fasham *et al.* (1990), and consequently Fasham (1993), modelled zooplankton grazing on three food types, namely phytoplankton, detritus and bacteria. The grazing formulation used by Fasham *et al.* (1990) was derived from a Holling type II grazing term which depended on a measure of the total available food. The formulation included feeding preferences of the zooplankton for the alternative foods. Fasham *et al.* (1990), hereafter denoted FDM, firstly ran their model with constant values for the feeding preferences, as used by Evans (1988) who called them 'palatabilities' of the zooplankton, but found the model results to be very sensitive to the choice of values. Very little data is available on such preferences, and so FDM adapted the preferences to vary dynamically depending on the total available food. The preferences vary so that zooplankton actively select the most abundant food (Hutson, 1984). Upon rearrangement the final form for zooplankton grazing on phytoplankton is

$$G_P = \frac{\lambda p_1 P^2 Z}{K(p_1 P + p_2 D) + p_1 P^2 + p_2 D^2}, \tag{7.1}$$

where λ is the maximum specific grazing rate, K is a half-saturation constant, and p_1 and p_2 are assumed nominal preferences (palatabilities) for phytoplankton and detritus when the concentrations of these foods are equal. (We have omitted the reference to bacteria that appears in the FDM function for G_P, since we do not explicitly model bacteria, and to include it here would unnecessarily complicate matters). Note that p_1 and p_2 are constant parameters - the aforementioned dynamically-varying preferences are defined in terms of p_1, p_2, P and D, and have been substituted for. A similar expression is obtained for zooplankton grazing on detritus, with p_2D^2 replacing p_1P^2 in the numerator of (7.1).

Although (7.1) looks similar to a Holling type III function, which is what our previous *NPZD* model has, it has been derived from a type II function. Setting $p_2 = 0$ so that zooplankton have no appetite for detritus whatsoever, or $D = 0$ so that there is no detritus available for consumption, it is seen that G_P reduces to a Holling type II function. For our model, it would be desirable for a formulation of G_P to reduce to a Holling type III function under such circumstances, since our previous *NPZD* model uses the type III function.

Rather than use the above formulation of G_P, Mike Fasham (personal communication) suggested the simpler form

$$G_P = \frac{\lambda p_1 P^2 Z}{K^2 + p_1P^2 + p_2D^2}, \tag{7.2}$$

where K is a constant. It is clear that

$$G_P \to \frac{\lambda p_1 P^2 Z}{K^2 + p_1P^2} \qquad \text{as } p_2 \to 0 \text{ or } D \to 0,$$

and we can make this limit of G_P equal to the function G_1 of the previous *NPZD* model, namely

$$\frac{\lambda P^2 Z}{\mu^2 + P^2}, \tag{7.3}$$

by defining $K^2 = p_1\mu^2$. This then results in the following grazing functions on phytoplankton, G_1, and on detritus, G_2:

$$G_1 = \frac{\lambda p_1 P^2 Z}{p_1\mu^2 + p_1P^2 + p_2D^2},$$
$$G_2 = \frac{\lambda p_2 D^2 Z}{p_1\mu^2 + p_1P^2 + p_2D^2}.$$

By dividing through by p_1 and defining

$$\omega = \frac{p_2}{p_1}$$

as the relative zooplankton palatability for detritus compared to phytoplankton, we obtain the final grazing functions

$$G_1 = \frac{\lambda P^2 Z}{\mu^2 + P^2 + \omega D^2},$$

$$G_2 = \frac{\lambda \omega D^2 Z}{\mu^2 + P^2 + \omega D^2}.$$

Setting $\omega = 0$ corresponds to $p_2 = 0$, meaning that zooplankton do not find detritus palatable at all, which corresponds to the previous $NPZD$ model studied in Chapter 6, whereby G_1 is given by (7.3) and $G_2 = 0$.

The multiple-grazing by zooplankton results in the new food web shown in Figure 7.1. Allowing zooplankton to graze on detritus creates the extra pathway from D to Z, plus the resulting recyclings of excretion into N, given by βG_2, and of faecal pellets back into D, $(1-\alpha-\beta)G_2$. The remainder of the food web is the same as for the $NPZD$ model in Chapter 6, except for the dependence of G_1 on D.

The resulting equations for the model are:

$$\begin{aligned}
\frac{dN}{dt} &= -\text{uptake} + Z \text{ excretion} + Z \text{ predation excretion} + D \text{ remineralisation} + \text{mixing},\\
\frac{dP}{dt} &= \text{uptake} - \text{respiration} - \text{grazing by } Z - \text{sinking} - \text{mixing},\\
\frac{dZ}{dt} &= \text{growth} - \text{higher predation},\\
\frac{dD}{dt} &= P \text{ respiration} + Z \text{ faecal pellets} - \text{grazing by } Z - \text{remineralisation}\\
&\qquad - \text{sinking} - \text{mixing}.
\end{aligned}$$

The specific functional forms used are:

$$\begin{aligned}
\frac{dN}{dt} &= -\frac{N}{e+N}\frac{a}{b+cP}P + \frac{\beta\lambda(P^2+\omega D^2)Z}{\mu^2+P^2+\omega D^2} + \gamma d Z^2 + \phi D + k(N_0 - N), &(7.4)\\
\frac{dP}{dt} &= \frac{N}{e+N}\frac{a}{b+cP}P - rP - \frac{\lambda P^2 Z}{\mu^2+P^2+\omega D^2} - (s+k)P, &(7.5)\\
\frac{dZ}{dt} &= \frac{\alpha\lambda(P^2+\omega D^2)Z}{\mu^2+P^2+\omega D^2} - dZ^2, &(7.6)\\
\frac{dD}{dt} &= rP + \frac{\left[(1-\alpha-\beta)P^2 - (\alpha+\beta)\omega D^2\right]\lambda Z}{\mu^2+P^2+\omega D^2} - (\phi+\psi+k)D. &(7.7)
\end{aligned}$$

The $(1-\alpha-\beta)P^2$ term in the numerator of the second term of (7.7) represents zooplankton faecal pellets which are the result of feeding on phytoplankton, as for the $NPZD$ model. The $-(\alpha+\beta)\omega D^2$ term represents the net loss of detritus due to zooplankton feeding on detritus – detritus is lost due to zooplankton grazing by an amount G_2, where $G_2 = \lambda\omega D^2 Z/(\mu^2+P^2+\omega D^2)$, but an amount $(1-\alpha-\beta)G_2$ is then

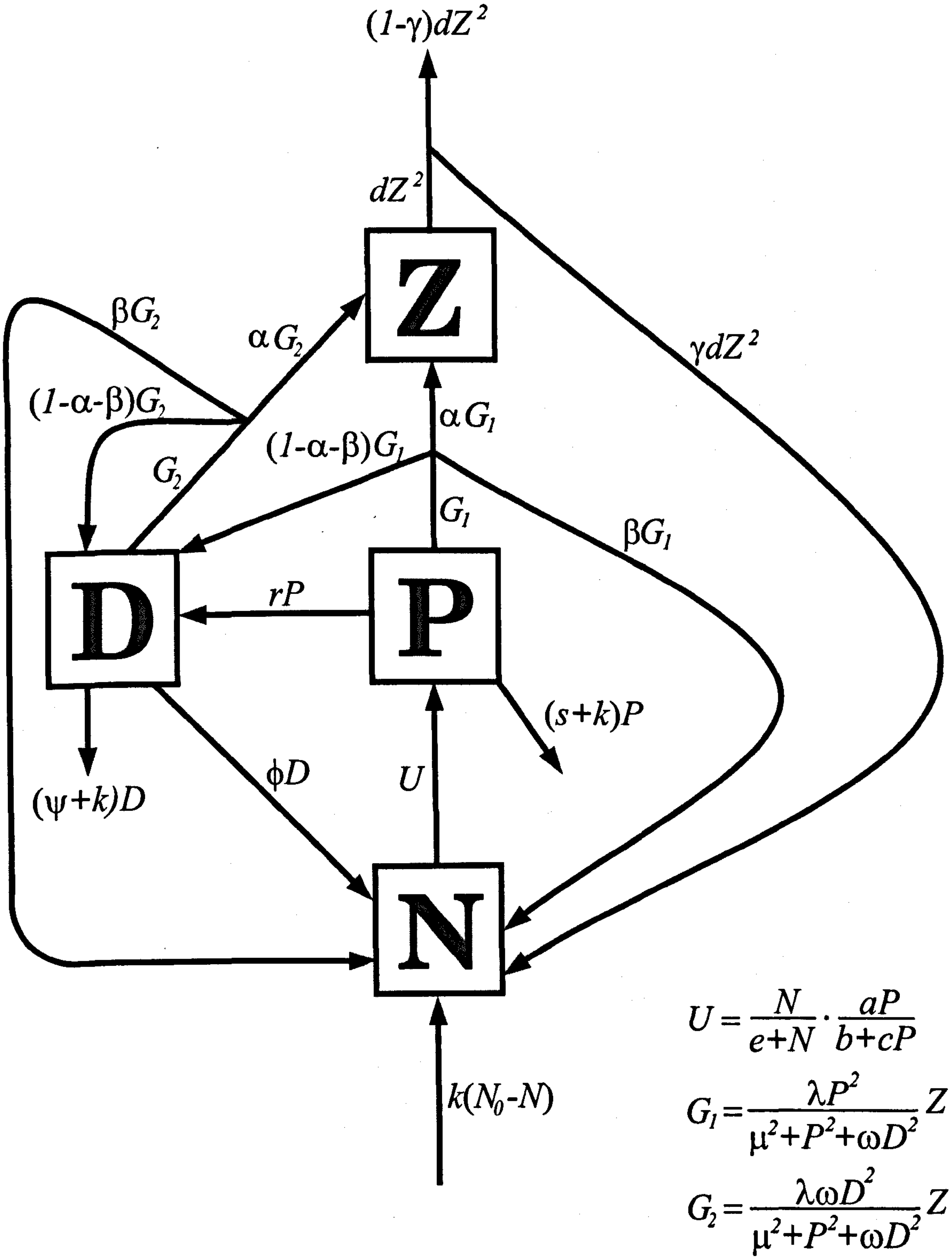

$$U = \frac{N}{e+N} \cdot \frac{aP}{b+cP}$$

$$G_1 = \frac{\lambda P^2}{\mu^2+P^2+\omega D^2} Z$$

$$G_2 = \frac{\lambda \omega D^2}{\mu^2+P^2+\omega D^2} Z$$

Figure 7.1: Zooplankton now graze on detritus in addition to phytoplankton, represented by G_2. As with grazing on phytoplankton, a proportion α fuels zooplankton growth, β is excreted and $(1 - \alpha - \beta)$ is returned to detritus as faecal pellets. The grazing-on-phytoplankton function, G_1, now depends on D as well as P and Z.

returned to detritus as faecal pellets, giving the net result of $-G_2 + (1-\alpha-\beta)G_2 = -(\alpha+\beta)G_2$. Setting $\omega = 0$ means that the preference of zooplankton for detritus is zero, which gives us the previous $NPZD$ model.

The incorporation of multiple zooplankton grazing into the model only adds one extra parameter, ω, to the system. Fasham (1993) had zooplankton grazing on phytoplankton, detritus and bacteria, for which the respective nominal preference values used were $p_1 = 0.5, p_2 = 0.25$ and $p_3 = 0.25$, (FDM did not state any values). Since $\omega = p_2/p_1$, we use Fasham's values to give a default value of $\omega = 0.5$. The zooplankton palatability for phytoplankton is therefore assumed to be twice that for detritus. We take a range of $\omega \in [0,2]$, so that the maximum value gives the converse situation to the default, in that the palatability for detritus is twice that for phytoplankton.

7.3 Analysis

The Jacobian of a steady state is given by

$$\mathbf{A} =$$

$$\begin{bmatrix}
-\frac{aeP}{(e+N)^2(b+cP)} - k & -\frac{abN}{(e+N)(b+cP)^2} + \frac{2\beta\lambda\mu^2 PZ}{\left(\mu^2+P^2+\omega D^2\right)^2} & \frac{\beta\lambda(P^2+\omega D^2)}{\mu^2+P^2+\omega D^2} + 2\gamma dZ & \frac{2\beta\lambda\mu^2\omega DZ}{\left(\mu^2+P^2+\omega D^2\right)^2} + \phi \\
\frac{aeP}{(e+N)^2(b+cP)} & \frac{abN}{(e+N)(b+cP)^2} - r - s - k - \frac{2\lambda(\mu^2+\omega D^2)PZ}{\left(\mu^2+P^2+\omega D^2\right)^2} & -\frac{\lambda P^2}{\mu^2+P^2+\omega D^2} & \frac{2\lambda\omega DP^2Z}{\left(\mu^2+P^2+\omega D^2\right)^2} \\
0 & \frac{2\alpha\lambda\mu^2 PZ}{\left(\mu^2+P^2+\omega D^2\right)^2} & \frac{\alpha\lambda(P^2+\omega D^2)}{\mu^2+P^2+\omega D^2} - 2dZ & \frac{2\alpha\lambda\mu^2\omega DZ}{\left(\mu^2+P^2+\omega D^2\right)^2} \\
0 & r + \frac{2\left[(1-\alpha-\beta)\mu^2+\omega D^2\right]\lambda PZ}{\left(\mu^2+P^2+\omega D^2\right)^2} & \frac{\left[(1-\alpha-\beta)P^2-(\alpha+\beta)\omega D^2\right]\lambda}{\mu^2+P^2+\omega D^2} & -\frac{2\left[P^2+(\alpha+\beta)\mu^2\right]\lambda\omega DZ}{\left(\mu^2+P^2+\omega D^2\right)^2} - \kappa
\end{bmatrix}$$

evaluated at the steady-state values of N, P, Z and D, where $\kappa = \phi + \psi + k$. The first column is the same as for the previous $NPZD$ model studied in Chapter 6. But the new multiple-grazing functions mean that D now appears in each of the other terms of the Jacobian. The steady states are obtained by solving the four simultaneous equations

$$0 = -\frac{N}{e+N}\frac{a}{b+cP}P + \frac{\beta\lambda(P^2+\omega D^2)Z}{\mu^2+P^2+\omega D^2} + \gamma dZ^2 + \phi D + k(N_0 - N), \quad (7.8)$$

$$0 = \frac{N}{e+N}\frac{a}{b+cP}P - rP - \frac{\lambda P^2 Z}{\mu^2+P^2+\omega D^2} - (s+k)P, \quad (7.9)$$

$$0 = \frac{\alpha\lambda(P^2+\omega D^2)Z}{\mu^2+P^2+\omega D^2} - dZ^2, \quad (7.10)$$

$$0 = rP + \frac{\left[(1-\alpha-\beta)P^2 - (\alpha+\beta)\omega D^2\right]\lambda Z}{\mu^2 + P^2 + \omega D^2} - (\phi + \psi + k)D. \qquad (7.11)$$

Clearly, solutions which have $Z = 0$ will be the same as the solutions of the previous $NPZD$ model, since the new grazing functions (the only difference between the models) always appear as a multiple of Z. Thus there is a steady state $(N_0, 0, 0, 0)$, for which the Jacobian is the same as that for $(N_0, 0, 0, 0)$ for the previous model. The four eigenvalues are therefore $-k$, Φ, 0 and $-\phi - \psi - k$, where

$$\Phi = \frac{aN_0}{b(e + N_0)} - r - s - k,$$

and numerical simulations again suggest that $(N_0, 0, 0, 0)$ is unstable for $\Phi > 0$, and stable for $\Phi < 0$.

The steady states $(N_1{}^*, P_1{}^*, 0, D_1{}^*)$ and $(N_2{}^*, P_2{}^*, 0, D_2{}^*)$ have the same definitions as in Chapter 6; $(N_2{}^*, P_2{}^*, 0, D_2{}^*)$ is not considered further since it can never enter the positive hexadectant, the region of phase space given by $\{N, P, Z, D \geq 0\}$. As for Chapter 6, we have $(N_1{}^*, P_1{}^*, 0, D_1{}^*) \rightarrow (N_0, 0, 0, 0)$ as $\Phi \rightarrow 0$.

The Jacobian at $(N_1{}^*, P_1{}^*, 0, D_1{}^*)$ is

$$\mathbf{A} =$$

$$\begin{bmatrix} -\frac{aeP}{(e+N)^2(b+cP)} - k & -\frac{abN}{(e+N)(b+cP)^2} & \frac{\beta\lambda(P^2+\omega D^2)}{\mu^2+P^2+\omega D^2} & \phi \\ \frac{aeP}{(e+N)^2(b+cP)} & \frac{abN}{(e+N)(b+cP)^2} - r - s - k & -\frac{\lambda P^2}{\mu^2+P^2+\omega D^2} & 0 \\ 0 & 0 & \frac{\alpha\lambda(P^2+\omega D^2)}{\mu^2+P^2+\omega D^2} & 0 \\ 0 & r & \frac{\left[(1-\alpha-\beta)P^2-(\alpha+\beta)\omega D^2\right]\lambda}{\mu^2+P^2+\omega D^2} & -\phi - \psi - k \end{bmatrix}$$

Only the third column is different to the equivalent Jacobian for the previous model, but, by looking at the third row, we see that

$$\frac{\alpha\lambda(P_1{}^{*2} + \omega D_1{}^{*2})}{\mu^2 + P_1{}^{*2} + \omega D_1{}^{*2}}$$

is an eigenvalue, and since it is always positive, for $P_1{}^*, D_1{}^* \neq 0$, the steady state $(N_1{}^*, P_1{}^*, 0, D_1{}^*)$ can never become stable. This is the case for the previous $NPZD$ model, plus for the equivalent steady state $(N_1{}^*, P_1{}^*, 0)$ of the original NPZ model studied in Chapter 3. By following the same arguments as for the previous $NPZD$

model, it can be shown that there are no other steady states with at least one of N, P, Z or D zero, and the remaining variables non-negative, and so we now look for steady-states (N^*, P^*, Z^*, D^*), with all the variables taking strictly positive values.

In the $NPZD$ model in Chapter 6, the dZ/dt equation only contains P and Z, and is independent of N and D. This means that $dZ/dt = 0$ can be rearranged to express Z in terms of P in order to calculate the steady states, as given by (6.13). However, in the multiple-grazing model we are considering now, D appears explicitly in the dZ/dt equation. So, from (7.10), we cannot express Z in terms of P alone, but as a function of P and D, viz

$$Z = \frac{\alpha\lambda(P^2 + \omega D^2)}{d(\mu^2 + P^2 + \omega D^2)}. \tag{7.12}$$

Adding (7.8), (7.9), (7.10) and (7.11) gives, upon rearrangement, the following expression for N:

$$N = N_0 - \frac{(1-\gamma)dZ^2}{k} - \frac{(s+k)P}{k} - \frac{(\psi+k)D}{k}. \tag{7.13}$$

Thus we can express N and Z in terms of P and D. When we substitute for N and Z into (7.8) and (7.11), we obtain a pair of multivariate polynomials in P and D. One polynomial is sixth order, and the other is eleventh order. This makes any further analysis impossible. This is unlike the previous $NPZD$ model, for which, although we could only reduce the solutions to a single tenth-order polynomial in P, we could show that the constant term of the polynomial tends to zero as $\Phi \to 0$, and so the (N^*, P^*, Z^*, D^*) solution degenerates to $(N_0, 0, 0, 0)$ at $\Phi = 0$, which is the three-way transcritical bifurcation. But the nature of solutions of the form (N^*, P^*, Z^*, D^*) for the multiple-grazing model must be determined by numerical means.

In Figure 7.2 we show how $(N_0, 0, 0, 0)$, $(N_1{}^*, P_1{}^*, 0, D_1{}^*)$ and (N^*, P^*, Z^*, D^*) vary with the value of r. The axes scales and the key are the same as for Figure 6.2 for the previous $NPZD$ model. At the default value of $r = 0.15$ we find a steady state (N^*, P^*, Z^*, D^*) in the strictly positive hexadectant; this cannot be calculated analytically, but by integrating the system in time from an initial condition a stable steady state is reached (this will be shown explicitly in Figure 7.3(a)). By starting

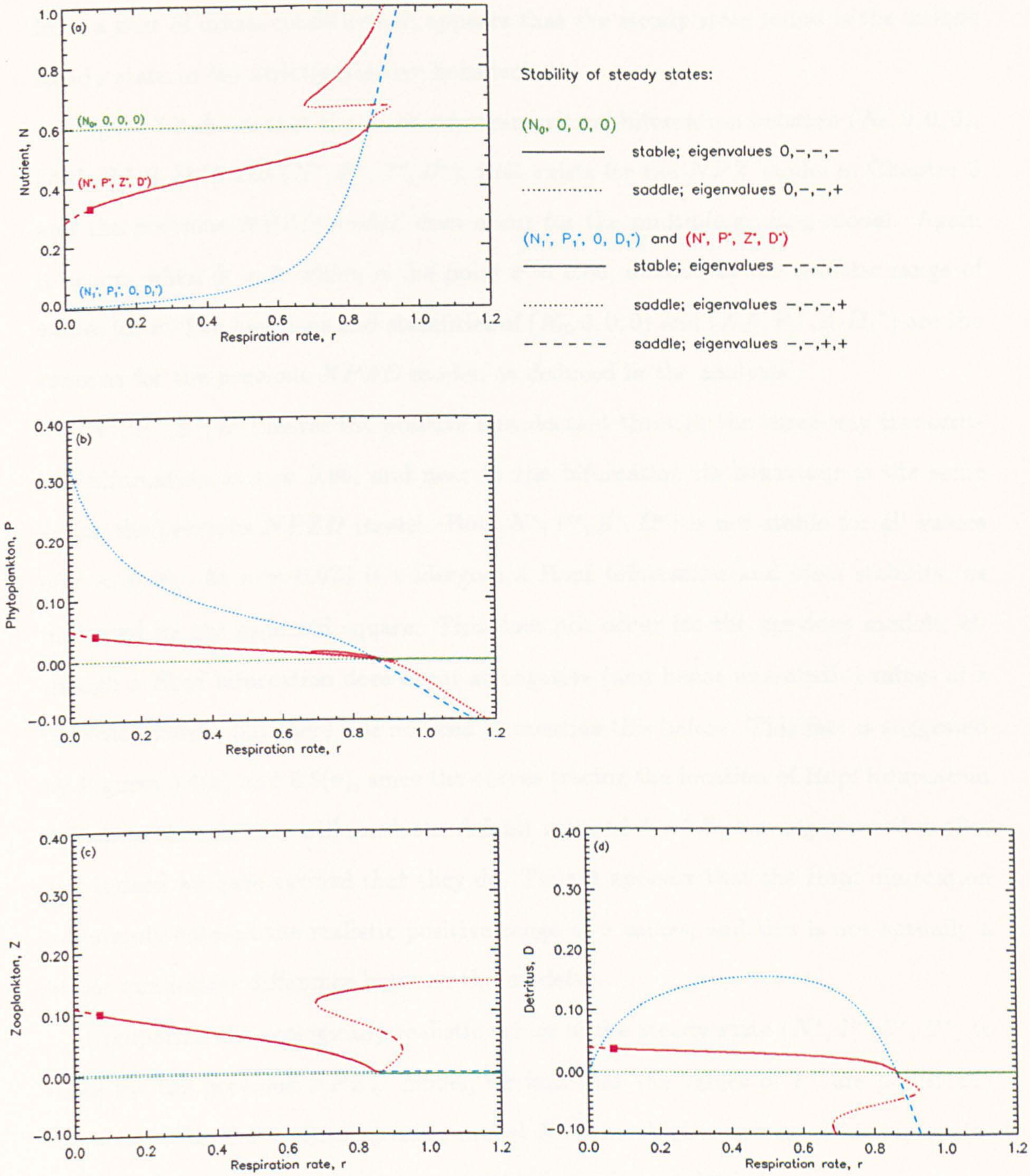

Figure 7.2: Location and stability of the steady states $(N_0, 0, 0, 0)$, $(N_1{}^*, P_1{}^*, 0, D_1{}^*)$ and (N^*, P^*, Z^*, D^*) as r is varied. The key indicates the signs of the real parts of the four eigenvalues, plus the corresponding stabilities. The three-way transcritical bifurcation again occurs at $r = 0.86$. (N^*, P^*, Z^*, D^*) undergoes a Hopf bifurcation at $r = 0.073$ (solid square), and further bifurcations when $D^* < 0$.

from a host of initial conditions, it appears that the steady state found is the unique steady state in the strictly positive hexadectant.

Figure 7.2 shows that the three-way transcritical bifurcation between $(N_0, 0, 0, 0)$, $({N_1}^*, {P_1}^*, 0, {D_1}^*)$ and (N^*, P^*, Z^*, D^*), that exists for the NPZ model in Chapter 3 and the previous $NPZD$ model, does occur for the multiple-grazing model. Again it occurs when $\Phi = 0$, which is the point $r = 0.86$, outside of the realistic range of values for r. The locations and stabilities of $(N_0, 0, 0, 0)$ and $({N_1}^*, {P_1}^*, 0, {D_1}^*)$ are the same as for the previous $NPZD$ model, as deduced in the analysis.

(N^*, P^*, Z^*, D^*) leaves the positive hexadectant through the three-way transcritical bifurcation at $r = 0.86$, and near to the bifurcation its behaviour is the same as for the previous $NPZD$ model. But (N^*, P^*, Z^*, D^*) is not stable for all values of $r < 0.86$. At $r = 0.073$ it undergoes a Hopf bifurcation and loses stability, as indicated by the solid red square. This does not occur for the previous models, although a Hopf bifurcation does occur at negative (and hence unrealistic) values of r in those models, but there was no need to mention this before. This fact is suggested by Figures 3.4(e) and 6.5(e), since the curves tracing the location of Hopf bifurcation A look as though they will reach the default value of $d = 1.0$ at a negative value of r, and indeed we have verified that they do. Thus it appears that the Hopf bifurcation has simply entered the realistic positive range of r values, and this is not actually a major qualitative difference between the models.

Comparing the ecologically realistic values of the steady state (N^*, P^*, Z^*, D^*) to those for the previous $NPZD$ model, we find that the values of P^* are practically the same. For the multiple-grazing model N^* takes higher values, Z^* is higher (as would be expected since it has more available food) and D^* is lower, since it is now consumed by the zooplankton.

We now explain the extra bifurcations of (N^*, P^*, Z^*, D^*) that are shown in Figure 7.2, once it has passed through the three-way transcritical bifurcation ('passed through' in the sense of r increasing through 0.86). Although N^* and Z^* remain positive, and P^* becomes positive again, Figure 7.2(d) shows that D^* remains negative, and so we are assured that (N^*, P^*, Z^*, D^*) does not re-enter the positive hexadectant, but that it remains outside, taking ecologically unrealistic values. We nevertheless explain the bifurcations that it undergoes, since for completeness they are shown in Figure 7.2. The value of r does not increase by much from the three-way transcritical bifurcation value of 0.86 before (N^*, P^*, Z^*, D^*), which has $P^*, D^* < 0$, undergoes a fold bifurcation at $r = 0.92$. (N^*, P^*, Z^*, D^*) does not become stable, but has two eigenvalues with negative real parts, and two with positive real parts, as indicated by the dashed red line. P^* then increases to zero as r decreases, and an eigenvalue passes through zero at a transcritical bifurcation with a steady state of the form $(N, 0, Z, D)$, with $N, Z > 0$ and $D < 0$. (N^*, P^*, Z^*, D^*) then has only one eigenvalue with positive real part, as indicated by the dotted red line (the behaviour of P^* shown in Figure 7.2(b) does not show up too clearly, but the stability is clearly shown in the other diagrams). (N^*, P^*, Z^*, D^*) then undergoes a second fold bifurcation, this time becoming stable (the positive real eigenvalue becomes negative). Although (N^*, P^*, Z^*, D^*) does become stable, trajectories starting within the ecologically realistic positive hexadectant cannot reach it, since $dD/dt > 0$ on the hyperplane $D = 0$ and so D cannot become negative. (N^*, P^*, Z^*, D^*) then loses stability at another transcritical bifurcation with a steady state of the form $(N, 0, Z, D)$, with $N, Z > 0$ and $D < 0$, and as r continues to increase it persists with one positive real eigenvalue.

7.4 Time series and phase portraits

Figure 7.3(a) shows the time series and trajectory (as an NPZ projection) of the system from the initial condition $(N, P, Z, D) = (0.4, 0.1, 0.05, 0.08)$, with all of the parameters fixed at their default values. The system settles down to a steady state with values $(N, P, Z, D) = (0.36, 0.035, 0.091, 0.036)$; this has already been indicated by Figure 6.2 at the default value of $r = 0.15$. Comparing these values to the equivalent steady state for the previous $NPZD$ model, given by $(N, P, Z, D) = (0.33, 0.034, 0.072, 0.060)$, we see that the steady state for the multiple-grazing model has slightly higher values of N and P, an increase in the Z steady-state value of 26%, and a reduction in the D steady-state value of 41%. The changes in Z and D

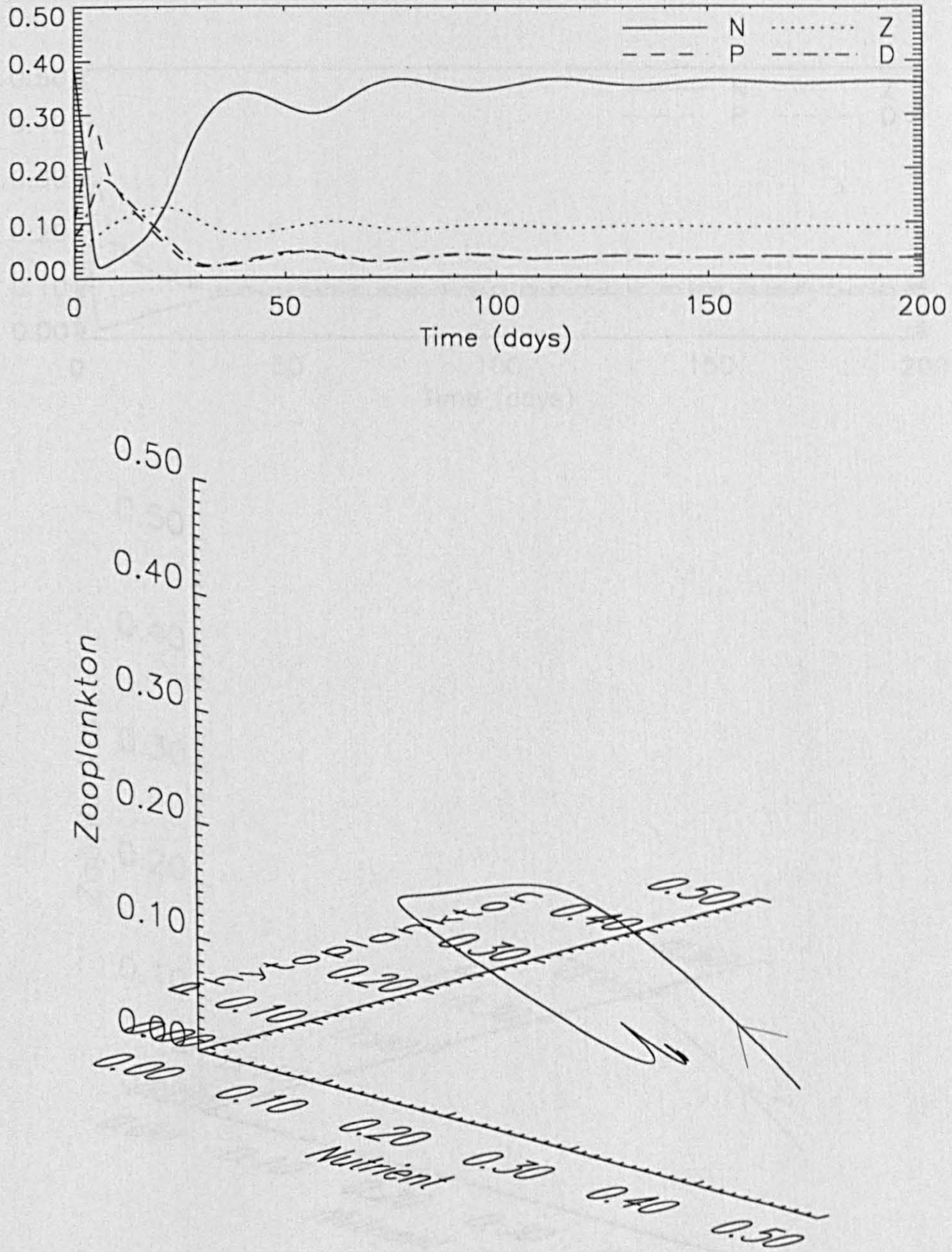

(a) $d = 1.0$ - N, P, Z and D settle down to steady-state values.

Figure 7.3: The time series and trajectory at (a) $d = 1.0$, (b) $d = 1.5$ and (c) $d = 1.25$, with all of the other parameters fixed at their default values. The trajectory is shown as the NPZ projection of the full $NPZD$ phase space.

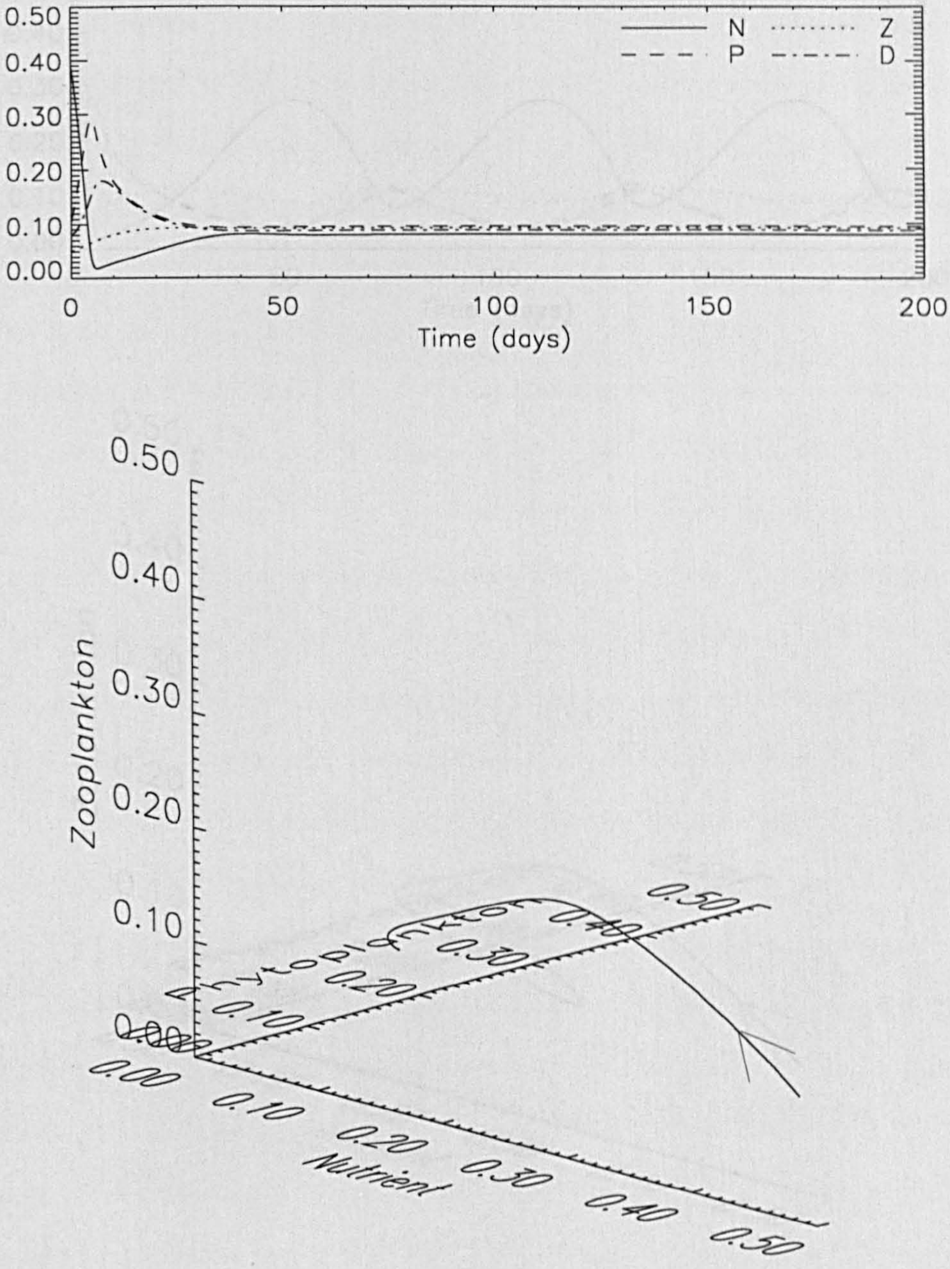

(b) $d = 1.5$ - the system settles down to a steady state, in contrast to the previous models, for which oscillations occur at this value of d.

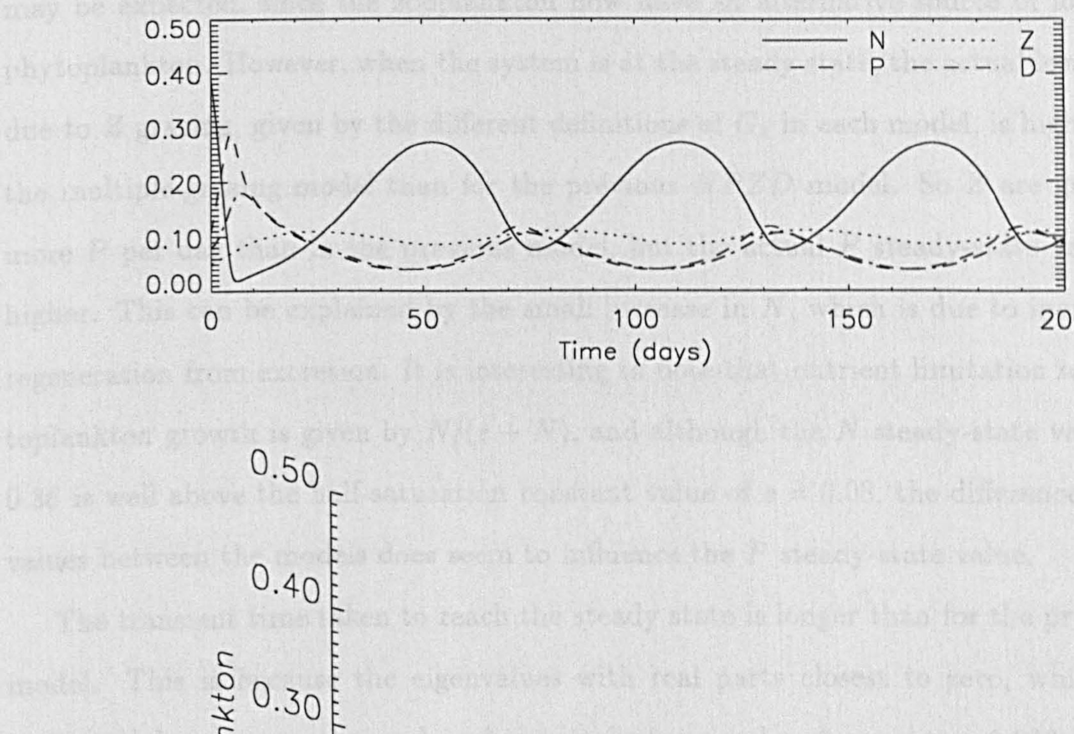

(c) $d = 1.25$ - the system settles down to a stable limit cycle at this intermediate value of d. The period is 59 days, much longer than that of the limit cycle at $d = 1.5$ for the previous $NPZD$ model.

values are what would be expected as a result of allowing the zooplankton to graze on the detritus. The minor increase in the P value from that of the previous model may be expected, since the zooplankton now have an alternative source of food to phytoplankton. However, when the system is at the steady state, the actual loss of P due to Z grazing, given by the different definitions of G_1 in each model, is higher for the multiple-grazing model than for the previous $NPZD$ model. So Z are grazing more P per day than in the previous model, but the actual P steady-state value is higher. This can be explained by the small increase in N, which is due to increased regeneration from excretion. It is interesting to note that nutrient limitation to phytoplankton growth is given by $N/(e+N)$, and although the N steady-state value of 0.36 is well above the half-saturation constant value of $e = 0.03$, the difference in N values between the models does seem to influence the P steady-state value.

The transient time taken to reach the steady state is longer than for the previous model. This is because the eigenvalues with real parts closest to zero, which for both models are a complex and conjugate pair, have real part equal to -0.078 for the original $NPZD$ model, whereas for the multiple-grazing model the real part is -0.022. Thus, the steady state in the multiple-grazing model is less strongly attracting, and hence the transient time is longer. Starting from a host of other initial conditions in the strictly positive hexadectant, all trajectories converge onto the same steady state, implying that $(N, P, Z, D) = (0.36, 0.035, 0.091, 0.036)$ is the unique steady state in the hexadectant. Unlike the previous models, we could not verify this from the analytical calculations.

In Figure 7.3(b) we show what happens when d is set to 1.5. A steady state is reached, which is unlike the previous $NPZD$ model and the original NPZ model, for which a stable limit cycle occurs for $d = 1.5$. All four variables take roughly the same values at the steady states; the values of N, P, Z and D are more easily compared to those for $d = 1.0$ by examining the one-parameter bifurcation diagrams to be shown in Section 7.5.

In Figure 7.3(c) we show that when $d = 1.25$, halfway between the previous two values, the system settles onto a limit cycle. The cycle has a period of 59 days, much larger than the period of 34 days attained by the limit cycle at $d = 1.5$ for the previous $NPZD$ model. Figure 6.4(e) showed, for the previous model, that the period remains close to 34 days as d is varied (and the other parameters kept constant).

So the oscillations have not disappeared, rather the range of d values for which they occur appears to have been shifted along, compared to the previous $NPZD$ model, and the period has lengthened. We now demonstrate this shifting by constructing one-parameter bifurcation diagrams, using d as the bifurcation parameter.

7.5 One-parameter bifurcation behaviour

Figure 7.4 shows that oscillations occur at lower d values, and across a much narrower range of d values, than for the previous $NPZD$ model. The Hopf bifurcations A and B occur at $d = 1.11$ and $d = 1.31$, compared to $d = 1.43$ and $d = 1.84$ for the previous model. Hopf bifurcation A is subcritical, rather than supercritical, but we see that the branch of unstable limit cycles emanating from it undergoes a fold bifurcation close by, resulting in a branch of stable limit cycles which then collapses onto Hopf B. Thus the fact that Hopf A is subcritical is not too important, and simply leads to a very narrow region of d values (between the fold bifurcation of the cycles and Hopf A) for which a stable limit cycle and a stable steady state coexist.

Comparing Figures 7.4(a) and 6.4(a), we see that at values of d above Hopf B, N^* is lower for the multiple-grazing model than for the previous $NPZD$ model, whereas at values of d below Hopf A, N^* is higher for the multiple-grazing model. The lowest minimum values of N reached along a cycle are similar for both models, but higher maximum values are attained for the multiple-grazing model.

From Figures 7.4(b) and 6.4(b) we see that at values of d below Hopf A, P^* is fairly similar for both models. But for values above Hopf B in the multiple-grazing model, P^* is much higher than for the previous $NPZD$ model. It even reaches higher values than the maximum values of P along the limit cycles in the previous model. In both the NPZ model and the previous $NPZD$ model, the maximum P values along the cycles exceeded the highest P^* value reached, whereas such high values are

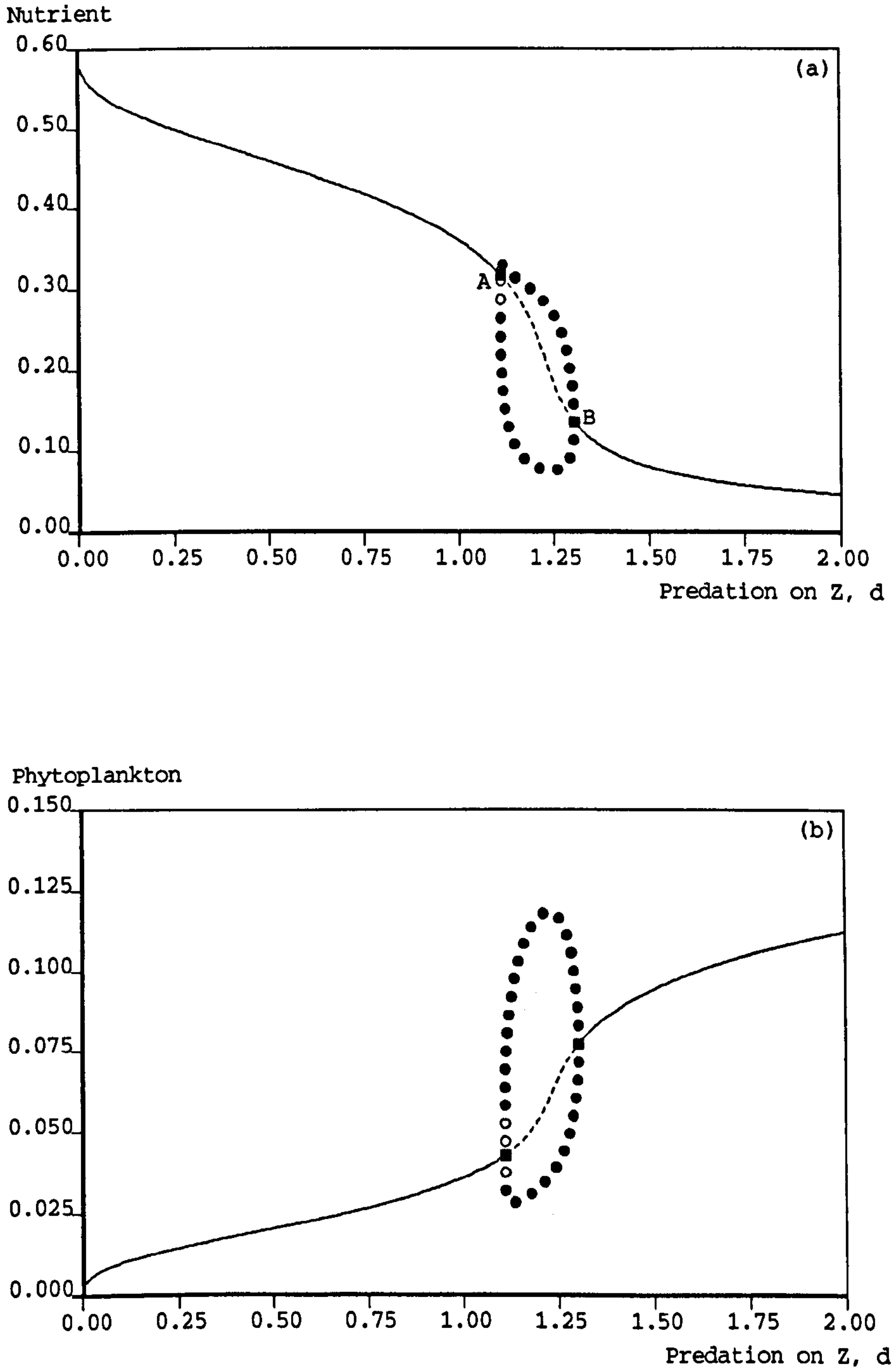

Figure 7.4: Variations in the steady-state values of (a) nutrient, (b) phytoplankton, (c) zooplankton and (d) detritus as d is varied. A solid line is a stable steady state, a dashed line is an unstable steady state, a solid square is a Hopf bifurcation, and solid (open) circles indicate the maximum and minimum values of the stable (unstable) limit cycles. Hopf bifurcation A is subcritical, whilst B is supercritical.

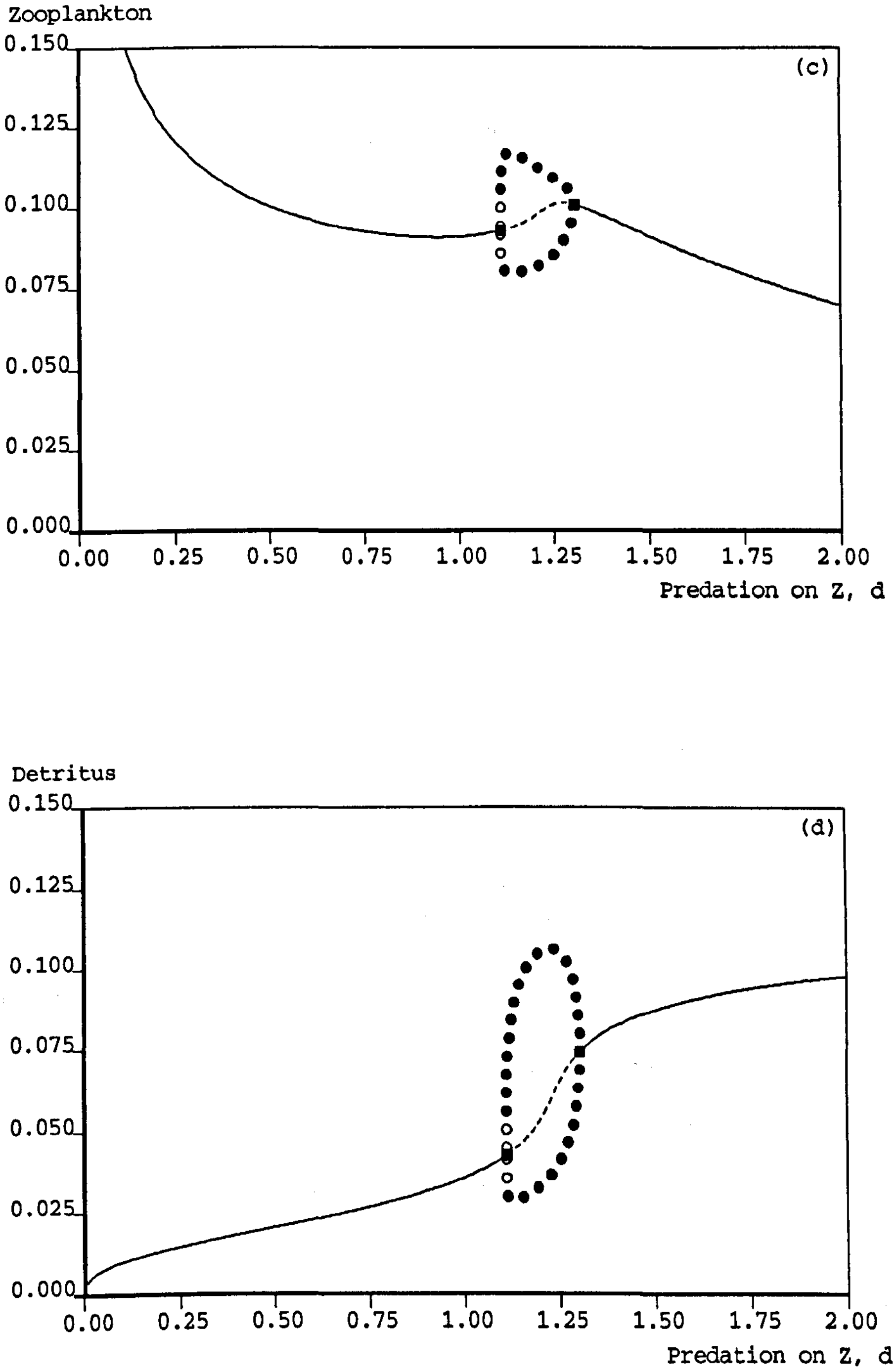

(c) The zooplankton steady-state values are higher than for the previous *NPZD* model, and the amplitude of the oscillations is greater, despite the oscillations occurring across a narrower range of *d*. (d) The detritus steady-state and limit cycle values correlate to the phytoplankton values.

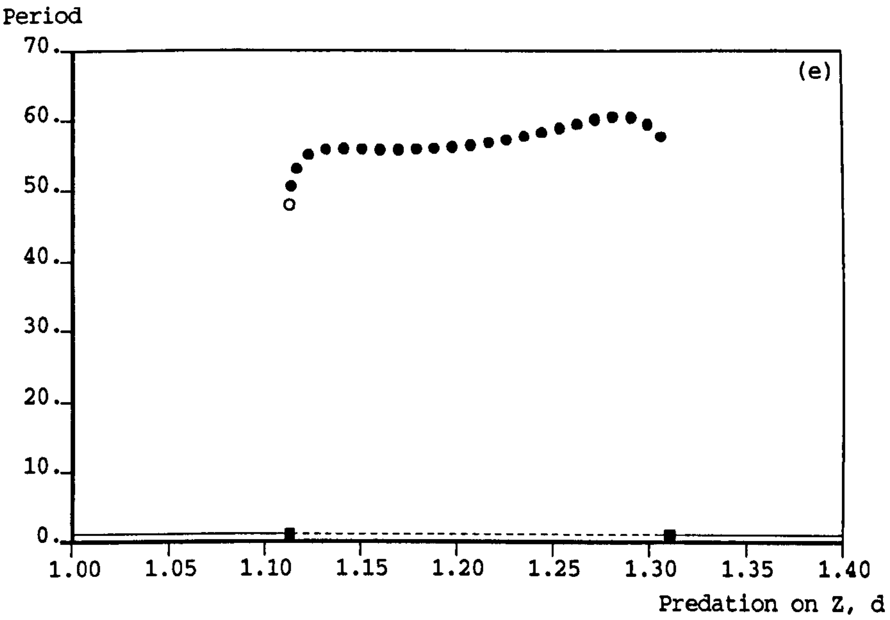

(e) The period of the stable limit cycles varies between 48 and 61 days. These are higher periods than shown in the equivalent Figure 6.4(e) for the previous $NPZD$ model, and the range of periods attained is greater, despite the actual range of d values exhibiting oscillations being smaller. The open circle indicates the period of the unstable cycle, close to subcritical Hopf bifurcation A.

reached by the steady state in the multiple-grazing model.

As expected, we see, from Figures 7.4(c) and 6.4(c) that the values of Z^* are greater for the multiple-grazing model. Also the values of Z during the oscillations are higher than the values attained in the previous model, both during the cycles and for steady states.

From Figures 7.4(d) and 6.4(d) we see that D^* is usually lower for the multiple-grazing model than for the previous $NPZD$ model. This would be expected, due to the consumption of detritus by zooplankton in the multiple-grazing model. However, for $d \in (1.32, 1.43)$, the steady state is stable for both models, and D^* is actually greater in the multiple-grazing model. This curious effect demonstrates that the nonlinearities and feedback loops in these models mean that the expected outcome of an alteration does not always occur, i.e. letting zooplankton eat the detritus will not always reduce the detritus concentration. Similar 'unexpected effects' are investigated by Yodzis (1981, 1988, 1989) and Edwards *et al.* (1997) in the context of perturbation experiments on ecological communities which lie in equilibrium. The region of d for which D^* is greater in the multiple-grazing model than in the previous $NPZD$ model lies to the right of the oscillatory region for the multiple-grazing model, but to the left of the oscillatory region for the previous $NPZD$ model. So the fact that the oscillations have shifted along, as indicated by the d values of the Hopf bifurcations moving, may be seen as a warning that the quantitative nature of the steady states may change significantly.

Finally, Figure 7.4(e) shows that the period of the oscillations ranges between 48 and 61 days as d varies. This is greater variation than for the previous $NPZD$ model, despite the range of d values being smaller. The period remains at higher values than those shown in the equivalent Figure 6.4(e) for the previous model, indicating that allowing the zooplankton to graze on the detritus causes a slowing down of the oscillations.

7.6 Two-parameter diagrams

In Figure 7.5 we present the two-parameter bifurcation diagrams which indicate how the Hopf bifurcations persist as each of the parameters is independently varied. The most striking difference between these diagrams and the corresponding ones in Figure 6.5 for the previous $NPZD$ model, is that the regions of oscillations are much narrower for the multiple-grazing model. This is not unexpected, since in Figure 7.4 we showed that the oscillations occur over a much narrower range of d than for the previous $NPZD$ model. However, despite this narrower range of d, the pictures for each parameter are still remarkably similar for the two models - the oscillations tend to persist or not persist, as each parameter is varied, in the same way for both models.

The most informative diagram is Figure 7.5(o) for ω, the zooplankton feeding preference, a parameter which does not appear in the previous $NPZD$ model. Recall that $\omega = 0$ means that zooplankton do not graze on detritus at all, and so $\omega = 0$

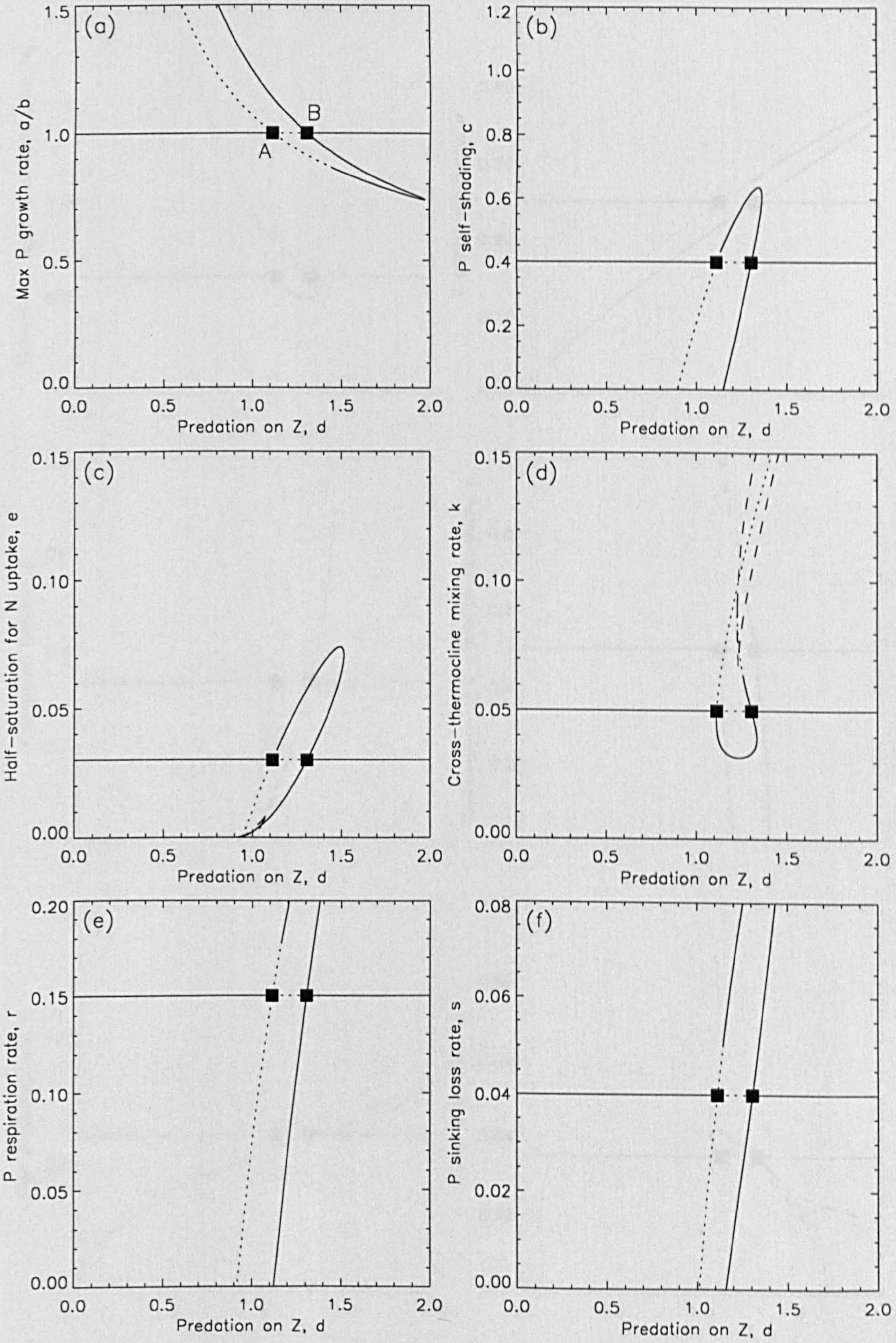

Figure 7.5: Two-parameter bifurcation diagrams showing how the positions of the Hopf bifurcations in Figure 7.4 change as each other parameter, together with d, is independently varied from its default value. The steady-state stabilities from Figure 7.4 are shown as a horizontal line at each default parameter value. Hopf A and (ctd.)

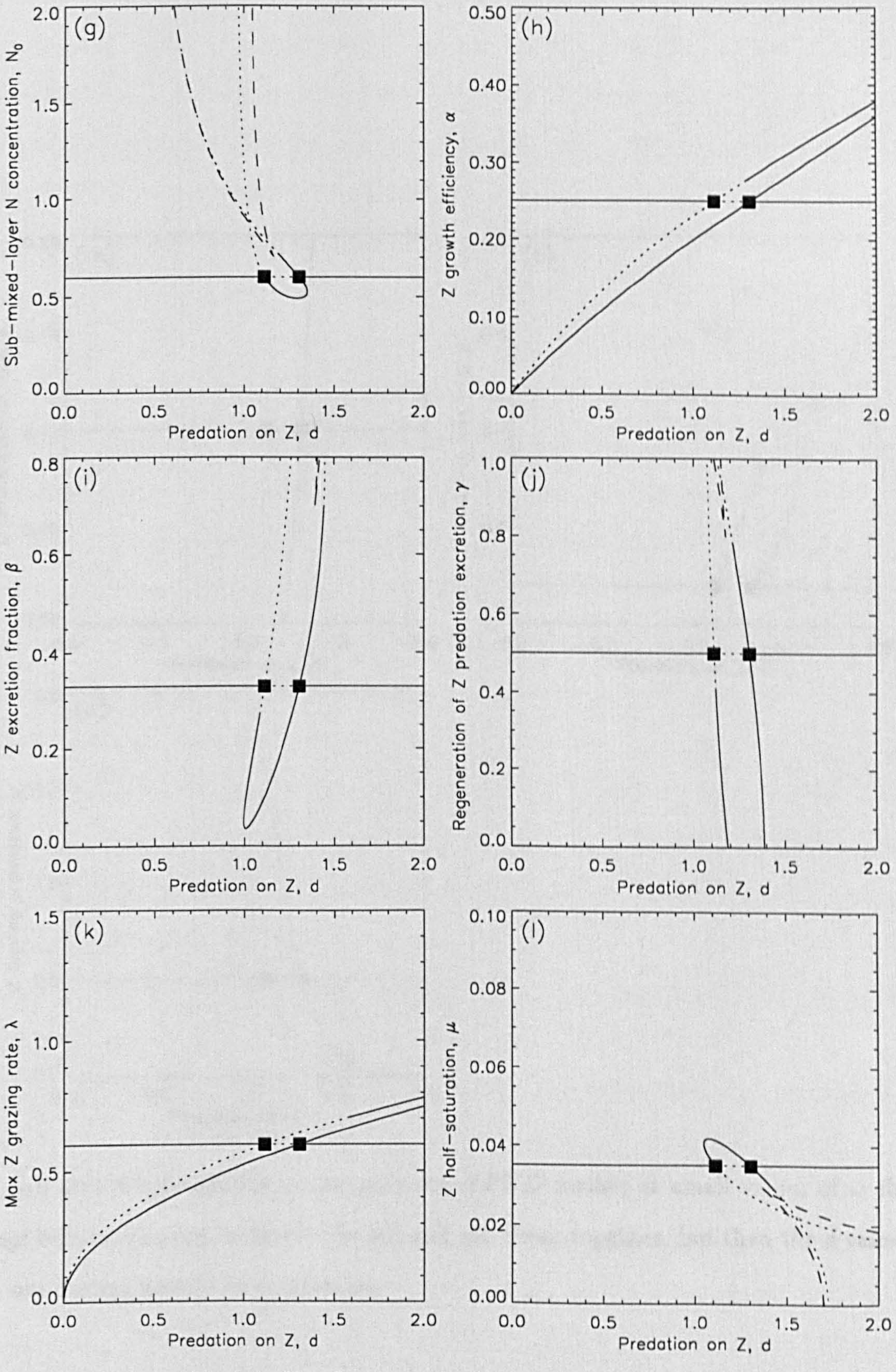

Hopf B are indicated in (a). Non-horizontal solid curves starting from Hopf B indicate supercritical Hopf bifurcations, and non-horizontal curves of short dashes from Hopf A represent subcritical Hopf bifurcations. In (c), (d), (g), (i), (j), (l), (n) and (o), curves of long dashes indicate fold bifurcations of the steady state. (ctd.)

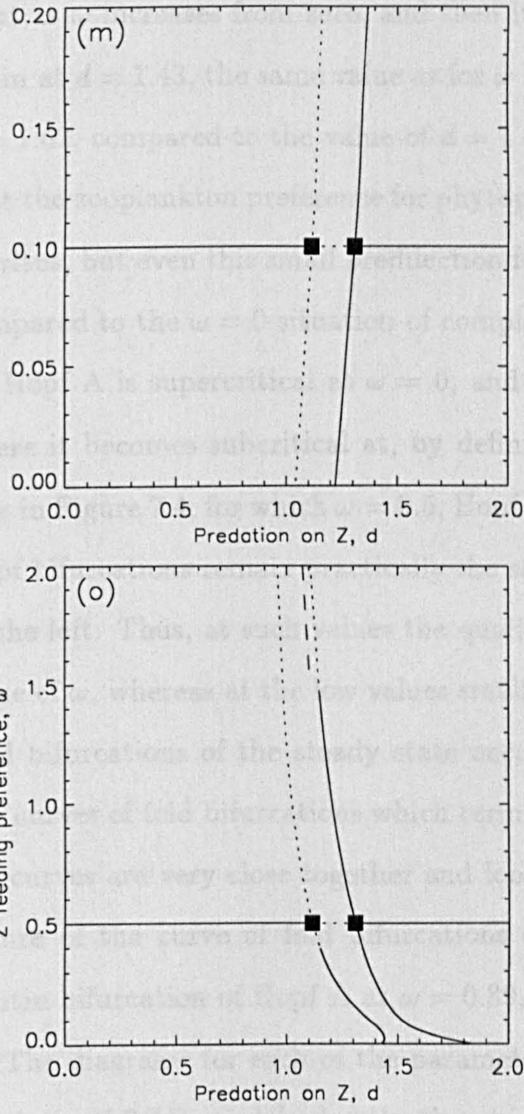

In (o), $\omega = 0$ corresponds to the previous *NPZD* model; at small values of ω the Hopf bifurcations are shifted to the left and get closer together, but then the *d* values do not change greatly as ω increases.

corresponds to the previous model. Thus on Figure 7.5, the d-values of the Hopf bifurcations at $\omega = 0$ are the default d-values of the Hopf bifurcations in the previous model. We see that a very small increase in ω from zero causes Hopf B to move to the left (its d value decreases) by a significant amount. Hopf A initially moves to the right as ω increases from zero, and then it moves to the left. At $\omega = 0.05$ Hopf A is again at $d = 1.43$, the same value as for $\omega = 0$. But at $\omega = 0.05$ Hopf B has moved to $d = 1.62$, compared to the value of $d = 1.84$ at $\omega = 0$. The value of $\omega = 0.05$ means that the zooplankton preference for phytoplankton is twenty times their preference for detritus, but even this small predilection for detritus has an impact on the dynamics, compared to the $\omega = 0$ situation of complete distaste for detritus.

Hopf A is supercritical at $\omega = 0$, and remains so as ω increases, until $\omega = 0.39$ where it becomes subcritical at, by definition, a Bautin bifurcation. This explains why in Figure 7.4, for which $\omega = 0.5$, Hopf A is subcritical. As ω increases further, the Hopf bifurcations remain practically the same distance apart, and move only slightly to the left. Thus, at such values the qualitative behaviour is fairly insensitive to the value of ω, whereas at the low values small changes in ω can have large consequences. Fold bifurcations of the steady state occur at high values of ω. There are actually two curves of fold bifurcations which terminate at a cusp point at $\omega = 1.56$, although the curves are very close together and look like just one curve in Figure 7.5(o). The nature of the curve of fold bifurcations of limit cycles, which originates from the Bautin bifurcation of Hopf A at $\omega = 0.39$, will be deduced in Section 7.7.

The diagrams for each of the parameters are remarkably similar to those for the previous $NPZD$ model, despite the narrower regions of oscillations and the fact that Hopf A is subcritical at the default values in the multiple-grazing model. For example, Figures 7.5(b) and 6.5(b) show that for both $NPZD$ models, oscillations do not occur for c greater than about 0.6, and can occur at all values below 0.6. Oscillations can occur across the full ranges of r, s and γ for both models. The fact that at the default parameters the oscillations occur across only a small range of d in the multiple-grazing model, makes it surprising that the oscillations should still persist across the full ranges of these parameters, and that the bifurcation diagrams in general remain so similar between the two models. Bogdanov-Takens bifurcations occur at $k = 0.091$ and $N_0 = 1.85$, lower values than for the previous $NPZD$ model and the original NPZ model.

In Figure 7.5(j), for γ, fold bifurcations of the steady state occur, but these are not present for the original $NPZD$ model. This can be explained because fold bifurcations occur at high levels of ω, and so if we had instead computed the bifurcation diagrams with ω set to a high default value, fold bifurcations would appear in each of the diagrams. The chosen value of $\omega = 0.5$ can be considered an intermediate value, for which the fold bifurcations start 'creeping in' to some of the diagrams.

The diagrams which show the most difference between the two $NPZD$ models are Figure 7.5(l) and Figure 6.5(l) for μ, the half-saturation constant for zooplankton grazing. This is not too surprising, since the zooplankton grazing phytoplankton function, G_1, has changed definition from the previous model, effectively replacing μ^2 with $\mu^2 + \omega D^2$, and the introduction of the zooplankton grazing detritus function, G_2, means that μ appears elsewhere in the equations. In Figure 7.5(l) we see that the two curves of Hopf bifurcations cross over, and fold bifurcations of the steady state occur. The two fold curves terminate at a cusp point. This looks quite different to the equivalent picture, Figure 6.5(l), for the previous $NPZD$ model. But in actual fact, the two pictures are qualitatively the same. For the previous model the picture is qualitatively the same as that for the multiple-grazing model, but is shifted to the right, outside of the plotted range. The cusp point of the curves of fold bifurcations occurs at $d = 2.26$. The original NPZ model also exhibits this bifurcational behaviour, with the cusp point occurring at $d = 2.29$, as discussed in Section 4.6. So Figure 7.5(l) and Figure 6.5(l) are not as qualitatively different as first appears.

The other parameters involved in the zooplankton grazing functions are α, β and λ. The corresponding bifurcation diagrams for these parameters show the same qualitative nature between the two models (except that the fold bifurcations for β in the first $NPZD$ model occur out of the range plotted).

Figure 7.5(m) shows that oscillations can occur across the whole range of ϕ, the remineralisation rate of detritus, whereas Figure 6.5(m) showed that the oscillations do not occur at low values of ϕ for the previous $NPZD$ model. It may appear as though the curve of Hopf bifurcations in Figure 6.5(m) has simply been stretched out, so that in Figure 7.5(m) a minimum still occurs, but at a negative value of ϕ. However, this is not the case. The curve from Hopf B in Figure 7.5(m) actually reaches a minimum d value and then a minimum ϕ value at $\phi = -0.44$, and then ϕ increases together with d, and the curve appears to asymptote to $\phi = 0$ as d increases. So it does not join up to the curve from Hopf A, as occurs in Figure 6.5(m).

Thus, the general qualitative nature of the bifurcational structure of the previous $NPZD$ model, and of the original NPZ model, is retained upon the introduction of multiple grazing by zooplankton, but there are significant quantitative changes.

7.7 Dependence of the period of oscillations on the parameter values

In Figure 7.6 we show the period-contour diagrams for ϕ, ψ and ω, the three parameters that appear in the multiple-grazing model but not in the original NPZ model. Figure 7.4(e) in Section 7.5 shows that as d changes, and the other parameters are set to their default values, the period of the oscillations varies between 48 and 61 days. Thus we know *a priori* that there must be 50-, 55- and 60-day contours passing through the default values of each of the parameters in the three diagrams of Figure 7.6.

We firstly discuss Figure 7.6(c) for the zooplankton feeding preference, ω; note that we have plotted d from 0.8 to 1.8 rather than the usual range of 1.0 to 2.0 in order to show the full behaviour. Since $\omega = 0$ corresponds to the previous $NPZD$ model, there is, as expected, a 35-day contour close to $\omega = 0$. Figure 7.6(c) shows that as ω increases from zero, the period of the oscillations increases quite sharply at first, attaining over 50 days when ω has only reached $\omega = 0.2$. As ω increases further, the period is roughly 60 days for most values of d. But at values of d close to Hopf B

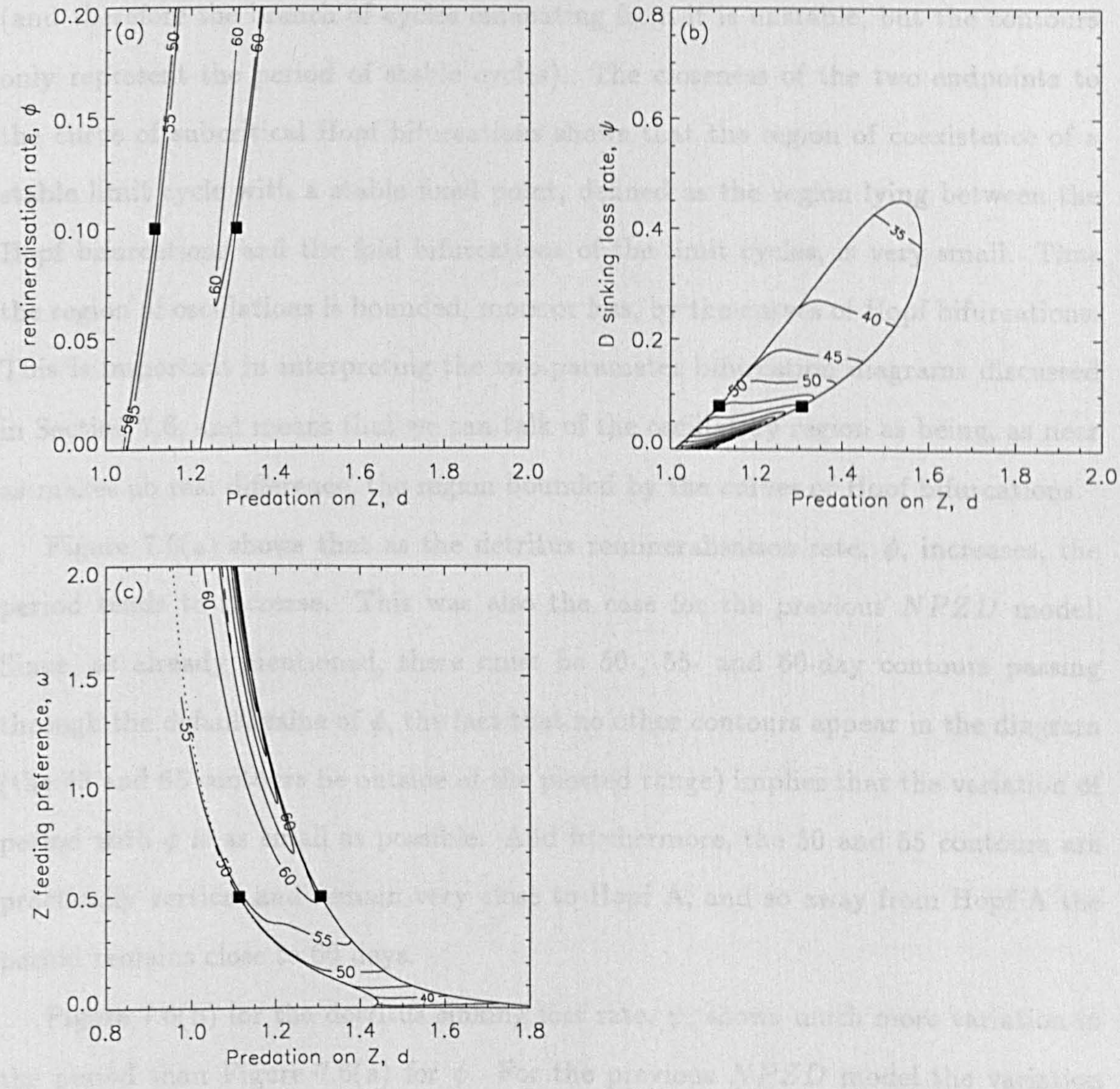

Figure 7.6: The period-contour diagrams for each of the parameters ϕ, ψ and ω which do not appear in the NPZ model. As ω decreases to zero, the period reduces to 35 days, corresponding to the previous $NPZD$ model.

higher periods are reached, as indicated by the closely-compacted contours, with the highest contour reached being that for a period of 100 days.

The left-hand endpoints of the 50 and 55 contours are fold bifurcations of the limit cycles. This must be so since at the corresponding values of ω Hopf A is subcritical (and therefore the branch of cycles emanating from it is unstable, but the contours only represent the period of stable cycles). The closeness of the two endpoints to the curve of subcritical Hopf bifurcations shows that the region of coexistence of a stable limit cycle with a stable fixed point, defined as the region lying between the Hopf bifurcations and the fold bifurcations of the limit cycles, is very small. Thus the region of oscillations is bounded, more or less, by the curves of Hopf bifurcations. This is important in interpreting the two-parameter bifurcation diagrams discussed in Section 7.6, and means that we can talk of the oscillatory region as being, as near as makes no real difference, the region bounded by the curves of Hopf bifurcations.

Figure 7.6(a) shows that as the detritus remineralisation rate, ϕ, increases, the period tends to increase. This was also the case for the previous $NPZD$ model. Since, as already mentioned, there must be 50-, 55- and 60-day contours passing through the default value of ϕ, the fact that no other contours appear in the diagram (the 45 and 65 contours lie outside of the plotted range) implies that the variation of period with ϕ is as small as possible. And furthermore, the 50 and 55 contours are practically vertical and remain very close to Hopf A, and so away from Hopf A the period remains close to 60 days.

Figure 7.6(b) for the detritus sinking loss rate, ψ, shows much more variation in the period than Figure 7.6(a) for ϕ. For the previous $NPZD$ model the variation for ψ is the same as that for ϕ, although the actual range of ψ exhibiting oscillations is smaller for the previous model than for the current multiple-grazing model. At high values of ψ the period gets as low as 35 days, and at values approaching zero it reaches 150 days.

Using the same approach discussed in Section 6.7 for the previous $NPZD$ model, we have verified whether or not the period changes in the same direction as for the NPZ model when each of the other parameters is increased and decreased. The starting point we used for each parameter was the limit cycle that occurs for $d = 1.21$, which is the midpoint of the region of oscillations, with all of the other parameters set to their default values. This cycle has a period of 56.6 days.

As for the previous $NPZD$ model, we find that the period tends to vary with each parameter in the same direction as that shown in Figure 3.7 for the NPZ model. The situation for β is not as clear cut as for the other parameters, with the 60-day contour running almost the full length (in a vertical direction) of the oscillatory region, whereas for the NPZ model the contours tend to be horizontal. At the maximum value of $\beta = 0.75$ the period reaches 89 days, much higher than the period attained at low levels of β. Thus, in agreement with the behaviour of the NPZ model, the greatest periods are reached at the high values of β. For e there is also a 60-day contour running from low to high values of e, and there is no clear trend in the period as e varies. For the remaining parameters the period does behave in the same qualitative way as for the NPZ model and the previous $NPZD$ model.

7.8 Discussion

We have incorporated the consumption of detritus by zooplankton into the model studied in Chapter 6. This has involved adding extra structure to the food web and making the equations of the model more complex, but only adds one extra parameter to the system. This parameter, ω, represents the zooplankton's preference for detritus compared to their preference for phytoplankton, and so $\omega = 0$ corresponds to the previous $NPZD$ model.

In Chapter 6 the bifurcational structure of the $NPZD$ model was found to be remarkably similar to that of the original NPZ model investigated in Chapter 3. In the current chapter we have found that allowing zooplankton to have an alternative source of food, namely detritus, does change the bifurcational structure, although the qualitative characteristics of the previous structure are still there. The three-way transcritical bifurcation, at which the positive steady state of the form (N^*, P^*, Z^*, D^*) enters the ecologically realistic positive hexadectant, still occurs, and takes place at the same parameter values as before.

The Hopf bifurcations, whose behaviour was investigated in Chapters 3 and 6, have also survived the inclusion of zooplankton grazing on detritus. The one-parameter diagrams of Section 7.5 show that the Hopf bifurcations occur at lower and closer together d values (with all other parameters set to their default values) than for the previous $NPZD$ model, and so the oscillations occur across a narrower range of d. However, the two-parameter diagrams of Section 7.6 illustrate that, as each of the other parameters is independently varied, the behaviour of the Hopf bifurcations is generally qualitatively the same as that for the previous $NPZD$ model. The fold bifurcations and Bogdanov-Takens bifurcations also behave similarly.

Figure 7.5(o) shows that when the zooplankton have only a small predilection for detritus the dynamical behaviour is quite sensitive to the precise value of ω, whereas when the zooplankton have similar likings for detritus and phytoplankton ($\omega \simeq 1$), the behaviour is relatively independent of the precise value of ω. So the qualitative change in the structure of the model introduced by allowing zooplankton to have a very slight taste for detritus, compared to having no taste at all (Chapter 6), does alter the dynamical behaviour of the system.

The period-contour diagram of Figure 7.6(c) shows that as ω is increased from zero, so that the previous $NPZD$ model is transformed continuously into the multiple-grazing model, the period increases. This explains why the periods of the oscillations in the time series and one-parameter bifurcation diagrams are longer than for the previous $NPZD$ model.

The results from this chapter plus Chapters 3 and 6 show that the NPZ model and the previous $NPZD$ model exhibit similar dynamical behaviour, which becomes shifted if zooplankton are allowed to graze on detritus. Thus we conclude that, at least for our models, if knowledge of the detritus concentration is not required then it only needs to be explicitly modelled if zooplankton consume it as an alternative food source to phytoplankton.

Chapter 8

Seasonal forcing of the mixed-layer depth

8.1 Introduction

We now add seasonal forcing to each of the models investigated in Chapters 3, 4, 6 and 7. The forcing is introduced by explicitly including the mixed-layer depth in the models, and then varying its value throughout the year. Time series are plotted, and the differences in behaviour between the models are explained using the analytical and numerical results derived in the aforementioned chapters. Parameter values are then altered, and the consequences are also explained using the previous results. This chapter exemplifies the usefulness of the many one- and two-parameter bifurcation diagrams and the period-contour diagrams computed in this thesis in explaining the output of models when parameter values are changed.

8.2 Explicit representation of the mixed-layer depth

The mixed-layer depth, subsequently denoted M, appears implicitly in the definitions of the parameters a, k and s in the NPZ model formulated in Chapter 2, and also in the detritus sinking loss rate ψ in the two $NPZD$ models of Chapters 6 and 7. Since M is no longer going to be held constant, we introduce new parameters a', k', s' and

ψ', such that

$$a = \frac{a'}{M}, \quad k = \frac{k'}{M}, \quad s = \frac{s'}{M}, \quad \psi = \frac{\psi'}{M}, \tag{8.1}$$

and use these substitutions to replace a, k, s and ψ in the equations for the models. The parameters s' and ψ' thus represent the sinking velocities of phytoplankton and detritus respectively (and are divided by M to give the proportions of P and D that are lost from the mixed layer each day, i.e. s and ψ). The default values of the new parameters are $a' = 2.5, k' = 0.625, s' = 0.5$ and $\psi' = 1.0$, so that $M = 12.5$, as used in the previous chapters, gives the default values of a, k, s and ψ.

We consider the effects of a deepening and shallowing of the mixed layer in the following manner, originally introduced by Evans and Parslow (1985), and subsequently adopted by Fasham *et al.* (1990) and Fasham (1993).

The time-dependent function h describes the rate of change of the mixed-layer depth, and is defined as

$$h(t) = \frac{dM}{dt}.$$

The water below the mixed layer is assumed to contain nutrients, at a concentration N_0, but no phytoplankton or zooplankton, as has already been assumed in all of our models. This water becomes entrained into the mixed-layer water when the mixed layer deepens. The total biomass of plankton is thus diluted into a greater volume of water, and so the mixed-layer concentrations of phytoplankton, P, and zooplankton, Z, which are measured as biomass per cubic metre of water, are decreased. The concentration of nutrients, N, will increase in proportion to the value of $(N_0 - N)$.

When the mixed layer shallows, nutrients and phytoplankton are left behind in the deep water, or detrained, but the volumetric concentrations (as biomass per cubic metre) within the mixed layer remain the same. The zooplankton are assumed to be motile and able to actively maintain themselves within the mixed layer, and so when shallowing occurs the zooplankton become more concentrated in the mixed layer, and Z increases. Evans and Parslow (1985) modelled this asymmetry by defining

$$h^+(t) = \max\{h(t), 0\},$$

and using $h^+(t)$ in the equations representing nonmotile entities, namely N and P.

The equations for the original NPZ model formulated in Chapter 2 thence become, upon inclusion of a varying mixed-layer depth:

$$\begin{aligned}
\frac{dN}{dt} &= -\frac{N}{e+N}\frac{a'}{(b+cP)M}P + rP + \frac{\beta\lambda P^2}{\mu^2+P^2}Z + \gamma dZ^2 + \frac{(k'+h^+)}{M}(N_0 - N), && (8.2)\\
\frac{dP}{dt} &= \frac{N}{e+N}\frac{a'}{(b+cP)M}P - rP - \frac{\lambda P^2}{\mu^2+P^2}Z - \frac{(s'+k'+h^+)}{M}P, && (8.3)\\
\frac{dZ}{dt} &= \frac{\alpha\lambda P^2}{\mu^2+P^2}Z - dZ^2 - \frac{h}{M}Z. && (8.4)
\end{aligned}$$

When the mixed-layer depth is constant, $h = 0$ and the equations are the same as those given in Chapter 2. During a deepening of the mixed layer, $h > 0$ and nutrients are entrained into the mixed layer from the nutrient-rich deeper water, and the phytoplankton and zooplankton become diluted. The precise expression for dilution of, say, zooplankton, comes from noting that the amount of zooplankton within the mixed layer beneath one square metre of surface water remains constant during deepening. This amount is given by MZ, and so we have (ignoring grazing and predation)

$$\begin{aligned}
0 = \frac{d}{dt}(MZ) = M\frac{dZ}{dt} + Z\frac{dM}{dt} = M\frac{dZ}{dt} + hZ\\
\Rightarrow \quad \frac{dZ}{dt} = -\frac{h}{M}Z.
\end{aligned}$$

During a shallowing of the mixed layer, $h < 0$ and the zooplankton concentration increases; $h^+ = 0$ and so the concentrations of nutrients and phytoplankton remain the same. Phytoplankton detrained from the mixed layer are assumed to be lost forever and cannot re-enter the mixed layer, and detrained nutrients are similarly lost, and have no effect on the constant concentration of nutrient in the sub-mixed-layer water, N_0. The equations for the NPZ model with linear zooplankton mortality, originally studied in Chapter 4, change in a similar fashion to the quadratic mortality case, with the zooplankton mortality term qZ replacing dZ^2 in (8.2) and (8.4).

The $NPZD$ model of Chapter 6 becomes, upon inclusion of a varying mixed-layer depth:

$$\frac{dN}{dt} = -\frac{N}{e+N}\frac{a'}{(b+cP)M}P + \frac{\beta\lambda P^2}{\mu^2+P^2}Z + \gamma dZ^2 + \phi D + \frac{(k'+h^+)}{M}(N_0 - N), \quad (8.5)$$

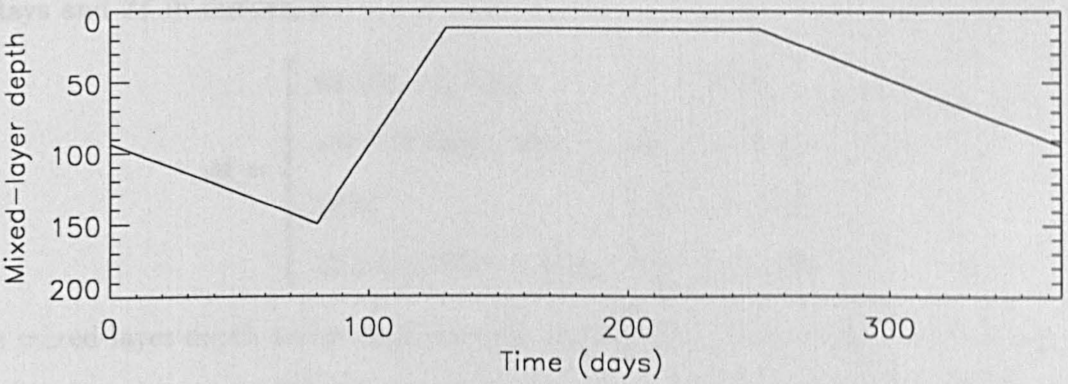

Figure 8.1: Variation in the mixed-layer depth (in metres) through one year, as used to force the models.

$$\frac{dP}{dt} = \frac{N}{e+N}\frac{a'}{(b+cP)M}P - rP - \frac{\lambda P^2}{\mu^2+P^2}Z - \frac{(s'+k'+h^+)}{M}P, \tag{8.6}$$

$$\frac{dZ}{dt} = \frac{\alpha\lambda P^2}{\mu^2+P^2}Z - dZ^2 - \frac{h}{M}Z, \tag{8.7}$$

$$\frac{dD}{dt} = rP + (1-\alpha-\beta)\frac{\lambda P^2}{\mu^2+P^2}Z - \phi D - \frac{(\psi'+k'+h^+)}{M}D. \tag{8.8}$$

The detritus is nonmotile, and is thus diluted during deepening and detrained during shallowing in the same manner as the phytoplankton. A varying mixed-layer depth is incorporated into the multiple-grazing $NPZD$ model of Chapter 7 in a similar way.

We consider the mixed-layer depth to vary through the year as shown in Figure 8.1, where time $t = 0$ represents midnight at the start of 1st January, and the depth is measured in metres. The piecewise-linear function gives a simple representation of the three major features of the annual cycle (e.g. Fasham, 1993) - a rapid shallowing in the spring, a constant shallow layer throughout the summer, and a deepening during the autumn and winter. Evans and Parslow (1985) also used a piecewise-linear approximation. For simplicity we do not consider seasonal changes in irradiance, as we want to demonstrate how the results of the previous chapters can be used to help understanding of a forced system.

The precise function used to represent the mixed-layer depth, where t is measured in days and M in metres, is

$$M = \begin{cases} 93.575 + 0.705t, & 0 \leq t < 80, \\ 150 - 2.75(t - 80), & 80 \leq t < 130, \\ 12.5, & 130 \leq t < 250, \\ 12.5 + 0.705(t - 250), & 250 \leq t < 365. \end{cases}$$

The mixed-layer depth varies continuously through the year, except at $t = 80$ where there is a small jump of 0.025 m. The value of h, defined as dM/dt, simply takes the values of 0.705, -2.75, 0 and 0.705 in the four time intervals given in the above definition of M. During the summer, from days 130 to 250, the physical conditions correspond to the fixed conditions used for the preceding chapters, i.e. $M = 12.5$ and $h = 0$.

8.3 A gallery of time series

We now present numerical simulations for each of the models, with the mixed-layer depth forced as given in Figure 8.1. For brevity, we shall abbreviate the four models as follows: NPZ model - the original three-component NPZ model formulated in Chapter 2 and investigated in Chapter 3; $NPZl$ model - the three-component model with linear zooplankton mortality investigated in Chapter 4; $NPZD$ model - the original four-component $NPZD$ model investigated in Chapter 6, for which zooplankton do not graze on detritus; and $NPZDm$ model - the multiple-grazing four-component model investigated in Chapter 7, for which zooplankton graze on both phytoplankton and detritus.

Figure 8.2 shows the simulations when all parameters are set to their default values. Each model is run until it settles down to a repeating annual cycle, which usually occurs after three or four years from an arbitrary initial condition. The final year is then plotted. The most notable observation from comparing the time series is verification of one of the general conclusions from the preceding chapters - that compared to the original NPZ model, Figure 8.2(a), the consequences of replacing the quadratic zooplankton mortality term with the linear term, Figure 8.2(b), are

(a) NPZ model

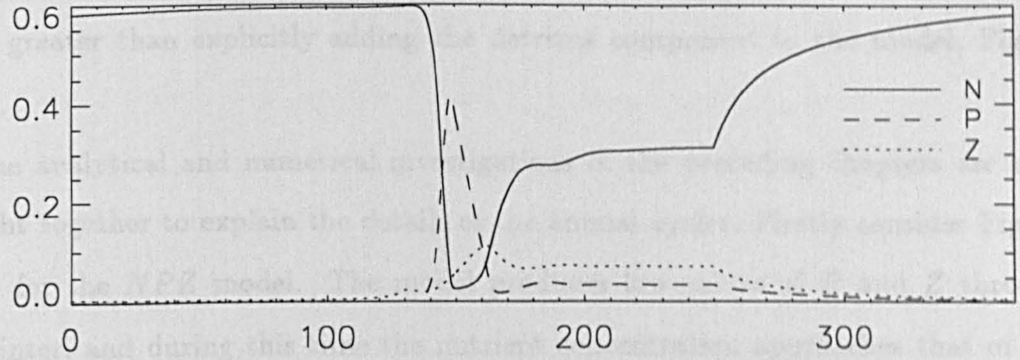

(b) NPZ with linear Z mortality

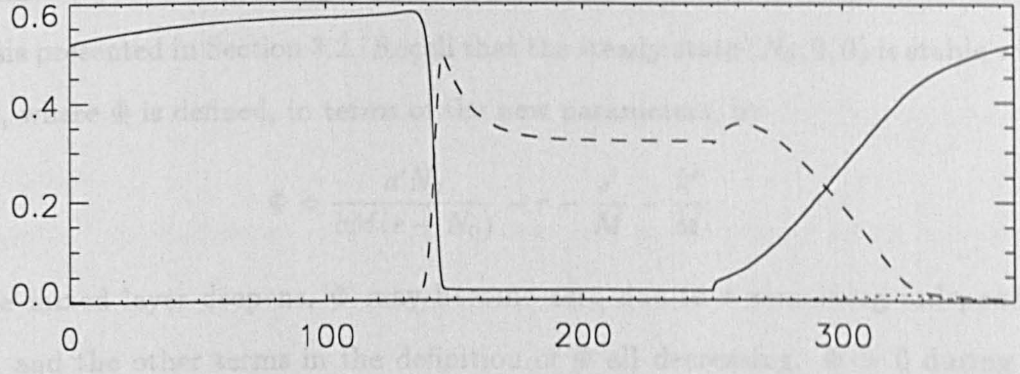

(c) NPZD model

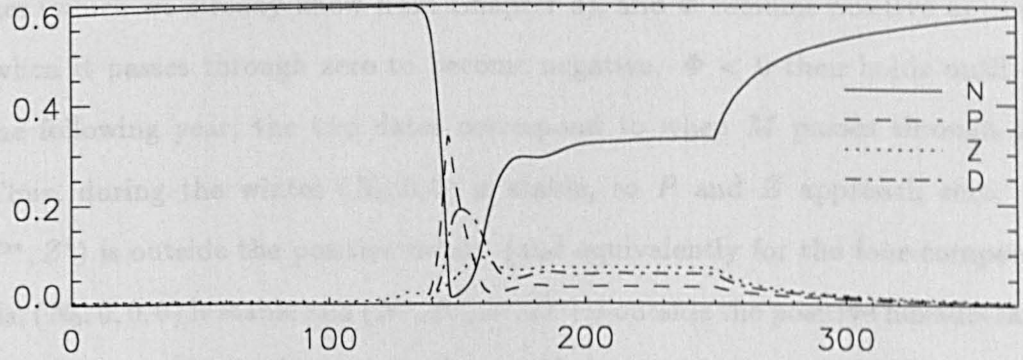

(d) NPZD with multiple grazing

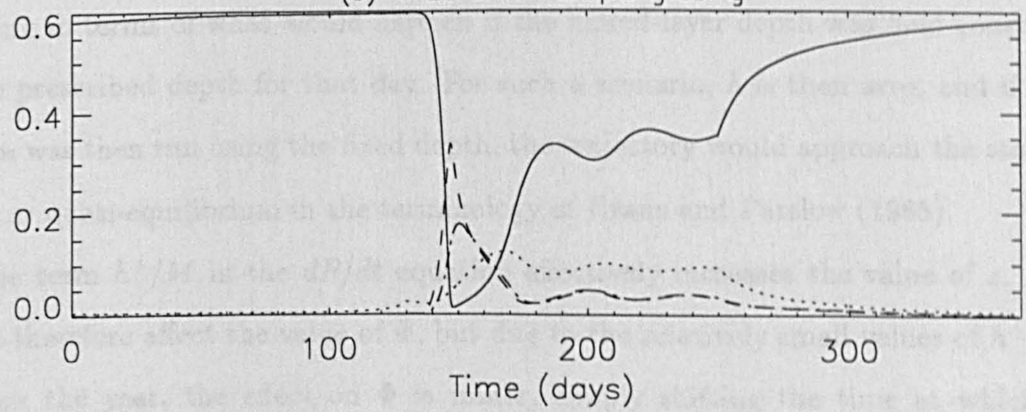

Figure 8.2: The time series for the four models when the mixed-layer depth is forced as given in Figure 8.1, and all parameters are set to their default values. All four time series repeat themselves each year. The analytical results of the previous chapters are used to explain the lack of zooplankton in the summer in (b).

much greater than explicitly adding the detritus component to the model, Figure 8.2(c).

The analytical and numerical investigations of the preceding chapters are now brought together to explain the details of the annual cycles. Firstly consider Figure 8.2(a) for the NPZ model. The model produces low values of P and Z through the winter, and during this time the nutrient concentration approaches that of the sub-mixed-layer water, namely $N_0 = 0.6$. This behaviour can be explained from the analysis presented in Section 3.2. Recall that the steady state $(N_0, 0, 0)$ is stable when $\Phi < 0$, where Φ is defined, in terms of the new parameters, by

$$\Phi = \frac{a' N_0}{bM(e + N_0)} - r - \frac{s'}{M} - \frac{k'}{M}.$$

As the mixed layer deepens, Φ may become zero due to r remaining independent of M, and the other terms in the definition of Φ all decreasing. $\Phi > 0$ during the summer (which we already know from Chapter 3), and Φ remains positive until day 335, when it passes through zero to become negative. $\Phi < 0$ then holds until day 109 the following year; the two dates correspond to when M passes through 71.9 m. Thus, during the winter $(N_0, 0, 0)$ is stable, so P and Z approach zero, and (N^*, P^*, Z^*) is outside the positive octant (and equivalently for the four-component models, $(N_0, 0, 0, 0)$ is stable and (N^*, P^*, Z^*, D^*) is outside the positive hexadectant). Note that when we talk about a steady state being stable on a certain day, we are thinking in terms of what would happen if the mixed-layer depth was held constant at the prescribed depth for that day. For such a scenario, h is then zero, and if the system was then run using the fixed depth, the trajectory would approach the steady state, or quasi-equilibrium in the terminology of Evans and Parslow (1985).

The term h^+/M in the dP/dt equation effectively increases the value of s, and would therefore affect the value of Φ, but due to the relatively small values of h^+/M through the year, the effect on Φ is minor, simply shifting the time at which Φ becomes zero in the autumn to seven days earlier (the other $\Phi = 0$ occasion, day 109, is unaffected since $h^+ = 0$ at this time).

In Figure 8.2(a) a pronounced bloom of phytoplankton occurs just after the mixed layer stabilises at the summer-time level. The nutrients are almost totally used up, and the zooplankton population increases due to the plentiful supply of food. The system then settles down to a steady state, the values of which are the same as those reached by the trajectory of Figure 3.2(a), since all parameters, plus the mixed-layer depth, are at their default values. The steady state (N^*, P^*, Z^*) arises from the steady state $(N_0, 0, 0)$ as Φ increases through zero, because at $\Phi = 0$ the three-way transcritical bifurcation occurs. The behaviour of (N^*, P^*, Z^*) will be qualitatively the same as that shown in the colour bifurcation diagram of Figure 3.1, although Φ is changing in a quantitatively different manner (a, s and k are decreasing, rather than r increasing).

Despite the continuous change of the location of the steady state, the bloom level of phytoplankton is much higher than the steady-state level. This is due to the forcing moving the steady state too fast for the trajectory to track it, together with the excitable nature of the system, as discussed by Truscott (1995). Excitability is usually thought of as a perturbation from equilibrium leading to a trajectory undergoing a large excursion before returning to equilibrium, and is characterised by the s-shape of one of the nullclines for a two-dimensional system. In this situation the nullsurfaces, as shown in Figure 4.4, are being shifted around by the forcing, and the shape of the P nullsurface, Figure 4.4(e), shows how a large increase in P can occur before the trajectory reaches the equilibrium (which has a low P-value)

The small increase in zooplankton prior to the spring bloom is due to the shallowing of the mixed layer concentrating the total zooplankton into a smaller volume of water, as modelled by the hZ/M term in (8.4).

At the end of the summer, the deepening of the mixed layer dilutes the phytoplankton and zooplankton populations, and decreases the phytoplankton growth rate. The abrupt non-smooth nature of the trajectory is due to the non-smooth change in the mixed-layer depth on day 250, and the consequent discontinuity in h, and could be smoothed out by using a smooth function to represent the mixed-layer depth. By the end of the year, $\Phi < 0$ and so $(N_0, 0, 0)$ is stable, and the annual cycle is repeated (exactly).

Figure 8.2(c), for the $NPZD$ model, displays very similar behaviour to that of the NPZ model, as expected from the results of Chapter 6, although the peak of the phytoplankton bloom is lower for the $NPZD$ model. The $NPZDm$ model exhibits similar behaviour, although the populations do not quite settle down to the steady state in the summer, they just appear to be approaching it. We can explain this from the one-parameter bifurcation diagrams of Figure 7.4 - at $d = 1.0$ the system is much closer to a Hopf bifurcation than for the previous two models, and so the steady state is less strongly attracting. This was also discussed in Section 7.4 (with reference to eigenvalues being closer to zero) in explaining the long transient time of the default trajectory of Figure 7.3(a).

Figure 8.2(b) for the $NPZl$ model presents a different picture to those for the other models. A phytoplankton bloom still occurs in the spring, but this is not followed by an increase in zooplankton. Rather, the zooplankton population remains very low, and does not recover until the autumn, by which time it is too late, since the mixed layer is deepening and the phytoplankton population is consequently decreasing. The analysis of Section 4.3.2 showed that the three-way transcritical bifurcation does not occur, but that two transcritical bifurcations occur, and the steady state $(N_1{}^*, P_1{}^*, 0)$ can become stable, as illustrated in the colour bifurcation diagrams of Figure 4.3 and the two-parameter bifurcation diagrams of Figure 4.8. When Φ increases through zero, $(N_1{}^*, P_1{}^*, 0)$, rather than (N^*, P^*, Z^*), becomes stable, and remains stable whilst the eigenvalue given by (4.15) is negative. This condition is also given by $\Omega < 0$, where Ω is defined by (4.28). The curves defining $\Omega = 0$ are shown in Figure 4.8, for each parameter being independently varied, and Figure 4.8(a) shows qualitatively how Ω will become negative when a becomes small due to the mixed-layer deepening (we say qualitatively since k and s will also vary, and slightly shift the picture).

$\Omega = 0$ occurs when $M = 66.3m$, which happens on days 111 and 327. When the mixed layer is shallowing $h = -2.75$, which essentially just reduces the value of q, and taking this into account in the definition of Ω, $\Omega = 0$ occurs on day 110, which is only one day after $\Phi = 0$. So $(N_1{}^*, P_1{}^*, 0)$ is stable for only one day - in terms of

Figure 4.8(a) a increases across the curve $\Phi = 0$ and then $\Omega = 0$ in one day.

But when Ω becomes positive, why does the Z value remain small and the trajectory stay close to $(N_1{}^*, P_1{}^*, 0)$ (which was only stable for a day) throughout the summer?

The eigenvalues of $(N_0, 0, 0)$ are $-k$, Φ and $-q$, and since the Jacobian at $(N_0, 0, 0)$ is upper-triangular, as given in Section 4.3.2, the local manifold for eigenvalue Φ is ~~corresponding local manifolds are in~~. $(-(k+\Phi)/\Phi+s+k, 1, 0)$, and so ~~the N, P and Z directions respectively. Thus~~ when Φ becomes positive, P will be repelled from zero but Z will remain small. For the day that $\Phi > 0$ and $\Omega < 0$, $(N_1{}^*, P_1{}^*, 0)$ is stable and attracts the trajectory. Then, when $\Omega > 0$, the eigenvalue given by (4.15), namely

$$\frac{\alpha \lambda P_1{}^{*2}}{\mu^2 + P_1{}^{*2}} - q,$$

is the only positive eigenvalue, and the corresponding local unstable manifold has a component in the Z-direction. The $Z = 0$ plane is a stable two-dimensional manifold for $(N_1{}^*, P_1{}^*, 0)$, and so, because Z is still small, N and P are attracted towards $N_1{}^*$ and $P_1{}^*$ rather than to N^* and P^*.

When the mixed layer reaches its constant summer-time level, $(N_1{}^*, P_1{}^*, 0) = (0.0196, 0.322, 0)$, as given by (4.18), and the trajectory in Figure 8.2(b) is close to this steady state, with Z still small. The eigenvalue given above takes the value 0.073, and so the trajectory is repelled from $(N_1{}^*, P_1{}^*, 0)$ very slowly. Another way of seeing this is that, from the dZ/dt equation, with $P \simeq P_1{}^*$, we have $dZ/dt = 0.073Z$, meaning that Z takes 9.5 days to double in size. Z manages to just reach a level high enough to show up on Figure 8.2(b) at the end of the summer, but then the mixed layer starts deepening. So although (N^*, P^*, Z^*) is stable during the summer, the trajectory remains close to $(N_1{}^*, P_1{}^*, 0)$. This is an example of why care has to be taken when using bifurcation diagrams corresponding to an unforced system to elucidate the behaviour of a forced system, and how a forced trajectory may stay close to an unstable steady state, as discussed in the 'Word of Caution' given by Wiggins (1990, page 384).

In Figure 8.3, r is set to 0.07, which is the value used by Evans and Parslow (1985). For $r = 0.07$, Φ remains positive throughout the year, and so $(N_0, 0, 0)$ does

(a) NPZ model

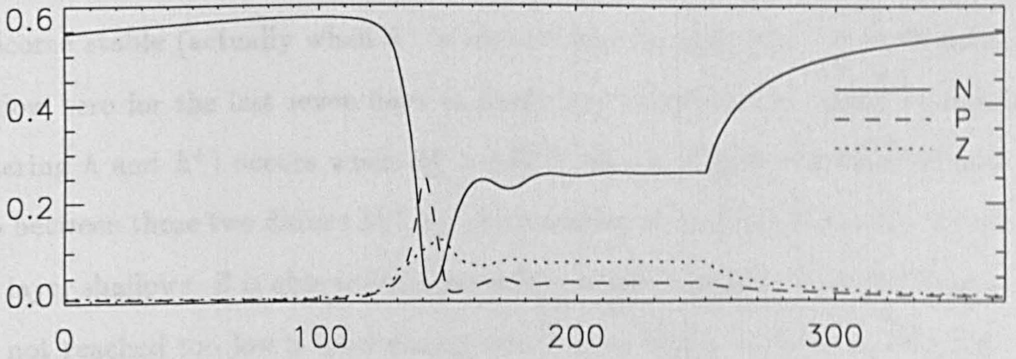

(b) NPZ with linear Z mortality

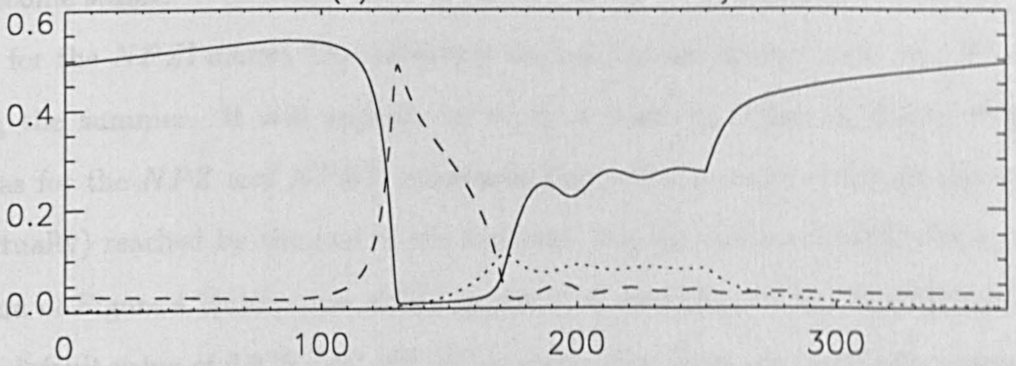

(c) NPZD model

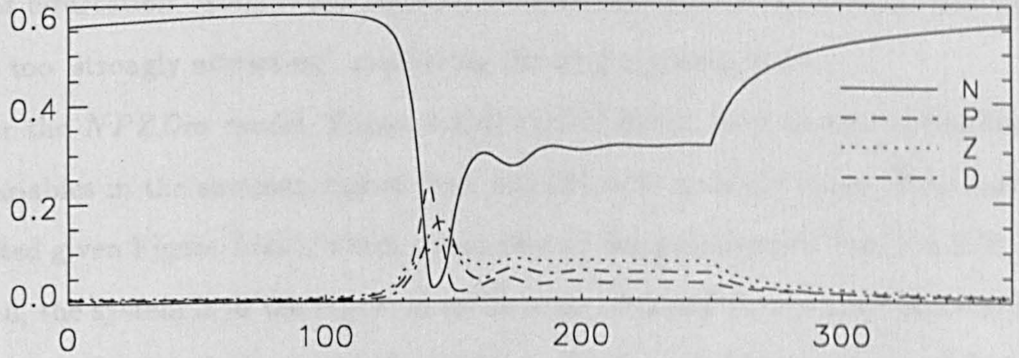

(d) NPZD with multiple grazing

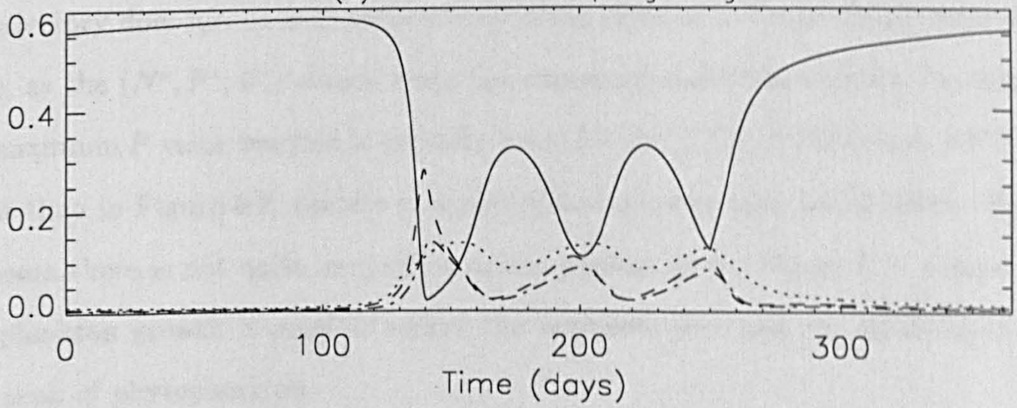

Figure 8.3: With $r = 0.07$ (the Evans and Parslow (1985) value), Φ does not quite become negative, and for the $NPZl$ model in (b), Z can increase in the summer. The $NPZDm$ model in (d) undergoes oscillations in the summer, as expected from the bifurcation diagram of Figure 7.5(e).

not become stable (actually when h^+ is included in the definition of Φ, Φ does just dip below zero for the last seven days of deepening of the mixed layer). $\Omega = 0$ (not considering h and h^+) occurs when $M = 142.0$, which happens on days 69 and 83, and so between these two dates $(N_1{}^*, P_1{}^*, 0)$ is stable for the $NPZl$ model. When the mixed layer shallows, Z is able to increase substantially, unlike in Figure 8.2(b), since it has not reached too low a level during the winter, which is because $(N_0, 0, 0)$ did not become stable.

So for the $NPZl$ model, the trajectory approaches the steady state (N^*, P^*, Z^*) during the summer. It still appears to be in a transient phase in Figure 8.3(b), whereas for the NPZ and $NPZD$ models in Figure 8.3(a) and (c) the steady state is (virtually) reached by the end of the summer. On the two-parameter bifurcation diagram of Figure 4.7(e) for the $NPZl$ model, it is seen that when $r = 0.07$ and q is at the default value of 0.075, (N^*, P^*, Z^*) is stable, but close (in parameter space) to a Hopf bifurcation. Thus it has eigenvalues with real parts close to zero, and hence is not too 'strongly attracting', explaining the long transient time.

For the $NPZDm$ model, Figure 8.3(d) clearly shows pronounced oscillations of the variables in the summer, rather than attraction to a steady state. This is to be expected given Figure 7.5(e), which shows that at the parameter values $r = 0.07$ and $d = 1.0$, the system is in the region of oscillations bounded by the Hopf bifurcations.

In all the models the spring bloom occurs earlier than for Figure 8.2; this is because the trajectory does not have to escape from being close to a stable steady state with $P = 0$, as the (N^*, P^*, Z^*) steady state has remained stable throughout the winter. The maximum P value reached is actually lower for the $NPZ, NPZD$ and $NPZDm$ models than in Figure 8.2, despite r, a phytoplankton loss rate, being lower. Before the bloom there is not quite as much nutrient present as for Figure 8.2, and so less phytoplankton growth is possible before the nutrients are used up, resulting in the lower peak of phytoplankton.

In Figure 8.4 we set $r = 0.05$, the value used by Henderson and Steele (1995). The minimum value of Φ now reached is 0.02, and so (N^*, P^*, Z^*) (or (N^*, P^*, Z^*, D^*)) remains stable and in the positive octant (hexadectant), and does not get as close to

(a) NPZ model

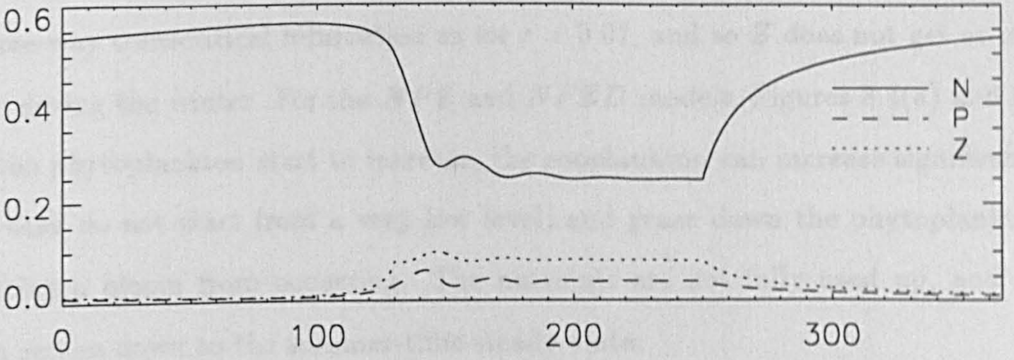

(b) NPZ with linear Z mortality

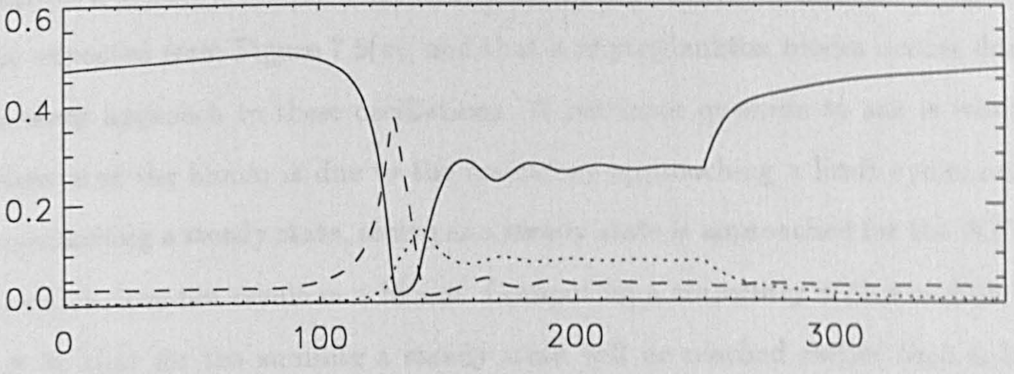

(c) NPZD model

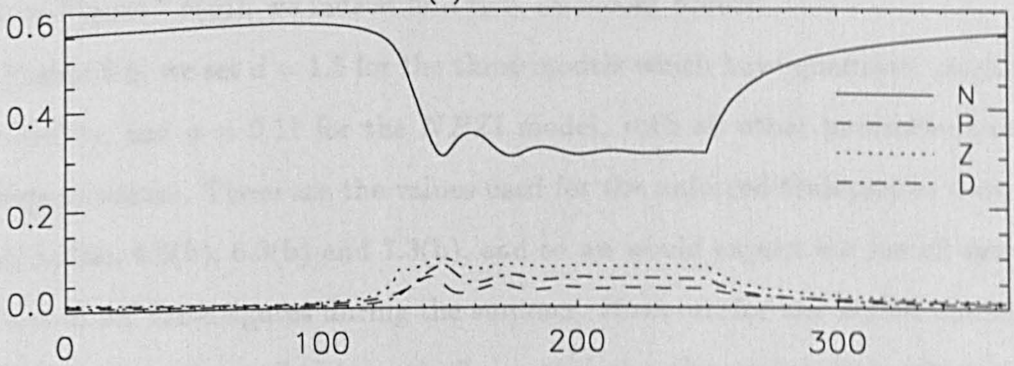

(d) NPZD with multiple grazing

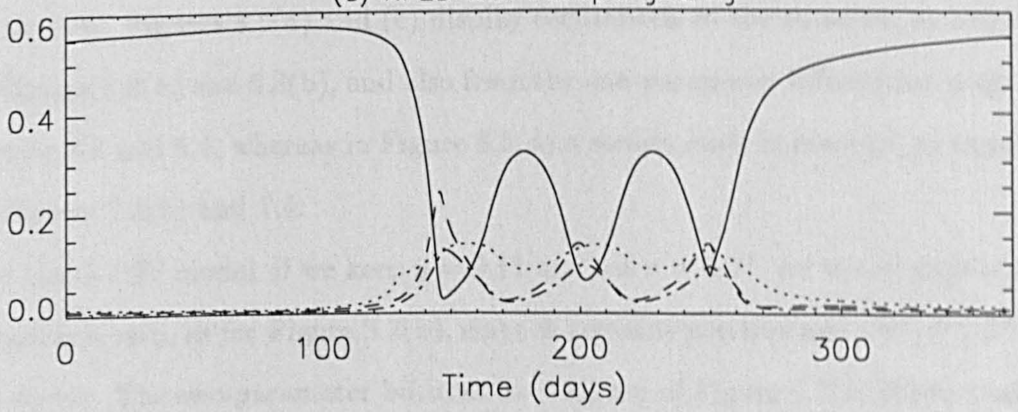

Figure 8.4: With $r = 0.05$ (the Henderson and Steele (1995) value), Z does not become too small in the winter, and so for (a) and (c), Z can keep up with the increase in P, preventing a bloom (note that N is not used up). For (d), Figure 7.5(e) explains why oscillations occur during the summer, rather than a steady state.

the three-way transcritical bifurcation as for $r = 0.07$, and so Z does not get as near to zero during the winter. For the NPZ and $NPZD$ models, Figures 8.4(a) and (c), when the phytoplankton start to increase, the zooplankton can increase significantly (since they do not start from a very low level) and graze down the phytoplankton, preventing a bloom from occurring. The nutrients are not fully used up, and the system settles down to the summer-time steady state.

Figure 8.4(d) shows that oscillations occur in the summer for the $NPZDm$ model, as to be expected from Figure 7.5(e), and that a phytoplankton bloom occurs during the transient approach to these oscillations. A pertinent question to ask is whether the presence of the bloom is due to the trajectory approaching a limit cycle, rather than approaching a steady state, seeing as a steady state is approached for the $NPZD$ model, which does not result in a bloom. Computing a trajectory with $r = 0.05$ and $d = 0.8$, so that for the summer a steady state will be reached rather than a limit cycle (see Figure 7.5(e)), we indeed find that no bloom occurs.

In Figure 8.5, we set $d = 1.5$ for the three models which have quadratic zooplankton mortality, and $q = 0.11$ for the $NPZl$ model, with all other parameters set to their default values. These are the values used for the unforced trajectories shown in Figures 3.2(b), 4.5(b), 6.3(b) and 7.3(b), and so we would expect the forced systems to behave as for these figures during the summer. However, for the $NPZl$ model the high Z mortality reduces Z to (practically) zero during the winter, from which it can never recover. Figures 8.5(a) and (c) display oscillations in the summer, as expected from Figures 3.2(b) and 6.3(b), and also from the one-parameter bifurcation diagrams of Figures 3.3 and 6.4, whereas in Figure 8.5(d) a steady state is reached, as expected from Figures 7.3(b) and 7.4.

For the $NPZl$ model, if we keep $q = 0.11$ and set $r = 0.07$, we would expect Z to not approach zero, as for Figure 8.3(b), since Φ remains positive and (N^*, P^*, Z^*) remains stable. The two-parameter bifurcation diagram of Figure 4.7(e) shows that oscillations are to be expected during the summer, with the period-contour diagram of Figure 4.12(e) implying that these oscillations will have a period of 30 days. However, unlike the time series in the previous figures, the computed trajectory for $q = 0.11$

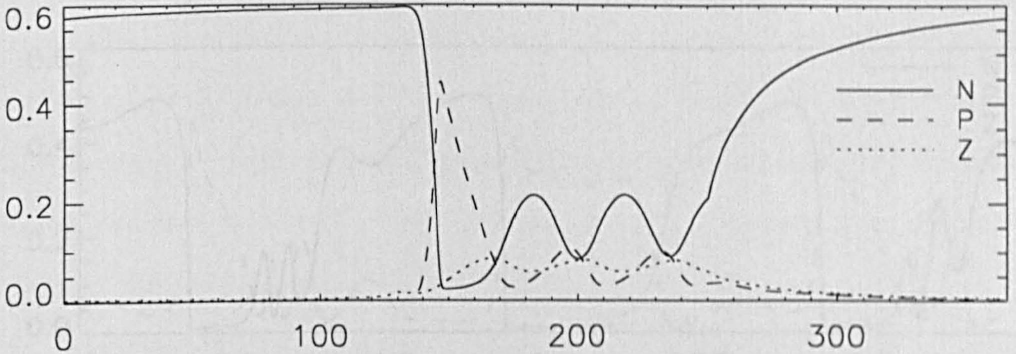
(a) NPZ model

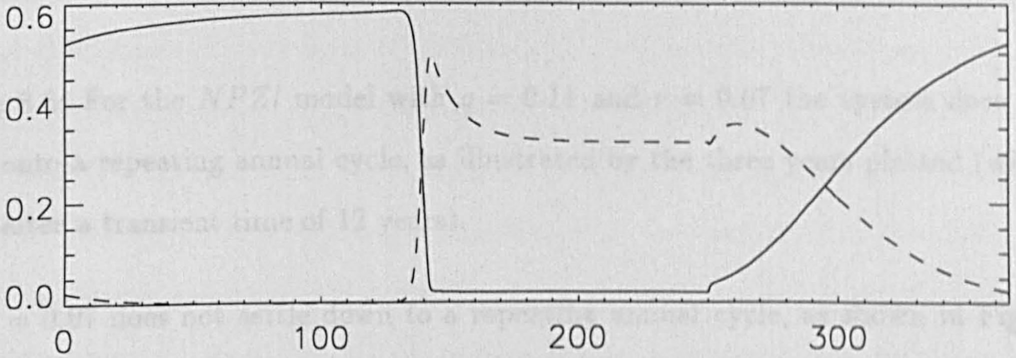
(b) NPZ with linear Z mortality

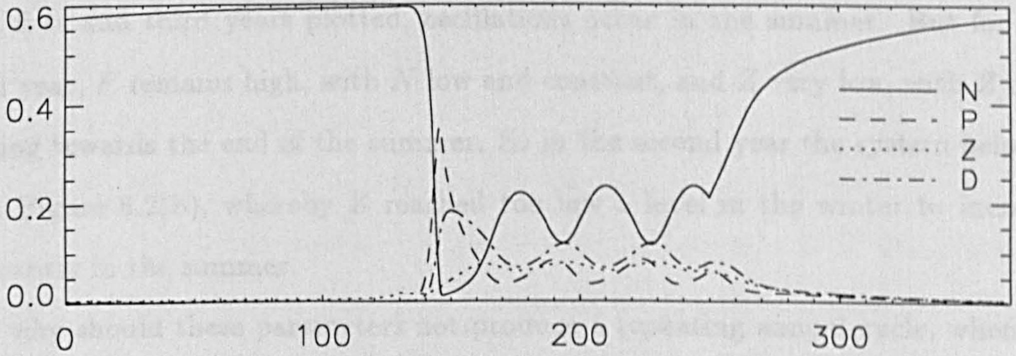
(c) NPZD model

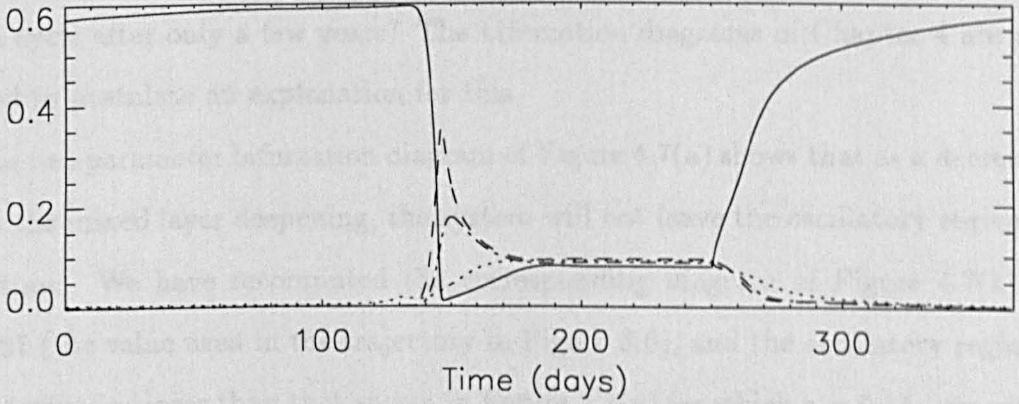
(d) NPZD with multiple grazing

Figure 8.5: Zooplankton mortality is set to $d = 1.5$ for (a), (c) and (d), and $q = 0.11$ for (b). For the *NPZl* model, Z reaches (virtually) zero in the winter from which it cannot recover, whereas the other models exhibit spring blooms, and then in the summertime are attracted to the attractors shown in Figures 3.2(b), 6.3(b) and 7.3(b).

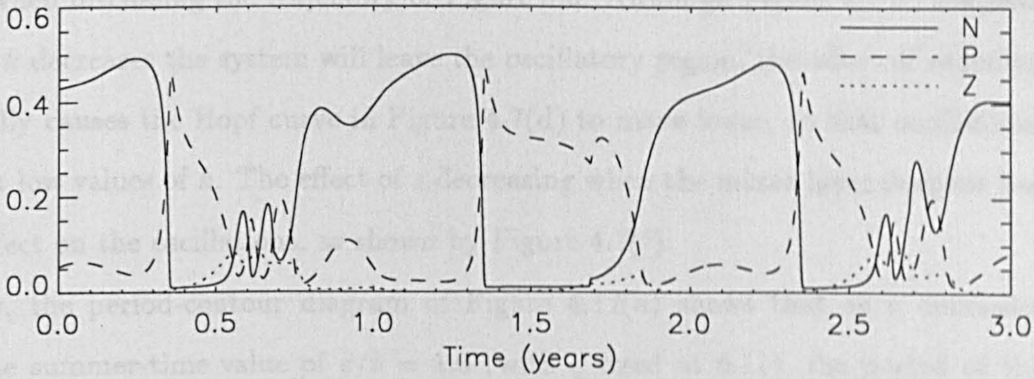

Figure 8.6: For the $NPZl$ model with $q = 0.11$ and $r = 0.07$ the system does not settle onto a repeating annual cycle, as illustrated by the three years plotted (which occur after a transient time of 12 years).

and $r = 0.07$ does not settle down to a repeating annual cycle, as shown in Figure 8.6. Three years are shown (after the system has already been run for 12 years), and in the first and third years plotted, oscillations occur in the summer. But for the second year, P remains high, with N low and constant, and Z very low, with Z only emerging towards the end of the summer. So in the second year the system behaves like in Figure 8.2(b), whereby Z reached too low a level in the winter to increase significantly in the summer.

So why should these parameters not produce a repeating annual cycle, when for the other parameter values and models investigated so far the system settles down to such a cycle after only a few years? The bifurcation diagrams of Chapter 4 are now invoked to postulate an explanation for this.

The two-parameter bifurcation diagram of Figure 4.7(a) shows that as a decreases, due to the mixed layer deepening, the system will not leave the oscillatory region for some time. We have recomputed the corresponding diagram of Figure 4.7(a) for $r = 0.07$ (the value used in the trajectory in Figure 8.6), and the oscillatory region is just marginally larger than that shown in Figure 4.7(a) for which $r = 0.15$ - we would expect such similarity given the nature of Figure 4.7(e), which shows the insensitivity of the Hopf bifurcations to the value of r. Thus we feel justified in referring to Figure

4.7(a) when discussing the trajectory of Figure 8.6. Although Figure 4.7(d) suggests that as k decreases the system will leave the oscillatory region, the effect of reducing a actually causes the Hopf curve in Figure 4.7(d) to move lower, so that oscillations occur at low values of k. The effect of s decreasing when the mixed layer deepens has little effect on the oscillations, as shown by Figure 4.7(f).

Now, the period-contour diagram of Figure 4.12(a) shows that as a decreases from the summer-time value of $a/b = 1.0$ (with q fixed at 0.11), the period of the oscillations increases dramatically. It only takes 18 days for the mixed layer to deepen to double its summer-time depth, and thus it takes 18 days for a/b to halve in value from 1.0 to 0.5. In this short time, the period of the unforced oscillations doubles to almost 70 days (Figure 4.12(a)). It is therefore not unreasonable to expect the forced trajectory to have difficulty in remaining close to a stable limit cycle during this forcing, and consequently the trajectory will be sensitive to the values of N, P and Z at the onset of the forcing. For the first and third years plotted in Figure 8.6, the system appears to have settled onto a limit cycle by the late summer. The mixed layer starts deepening on day 250 of each year (which is at 0.68 and 2.68 years in the figure). At this point, the trajectories may well be on the 'same' stable limit cycle, but are at different positions along it - for the first year N is decreasing (at time 0.68), but for the third year N is increasing (at time 2.68). This leads to the different trajectories in the final months of these years (most clearly seen for N), and so the conditions at the start of the proceeding years are slightly different. The year following the three years shown exhibits oscillations in the summer with a healthy Z population, and so the summer-time behaviours do not simply alternate between the two regimes pictured. Hence the long periods shown in Figure 4.12(a) serve as a plausible explanation of why the system does not 'reset itself' at the end of each year to exhibit repeating annual cycles.

In Figure 8.7, the zooplankton excretion parameter β is set to the increased level of 0.6, with $d = 1.5$. For the $NPZl$ model in (b), $q = 0.11$, $r = 0.07$ (so that the zooplankton do not die out) and $\beta = 0.6$; there is not an annually-repeating cycle (most likely for the same reasons as for Figure 8.6), and we plot three years as an

(a) NPZ model

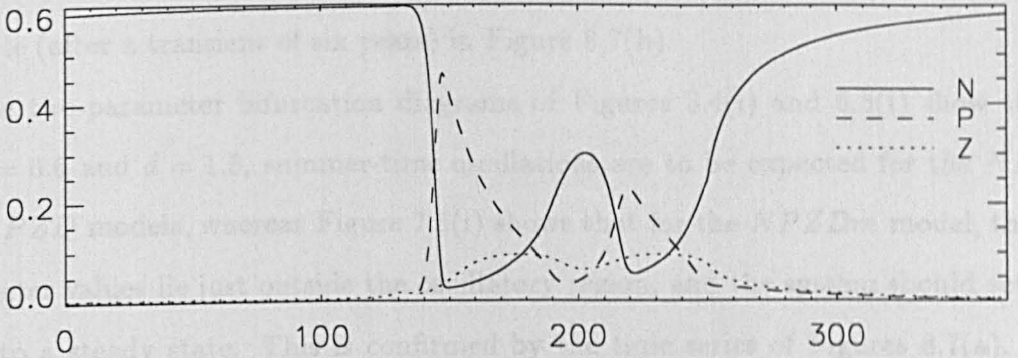

(b) NPZ with linear Z mortality

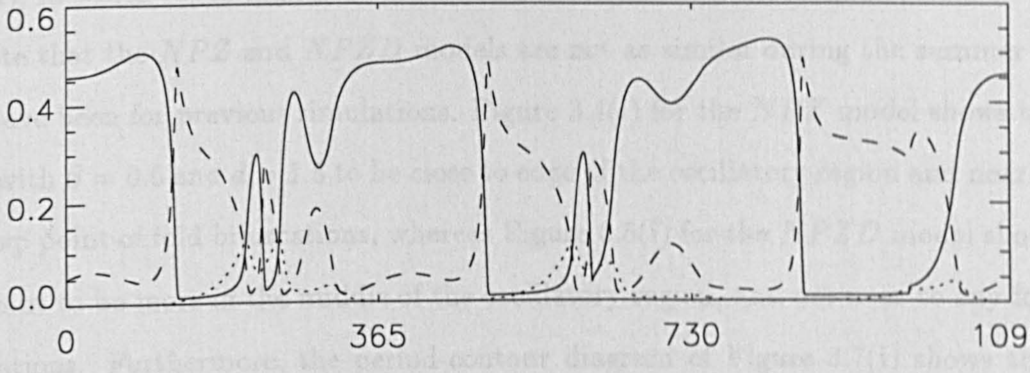

(c) NPZD model

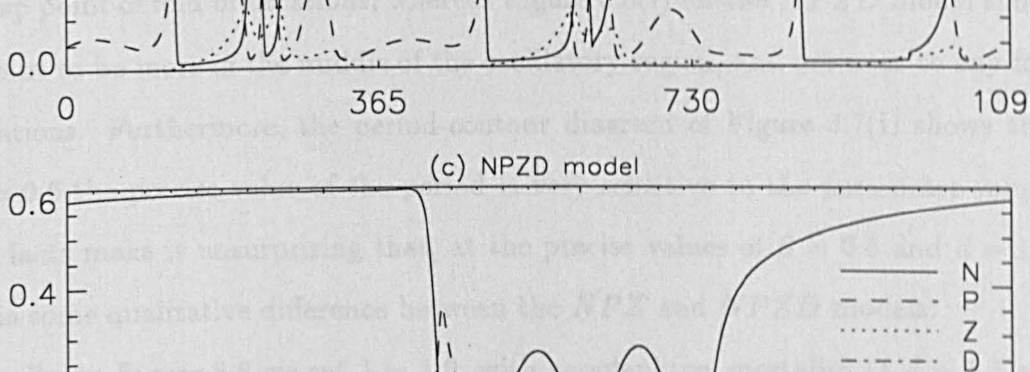

(d) NPZD with multiple grazing

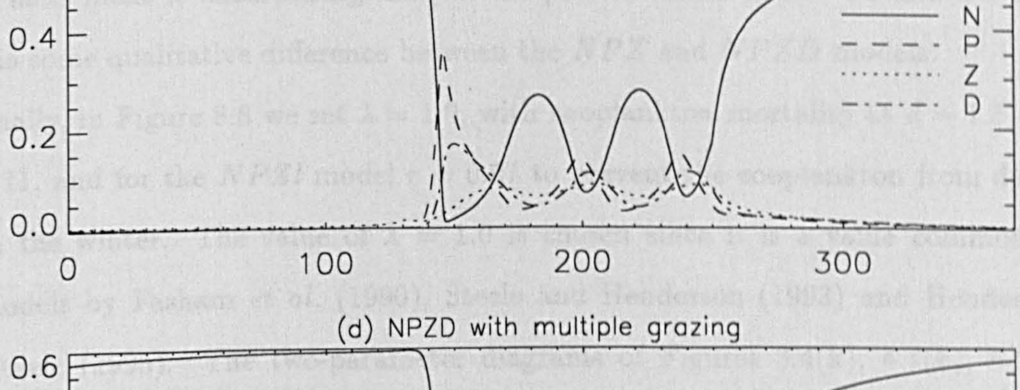

Figure 8.7: With $\beta = 0.6$ and $d = 1.5$ the NPZ and $NPZD$ models exhibit summer-time oscillations, whereas the $NPZDm$ does not, as to be expected from the corresponding two-parameter bifurcation diagrams. For the $NPZl$ model $\beta = 0.6, q = 0.11$ and $r = 0.07$; three years are plotted to show that no annual cycle is reached.

example (after a transient of six years) in Figure 8.7(b).

The two-parameter bifurcation diagrams of Figures 3.4(i) and 6.5(i) show that for $\beta = 0.6$ and $d = 1.5$, summer-time oscillations are to be expected for the NPZ and $NPZD$ models, whereas Figure 7.5(i) shows that for the $NPZDm$ model, these parameter values lie just outside the oscillatory region, and the system should settle down to a steady state. This is confirmed by the time series of Figures 8.7(a), (c) and (d), in which repeating annual cycles are shown.

Note that the NPZ and $NPZD$ models are not as similar during the summer as they have been for previous simulations. Figure 3.4(i) for the NPZ model shows the point with $\beta = 0.6$ and $d = 1.5$ to be close to edge of the oscillatory region and near to the cusp point of fold bifurcations, whereas Figure 6.5(i) for the $NPZD$ model shows this point to be more in the middle of the oscillatory region, and not near to any fold bifurcations. Furthermore, the period-contour diagram of Figure 3.7(i) shows that at $\beta = 0.6$ the precise value of the period is very sensitive to the parameter values. These facts make it unsurprising that, at the precise values of $\beta = 0.6$ and $d = 1.5$, there is some qualitative difference between the NPZ and $NPZD$ models.

Finally, in Figure 8.8 we set $\lambda = 1.0$, with zooplankton mortality at $d = 1.5$ and $q = 0.11$, and for the $NPZl$ model $r = 0.07$ to prevent the zooplankton from dying out in the winter. The value of $\lambda = 1.0$ is chosen since it is a value common to the models by Fasham *et al.* (1990), Steele and Henderson (1993) and Henderson and Steele (1995). The two-parameter diagrams of Figures 3.4(k), 4.7(k), 6.5(k) and 7.5(k) show that with $\lambda = 1.0$ the systems are outside the oscillatory regions, and hence in the summer all the models converge to steady states. The bifurcation diagrams show locations of Hopf and fold bifurcations, and suggest that the NPZ and $NPZD$ models are similar in behaviour; this example shows that even away from any bifurcations this is still true. The $NPZDm$ model is fairly similar to the NPZ and $NPZD$ models, with the $NPZl$ model exhibiting a much larger and earlier phytoplankton bloom, but this is to be expected since a lower value of r is used (as discussed with reference to Figure 8.3).

(a) NPZ model

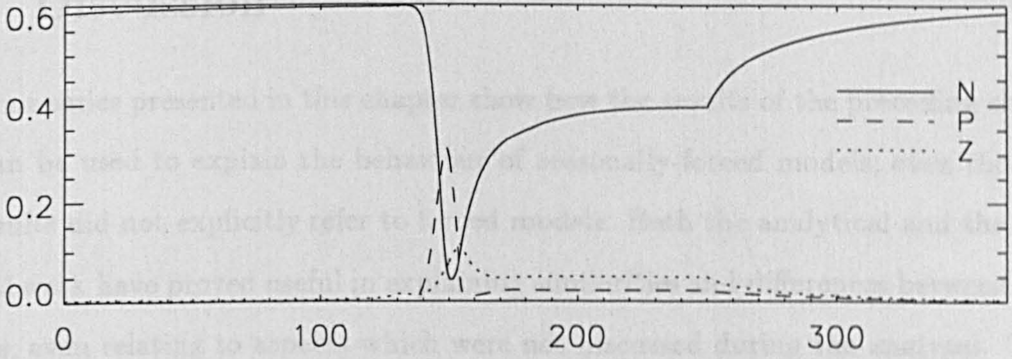

(b) NPZ with linear Z mortality

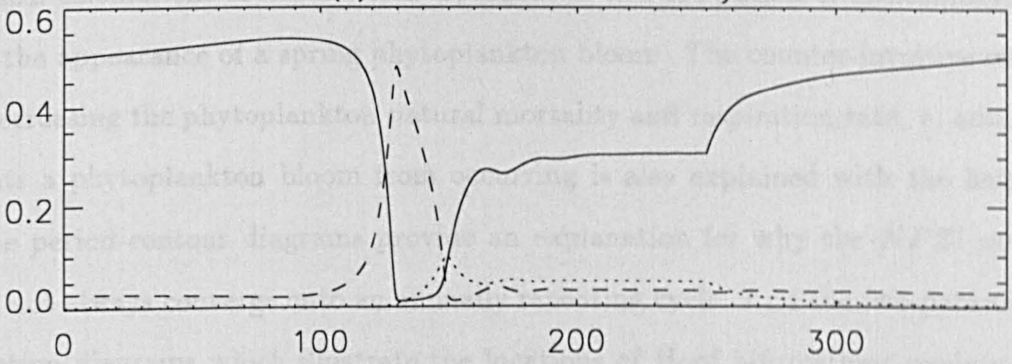

(c) NPZD model

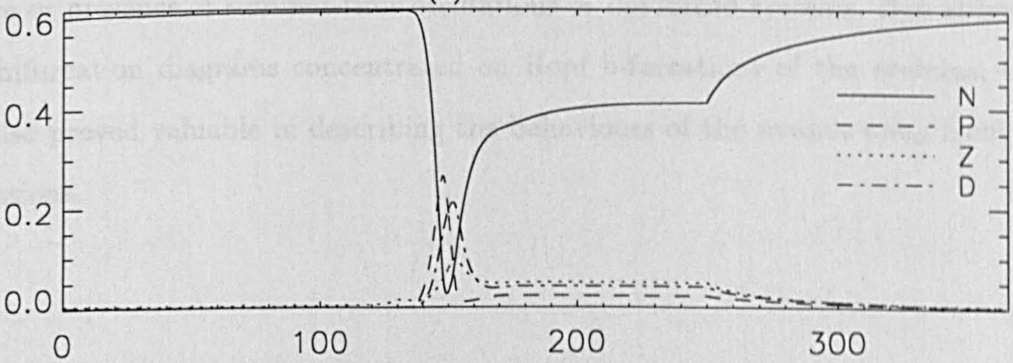

(d) NPZD with multiple grazing

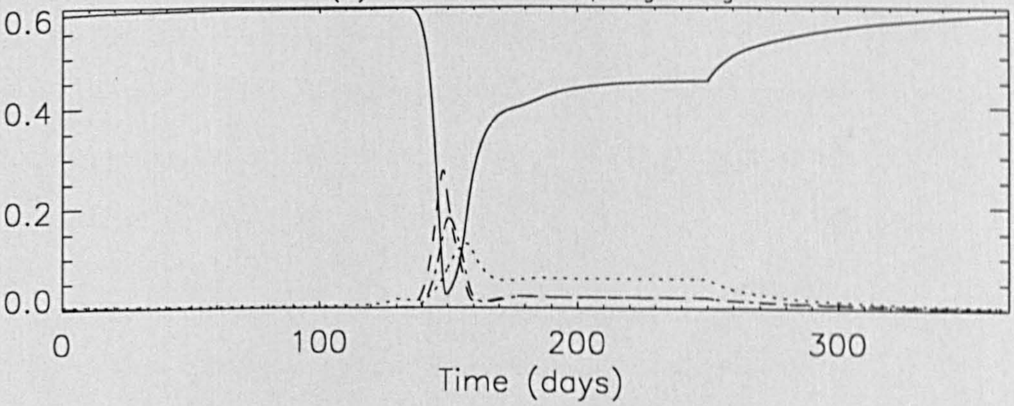

Figure 8.8: With $\lambda = 1.0$ and $d = 1.5$, ($q = 0.11$ and $r = 0.07$ for the $NPZl$ model), all models are attracted to a steady state in the summer.

8.4 Discussion

The time series presented in this chapter show how the results of the preceding chapters can be used to explain the behaviour of seasonally-forced models, even though the results did not explicitly refer to forced models. Both the analytical and the numerical work have proved useful in explaining similarities and differences between the models, even relating to aspects which were not discussed during the analyses. The analytical calculations of the function Φ, together with the notion of excitability, explains the appearance of a spring phytoplankton bloom. The counter-intuitive result that decreasing the phytoplankton natural mortality and respiration rate, r, actually prevents a phytoplankton bloom from occurring is also explained with the help of Φ. The period-contour diagrams provide an explanation for why the $NPZl$ model should not always converge onto an annually repeating cycle. And the two-parameter bifurcation diagrams which illustrate the locations of Hopf bifurcations explain the absence or presence of summer-time oscillations of the forced systems. But although these bifurcation diagrams concentrated on Hopf bifurcations of the systems, they have also proved valuable in describing the behaviours of the models away from the bifurcations.

Chapter 9

Conclusions

In this thesis we have systematically investigated the dynamical behaviour of four plankton models, and re-examined the work of Steele and Henderson (1992). Chapter 8 has served to illustrate the usefulness of our analytical results and numerically-computed bifurcation diagrams in explaining and comparing the output of the models. The main conclusions of our research can be summarised as follows:

- in agreement with Steele and Henderson (1992), we have found our NPZ model to be sensitive to the form of the zooplankton mortality function (linear or quadratic) and the subsequent parameter values used, but, in contrast to their results, we have shown that unforced oscillations can occur when the quadratic function is used;

- our two-parameter bifurcation diagrams indicate the effects of varying each of the parameters in the models, demonstrating which parameters are most crucial in influencing model behaviour - this is of importance given the difficulties involved in parameter estimation;

- in general, the sensitivity to a particular parameter tends to be the same across all four of the models investigated - for example, Figures 3.4(j), 4.7(j), 6.5(j) and 7.5(j) all show that the oscillations occur across the full range of the excretion regeneration parameter γ;

- oscillations appear to occur over a greater range of parameter values for the linear zooplankton mortality function than for the quadratic function, and so are more likely to be observed for the linear function, in accord with the findings of Steele and Henderson (1992);

- the array of bifurcations - 'three-way transcritical', Hopf, fold (of steady states and limit cycles), Bogdanov-Takens and homoclinic connections - exhibited by our NPZ model with quadratic zooplankton mortality is preserved when a fourth equation, explicitly modelling detritus, is added to the system;

- if an ecosystem can be modelled by the $NPZD$ model of Chapter 6, but knowledge of the level of detritus is not explicitly required and zooplankton do not consume detritus, then the NPZ model of Chapter 3 will adequately describe the dynamics;

- if zooplankton do graze on detritus, even only slightly, then the full $NPZD$ model of Chapter 7 is required to determine the behaviour;

- for the NPZ model with linear zooplankton mortality, the Hopf bifurcations are the only ones from the aforementioned list that occur, with the three-way transcritical bifurcation splitting into two transcritical bifurcations, meaning that zooplankton can die out even if their phytoplankton prey do not;

- the NPZ model with linear zooplankton mortality is the only model that appears to exhibit period-doubling bifurcations of limit cycles, with a subsequent cascade to chaos, although such behaviour only occurs across a very limited range of parameter values;

- we have corrected the anomalous normalisation of the NPZ model of Steele and Henderson (1992), and then by using the bifurcation diagrams of Chapter 3, we have shown that their NPZ model can exhibit oscillations when the quadratic mortality function is used.

We would hope that our results, particularly the two-parameter bifurcation diagrams, prove useful to modellers in interpreting the output of models. It is of interest to ascertain if the results apply to other models. Fasham *et al.* (1993) coupled the seven-component model of Fasham *et al.* (1990) to a general circulation model of the North Atlantic, and did not find any large-amplitude limit cycles. However, they noted that Toggweiler (1990) used the same ecosystem model and did observe such cycles for high nitrate input conditions corresponding to the Peruvian upwelling region of the Pacific. High nitrate input in our models is given by high values of the cross-thermocline exchange rate, k, or the sub-mixed-layer nutrient concentration N_0. For all of our models, the corresponding two-parameter bifurcation diagrams indicate that limit cycles do not occur at low values of these parameters but can at higher values, in accord with the comments of Fasham *et al.* (1993).

Ryabchenko *et al.* (1997) have found, using a model based on that of Fasham (1993), that short-term oscillations can occur when there is a combination of high photosynthetically active radiation, a high nitrogen concentration below the mixed layer, small thickness of the upper mixed layer and significant mean annual entrainment velocity. For our models, the first two conditions correspond to high values of a and N_0 respectively. A shallow mixed layer is given by high values of a, k and s; we only consider entrainment in Chapter 8, and so none of the bifurcation diagrams are relevant. Our two-parameter bifurcation diagrams throughout the thesis all show that high values of a, k, s and N_0 give oscillations, whilst low values of a, k and N_0 do not. The results of Ryabchenko *et al.* (1997) are thus also consistent with ours.

Furthermore, Yool (1997) has found oscillations in the seven-component Fasham (1993) model (with the forcing switched off), and his results are in broad agreement with our two-parameter bifurcation diagrams. For example, limit cycles can occur at high values of sub-mixed-layer nutrient concentration, phytoplankton growth rate and detritus breakdown rate, although the latter requires an unrealistically high value. These correspond in our models to the parameters N_0, a and ϕ, and again the two-parameter bifurcation diagrams show that oscillations do not occur at low values of these parameters (except for ϕ in our multiple-grazing $NPZD$ model).

We have found chaotic dynamics only when the linear zooplankton mortality function is used, whereas Caswell and Neubert (1997) have found that chaos can occur for both mortality functions in a simple three-species food chain model. Therefore we do not extrapolate our results to propose a hypothesis that the choice of mortality function is the sole determinant of chaos in general three-species models.

By investigating the sensitivities of our models to *all* of the parameters, and not just concentrating on one or two, we have shown which parameters are most crucial in determining the dynamics of our models. If these results do indeed hold across a broader class of models than those investigated here, as is suggested above, then by indicating which parameter values need to be obtained most accurately, such information could help direct measurement efforts in the most efficient manner.

The work presented in this thesis could be extended in a number of directions. The only functional form that we have changed in the models has been that representing zooplankton mortality. It would be insightful to repeat our investigations using alternative functions for some of the other processes, the principal candidate would be to use a Holling Type II form for zooplankton grazing. Another extension would involve adding a fifth component, such as bacteria, to the $NPZD$ models to bring the structure a step closer to that of the seven-component model of Fasham (1993). Subsequently the sixth and seventh components of Fasham's model could be added, to see how the bifurcations persist. The resulting seven-component model would have the same ecosystem structure as Fasham's model, but with some differing functional forms. Alternatively, since the dynamics of our three- and four-component models are now well understood, the models could be extended by adding spatial dimensions and incorporating effects such as diffusion or vertical migration by zooplankton.

Fasham (1993) discussed whether one generic plankton model can be constructed that would be sufficient to model all the areas of the world's oceans. At present this question remains unanswered. The results in this thesis improve the understanding of the dynamics of plankton models, and we hope that they will play a small part towards future development of models, possibly culminating with such a generic model.

Appendix A

Formulation of phytoplankton growth rate

The following analysis shows how the phytoplankton growth (or primary production) term $aP/(b+cP)$ used by Steele and Henderson (1981), and therefore in our models, can be obtained from the canonical form derived by Platt *et al.* (1990) and Platt and Sathyendranath (1993). Nutrient limitation is represented by the independent term $N/(e+N)$ in the original equation (2.2) in Chapter 2, and plays no further part in this analysis. We are essentially just redefining the parameter a, since the original definition by Steele and Frost (1977) was based on the unsatisfactory photosynthesis-light curve given by Steele (1962). We take summertime data and parameter values at two geographical locations as used by Fasham (1993), plus further parameter values used by Evans and Parslow (1985) and Wroblewski (1989), to obtain a range of values for a. This range for a is 0.11-0.16, which actually falls well within the range of 0.07-0.28 obtained from using the a/b values of Steele and Henderson (1992), Armstrong (1994) and Henderson and Steele (1995) in Chapter 2. Hence the following analysis simply results in values which have already been included in our range for a. It shows how our $aP/(b+cP)$ is consistent with the canonical form of Platt *et al.* (1990) and Platt and Sathyendranath (1993), and demonstrates how seasonal variation in sunlight can be incorporated into our model.

We now derive the function $aP/(b+cP)$ from the primary production canonical form of Platt and Sathyendranath (1993) (hereafter referred to as PS93), retaining their notation. The canonical form gives an analytical expression which can be approximated by a fifth order polynomial (whose coefficients are known), resulting in a simpler expression than the analytical function derived by Evans and Parslow (1985), which Fasham (1993) subsequently used. All new parameter definitions and units are summarised in Table A.1.

The function $aP/(b+cP)$ is the (non-nutrient limited) primary production rate per unit volume per day, which has units of $g\ C\ m^{-3}\ d^{-1}$, where P (measured in $g\ C\ m^{-3}$) is the phytoplankton concentration, b (m^{-1}) represents light attenuation by water, c ($m^2(g\ C)^{-1}$) parameterises the attenuation due to the phytoplankton population and a ($m^{-1}\ d^{-1}$) is a parameter whose magnitude shall be re-evaluated here.

The daily primary production for a mixed layer of depth Z_m (units m) is denoted by $P_{Z_m,T}$ ($mg\ C\ m^{-2}$) and given by equation (39) of PS93, viz:

$$P_{Z_m,T} = \frac{BP_m^BD}{K}\left[f\left(I_*^m\right) - f\left(I_*^m e^{-KZ_m}\right)\right], \tag{A.1}$$

where B is the biomass concentration ($mg\ Chl\ m^{-3}$), P_m^B is the specific production at saturating light ($mg\ C\ (mg\ Chl)^{-1}\ h^{-1}$), D is the number of hours of sunlight in a day (h) and is dependent on both time of year and latitude, K is the vertical attenuation coefficient for irradiance (m^{-1}), I_*^m is the dimensionless noon irradiance (explained later) and f is a dimensionless function of I_*^m, which can be approximated (as good as error free) by a fifth order polynomial.

Irradiance is attenuated through the water column due to both turbidity of the water and shading effects of the phytoplankton, and so the coefficient K equals our $(b+cP)$ term. $P_{Z_m,T}$ is the daily primary production for the mixed layer under one square metre, and since we require the primary production per unit volume per day we define $< P_{Z_m,T} >$ ($mg\ C\ m^{-3}\ d^{-1}$) to be $P_{Z_m,T}$ divided by Z_m and divided by one day. $< P_{Z_m,T} >$ now has the same definition as $aP/(b+cP)$, although the units are not yet the same (but the dimensions are equivalent).

Parameter	Symbol	Units
Platt and Sathyendranath (1993):		
Initial slope of photosynthesis-irradiance (P-I) curve	α	$mg\ C\ h^{-1}$ $(W\ m^{-2})^{-1} m^{-3}$
Initial slope of normalised photosynthesis-irradiance curve	α^B	$mg\ C\ (mg\ Chl)^{-1}$ $h^{-1}\ (W\ m^{-2})^{-1}$
Phytoplankton biomass, as concentration of chlorophyll *a*	B	$mg\ Chl\ m^{-3}$
Daylength, number of hours of sunlight in a day	D	h
Function of I_*^m	f	dimensionless
Dimensionless irradiance at local noon, $I_*^m := I_0^m/I_k$	I_*^m	dimensionless
Surface irradiance at local noon	I_0^m	$W\ m^{-2}$
Photoadaption parameter of the P-I curve, $I_k := P_m/\alpha$	I_k	$W\ m^{-2}$
Vertical attenuation coefficient for irradiance	K	m^{-1}
Primary production (maximum) at saturating light	P_m	$mg\ C\ m^{-3}\ h^{-1}$
Specific production at saturating light, $P_m^B = P_m/B$	P_m^B	$mg\ C\ (mg\ Chl)^{-1}$ h^{-1}
Daily primary production for the mixed layer	$P_{Z_m,T}$	$mg\ C\ m^{-2}$
Mixed layer depth	Z_m	m
Fasham (1993):		
Phytoplankton maximum growth rate	V_p	d^{-1}
Initial slope of normalised photosynthesis-irradiance curve	α_F	$(W\ m^{-2})^{-1}\ d^{-1}$

Table A.1: Parameter definitions and units, grouped according to source. Abbreviations of units are: C - carbon, Chl - chlorophyll, d - days, h - hours, m - metres, mg - milligrammes, $mMol\ N$ - millimoles of nitrogen, W - watts. The superscript ^{B} indicates normalisation to biomass (continued overleaf).

Parameter	Symbol	Units
From Chapter 2:		
Redefined in equation (A.9)	a	$m^{-1}\ day^{-1}$
Light attenuation by water	b	m^{-1}
Phytoplankton self-shading coefficient	c	$m^2(g\ C)^{-1}$
Phytoplankton concentration	P	$g\ C\ m^{-3}$
Defined here:		
Carbon to chlorophyll ratio, assumed constant	χ	$mg\ C\ (mg\ Chl)^{-1}$
Daylength as a fraction, $D' := D/24$	D'	dimensionless
Primary production rate in the mixed layer averaged over depth and over the entire day	$< P_{Z_m,T} >$	$mg\ C\ m^{-3}\ d^{-1}$

Table A.1 (ctd.).

Thus we have

$$< P_{Z_m,T} >= \frac{BP_m^B D}{(b+cP)Z_m}\left[f\left(I_*^m\right) - f\left(I_*^m e^{-KZ_m}\right)\right], \tag{A.2}$$

which we wish equate to $aP/(b+cP)$; $< P_{Z_m,T} >$ is measured in $mg\ C\ m^{-3}$ whilst $aP/(b+cP)$ has units of $g\ C\ m^{-3}$. We are assuming a constant carbon-to-chlorophyll ratio of 50:1, and define this conversion as $\chi = 50\ mg\ C\ (mg\ Chl)^{-1}$. Thus $B = P/(1000\ \chi)$ since P is measured in $g\ C\ m^{-3}$ in Chapter 2. Substituting for B in (A.2) gives $< P_{Z_m,T} >$ as

$$< P_{Z_m,T} >= \frac{PP_m^B D}{(b+cP)Z_m 1000\chi}\left[f\left(I_*^m\right) - f\left(I_*^m e^{-KZ_m}\right)\right]. \tag{A.3}$$

Now, we have

$$1000 < P_{Z_m,T} >= \frac{aP}{b+cP}, \tag{A.4}$$

(the 1000 converts the $mg\ C$ to $g\ C$) and see that the definition for a is thus

$$a = \frac{P_m^B D}{\chi Z_m}\left[f\left(I_*^m\right) - f\left(I_*^m e^{-KZ_m}\right)\right]. \tag{A.5}$$

Fasham (1993), hereafter Fa93, gave a maximum phytoplankton growth rate of V_p (d^{-1}), assumed constant throughout the year, from which P_m^B is obtained by

$$P_m^B = \frac{V_p\,\chi}{24}, \tag{A.6}$$

where the scalings are needed to convert to the appropriate units (the 24 represents the number of hours in a day).

The number of hours of sunlight in one day, D (h), is given by $D = 24\ D'$ where D' (dimensionless) is the fraction of the day for which there is sunlight, calculated from the following formula given by Brock (1981):

$$D' = \frac{1}{\pi} \arccos(-\tan\ \delta\ \tan\ \phi), \tag{A.7}$$

where (all angles being measured in radians) ϕ is the latitude, and the declination δ (the angle between the equatorial plane of the earth and the axis joining the centres of the sun and the earth) is given by

$$\delta = 0.409\ \sin\left(\frac{2\pi}{365}(284 + T)\right), \tag{A.8}$$

where T is the Julian Day, such that 1st January is Julian Day 1.

Substituting from (A.6) and $D = 24\ D'$ we obtain the following final form for a:

$$a = \frac{V_p D'}{Z_m}\left[f\left(I_*^m\right) - f\left(I_*^m e^{-KZ_m}\right)\right]. \tag{A.9}$$

There is a problem here that K actually depends on P, but we will investigate how important this dependence is when the parameter values are inserted. The normalised dimensionless noon irradiance I_*^m is defined as $I_*^m = I_0^m / I_k$ where I_0^m $(W\ m^{-2})$ is the surface irradiance at local noon (dependent on latitude, time of year and cloudiness), and I_k $(W\ m^{-2})$ is the photoadaption parameter of the photosynthesis-irradiance curve, defined as $I_k := P_m/\alpha$. It can be expressed in terms of the Fa93 parameters due to the following formula (which accounts for the differences in units):

$$I_k = \frac{P_m}{\alpha} = \frac{P_m^B}{\alpha^B} = \frac{\left(\frac{\chi V_p}{24}\right)}{\left(\frac{\chi \alpha_F}{24}\right)} = \frac{V_p}{\alpha_F}, \tag{A.10}$$

where α_F $((W\ m^{-2})^{-1}\ d^{-1})$ is the initial slope of the Fa93 (normalised) photosynthesis-irradiance curve.

Firstly, we are going to consider the daylength and irradiance conditions fixed at the values for 22nd June ($T = 173$) at Bermuda Station "S" (32° 10′N, 64° 30′W), in the North Atlantic Ocean. This is the day which has the most hours of sunlight, and the noon surface irradiance is practically at its maximum value. Bermuda is one of the two locations modelled by Fa93, the other being Ocean Weather Station "India" (59°N, 19°W), also in the North Atlantic Ocean.

We retain the SH81 default values of $b = 0.2$, $c = 0.4$ and $Z_m = 12.5$. The value used by Fa93 for V_p was $2.9d^{-1}$, and $\alpha_F = 0.025$ $(W\ m^{-2})^{-1}\ d^{-1}$, giving $I_k = 116\ W\ m^{-2}$. Using, as Fa93 did, the Smith and Dobson (1984) atmospheric transmittance algorithm with a cloud cover of 4 oktas yields a value of $I_0^m = 416\ W\ m^{-2}$ (using a program written by Andrew Yool, University of Warwick). This gives $I_*^m = 3.586$, for which $f(I_*^m) = 1.359$ using the polynomial approximation for $f(I_*^m)$ given by PS93, which is valid for the range $0.2 \leq I_*^m \leq 20$. [The polynomial approximation is $f(I_*^m) = 0.61035 I_*^m - 8.9251 \times 10^{-2}(I_*^m)^2 + 8.1477 \times 10^{-3}(I_*^m)^3 - 3.7427 \times 10^{-4}(I_*^m)^4 + 6.6103 \times 10^{-6}(I_*^m)^5$]. The Bermuda latitude of $\phi = 0.561^c (\equiv 32^\circ\ 10')$ gives, from (A.7) and (A.8), $D' = 0.5879$, equivalent to 14.1 hours. Substituting these values gives

$$a = 0.1364 \left[1.359 - f\left(3.586 e^{-12.5(0.2+0.4P)}\right)\right]. \tag{A.11}$$

Looking at the data for both Bermuda and India given by Fa93, concentrations of P are in the range 0.0025 - 0.16 $g\ C\ m^{-3}$ (equivalent to $0.05 - 3.2\ mg\ Chl\ m^{-3}$). In Figure A.1 we plot the values of a for a slightly larger range of P (the curve labelled 'summer'). It is seen that a does not vary much with P, and so for our model we can take the value calculated for $P = 0$, namely $a = 0.162$. This is equivalent to ignoring the self-shading component, cP, in the definition of a. This can be done since the value of the first term, $f(I_*^m)$, within the square brackets in (A.9) is much larger than the value of the second term, $f\left(I_*^m e^{-(b+cP)Z_m}\right)$, which reduces the value of a due to the light attenuation through the water column. The values are $f(I_*^m) = 1.359$, and $f\left(I_*^m e^{-(b+cP)Z_m}\right) = 0.172$ for $P = 0$ and $f\left(I_*^m e^{-(b+cP)Z_m}\right) = 0.0792$ for $P = 0.16$, and thus the P-dependence is not significant.

Therefore, for these parameter values at least, we can define a as

$$a = \frac{V_p D'}{Z_m}\left[f(I_*^m) - f\left(I_*^m e^{-bZ_m}\right)\right], \tag{A.12}$$

which is independent of P. But note that self-shading is not completely disregarded, as it is still considered in the final function $a/(b + cP)$ in the model. Although the

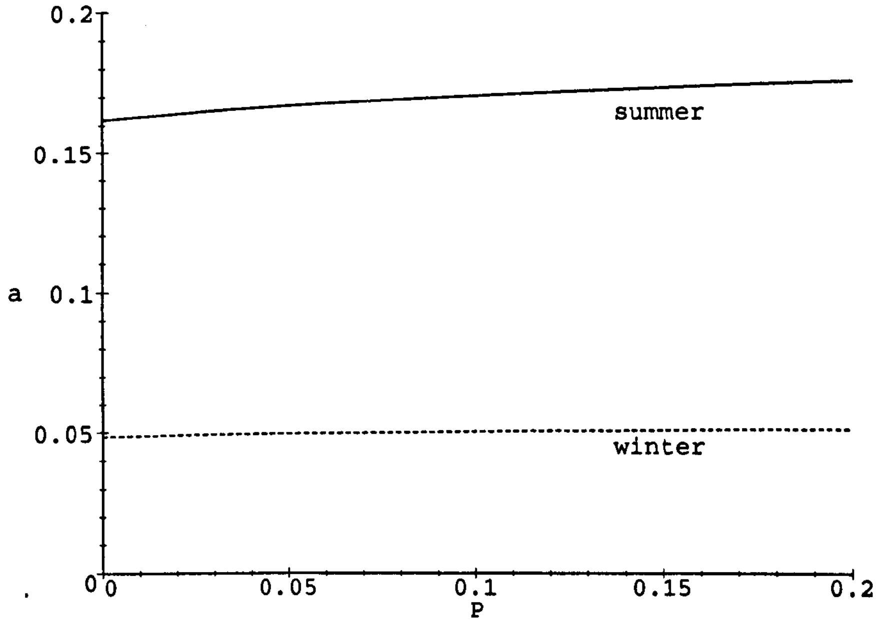

Figure A.1: The value of a, as defined by (A.9), does not vary significantly with P for either summertime or wintertime irradiance conditions at Bermuda; thus we can ignore the P-dependence of a.

value of a increases with P in Figure A.1, the specific growth term $a/(b + cP)$ does decrease with P, as would be expected due to the self-shading effect. The full growth term $aP/(b + cP)$ does then increase with P, as expected.

The second curve in Figure A.1, labelled 'winter', is the plot of a versus P for Julian Day 356 (22nd December), which is the shortest day of the year and has the minimum noon irradiance. Thus we have $T = 356$, which gives $D' = 0.4121$ (9.9 hours), and, from the program by Andrew Yool, $I_0^m = 124$. We retain $Z_m = 12.5$ for now, since this value of Z_m is also implicit in some of the other parameters in our model. Again we see that the value of a does not depend significantly on the level of P, and so using (A.12) to define a would again be a valid approximation. Setting Z_m to a winter mixed-layer depth would give yet a lower value of a.

We now consider the conditions for Ocean Weather Station 'India', for which Fa93 used $V_p = 1.25$. The latitude of 59° gives, for Julian Day 173, the longest daylength of 18.2 hours ($D' = 0.7565$), and noon irradiance of $I_0^m = 269$. This results in a value of $a = 0.108$ for $P = 0$, only rising to $a = 0.119$ for $P = 0.16$.

EP85 and Wr89 used a value of $V_p = 2.0$, which is between the two values used by Fa93. For the Bermuda conditions this gives a summer value of $a = 0.133$ for $P = 0$, and $a = 0.145$ for $P = 0.16$, which both fall, as expected, within the range of previously calculated values.

Pooling all of the summertime values together gives a range for a of 0.11-0.16, which falls well within the range given in Chapter 2. The insignificant P-dependence, as shown in Figure A.1, of the full a definition (equation (A.9)) allows the approximation in (A.12) to be used. The inaccuracies which arise due to using this approximation are clearly far outweighed by the overall changes in the value of a due to (i) time of year, as shown by Figure A.1; (ii) location, as seen by comparing Bermuda and 'India' values; or (iii) changes in parameter values (alternative V_p values or equivalent a/b values). Furthermore, other significant uncertainties arise, not only in values of the parameters, but even in the type of cloud cover algorithm used (for example, see Figure 4 of Fa93).

Bibliography

Adams, J. A. and Steele, J. H. (1966). Shipboard experiments on the feeding of *Calanus finmarchicus* (Gunnerus). In Barnes, H., editor, *Some Contemporary Studies in Marine Science*, pages 19–35. George Allen and Unwin Ltd., London.

Anderson, D. M. (1994). Red tides. *Scientific American*, 271(2):52–58.

Armstrong, R. A. (1994). Grazing limitation and nutrient limitation in marine ecosystems: Steady state solutions of an ecosystem model with multiple food chains. *Limnology and Oceanography*, 39(3):597–608.

Bougis, P. (1976). *Marine Plankton Ecology.* North-Holland Publishing Company, Amsterdam-Oxford.

Brock, T. D. (1981). Calculating solar radiation for ecological studies. *Ecological Modelling*, 14:1–19.

Caswell, H. and Neubert, M. G. (1997, in preparation). Chaos and closure terms in plankton food chain models.

Coale, K. H., Johnson, K. S., Fitzwater, S. E., Gordon, R. M., Tanner, S., Chavez, F. P., Ferioli, L., Sakamoto, C., Rogers, P., Millero, F., Steinberg, P., Nightingale, P., Cooper, D., Cochlan, W. P., Landry, M. R., Constantinou, J., Rollwagen, G., Trasvina, A., and Kudela, R. (1996). A massive phytoplankton bloom induced by an ecosystem-scale iron fertilization experiment in the equatorial Pacific Ocean. *Nature*, 383:495–501.

Collie, J. S. and Spencer, P. D. (1994). Modeling predator-prey dynamics in a fluctuating environment. *Canadian Journal of Fisheries and Aquatic Sciences*, 51:2665–2672.

Davis, C. S. and Steele, J. H. (1994). Biological/Physical Modeling of Upper Ocean Processes. Woods Hole Oceanographic Institution Technical Report, WHOI-94-32.

Denman, K., Hofmann, E., and Marchant, H. (1996). Marine biotic responses to environmental change and feedbacks to climate. In Houghton, J. T., Meira-Filho, L. G., Callander, B. A., Harris, N., Kattenberg, A., and Maskell, K., editors, *Climate Change 1995 - The Science of Climate Change. Contribution of Working Group I to the Second Assessment Report of the Intergovernmental Panel on Climate Change*, pages 482–516. Cambridge University Press, Cambridge.

Doedel, E., Wang, X., and Fairgrieve, T. (1994). AUTO: Software for continuation and bifurcation problems in ordinary differential equations. Applied Mathematics Report, California Institute of Technology.

Edwards, A. M. and Brindley, J. (1996). Oscillatory behaviour in a three-component plankton population model. *Dynamics and Stability of Systems*, 11(4):347–370.

Edwards, A. M., Hurtt, G. C., Ruesink, J., Zheng, D. W., and van den Driessche, P. (1997, in press). Predicting the effects of press perturbations on food webs. In Solow, A. R. and DeAngelis, D. D., editors, *Marine Food Webs*. Chapman and Hall.

Evans, G. T. (1988). A framework for discussing seasonal succession and coexistence of phytoplankton species. *Limnology and Oceanography*, 33(5):1027–1036.

Evans, G. T. and Fasham, M. J. R. (1993). Themes in modelling ocean biogeochemical processes. In Evans, G. T. and Fasham, M. J. R., editors, *Towards a Model of Ocean Biogeochemical Processes*, pages 1–19. Springer-Verlag, Berlin Heidelberg.

Evans, G. T. and Parslow, J. S. (1985). A model of annual plankton cycles. *Biological Oceanography*, 3(3):327–347.

Fasham, M. J. R. (1993). Modelling the marine biota. In Heimann, M., editor, *The*

Global Carbon Cycle, pages 457–504. Springer-Verlag, Berlin.

Fasham, M. J. R. (1995). Variations in the seasonal cycle of biological production in subarctic oceans: A model sensitivity analysis. *Deep-Sea Research I*, 42(7):1111–1149.

Fasham, M. J. R., Ducklow, H. W., and McKelvie, S. M. (1990). A nitrogen-based model of plankton dynamics in the oceanic mixed layer. *Journal of Marine Research*, 48:591–639.

Fasham, M. J. R., Sarmiento, J. L., Slater, R. D., Ducklow, H. W., and Williams, R. (1993). Ecosystem behavior at Bermuda Station "S" and Ocean Weather Station "India": a general circulation model and observational analysis. *Global Biogeochemical Cycles*, 7(2):379–415.

Fell, N. and Liss, P. (1993). Can algae cool the planet? *New Scientist*, 21 August:34–38.

Franks, P. J. S., Wroblewski, J. S., and Flierl, G. R. (1986). Behavior of a simple plankton model with food-level acclimation by herbivores. *Marine Biology*, 91:121–129.

Frost, B. W. (1987). Grazing control of phytoplankton stock in the open subarctic Pacific Ocean: a model assessing the role of mesozooplankton, particularly the large calanoid copepods *Neocalanus* spp. *Marine Ecology Progress Series*, 39:49–68.

Frost, B. W. (1996). Phytoplankton bloom on iron rations. *Nature*, 383:475–476.

Gaspard, P. and Wang, X.-J. (1987). Homoclinic orbits and mixed-mode oscillations in far-from-equilibrium systems. *Journal of Statistical Physics*, 48(1/2):151–199.

Glendinning, P. (1994). *Stability, Instability and Chaos: An Introduction to the Theory of Nonlinear Differential Equations.* Cambridge Texts in Applied Mathematics. Cambridge University Press, Cambridge.

Glendinning, P. and Laing, C. (1996). A homoclinic hierarchy. *Physics Letters A*, 211:155–160.

Glendinning, P. and Sparrow, C. (1984). Local and global behavior near homoclinic orbits. *Journal of Statistical Physics*, 35(5/6):645–696.

Guckenheimer, J. and Holmes, P. (1983). *Nonlinear Oscillations, Dynamical Systems, and Bifurcations of Vector Fields*, volume 42 of *Applied Mathematical Sciences*. Springer-Verlag, New York.

Guckenheimer, J., Myers, M. R., Wicklin, F. J., and Worfolk, P. A. (1991). Dstool: A dynamical system toolkit with an interactive graphical interface. Center for Applied Mathematics, Cornell University, New York.

Hastings, A. and Powell, T. (1991). Chaos in a three-species food chain. *Ecology*, 72(3):896–903.

Henderson, E. W. and Steele, J. H. (1995). Comparing models and observations of shelf plankton. *Journal of Plankton Research*, 17(8):1679–1692.

Hofmann, E. E. and Ambler, J. W. (1988). Plankton dynamics on the outer southeastern U.S. continental shelf. Part II: A time-dependent biological model. *Journal of Marine Research*, 46:883–917.

Hutson, V. (1984). Predator mediated coexistence with a switching predator. *Mathematical Biosciences*, 68:233–246.

Jones, R. and Henderson, E. W. (1986). The dynamics of nutrient regeneration and simulation studies of the nutrient cycle. *Journal du Conseil*, 43(3):216–236.

Khibnik, A. I., Kuznetsov, Y. A., Levitin, V. V., and Nikolaev, E. V. (1992). Interactive LOCal BIFurcation analyzer. Computer Algebra Netherlands.

Kuznetsov, Y. A. (1995). *Elements of Applied Bifurcation Theory*, volume 112 of *Applied Mathematical Sciences*. Springer-Verlag, New York.

Levitin, V. and Khibnik, A. (1991). TraX simulation and analysis of dynamical systems. Applied Biomathematics, New York.

Martin, J. H., Coale, K. H., Johnson, K. S., Fitzwater, S. E., Gordon, R. M., Tanner, S. J., Hunter, C. N., Elrod, V. A., Nowicki, J. L., Coley, T. L., Barber, R. T., Lindley, S., Watson, A. J., Scoy, K. V., Law, C. S., Liddicoat, M. I., Ling, R., Stanton, T., Stockel, J., Collins, C., Anderson, A., Bidigare, R., Ondrusek, M., Latasa, M., Millero, F. J., Lee, K., Yao, W., Zhang, J. Z., Friederich, G., Sakamoto, C., Chavez, F., Buck, K., Kolber, Z., Greene, R., Falkowski, P., Chisholm, S. W., Hoge, F., Swift, R., Yungel, J., Turner, S., Nightingale, P., Hatton, A., Liss, P., and Tindale, N. W. (1994). Testing the iron hypothesis in ecosystems of the equatorial Pacific Ocean. *Nature*, 371:123–129.

Matthews, L. and Brindley, J. (1997). Patchiness in plankton populations. *Dynamics and Stability of Systems*, 12(1):39–59.

McCann, K. and Yodzis, P. (1995). Bifurcation structure of a three-species food chain model. *Theoretical Population Biology*, 48:93–125.

McCauley, E. and Murdoch, W. W. (1987). Cyclic and stable populations: plankton as paradigm. *The American Naturalist*, 129(1):97–121.

Mullin, T. (1993). A multiple bifurcation point as an organizing centre for chaos. In Mullin, T., editor, *The Nature of Chaos*, pages 51–68. Oxford University Press, Oxford.

Murray, J. D. (1989). *Mathematical Biology*, volume 19 of *Biomathematics*. Springer-Verlag, Berlin Heidelberg.

Nybakken, J. W. (1982). *Marine Biology: An Ecological Approach*. Harper and Row, New York.

Parsons, T. R., LeBrasseur, R. J., Fulton, J. D., and Kennedy, O. D. (1969). Production studies in the Strait of Georgia. Part II. Secondary production under the Fraser River plume, February to May, 1967. *Journal of Experimental Marine Biology and Ecology*, 3:39–50.

Parsons, T. R. and Takahashi, M. (1973). *Biological Oceanographic Processes*. Pergamon Press Ltd., Oxford.

Perko, L. (1993). *Differential Equations and Dynamical Systems*, volume 7 of *Texts in Applied Mathematics*. Springer-Verlag, New York.

Pitchford, J. W. (1997). *Dynamics of Multi-Species Plankton Populations.* PhD thesis, University of Leeds.

Platt, T., Broomhead, D. S., Sathyendranath, S., Edwards, A. M., and Murphy, E. J. (1997, in preparation). Phytoplankton biomass and residual nitrate in the pelagic ecosystem.

Platt, T., Mann, K. H., and Ulanowicz, R. E., editors (1981). *Mathematical Models in Biological Oceanography,* volume 7 of *Monographs on Oceanographic Methodology.* The Unesco Press, Paris.

Platt, T. and Sathyendranath, S. (1993). Estimators of primary production for interpretation of remotely sensed data on ocean color. *Journal of Geophysical Research,* 98(C8):14,561–14,576.

Platt, T., Sathyendranath, S., and Ravindran, P. (1990). Primary production by phytoplankton: analytic solutions for daily rates per unit area of water surface. *Proceedings of the Royal Society of London, Series B,* 241:101–111.

Raymont, J. E. G. (1980). *Plankton and Productivity in the Oceans. Second Edition. Volume 1 - Phytoplankton.* Pergamon Press Ltd., Oxford.

Raymont, J. E. G. (1983). *Plankton and Productivity in the Oceans. Second Edition. Volume 2 - Zooplankton.* Pergamon Press Ltd., Oxford.

Robinson, I. S. (1990). Remote sensing - information from the colour of the seas. In Herring, P. J., Campbell, A. K., Whitfield, M., and Maddock, L., editors, *Light and life in the sea,* pages 19–38. Cambridge University Press, Cambridge.

Ryabchenko, V. A., Fasham, M. J. R., Kagan, B. A., and Popova, E. E. (1997, in press). What causes short-term oscillations in ecosystem models of the ocean mixed layer? *Journal of Marine Systems.*

Sarmiento, J. L., Slater, R. D., Fasham, M. J. R., Ducklow, H. W., Toggweiler, J. R., and Evans, G. T. (1993). A seasonal three-dimensional ecosystem model of nitrogen cycling in the North Atlantic euphotic zone. *Global Biogeochemical Cycles,* 7(2):417–450.

Sathyendranath, S. and Platt, T. (1990). The light field in the ocean: its modification and exploitation by the pelagic biota. In Herring, P. J., Campbell, A. K., Whitfield, M., and Maddock, L., editors, *Light and Life in the Sea*, pages 3–18. Cambridge University Press, Cambridge.

Smith, S. D. and Dobson, F. W. (1984). The heat budget at Ocean Weather Station *Bravo*. *Atmosphere-Ocean*, 22(1):1–22.

Steele, J. H. (1962). Environmental control of photosynthesis in the sea. *Limnology and Oceanography*, 7(2):137–150.

Steele, J. H. and Frost, B. W. (1977). The structure of plankton communities. *Philosophical Transactions of the Royal Society of London, Series B*, 280:485–534.

Steele, J. H. and Henderson, E. W. (1981). A simple plankton model. *The American Naturalist*, 117(5):676–691.

Steele, J. H. and Henderson, E. W. (1992). The role of predation in plankton models. *Journal of Plankton Research*, 14(1):157–172.

Steele, J. H. and Henderson, E. W. (1993). The significance of interannual variablitiy. In Evans, G. T. and Fasham, M. J. R., editors, *Towards a Model of Ocean Biogeochemical Processes*, pages 237–260. Springer-Verlag, Berlin Heidelberg.

Steele, J. H. and Henderson, E. W. (1995). Predation control of plankton demography. *ICES Journal of Marine Science*, 52:565–573.

Tait, R. V. (1981). *Elements of Marine Ecology - Third Edition*. Butterworth & Co., London.

Taylor, A. H., Harbour, D. S., Harris, R. P., Burkill, P. H., and Edwards, E. S. (1993). Seasonal succession in the pelagic ecosystem of the North Atlantic and the utilization of nitrogen. *Journal of Plankton Research*, 15(8):875–891.

Taylor, A. H. and Joint, I. (1990). A steady-state analysis of the 'microbial loop' in stratified systems. *Marine Ecology Progress Series*, 59:1–17.

Thompson, J. M. T. and Stewart, H. B. (1986). *Nonlinear Dynamics and Chaos.* John Wiley and Sons, Chichester.

Thurman, H. V. (1997). *Introductory Oceanography - Eighth Edition.* Prentice-Hall, New Jersey.

Toggweiler, J. R. (1990). Modeling workshop offers first look at new simulation of Equatorial Pacific. *U.S. JGOFS News*, 2(2):1 and 11.

Totterdell, I. J. (1993). An annotated bibliography of marine biological models. In Evans, G. T. and Fasham, M. J. R., editors, *Towards a Model of Ocean Biogeochemical Processes*, pages 317–339. Springer-Verlag, Berlin Heidelberg.

Totterdell, I. J., Armstrong, R. A., Drange, H., Parslow, J. S., Powell, T. M., and Taylor, A. H. (1993). Trophic resolution. In Evans, G. T. and Fasham, M. J. R., editors, *Towards a Model of Ocean Biogeochemical Processes*, pages 71–92. Springer-Verlag, Berlin Heidelberg.

Truscott, J. E. (1994). *Temporal and Spatial Behaviour of Plankton Ecosystems.* PhD thesis, University of Leeds.

Truscott, J. E. (1995). Environmental forcing of simple plankton models. *Journal of Plankton Research*, 17(12):2207–2232.

Truscott, J. E. and Brindley, J. (1994). Equilibria, stability and excitability in a general class of plankton population models. *Philosophical Transactions of the Royal Society of London, Series A*, 347:703–718.

Turner, S. M., Nightingale, P. D., Spokes, L. J., Liddicoat, M. I., and Liss, P. S. (1996). Increased dimethyl sulphide concentrations in sea water from *in situ* iron enrichment. *Nature*, 383:513–516.

Ulanowicz, R. E. and Platt, T., editors (1985). *Ecosystem Theory for Biological Oceanography*, volume 213 of *Canadian Bulletin of Fisheries and Aquatic Sciences.*

Wiggins, S. (1988). *Global Bifurcations and Chaos: Analytical Methods*, volume 73 of *Applied Mathematical Sciences.* Springer-Verlag, New York.

Wiggins, S. (1990). *Introduction to Applied Nonlinear Dynamical Systems and Chaos*, volume 2 of *Texts in Applied Mathematics.* Springer-Verlag, New York.

Williams, R. (1988). Spatial heterogeneity and niche differentiation in oceanic zooplankton. In Boxshall, G. A. and Schimke, H. K., editors, *Biology of Copepods. Hydrobiologia*, 167/168:151–159.

Woods, J. and Barkmann, W. (1994). Simulating plankton ecosystems by the Lagrangian Ensemble method. *Philosophical Transactions of the Royal Society of London, Series B*, 343:27–31.

Wroblewski, J. S. (1989). A model of the spring bloom in the North Atlantic and its impact on ocean optics. *Limnology and Oceanography*, 34(8):1563–1571.

Yodzis, P. (1981). The stability of real ecosystems. *Nature*, 289:674–676.

Yodzis, P. (1988). The indeterminacy of ecological interactions as perceived through perturbation experiments. *Ecology*, 69(2):508–515.

Yodzis, P. (1989). *Introduction to Theoretical Ecology.* Harper and Row, New York, NY.

Yool, A. (1997, in preparation). *The Dynamics of Open-Ocean Plankton Ecosystem Models.* PhD thesis, University of Warwick.